Hybrid nanostructures mediated biosensing and epigenetically controlled neurotherapeutic applications in neurodegenerative diseases

Anup Kumar Srivastava

A thesis submitted for partial fulfilment of
the degree of

Doctor of Philosophy

Institute of Nano Science and Technology, Mohali, India

Indian Institute of Science Education and Research, Mohali, India

December 2019

Dedicated to my parents.

Declaration

The work presented in this thesis has been carried out by me under the guidance of Dr. Surajit Karmakar at the Institute of Nano Science and Technology Mohali. This work has not been submitted in part or in full for a degree, diploma or a fellowship to any other University or Institute. Whenever contributions of others are involved, every effort has been made to indicate this clearly, with due acknowledgment of collaborative research and discussions. This thesis is a bonafide record of original work done by me and all sources listed within have been detailed in the bibliography.

Place: .....

Date: **Anup K. Srivastava**

In my capacity as the supervisor of the candidate's Ph.D. thesis work, I certify that the above statements by the candidate are true to the best of my knowledge.

.....

Place: **Dr. Surajit Karmakar**

Date: Scientist-F/ Professor

Institute of Nano Science and Technology, Mohali

Acknowledgments

I thank my Ph.D. supervisor Dr. Surajit Karmakar for his guidance and constant support throughout the duration of my thesis work. I express my gratitude towards him for being a great mentor and an outstanding personality.

I am thankful to Prof. Amitava Patra (Director, INST) Prof. Ashok K. Ganguli, (Former Director, INST), Prof. H.N. Ghosh (Officiating Director, INST), Prof. N. Sathyamurthy (Former Director, IISERM) and Prof. J. Gowrishankar (Director, IISERM) for their support and encouragement. I would express my sincere gratitude to Dr. Subhasree Roy Choudhury (INST, Mohali), Prof. Prasenjit Guchhait (Regional Centre for Biotechnology, Faridabad, India) and Prof. Shyam Sunder Sharma (NIPER, Mohali) for their supportive collaboration for the thesis work.

I am grateful to the doctoral committee members – Dr. Sharmistha Sinha and Dr. Prakash P. Neelakandan for their suggestions and timely review of the progress of my Ph.D. work. I am grateful to Prof. Anand Bacchawat (IISER, Mohali), Prof. Purnanand Guptasharma (IISER Mohali), Dr. Sharvan Sehrawat (IISER Mohali) and their lab members (Muskaan, Bhishem, Manpreet and Dhanesh) for their extended support. I want to extend my sincere thanks to Dr. Sanjeev (Presently Associate Professor at Dept of Zoology, BHU, Varanasi), Dr. Madhunika and Dr. Pankaj. K. Singh (Presently Scientist at NIPER Hyderabad). I thank my group members Mr. Atul Sharma, Ms. Babita, Mr. Nadim Sardoiwala, Avinash, Jignesh, for extending their help whenever needed. This acknowledgment would be incomplete without a mention of a few people – Abhishek Mishra, Gaurav Sharma, Swati Tanwar, Ankush Garg, Naimat K. Bari, Rajinder K. Chaudhury, Satish Tiwari, Anuj Shukla and Vinod Kumar.

I would like to thank my teachers – Mr. Akhilesh Yadav, Prof. Ashok Kumar (SBT, BHU), Prof. S.M. Singh (SBT, BHU), and Prof. A. Kayastha (SBT, BHU) for motivating me to do research. Besides, I thank the Council for Scientific and Industrial Research (CSIR), India for providing fellowship as a junior research fellow and senior research fellow and international travel award. I also gratefully acknowledge the Department of Biotechnology (DBT) for providing international travel support. My deepest gratitude to my parents and family members for their patience and moral supports.

Anup K. Srivastava

List of publications

Relevant to the thesis

- Near-Infrared Responsive Dopamine/Melatonin Derived Nanocomposites Abrogating In-situ Amyloid Beta Nucleation, Propagation and Ameliorate Neuronal Function. **Anup K. Srivastava**; S.R. Choudhury; S. Karmakar; ACS Applied Materials and Interface. 2020, 12, 5, 5658-5670.

- Melatonin/Polydopamine Nanostructures for Collective Neuroprotection based Parkinson's Disease Therapy. **Anup K. Srivastava**; S.R. Choudhury; S. Karmakar. Biomaterials science; 2020,8, 1345-1363.

- New insight into curcumin tethered lanthanum carbonate nanospheres and protein corona conferring fluorescence enhancement based sensitive detection of Amyloid-β aggregates. ***Anup K. Srivastava***; A. Dev; S.R. Choudhury; S. Karmakar Sensors and Actuators B: Chemical. 2018;262(1)

- Nanosensors and nanobiosensors in food and agriculture; **Anup K Srivastava**, Atul Dev and Surajit Karmakar; Review: December 2017; DOI: 10.1007/s10311-017-0674-7; Environmental Chemistry Letters 16(4).

- Neuronal BMI-1 mediates ubiquitination and proteasomal degradation of alpha-synuclein in Parkinson's Disease. **Anup K. Srivastava**; S.R. Choudhury; S. Karmakar. (Under Review).

Other publications

- Nanostructure Endows Neurotherapeutic Potential in Optogenetics: Current Development and Future Prospects. Sardoiwala, M. N., **Srivastava Anup K.,** Karmakar. S., Choudhury S. R., ACS Chem Neurosci 10(8): 3375-3385.

- Recuperative effect of metformin loaded Polydopamine Nanoformulation promoting EZH2 mediated proteasomal degradation of phospho-α-Synuclein in Parkinson's disease model. Sardoiwala, M. N., **Srivastava Anup K**., Kaundal B., Karmakar. S., Choudhury S. R., Nanomedicine: Nanotechnology, Biology and Medicine: 102088.

- Nanoformulation of EPZ011989 Attenuates EZH2–c-Myb Epigenetic Interaction by Proteasomal Degradation in Acute Myeloid Leukemia. B. Kaundal, **A. K. Srivastava**, A. Dev, J.M. soni, S.Karmakar, S.R. Choudhury., ACS Mol Pharm, 2020, 17, 2, 604–621.

- NIR-responsive Indocyanine green-Genistein Nanoformulation controlling Polycomb epigenetic machinery for efficient Photo-Chemo-Combotherapy of Glioblastoma; B. Kaundal, **Anup K. Srivastava**, Mo. N. Sardoiwala, S. Karmakar, S. R. Choudhury; Nanoscale Advances; 20191.

- 1,3 beta-Glucan anchored, paclitaxel loaded chitosan nanocarrier endows enhanced hemocompatibility with efficient anti-glioblastoma stem cells therapy Singh PK1, **Srivastava AK1**, Dev A, Kaundal B, Choudhury SR, Karmakar S. Carbohydrate polymers. 2018; 180:365-75.

- Hypoxia-mediated alteration in cholesterol oxidation and raft dynamics regulates BDNF signaling and neurodegeneration in the hippocampus. Sharma, D., Barhwal, K. K., Biswal, S. N., **Srivastava, A. K.**, Bhardwaj, P., Kumar, A., Chaurasia, O. P. and Hota, S. K. (2019), J. Neurochem., 148: 238-251.

- Nanomelatonin triggers superior anticancer functionality in a human malignant glioblastoma cell line; Kumar Yadav S1, **Kumar Srivastava A1**, Dev A, Kaundal B, Roy Choudhury S, Karmakar S. Nanotechnology. 2017 Aug 18;28(36):365102. doi: 10.1088/1361-6528/aa7c76

- Nano-curcumin influences blue light photodynamic therapy for restraining glioblastoma stem cells growth; A. Dev, **A. K. Srivastava**, S. Roy Choudhury and S. Karmakar* DOI: 10.1039/C6RA20269A (Communication) RSC Adv., 2016, 6, 95165-95168

- Nanomaterial toxicity for plants; Atul Dev, **Anup K Srivastava** and Surajit Karmakar Review: October 2017; DOI: 10.1007/s10311-017-0667-6; Environmental Chemistry Letters

- New Generation hybrid nanobiocatalysts: The catalysis redefined, Handbook of Nanomaterials for Industrial Applications Atul Dev; **Anup K Srivastava** and Surajit Karmakar; Chapter: Handbook of Nanomaterials for Industrial Applications

- Nanosensors for Food and Agriculture; **Anup K Srivastava**, Atul Dev and Surajit Karmakar Chapter · July 2017; DOI: 10.1007/978-3-319-58496-6_3; In book: Nanoscience in Food and Agriculture 5, pp.41-79

- Uptake and Toxicity of Nanomaterials in Plants; Atul Dev, **Anup K Srivastava** and Surajit Karmakar; Chapter · July 2017; DOI: 10.1007/978-3-319-58496-6_7; In book: Nanoscience in Food and Agriculture 5, pp.169-204

Contents

	# Page
Abstract	**1**
Synopsis	**2-10**
Chapter 1: Introduction	**11-24**
1. Neurodegeneration	11
2. Pathobiology of Alzheimer's disease (AD)	11
2.1 Management of AD	
2.1.1 APP processing and Aβ targeting	14
2.1.2 Targeting Aβ aggregation kinetics	14
2.1.3 Aβ clearance pathway	15
3. Parkinson's disease	16
3.1 The implication of α-SYN phosphorylation at serine 129	17
3.2 Molecular pathobiology of PD	18
4. Epigenetic- polycomb group of proteins (PcG) function	19
5. Nanotechnology in neuroscience	21
5.1 Nanostructures based neurotherapeutics	21
6. Melatonin as a potent neuroprotective	22
7. Objective and outline of the thesis	23
Chapter 2: Materials and methods	**25-44**
1. Reagents	25
2. Preparations and purifications	
2.1 Synthesis of melatonin/polydopamine hybrid nanostructures	25
2.2 Synthesis of lanthanum carbonate nanospheres	26
3. Morphological and structural characterizations	
3.1Dynamic light scattering	27
3.2 Transmission electron microscopy (TEM)	27
3.2 Scanning electron microscopy- energy dispersive X-ray spectroscopy (SEM-EDS)	27
3.4 Steady-state fluorescence emission measurements	28
3.5 UV−Vis absorption spectroscopy measurement	28
3.6 Fourier-transformed Infra-red spectroscopy measurement	29
3.7 Thermogravimetric Analysis (TGA)	29
3.8 X-ray photoelectron spectroscopy (XPS)	29

3.9 Nuclear Magnetic Resonance (NMR) Studies 29
4. Particle Stability, Integrity and drug release studies 29
5. Monolayer cell and three-dimensional organoid culture 30
6. Treatments 30
6.1 In-vitro Parkinson's disease model 31
6.2 In-vitro Alzheimer's disease model 32
7. Mitochondrial membrane potential ($\Delta\Psi m$) measurement 32
8. Immunofluorescence staining 33
9. Intracellular reactive oxygen species (ROS) estimation 33
10. Apoptosis assay 34
11. Organotypic whole brain slice culture and immunostaining 34
12. Animals and Administrations 35
13. In-vivo imaging and Biodistribution study 36
14. Brain Tissue Processing and Immunohistochemistry 37
15. Total RNA extraction, cDNA synthesis, and
Quantitative Real-Time PCR (qPCR) 37
16. Protein preparation and western-blot 39
17. Immunoprecipitation assay 40
18. Assessment of the photothermal effect 41
19. Amyloid beta (Aβ) fibrillation and anti-aggregation assessment 41
20. Aβ- Protein Misfolding Cyclic Amplification (Aβ-PMCA) Assay 42
21. In-vitro Aβ disaggregation studies 42
22. Protein adsorption measurement and surface covering 42
23. Steady-state fluorescence anisotropy measurement 43
24. Data processing and significance analysis 43

Chapter 3: Studying intrinsic reactivity between dopamine derived intermediates and melatonin, upon co-abundance forming Melatonin/Polydopamine nanostructure 45-63

1. Background 45
2. Results and discussions
2.1 Fabrication and Characterization of melatonin/polydopamine hybrid
Nanostructures 46
2.2 The hybrid nanostructures evolution mechanism and interactions 50
2.3 Stability and Integrity of nanostructure 55
2.4 Melatonin cumulative release pattern 58
3. Conclusion 59

Chapter 4: Brain targeting of melatonin loaded polydopamine nanostructures (mPDAN) for collective neuroprotection in Parkinson 's disease models 64-78
1. Background 64
2. Results and Discussion
2.1 In-vitro SH-SY5Y PD model preparation 65
2.2 Estimation of effective neuroprotective concentration 65
2.3 Internalization in Monolayer and three-dimensional organoid 66
2.4 Anti-oxidant potential measurement 67
2.5 Anti-Apoptotic activity estimation 68
2.6 Mitochondrial membrane potential measurement 69
2.7 Estimation of Caspase-3 level 69
2.8 Anti-inflammatory effect 70
2.9 mPDAN controls the alpha-synuclein phosphorylation associated Oligomerization 72
2.10 In-vivo and ex-vivo distribution of the mPDAN 73
2.11 Neuroprotective effect on ex-vivo PD model 74
2.12 Therapeutic efficacy on in-vivo PD mice model 75
3. Conclusion 77

Chapter 5: Enriched melatonin facilitates Polycomb protein BMI-1 mediated ubiquitination and proteasomal degradation of alpha-synuclein in Parkinson's disease (PD) model 79-90
1. Background 79
2. Results and Discussions
2.1 Alpha-synuclein hyperphosphorylation (pα-SYN (S129)) and cellular accumulation substantiates PD model 80
2.2 Implication of decreased polycomb repressor complex 1 subunit BMI-1 and H2AK119ub in PD 81
2.3 Melatonin enrichment suppresses rotenone-induced Bmi-1 phosphorylation 81
2.4 BMI-1 and pα-SYN (S129) are reciprocally regulated upon Mel enrichment 82
2.5 BMI-1 mediates ubiquitin-dependent proteasomal degradation of pα-SYN (S129) in PD 84
2.6 Mel enrichment mediates BMI-1 dependent regulation of pα-SYN (S129) level in PD 85
2.7 Enriched Mel induces superior neuroprotection on in-vivo PD model 89
3. Conclusion 90

Chapter 6a: Dopamine inspired quantum sized dots for multimodal fluorescence screening of the live and dead dopaminergic neuronal cell population 91-99
1. Background 91
2. Results and discussion
2.1 Preparation of DI-10 92
2.2 Morphological and structural characterization 93
2.3 Multimodal optical characteristics of DI-10 94
2.4 Cellular compatibility of DI-10 96
2.5 In-vivo biodistribution and histopathological effect of DI-10 97
2.6 FACS based screening of the live and dead population 98
3. Conclusion 99
Chapter 6b: Developing stimuli-responsive amyloid-beta anti-aggregation agent and neuroprotection in Alzheimer's disease model 100-112
1. Background 100
2. Results and Discussions
2.1 NIR Responsive Photothermal Effect of DM-NCs 101
2.2 Aβ anti-aggregation effect 102
2.3 Aβ disaggregation effect 104
2.4 Aβ-Protein Misfolding Cyclic Amplification (Aβ-PMCA) Assay 105
2.5 Cell viability assay 106
2.6 DM-NCs scavenge Intracellular ROS 107
2.7 Compatibility to Neurite processes 108
2.8 Estimation of in-situ Aβ Processing 109
2.9 Therapeutic assessment in mice mid-brain slice culture AD model 110
3. Conclusions 112
Chapter 6c: Protein-nanoparticles corona-based fluorescence biosensor for sensitive detection of Amyloid-β protein 113-125
1.Background 113
2. Results and Discussion
2.1 Synthesis and characterization of Lanthanum carbonate nanospheres (REM_{100}) 114
2.2 REM_{100} and curcumin interaction 117
2.3 Protein adsorption on Cur-REM_{100} 119
2.4 Confirmation of Protein-Cur-REM_{100} 121
2.5 Detection of Aβ conformations 123
3. Conclusion 124
Summary 126-129
References 130-146

List of figures

Figure 1.1. The Amyloid beta (Aβ) processing, aggregation, and therapeutic targets.

Figure 1.2. The representation of α-SYN aggregation and pathobiology in PD.

Figure 1.3. Polycomb group of protein complexes function.

Figure 3.1. The schematic illustrates the steps for mPDAN preparation.

Figure 3.2. The photon correlation spectroscopic measurement of mPDAN variants.

Figure 3.3. Morphological characterization of the mPDAN variants.

Figure 3.4. The mean hydrodynamic diameter of the DM-NCs obtained by dynamic light scattering (DLS) measurement.

Figure 3.5. UV-vis spectroscopic analysis of DM-NCs synthesis.

Figure 3.6. ^{1}H NMR study of DM-NCs synthesis.

Figure 3.7. The 1H NMR spectrums acquired (0 ppm to 8 ppm, right to left) 1 mM Dopamine (DA) in deuterium dioxide (D_2O).

Figure 3.8. The 1H NMR spectrum acquired (0 ppm to 8 ppm, right to left) for 1 mM dissolved in Deuterium dioxide and dimethyl sulphoxide solvent mixture.

Figure 3.9. The 1H NMR spectrum acquired (0 ppm to 8 ppm, right to left) for 1mM Mel with 1 mM DA in Deuterium dioxide and dimethyl sulphoxide solvent mixture.

Figure 3.10. The 1H NMR spectrum acquired (0 ppm to 8 ppm, right to left) for DA, 120 min after addition of 1 mM $NaIO_4$.

Figure 3.11. The 1H NMR spectrum acquired (0 ppm to 8 ppm, right to left) for 1 mM Mel with 1 mM DA, 120 min after addition of 1mM $NaIO_4$ in Deuterium dioxide and dimethyl sulphoxide solvent mixture.

Figure 3.12. The hydrodynamic particle size distribution of DM-NCs (1:1).

Figure 3.13. The DM-NCs stability and integrity studies.

Figure 3.14. The fluorescence emission intensity of the DM-NCs and PDANPs incubated in hydrogen peroxide (5 mM and 10 mM).

Figure 3.15. Estimation of melatonin loading and cumulative release (%).

Figure 4.1. Rotenone induced in-vitro model preparation and estimation of effective neuroprotection dose.

Figure 4.2. Cellular internalization of mPDAN in monolayer and three-dimensional neuroblastoma culture.

Figure 4.3. Measurement of intracellular ROS scavenging ability of mPDAN.

Figure 4.4. Annexin V-PE and 7-AAD based apoptosis measurement.

Figure 4.5. Confocal microscopy analysis of mitochondrial membrane potential and caspase-3 level in three-dimensional neuroblastoma PD model.

Figure 4.6. qPCR based gene expression analysis of inflammation and apoptosis-associated genes.
Figure 4.7: The western blot examination of pα-SYN(S129) and caspase-3 protein on the *in-vitro* PD model.
Figure 4.8. The *in-vivo and ex-vivo* biodistribution and histopathological analysis.
Figure 4.9. The assessment of mPDAN in organotypic adult mice brain slice culture.
Figure 4.10. The immunofluorescence-based examination pα-SYN(S129) and tyrosine hydroxylase (TH) on in-vivo PD mice model the midbrain section.
Figure 5.1. The rotenone triggers α-synuclein hyperphosphorylation and downregulates polycomb repressor complex 1 (PRC1) function in SH-SY5Y cells.
Figure 5.2. Rotenone and melatonin are differently regulating BMI-1 phosphorylation and expression of polycomb repressor complex (PRC) subunit genes.
Figure 5.3. BMI-1 and pα-SYN (S129) are reciprocally regulated upon Mel enrichment in the SH-SY5Y PD model.
Figure 5.4. Role of proteasomal degradation machinery and BMI-1 in pα-SYN (S129) regulation.
Figure 5.5. Melatonin enrichment regulates BMI-1 dependent pα-SYN (S129) level in PD.
Figure 5.6. BMI-1 mediates ubiquitin-dependent proteasomal degradation of pα-SYN (S129) in PD.
Figure 5.7. mPDAN induces superior neuroprotection on in-vivo PD model.
Figure 5.8. The immunofluorescence studies in the brain section of the PD mice model.
Figure 6.11. Synthesis and optical characterization of DI-10.
Figure 6.12. Morphological characterization of DI-10.
Figure 6.13. Structural characterization of DI-10.
Figure 6.14. Photonic characteristics and thermal stability.
Figure 6.15. Cell viability assay of DI-10.
Figure 6.16. Multiplex bioimaging property of DI-10.
Figure 6.17. The *in-vivo* and *ex-vivo* whole-body distribution and an anti-apoptotic assay of DI-10.
Figure 6.18. DI-10 for live/dead FACS based assay.
Figure 6.21. The NIR responsive photothermal effect of DM-NCs.
Figure 6.22: The NIR responsive melatonin release pattern of DM-NCs.
Figure 6.23. The NIR responsive Aβ anti-aggregation effect of DM-NCs.
Figure 6.24. The Aβ fibrils disaggregation assay using DM-NCs.
Figure 6.25. Aβ-protein misfolding cyclic amplification (Aβ-PMCA) assay.
Figure 6.26. The SH-SY5Y cell viability measured using MTT assay.

Figure 6.27. FACS based estimation of intracellular reactive oxygen species (ROS) on *in-vitro* AD model
Figure 6.28. Axonal Differentiation Assay.
Figure 6.29. Lower Aβ processing in the AD cellular model.
Figure 6.30. Therapeutic assessment in ex-vivo adult mice midbrain slice culture AD model.
Figure 6.31. The particle size distribution and zeta potential of REM_{100}.
Figure 6.32. Morphological and structural characterization of $REM_{100.}$
Figure 6.33. The energy-dispersive X-ray spectroscopy of $REM_{100.}$
Figure 6.34. The UV-vis studies of curcumin- REM_{100} interaction.
Figure 6.35. The Fourier Transformed Infra-Red (FTIR) and fluorescence emissios spectroscopic results for Cur and REM_{100} interaction.
Figure 6.36. The steady-state fluorescence spectrum measurement of Protein-Cur-REM_{100}.
Figure 6.37. The maximum surface coverage and specific biding of proteins on Cur-REM_{100}.
Figure 6.38. The steady-state fluorescence anisotropy measurement.
Figure 6.39. Fluorescence-based detection of the Aβ monomer and Aβ aggregates.

List of Schematics

Scheme 1. The illustration of mPDAN targeting to the brain regulating alpha-synuclein processing and confers therapeutic effect in Parkinson's disease.

Scheme 6.3. The illustration representing the fabrication of Cur-REM_{100} as a protein nanoparticle corona-based biosensor for the detection of the Aβ monomer and Aβ aggregated states.

List of Tables

Table 2.1. The cDNA synthesis reaction mixture

Table 2.2. The qPCR reaction component

Table 2.3. The primer set used for the qPCR studies

Table 3.1. The NMR results of dopamine (1 mM).

Table 3.2. The NMR results of Melatonin (1 mM).

Table 3.3. The NMR results of Melatonin (1 mM) with dopamine (1 mM)

Table 3.4. The NMR results of dopamine (1 mM) in the presence of sodium periodate (1 mM) at 120 min.

Table 3.5. The NMR results of Melatonin (1 mM) with dopamine (1 mM) in the presence of sodium periodate (1 mM) at 120 min.

Abstract

The present thesis elaborates the evolution of bioinspired hybrid nanostructures, their therapeutic potential and underlying neuroprotective mechanisms for the two most common and prevalent neurodegenerative diseases worldwide namely Alzheimer's disease (AD) and Parkinson's disease (PD). Predominantly, the role of two neurohormones, dopamine and melatonin, has been investigated in the regulation of these neurodegenerative diseases; however, the evolution of nanosized hybrid structures from these precursors under physiologically stressed environment was the new development emphasized in the thesis. The present nanostructures showed brain tissue accumulation, sustainable release of neuroprotective melatonin, and prevents PD progression. The synergistic neuroprotection re-establishes the mitochondrial membrane potential, suppresses cellular reactive oxygen species (ROS) generation, inhibits activation of both caspase-dependent and independent apoptotic pathways and confer a strong anti-inflammatory effect. It suppresses α-synuclein phosphorylation at Serine 129 pα-SYN (S129) with reduced pathological processing, and cellular accumulations investigated in *ex-vivo* organotypic brain slice culture and *in-vivo* experimental PD models. The epigenetic polycomb repressor complex 1 (PRC1) subunit BMI-1, which plays a crucial role in the repression of key regulatory genes in neurogenic tissues linked as a critical negative regulator of pα-SYN (S129) and underlying regulatory mechanism of pathogenic processing in different PD models. The nanostructures exposure upregulates BMI-1 expression and associated polycomb E3 ligase activity, whereas significantly downregulates the pα-SYN (S129) level in the substantia nigra and hippocampal region of the brain. Further, the regulatory interaction between BMI-1 and pα-SYN (S129), promotes ubiquitin-mediated proteasomal degradation of pα-SYN (S129) and alleviates neuronal functions. The fine-tuning of present nanostructures provided multimodal characteristics as near-infrared responsive combined photothermal/chemo-inhibitory role on exogenous and in-situ Amyloid beta (Aβ) aggregation, disintegrate preformed Aβ aggregates and disrupt Aβ self-seeding capacity. With a profound resilience effect on axonal degeneration, it lowers the cellular Aβ processing and accumulations in the hippocampal region studied using *ex-vivo* midbrain slice culture (MBSC) experimental AD model. Besides, state of the art, bottom-up approach, solvothermal route has been used to achieve the highly biocompatible quantum sized dots for the multi-wavelength fluorescence imaging and differential screening of neuronal cell viability. The nanoparticle-protein corona-based fluorescence biosensor has been developed for selective detection of the Aβ protein, which can also delineate pathological Aβ states. Conclusively, the thesis explores the evolution of nature-inspired nanostructure, conferring multimodal biosensing and collective neuroprotective sequels of anti-oxidative, anti-inflammatory, anti-apoptotic pathways activation, and underlying brain region-specific crucial epigenetic regulatory interactions as a potential therapeutic target in neurodegeneration.

Synopsis

Hybrid nanostructures mediated biosensing and epigenetically controlled neurotherapeutic applications in neurodegenerative diseases

Parkinson's disease (PD) is the second most common neurodegenerative disease after Alzheimer's Disease (AD), affecting more than 28.8 million people globally.[1, 2] In neurophysiological context, PD is associated with progressive deterioration of dopaminergic and catecholaminergic system in the substantia nigra (SN), along with the localized accumulation of proteinaceous Lewy bodies (LWs). The increasing knowledge of PD pathobiology is still confined to the understanding of the common risk factors manifested in disease progression and prevalence. [3, 4] The alpha-synuclein (α-SYN) is a 140 amino acid protein product of the SNCA gene, which functionally resides at the synaptic membrane in neurons, abruptly undergoes an amyloidogenic conversion and misfolds to acquire toxic oligomer, fibrils and mature fibrillar structures clinically evident in PD. The phosphorylation of α-SYN at serine 129 (pα-SYN(S129)) has been observed in the patients and transgenic animals suffering from synucleinopathies. [5-8] On the other hand, Alzheimer's disease (AD) is a chronic, progressive, and prevalent neurodegenerative disease, characterized by the existence of extracellular amyloid plaques and intraneuronal neurofibrillary tangles in the brain. The β/ɣ secretase dependent enzymatic amyloidogenic processing of amyloid precursor protein (APP) generates cellular amyloid-beta (Aβ), which undergoes misfolding to form soluble oligomers, insoluble aggregates, prominent fibrils which deposited as senile plaque in hippocampal (HIP) and frontal cortex region of the brain. This amyloidogenic transformation and in-situ Aβ fibrillogenesis alters the synaptic plasticity, induces neuronal disarray and led to neuronal cell death.

Recently, Dopamine (DA), levodopa (L-dopa), and other dopamine agonists are preferred for symptomatic neuroprotection therapy. Although these treatments transiently control the symptoms with a progressive decrease in efficacy leads to drug-dependency and adverse effects such as dyskinesia. Melatonin (N-acetyl-5-methoxytryptamine) (Mel) is an indoleamine based pineal product, controls circadian rhythm, adaption, development, functions as a free radical scavenger as well as a potent antioxidant. Reduced level of melatoninergic receptors (MT1 and MT2) recruitment in the amygdala and SN with lower melatonin buffering is implicated in neurodegeneration. The intravenous or intranasal administration of exogenous melatonin has shown similar biological function as endogenous melatonin. [9] Though melatonin can cross the blood-brain barrier (BBB), but the transient and temporary higher dosed triggers immediate calcium signaling responsible for unregulated dopamine availability and associated motor responses. [10-12] Recent

innovations in nanotechnology led to the development of polymeric nanocarrier displayed excellent therapeutic efficacy. The specific thrust is being made on developing the bioinspired nanostructures for targeted drug delivery, which confers an inherent feature such as enhanced biocompatibility and biodegradability. [13]

The present thesis details the preparation of melatonin/polydopamine based hybrid nanostructures of the variable size range and essential physicochemical characteristics. With the understanding of the exact mechanism of nanostructure evolution and underlying non-covalent interactions stabilizing these nanostructures, it further developed for a stimuli-responsive delivery system and as a robust imaging agent. These materials, as a versatile drug delivery system, can penetrate the blood-brain barrier (BBB) and retain in diverse brain regions. These nanostructures confer superior neuroprotection with an anti-oxidative and anti-inflammatory effect, which regulates the alpha-synuclein phosphorylation at serine 129 and controls amyloidogenic transformation in heavy molecular weight oligomers. The polycomb repressor complex-1 (PRC-1) subunit BMI-1 interacts with pathological (pα-SYN(S129)) and promotes it towards ubiquitin-dependent proteasomal clearance in PD models. Furthermore, hybrid nanostructures mimicking protein-nanoparticle corona have been fabricated, which can precisely detect specific Aβ conformations. Therefore, the approach of prolonged and sustainable bio-availability of the neuroprotectant in the brain that could control the disease progression with enhanced therapeutic efficacies via a precise molecular mechanism of action, corroborated with parallel sensing of the disease status is achieved in following specific aims;

Specific Aim I: *Studying intrinsic reactivity of dopamine derived intermediates and melatonin, upon co-abundance forming melatonin/polydopamine nanostructures*

Specific Aim II: *Brain targeting of melatonin/polydopamine nanostructures (mPDAN) for collective neuroprotection in Parkinson ’s disease model*

Specific Aim III: *Enriched melatonin facilitates Polycomb protein BMI-1 mediated ubiquitination and proteasomal degradation of alpha-synuclein in Parkinson’s Disease (PD) model*

Specific Aim IV: *Engineering hybrid nanostructures for fluorescence-based sensing and stimuli-responsive neuroprotection in Alzheimer’s disease*

Specific Aim I: ***Studying intrinsic reactivity of dopamine derived intermediates and melatonin, upon co-abundance forming melatonin/polydopamine nanostructures***

Several lines of evidence have shown the central role of dopamine and melatonin in the etiology of neurodegenerative diseases. Dopamine is a catecholamine-based neurotransmitter localizes in the neuron (DAergic), functionally controls the reward, cognition, and motor functions. [14, 15] As a consequence of oxidative damages, dopamine oxidizes to form insoluble dark polydopamine/neuromelanin end product. Polydopamine (PDAN) nanostructures conferred excellent biocompatibility and preferred as a drug-carrier, which has been further developed as a stimuli-responsive precision drug delivery system. [16] The insufficient melatoninergic system under neurodegeneration leads to a reduced level of melatonin. The previous reports suggest the reciprocal relation between DAergic and the melatoninergic system. Therefore, considering these pieces of information, we hypothesized the interaction between dopamine derived intermediates with melatonin and its neuroprotection potential in neurodegenerative disease models.

The multiple melatonin/polydopamine nanostructures (mPDAN) were prepared by considering the variable ratio of dopamine/melatonin (1, 2.5, 5, 10, 25, and 50) as a precursor for synthesis. The obtained mPDANs were characterized for the hydrodynamic diameter, polydispersity index, and zeta potential using dynamic light scattering based particle size analyzer. The increasing abundance of melatonin in the nanoformulation reflects in zeta potential value as it was more negative (-29.4 mV) for mPDAN achieved at maximum dopamine/ melatonin ratio (mDPAN2.5). Transmission electron microscopy (TEM) and scanning electron microscopy (SEM) based morphological characterization of mPDAN variants revealed a similar mean particle diameter and solid uniform spherical morphology. The high-performance liquid chromatography (HPLC) provided the existing melatonin content in mPDAN and also shown the sustained release in simulated physiological conditions due to progressive swelling of the polydopamine matrix.

Melatonin/polydopamine nanostructure obtained at varying melatonin/dopamine concentration catalyzed by sodium periodate. The time-dependent UV-vis measurement provided the evolution and relative abundance of the dopamine, dopamine-o-quinone (DQ), and aminochrome (AC) during the reaction. The kinetics of this dopamine oxidation process was significantly affected by the presence of melatonin in reaction. Kinetic analysis shows early saturation in the generation of dopamine-o-quinone and aminochrome due to the interference of melatonin to the dopamine oxidation process, possibly due to interaction with oxidative dopamine intermediates. ^{1}H Nuclear magnetic resonance (NMR) based investigation of reaction indicates complete disappearance of the peaks assigned to these oxidative intermediates with a simultaneous residual downfield shift of dopamine backbone

proton resonance peak confirmed the transient reactivity of the melatonin toward these intermediates. These results firmly established the basis of these nanostructures evolution, which is due to the inherent reactivity of melatonin towards dopamine intermediates during the synthesis process. Next, we studied the stability and integrity of these nanostructures against H_2O_2 with time-dependent measurement of change in particle size and optical characteristics. The results suggested that dopamine derived products (PDAN) prepared without melatonin are highly unstable and prone to the peroxide mediated degradation than that of melatonin/polydopamine nanostructures, which exhibits significant resistance against peroxide-induced degradation.

Conclusion: Herein, the range of nanostructures was derived from dopamine/melatonin and characterized for structural and morphological features. The precise monitoring of the synthesis mechanism revealed the crucial interaction between melatonin and dopamine derived intermediates and established as the chemical basis of these hybrid nanostructures evolution.

Specific Aim II: ***Brain targeting of melatonin loaded polydopamine nanostructures (mPDAN) for collective neuroprotection in Parkinson's disease model***

The present chapter describes the neuroprotection efficacy of the melatonin loaded polydopamine nanostructures (mPDAN) that were checked on rotenone (Rot)-induced *in-vitro*, *ex-vivo,* and *in-vivo* Parkinson's disease models. Primarily, sufficient neuroprotection ability of the mPDAN was determined on the *in-vitro* PD model and found to be more effective than that of bare drug and vehicle. This mPDAN can quickly internalize in monolayer neuroblastoma cells and three-dimensional organoids and quench cellular reactive oxygen species (ROS) in the cells. It prevents the rotenone-induced activation of the caspase-3 dependent apoptotic pathway and resists the loss in the mitochondrial membrane potential. The mPDAN exposure control PD associated overexpression of the caspase-3, IL-1B, IL-6, and NFkB and cellular phosphatase PP2A, Kinase 3pK gene. Based on the previous knowledge, a significant part of pα-SYN (more than 90%) protein in Lewy bodies is phosphorylated at serine 129 positions denoted as pα-SYN(S129)).[17] we specifically examined the content of monomeric and high molecular weight (HMW) pα-SYN(S129)) deposits in PD models, which robustly suppressed upon mPDAN exposure.

The mPDAN can retain in the mice brain in a time-dependent manner and highly compatible with other vital organs confirms using *in-vivo* and *ex-vivo* animal imaging. These mDPAN displayed significant neuroprotective therapeutic efficacy on rotenone-induced mice mid-brain slice culture (MBSC) model. The remarkable reduction of pα-SYN(S129) in hippocampal (HIP) of the brain suggests the strong anti-PD effect. Besides, it protects the PD associated dopaminergic neurons in the HIP and SN region of the brain with viable

Tyrosine Hydroxylase (TH) positive neurons in the midbrain sections. The mPDAN collectively regulated both, loss of the dopaminergic neurons and resisted the increase in pα-SYN(S129) level. Therefore, mPDAN has been investigated for superior therapeutic values, which is, after retaining in the target tissue, control pα-SYN(S129) level and reduce the PD associated degeneration of the dopaminergic neurons.

Conclusion: In summary, the dopamine/melatonin interactions led to the fabrication of melatonin enriched polydopamine nanoformulation (mPDAN) confers a prolonged and sustainable melatonin release. The rotenone-induced *in-vitro* and organotypic mice brain slice culture-based PD model reproducing features of mitochondrial damage, oxidative stress, activation of caspase-dependent apoptosis, upregulated inflammation leading to neurodegeneration, are efficiently restored upon mPDAN exposure. The mPDAN abrogates rotenone-induced α-SYN phosphorylation at serine 129 and significantly prevents amyloidogenic transformation and deposition as high molecular weight oligomers, protected dopaminergic neuronal cell loss in HIP and SN of experimental mice PD model. Finally, the results demonstrated the fabrication of a highly potent nanoformulation based neuroprotectant providing excellent therapeutic potential against PD induced neurodegeneration by regulating multiple cellular pathways.

Specific Aim III: *Enriched melatonin facilitates Polycomb protein BMI-1 mediated ubiquitination and proteasomal degradation of alpha-synuclein in Parkinson's Disease (PD) model*

The present chapter details the underlying neuro-epigenetic mechanism of neuroprotection-based regulation of PD. The BMI-1 is a subunit of the polycomb repressor complex-1 (PRC-1) functions to maintain the differentiation in neurogenic tissue and plays a vital role in normal brain function. [18] As a subunit of the PRC-1 complex, it regulates the E3 ligase function and monoubiquitinates the histone 2A at the K119 position. Rotenone based induction of PD corroborated with lower BMI-1 and reduced canonical E3 ligase function measured as monoubiquitylation of histone 2A at lysine 119 (H2AK119ub). Phosphorylation of BMI-1 at multiple serine residues triggers a de-repressed state and promotes its dissociation from the chromatin, thus crucial for its functional diversity in transcriptional repression. Lower expression and higher phosphorylation at serine residue of the BMI-1 have been observed in the PD model, which is significantly restored upon melatonin exposure. A reciprocal relation in the cellular level of BMI-1 and pα-SYN (S129) is observed in the PD model and even upon melatonin or mPDAN exposure. Besides, mPDAN exposure re-established the polycomb E3 ligase function, which was significantly affected in the PD. mPDAN exposure can reduce both pα-SYN (S129) monomer as well as HMW oligomers in rotenone-induced PD models. mPDAN exposure can rescue the PD associated

downregulation of the BMI-1, H2AK119ub, and suppress phosphorylation and oligomerization of the pα-SYN(S129). Pharmacological inhibition of BMI-1 associated polycomb E3 ligase function reveals that BMI-1 is requisite for the neuroprotective function of mPDAN. The neuroprotective function of mDPAN is compromised upon cellular BMI-1 depletion, which to some extent insufficient in regulating pα-SYN(S129) oligomeric deposition.

The proteasomal machinery plays a crucial role in maintaining the cellular protein homeostasis. The increased accumulation of the pα-SYN (S129) monomer and oligomers were seen upon inhibition of cellular proteasome machinery. mPDAN co-treatment increased the association of the ubiquitin with pα-SYN (S129) suggested the ubiquitin-dependent proteasomal degradation of the pα-SYN (S129). However, upon mPDAN exposure, BMI-1 physically interacts with pα-SYN (S129) directs the ubiquitin-dependent proteasomal degradation of pα-SYN(S129). The rotenone-induced *in-vivo* PD model has been used to investigate the mPDAN efficacy as a function of BMI-1, H2AK119ub, pα-SYN(S129) monomer and pα-SYN(S129) HMW level. The HIP and SN region in the contralateral side of the midbrain shows lower neuronal BMI-1 expression. However, similar tissue regions are observed for a significant overexpression and deposition of pα-SYN(S129). Interestingly, mPDAN administered brain tissued shows higher BMI-1 and lower pα-SYN (S129). Hence, this mutual expression of these proteins in midbrain regions indicates the coupled epigenetic and neuronal pathways regulating the PD progression.

Conclusion: Thus, polycomb repressor complex 1 (PRC1) subunit BMI-1 is a transcription repressor protein that is merely linked to alpha-synuclein phosphorylation and its pathological transformation. The first time, the role of BMI-1 as a critical negative regulator of α-SYN phosphorylation at serine 129 (pα-SYN (S129)) and its aggregation are investigated on *in-vitro* and *in-vivo* PD models. Melatonin enrichment upregulates BMI-1 expression and its E3 ligase activity, whereas it significantly downregulates the pα-SYN (S129) level in the SN and HIP region of the brain. BMI-1 is directly interacting and regulating the pα-SYN (S129) on melatonin exposure confirmed via depleting cellular BMI-1. The BMI-1 expression and interaction with pα-SYN (S129) are facilitating the ubiquitination of pα-SYN (S129) and directs its proteasomal degradation. This brain region-specific crucial regulatory interaction between BMI-1 and pα-SYN (S129) elucidated the non-canonical function of BMI-1 for melatonin dependent neuroprotection and identified as a potential epigenetic target for PD therapy.

Specific Aim IV-A: Dopamine inspired quantum sized dots for multimodal fluorescence screening of the live and dead dopaminergic neuronal cell population

This chapter reports a facile method for preparing dopamine derived quantum sized dot (DI-10), which is highly biocompatible and can be used for multimodal fluorescence-based sensing and super-resolution bio-imaging. The optimization of the prepared materials with hydrothermal/pyrolysis processes further enhances functional stability. The purified material exhibited excitation dependent fluorescence emission in the four spectral regions from blue to NIR, characterized by excitation wavelength-dependent emission mapping. Their fluorescence intensity and quantum yield showed a direct relationship with the degree of dopamine oxidation. The high-resolution transmission electron microscopy (TEM) observation revealed the dispersed structure with an average particle size confined in the dimension of ~10 nm with well-resolved lattice structures with a spacing of 0.223 nm corresponding to the lattice parameter of conventional quantum sized materials. Based on X-ray photoelectron spectroscopy (XPS), Fourier transformed infrared (FTIR) and High-Resolution Mass spectrometry (HR-MS) studies, the molecular structure, composition, and interactions were studies. The DI-10 successfully demonstrated cellular biocompatibility using viability and flow cytometry-based assays. Further, the *in-vivo* studies confirmed the negligible systemic effect with the wide whole-body distribution. Thus, DI-10 has demonstrated as a confocal based high-resolution imaging probe in monolayer and three-dimensional organoids and further evaluated for its capability to discriminate between viable and non-viable neuronal cell populations.

Conclusion: The dopamine derived highly biocompatible quantum sized dots were fabricated and characterized for the vast optical properties. The detailed structural and morphological characterization displayed its quantum sized characteristics, functionality, and evolution mechanism. The nanostructures showed enormous *in-vitro* and *in-vivo* biocompatibility thus demonstrated its applicability as fluorescence-based cellular imaging probe that can discriminate viable/non-viable neuronal cell populations.

Specific Aim IV-B: ***Developing stimuli-responsive amyloid-beta anti-aggregation agent and neuroprotection in Alzheimer's Disease Model***

The polydopamine characteristically absorbs the electromagnetic radiations in the near-infrared (NIR) region and converts these energies into heat, which can be measured as photothermal conversion capability (PTC).[16] This PTC effect is conserved in dopamine/melatonin nanocomposites (DM-NCs) shows a concentrations dependent increase in the dispersion temperature. DM-NCs under intermittent ON/OFF cyclic NIR exposure accompanied by continuous measurement of the temperature change validates

the stability and sustainability, which is one of the critical factors determining the translational potential of PTC agent.

The drug-loaded core polydopamine serves as an efficient drug delivery vehicle and shows superior penetration and retention effect in multiple disease models. Besides, DM-NCs demonstrated as a next-generation stimulus-responsive drug release system, which can precisely control the spatiotemporal release of the drug molecules at the target site in the response of NIR. DM-NCs undergoes immediate burst release of the constituted melatonin upon NIR induction. DM-NCs significantly inhibited the Aβ aggregation by diminishing the exponential growth phase of the aggregation kinetics but doesn't affect the Aβ nucleation. Aβ in the presence of DM-NCs failed to form such prominent fibers and appeared as the oligomeric and amorphous deposits investigated under TEM. These DM-NCs upon NIR irradiation limit the Aβ peptide to confine in small oligomeric peptides clusters. The DM-NCs with NIR irradiation triggers the complete abolishment of the self-propagating capability. Therefore, DM-NCs with NIR irradiation confer anti-aggregation, disaggregation and stop the propagation of the Aβ.

The DM-NCs exposure with pulsed NIR irradiation significantly reduces the ROS level in AD induced neuroblastoma cells. The prolonged exposure of DM-NCs to differentiated neuroblastoma cells shows that it can protect the neuronal cells against AD-associated axonal degeneration. The Immunofluorescence and immunoblot based examination of the cellular Aβ confirmed the lower processing and cytoplasmic localization of Aβ upon DM-NCs treatment following NIR irradiation. Thus, these cell-based assays confirmed that DM-NCs upon NIR illumination are undergoing two of the mutually exclusive processes. First, upon NIR illumination, it disintegrates to burst release the encapsulated melatonin in the cytoplasm, which further regulates multiple neuroprotective pathways to downregulate *in-situ* Aβ processing. Secondly, the dissociated polydopamine interacts with cytoplasmic inclusions and disintegrates the pre-formed Aβ aggregates via the PTC effect. This efficacy of DM-NCs is further validated on the midbrain slice culture (MBSC)-based AD model using immunofluorescence analysis of Aβ expression level and localization. Only DM-NCs exposure significantly reduced the Aβ processing and deposition in MBSC based AD mode, but this inhibition was more profound upon NIR illumination. The investigation of brain region-specific change in the Aβ expression revealed that DM-NCs upon NIR irradiation significantly lowers both in-situ Aβ processing and expression of CD-54. Thus, DM-NCs with photothermal effect demonstrated as NIR responsive agent that can control both Aβ pathobiology and associated microglial accumulation in the brain area.

Conclusion: The NIR responsive photothermal effect of polydopamine and chemo-inhibitory effect of melatonin synergistically prevented spontaneous Aβ aggregation and self-seeding capability in cell-free conditions. It conferred higher compatibility without

affecting the neuronal processes and also scavenged cellular reactive oxygen species generated in AD pathology. It prevented the AD-associated processing of the Aβ, with a lesser accumulation of microglial cells in the hippocampal region of the midbrain examined on *ex-vivo* adult murine brain slice culture-based AD model. Collectively, The NIR responsive DM-NCs conferred synergistic photothermal and chemo-inhibitory effect to control AD pathophysiology.

Specific Aim IV-C: ***Protein-Nanoparticles corona-based fluorescence biosensor for sensitive detection of Amyloid-β protein***

In this chapter, the interfacial chemistry of nanoparticles and protein corona (PC) system is manipulated to develop a small molecule tethered fluorescent biosensors, which with an enhanced biological response, can detect and delineate pathological Aβ forms. The dynamic nature of protein-nanoparticle corona structures allows the estimation of associated proteins, used for precise drug delivery and biosensing applications. In present work, the chemical characteristics and optical properties of curcumin (Cur) were used to analyze the lanthanum carbonate nanospheres (REM_{100}) and protein interactions. The REM_{100} nanospheres function as the substrate is prepared using a newer surfactant-assisted homogeneous precipitation method. Cur form a hard corona layer on the REM_{100} surface are incubated with Human Serum Albumin (HSA), Casein, Lysozyme (LZ), and Bovine Serum Albumin (BSA), Aβ proteins. These proteins form a tertiary layer on the Cur-REM_{100} probe, where the fluorescence emission of curcumin is correlated with the type and amount of interacting proteins. The Langmuir protein adsorption model provided the maximum surface coverage and an apparent dissociation constant for these proteins. These observations suggest that curcumin forming a highly stable hard corona over REM_{100} surface and accommodated the proteins as the soft corona layer. Therefore, Cur-REM_{100} has been demonstrated as an efficient fluorescent probe that can estimate the analyte present in the soft corona layer and can detect and discriminate the Aβ monomeric and Aβ aggregate states with a limit of detection (LOD) of 0.2 ±0.045 μM and this sensitivity is considerably more than that of conventional Thioflavin T (ThT). Thus, this protein-nanoparticle corona-based tool is constructed for its promising application in the quick and sensitive detection of AD biomarkers.

Conclusion: The nanoparticle-corona based fluorescence probe has been developed utilizing the lanthanum carbonate nanospheres and curcumin. This probe provides a sensitive interfacial mechanism for the compositional quantification of the Aβ protein. It pursued an increased sensitivity differentially towards pathological Aβ states and can be used for delineating the monomer and aggregated states of the Aβ.

Chapter 1

Introduction

1. Neurodegeneration

Aging is the natural process that progresses with the sequence of the early, middle-age changes and undergoes a complete slowdown of cognition in later decades of life.[19] The series of this aging process in decades can be correlated with progressive neurodegeneration. In contrast, the premature appearance of similar symptoms with loss of neuroanatomical structure and function that clinically appears with extrapyramidal, pyramidal movement disorders, cognitive and behavioural changes are referred as “neurodegenerative diseases.”[20] The compelling outcomes from molecular, pathological, biochemical, and cellular investigations provided the sense of causal factor for increasingly prevalent disease even in the elderly population.[21] Based on heterogeneous pathological and clinical expressions associated with specific functional brain area, these diseases are classified as Alzheimer's disease (AD),[22] Parkinson's disease (PD),[23] Huntington's disease (HD),[24] amyotrophic lateral sclerosis (ALS),[25] frontotemporal dementia and the spinocerebellar ataxias.[26] It has been shown that loss in the key protein and accumulations as oligomeric and aggregated state in brain tissues are the key features linked to the pathobiology and neurodegeneration.[27] The pathobiology of these debilitating diseases is largely unknown and limited to the understanding of key neurological changes associated with the deposition of misfolded aggregates of amyloid-beta (Aβ) in AD and alpha-synuclein (α-SYN) in PD, implicated under the common cause of neurodegeneration. [28, 29]

2. Pathobiology of Alzheimer’s disease (AD)

Alzheimer's disease (AD) is one of the chronic, progressive, and prevalent neurodegenerative disease contributing more than 80% of cases of dementia globally.[2] The hallmark of age-associated loss of memory, behavior, and cognition in 46.8 million people worldwide categorized it as a global threat with a terrible burden on society with the prediction of a new AD case in every 33 seconds.[30] The AD-associated atrophy in the hippocampus and associated subiculum, dentus gyrus and entorhinal cortex are linked to the early phase neurocognitive, memory and learning deficit in the population.[31, 32] The underlying pathogenesis of AD is explained based on several hypotheses as (1) the amyloid hypothesis (2) the Tau hypothesis, (3) the presenilin hypothesis, (4) the Ca^{2+} dysregulation hypothesis, (5) the lysosome hypothesis, and (6) inflammation hypothesis.[33, 34] However, the amyloid hypothesis was investigated best for the understanding of AD pathogenesis, The first time Dr. Alois Alzheimer identified the presence of the amyloid in the form of senile plaque and neurofibrillary tangle during brain autopsies.[35] The deposition of these amyloid plaques in the brain parenchyma and brain capillaries were characterized as cerebral amyloid angiopathy.[36] The histopathological evaluation

displayed the accumulation of neuritic plaque and neurofibrillary tangles in the hippocampus with degenerated localized neurons and damaged entorhinal cortex projections.[37] The pathobiology of the AD is not only limited to the degeneration of neurons, neurite dystrophy and spline loss in the diverse brain area but also affects the non-neuronal oligodendrocytes, astrocytes, endothelial and glial cells present in the vicinity.[38] The neuronal degeneration accompanying both the loss of the synapse and reduced in the number of dendritic spines is proportionally linked to the severity of the symptoms.[39] As per the amyloid hypothesis cascade, the membrane-bound amyloid precursor protein (APP) is enzymatically cleaved by α secretase and performs the normal neurological function.[40] β Secretase (BACE1), which is a transmembrane aspartic protease, spontaneously cleaves the APP and generates sAPPβ ectodomain and APP C- terminal fragment. Aβ peptides (1–40 and 1–42) generated by γ-secretase complex undergoes a cascade of the oligomer, insoluble aggregates, prominent fibrils, deposited as senile plaque and alters synaptic plasticity, induce neuronal disarray and cell death as represented in Figure 1.1[41-43]. The Aβ aggregation is a complex self-assembly reaction process involve multiple intermediate steps. The first event occurs the primary nucleation, characterized by initial small soluble aggregates functions as a template for Aβ monomers.[44] The elongation is the second step of cascade comprised self-assembly of monomers leading to an increase in the length of Aβ fibrils, which exist as a mixture of delicate and prominent Aβ fibrils.[45] Aβ propagation is secondary nucleation of Aβ monomers, proceeds with abrupt dissociation of preformed aggregates in small units that can re-seed Aβ aggregation.[46] The final stage of the Aβ aggregation process is the fragmentation of existing fibrils in small aggregates, which with similar mechanisms, increase the Aβ aggregation kinetics. All these intermediate states in Aβ aggregation process with mixed secondary structures transformed into Aβ fibrils are parallel or antiparallel cross-β sheets.[47] Characteristics intermolecular hydrogen bonding in these secondary structures in Aβ aggregates contributed with additional hydrophobic or polar interactions leading to conformational rigidity and resistance against thermal and protease associated degradation.[48, 49] The neuronal cells and astrocytes synergistically regulate the amyloidogenic processing of the APP and the amount of soluble Aβ oligomeric fractions, which triggers oxidative stress and mitochondrial dysfunction in these cells.[50] In general, at the late onset of the disease, Aβ senile plaque induces recruitment of brain microglial cells, which start releasing the proinflammatory cytokines and stimulates the amyloidogenic pathway in adjacent neurons to produce more Aβ monomers.[51] This particular cascade further elicits the processing, accumulation, and dispersal of toxic oligomeric Aβ in the brain tissue.[51] The oligodendrocyte cells are investigated for increased oxidative and mitochondrial stress, lower cellular glutathione, and reduced reactive oxygen scavenging function. This particular Aβ cascade further elicits the

processing, accumulation, and dispersal of toxic Aβ oligomers in the brain tissue.[52] It has also been investigated that collectively these Aβ conformations affect the crucial neuroprotective, functional signaling and recruitment of the receptors on the synaptic terminals of the neurons.[53] The proteolytic pathways, which function to maintain the protein homeostasis in the cells, are damaged and fail to clear pathological Aβ proteins. The neprilysin and insulin-degrading enzymes (IDE) are the main proteases regulating Aβ depositions.[54, 55] Cerebrospinal fluid (CSF) and vascular systems sequester some soluble fraction of these oligomers defined as a one of the clearance mechanism of Aβ aggregates. Recently, it has been found that AD induced cells derived extracellular microvesicles and exosomes can transmit the Aβ oligomers and hyperphosphorylated tau to the target oligodendrocytes and astrocytes cells.[56] These "contagion" if injected in a healthy organism, based on the concentration, can induce a similar AD pathology.[57] Thus, understanding this Aβ pathobiology helped in the development of several therapeutic approaches that can be precisely targeted for effective management of the AD.

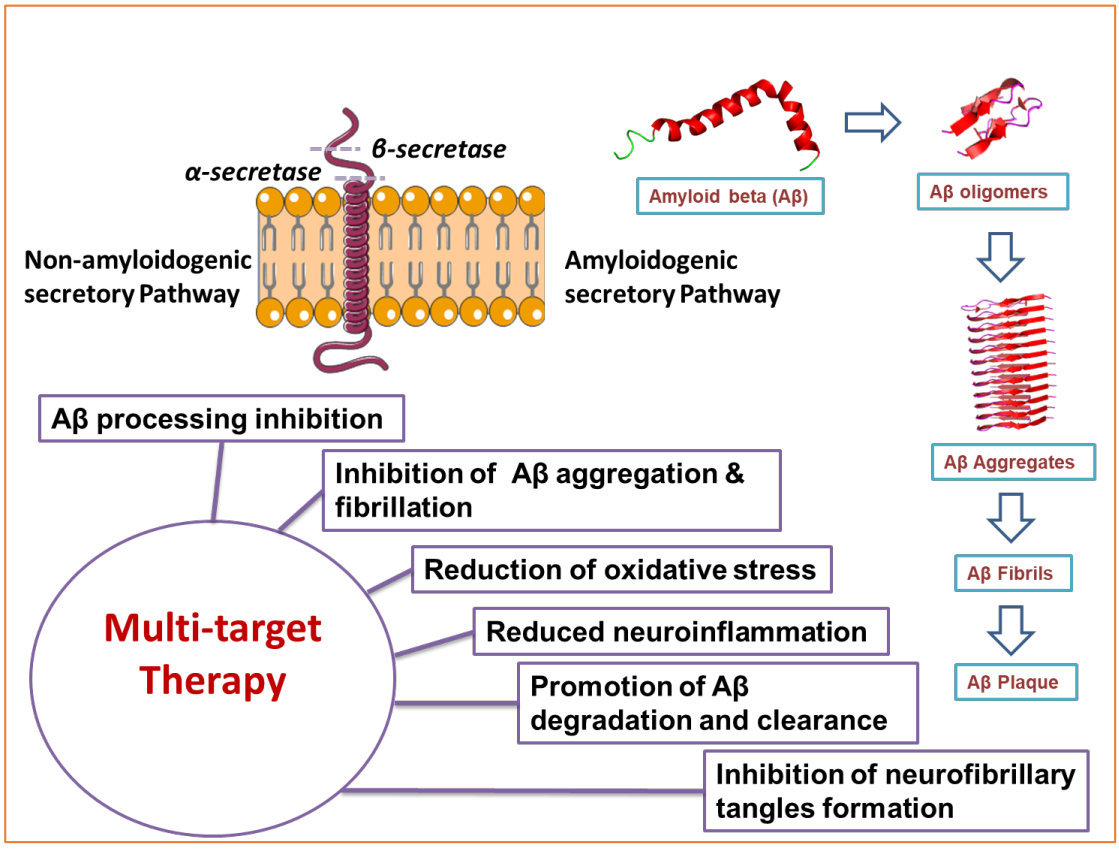

Figure 1.1 **The schematic illustrates Amyloid beta (Aβ) aggregation and associated cellular pathobiology.**

2.1 Management of AD

2.1.1 APP processing and Aβ targeting

β-secretase 1(BACE-1) is the key rate-limiting protease that regulates the cerebral Aβ concentrations has been considered as one of the promising targets for therapeutic development.[58] The approach of eliciting the α-secretase function and simultaneously depleting β-secretase activity has been used for the effective management of AD.[59] Muscarinic/GABA agonist and PKC regulate the activity of α-secretase.[60, 61] Recently, a specific PKC inhibitor Bryostatin 1 displayed promising therapeutic potential in AD.[62] Alternatively, the effort is being made to develop specific β-secretase inhibitors, such as GRL-8234, which is found to be effective in regulating the APP processing and AD pathology.[63] A carrier peptide linked BACE-1 inhibitor [OM00-3]DR9 can easily limit cerebral Aβ levels after retaining in the brain.[64] TAK-070 and LY2886721 administration in the preclinical model rescues the symptomatic memory and cognitive function.[65, 66] The chronic dose of compound C triggers the glial activation and promotes the clearance of the Aβ aggregates; however, the exact mechanism of this function is not established.[67] These strategies regulating the BACE-1 function are explored as a pharmacological target in the management of AD.

2.1.2 Targeting Aβ aggregation kinetics

Presently the approaches of fabricating the biomolecular anti-aggregation compound with extreme specificity to the Aβ oligomeric and fibrillar state are achieved an enormous interest.[68] In addition to designing small molecular organic probes, engineered antibodies, and oligonucleotides, naturally purified active compounds are also repurposed as therapeutics.[69] These anti-aggregation and disaggregation agents are functions in either of two ways; first, it interacts with the Aβ monomeric sequences and prevents their self-assembly from forming the aggregates; second, they interact with preformed Aβ oligomers/fibrils and dissociate them into monomers and categorized as the β-sheet breakers.[70] Recently, a peptide β-wrapins, acquires a β-hairpin structure upon interacting Aβ sequence are validated as a potent β-sheet breaker. [71] Aducanumab is an Aβ aggregates specific human monoclonal antibody retain in the brain parenchyma and reduces the Aβ aggregate accumulation in a dose-dependent manner. [72] A humanized antibody BAN2401 can specifically interact with Aβ fibrils among the mixed Aβ fractions, and the study reported the reduction of Aβ soluble aggregates by ~42% and ~53 % in the brain and CSF, respectively. Besides, the number of therapeutics under phase-trail, few agents such as tramiprosate, ELND, and Colostrinin demonstrated a strong anti-oligomerization effect and prevented Aβ monomer to oligomer transition.[73] Recently, an

antibody variant named “gammabodies” has shown strong reactivity to Aβ oligomers and aggregates, which is generated by grafting a 4-10 amino acid sequence from the Aβ protein to the complementary binding domain of the antibody.[74] Thus, these antibodies demonstrate an effective and conformation-specific therapeutics in AD. The polyphenol compounds which are structurally rich in the phenolic group are explored for Aβ anti-aggregation properties. Some of these compounds, such as (-) epigallocatechin (EGC) and gallic acid (GA) can direct the Aβ fibrillation cascade towards off-target pathways by directly interacting with Aβ conformations and leads to a product with low toxicity.[75] The molecular structures of these compounds allow them to interact with backbone amino acids via major hydrophobic interactions and covalently link with the lysin residues to form Schiff base. Thus, multiple covalent and noncovalent interactions may be the reason for the irreversible binding of these compounds with the Aβ sequence. The resveratrol has specific regulation on oligomer to fibrils conversion, and mechanistically it disintegrates the preformed Aβ fibrils without affecting oligomeric Aβ fraction. [76] Curcumin ((1E,6E)-1,7-bis(4-hydroxy-3-methoxyphenyl)-1,6-heptadiene-3,5-dione) is small molecule isolated from a rhizomatous plant. It interacts and prevents the Aβ oligomerization and dis-integrate preformed fibrils via stacking interactions between aromatic rings and hydroxy groups.[77] Besides small molecule and peptide-based anti-aggregation agent, the number of nanostructures has been demonstrated as anti-Aβ aggregation and desegregation agent. Some of these diverse range of these nanostructures metallic (gold, silver and iron) nanoparticles, carbohydrate, protein, polymers derived nanoparticles displayed capacity of interfering with the Aβ aggregation process.

2.1.3 Aβ clearance pathway

There are two major non-enzymatic and enzymatic pathways that clear the deposited Aβ aggregates. The non-enzymatic pathway includes the interstitial fluid drainage mechanism, where the Aβ deposits are translocated across perivascular Virchow-Robin arterial space to blood flow in the brain.[78] The resident mononuclear phagocytic glia and astrocytes cells play another role in the clearance of Aβ deposits via phagocytosis and intracellular cleavage.[79] However, the activation of these cells at the early onset of the disease is a crucial factor that affects the function of this pathway. Another pathway, where Aβ scavenger receptors include low-density lipoprotein receptor-related protein 1(LRP1), scavenger receptor class B member 1 (SCARB1), and macrophage receptor with collagenous structure (MARCO) is helping in the transcytosis of Aβ into the circulation.[80] The enzymatic clearance of the Aβ deposits by zinc metalloendopeptidase neprilysin (NEP), thiol dependent metalloendopeptidase insulin-degrading enzyme (IDE) and matrix metalloproteinase (MMPs) facilitated by catalytic cleavage within Aβ protein. The

therapeutic approaches used the plasminogen activator inhibitor -1 and peptide hormone somatostatin administration confers potential effect via activating the NEP activity. [81] Therefore, understanding of AD pathobiology and underlying molecular events influence disease severity can be manipulated to develop a superior anti-AD therapeutic approach.

3. Parkinson's disease

Parkinson's disease (PD) is the second most cause of neurodegeneration with the prevalence of 10 million cases worldwide.[82-85] It is characterized by the symptomatic feature of the motor deficit, resting tremor, parkinsonian gait, rigidity, posture instability, and bradykinesia.[86] The occurrence of cognitive dysfunction of attention deficit, memory function, and verbal disturbances are due to the disorganization of the frontal-striatal region of the brain.[87] The psychological alteration, loss of olfaction, sleep cycle alterations, mood disorders, and constipation are associated non-motor symptoms of PD.[88] The progressive loss of dopaminergic and catecholaminergic neurons and reduction in dopamine buffering in the substantia nigra pars compacta (SNpc), and locus coeruleus are clinically associated characteristic features of PD.[3, 4] The SNpc is a central part of the basal ganglia, where synthesis of dopamine occurs and regulates the neurotransmitter associated excitatory function and motor response.[89] The continuous decrease in dopamine buffering in SNpc produces an irregulated excitatory response of the striatal neurons as a major reason for motor symptoms in PD.[90] The multifactorial and mutually associated genetic, non-genetic, and environmental risk factors with distinct molecular mechanisms of initiation and progression are major determinants of sporadic or familial PD. However, most of these factors cue common neurological sequelae of oxidative stress, mitochondrial membrane potential loss, proteomic stress, inflammation, loss of trophic factors and apoptotic cell death.[87] The clinically investigated hallmark of PD is intracellular deposition of protein aggregates in dopaminergic neurons of the SNpc known as Lewy body (LB). LB is characterized for the presence of misfolded protein alpha synuclein (α-SYN) and other proteins exist in the vicinity. The SNCA gene, encoding a 140 amino acid soluble alpha-synuclein (α-SYN) protein, which in free form exists as a random coil structure and carboxy-terminal (C-terminal) sequence of this protein acquire α-helix conformation upon binding to the pre-synaptic membrane. This protein functionally regulates vesicle translocation, neuronal plasticity, and neurotransmitter release at synapse.[91] The amino acid at the C-terminal sequence undergoes differential posttranslational modifications, including phosphorylation at Y125, S129, Y133, and Y136, protein truncation at D115, D119, P120, E130, D135 and ubiquitination at K96.[92] Among these modifications, the phosphorylation at serine 129 has mainly been correlated with the severity of the PD and established as one of the biomarkers of PD progression.

3.1 The implication of α-SYN phosphorylation at serine 129

Recently the phosphorylation at serine 129 has been investigated in more detail for its regulatory role in the diverse neuronal functions. This modification retains α-SYN in the free form via inhibiting the membrane binding and regulate the synaptic plasticity.[93] G protein-coupled receptor kinases (GRKs) associated S129 phosphorylation enhances the reuptake of synaptic dopamine without any change in the recruitment of dopamine receptors on the synaptic membranes.[94] Besides, the S129 phosphorylation of α-SYN enhance binding to divalent ions, increase the turnover of α-SYN, impact cytoskeleton protein interaction, and regulates α-SYN nuclear translocation.[95] The progressive accumulation of the α-SYN phosphorylated at S129 in the PD brain suspected as a key pathogenic event in the PD initiation and progression. The role of this modification is highly debated but evident that more than 90% α-SYN deposited as Lewy body in the SNpc is phosphorylated at S129. Whereas, only 4% of the α-SYN is estimated with this modification in a healthy brain.

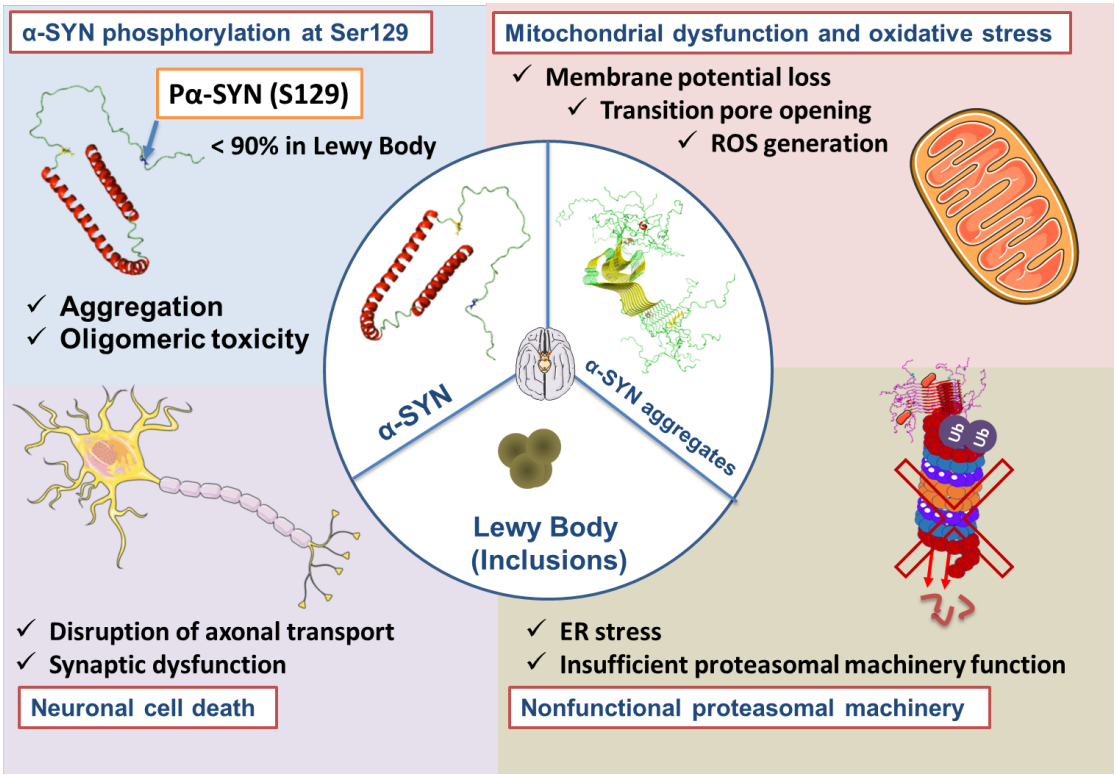

Figure 1.2 **The representation of α-SYN aggregation and pathobiology in PD.**

In relevance, pS129 modification has been linked with amyloidogenic transformation, oligomerization, and fibrillation of the α-SYN in multiple *in-vitro* and *in-vivo* models.[96, 97] Studies demonstrated that cellular toxicity of the α-SYN phosphorylated at S129 is heavily linked with kind of kinases catalyzing the phosphorylation of α-SYN.[98] The estimation of

immune-reactive pS129 in the PD models has been positively correlated with the severity of the disease, which turns to be a reliable biomarker to detect the synucleinopathies from cerebrospinal fluid, blood and biopsies samples of PD patients.[99, 100]

3.2 Molecular pathobiology of PD

The oxidative stress hypothesis explains that neuronal reactive oxygen species generation and mitochondrial dysfunction are key events that induce the neuronal degeneration process.[101] The perturbation of complex-I of the electron transport system (ETS) affects the overall mitochondrial function, inhibits the metabolic pathways, ATP synthesis, and promotes the ROS generation.[102] These accumulated neuronal ROS impact the normal functioning of cellular machinery and leads to oxidative stress, induction of apoptosis, increase in Bax level, and leads to neuronal cell death.[103] Rotenone is a mitochondrial complex-I inhibitor which upon exposure to neuronal cells, disarray the iron-sulfur complex, increase oxidative stress, inhibit proteasomal function, and induce α-SYN aggregation. [104] Microglia, as distinct CNS resident cells regulate the inflammatory responses, are evident to accumulate in SNc reason of the PD brain and key suspect of the inflammation leading to dopaminergic cell loss.[105] The neuronal cells upon degeneration releases α-SYN, ATP and matrix metalloproteases (MMPs) induce these microglial cells in the vicinity for enhanced release of proinflammatory cytokines including interleukin-1β (IL-1β), tumor necrosis factor-α (TNF- α), interleukin-6 (IL-6) and interferon-gamma (INF-γ) further elicit the dopaminergic neuron degeneration.[106] The increasing deposition of the misfolded α-SYN in the endoplasmic reticulum (ER) facilitates the activation of protein degradation pathways due to unfolded protein response (UPR).[107] Ubiquitin proteasomal system (UPS) functions most efficiently to clear off the intracellular and misfolded proteins. However, impaired UPS in PD is one of the key pathogenic events facilitating the accumulation of aggregated α-SYN in LB, as illustrated in Figure 1.2. The UPS associated protein UCH-L1 and Parkin catalyzes the ubiquitination of the α-SYN are studied as the component of LB.[108] Another way, the selective inhibition of the UPS has reproduced similar PD pathobiology and associated dopaminergic cell degeneration in several models. The optimum doses of the lactacystin, MG115, epoxomicin, and synthetic inhibitor PSI exposure induced the UPS dysfunction that further triggers the α-SYN aggregation, mitochondrial dysfunction, ER stress and dopaminergic cell degeneration.[109-111] The molecular chaperones includes the range of heat shock protein (HSPs) HSP-40, HSP-60 and HSP-90 are functioning to maintain folding state of the cellular proteins.[112] PD substantiate with the impaired response of these HSPs, which upon induction can clears the accumulated α-SYN soluble fractions.[113] However, the large macromolecular deposits of the α-SYN aggregates and fractions of LB are functionally do not degraded

either by UPS and HSPs. The autophagy lysosomal pathway (ALP) functions via chaperon mediated autophagy directs the large macromolecular structures into lysosome for hydrolytic degradation. However, lower expression of autophagy associated genes and LAMP1 and LAMP2A lysosome membrane markers are associated with PD, which indicated the dysfunctional ALP in PD. [113] Therefore, the understanding of these neuropathological sequels in the progression of PD opens the way for establishing models that can reproduce the identical pathology and supports to screen the therapeutic effect for the development of superior anti-PD therapy.

4. Epigenetic- polycomb group of proteins (PcG) function

The term “epigenetics” can be very precisely defined as phenotypic regulation of developmental programs, but broadly are key genetic events essential for heritable changes required for transcriptional states and cellular identity.[114, 115] Thus, the current efforts are being made to emphasize the precise epigenetic control of cell identity and fate under development and disease progression.[116] The nucleosome is a superhelical structure of histone protein octamer comprises H3-H4 tetramer and H2A-H2B dimers, interconnected by a linker histone H1.[117, 118] These three-dimensional spatial arrangements of the histone are crucial for the key genetic function, which also allows the post-translational modifications, which are prerequisites for the epigenetic regulation of gene expression.[119] Polycomb group of proteins (PcG) are one of the key epigenetic regulatory protein complex studied for playing a critical role among the developmental process.[120] This protein complex regulates homeotic (Hox) gene expression is first identified in Drosophila and later investigated that it is evolutionary conserved in humans.[121] PcG functions to regulate the transcriptional repression state via specific post-translational modifications in the histone. Based on the transcription repression function, mammalian PcG proteins structurally exist in two multimeric domains termed as polycomb repressor complex (PRC-1 and PRC-2).[122] The mammalian PRC-1 is composed of four subunits; BMI1/MEL18 (vertebrate ortholog of posterior sex combs), RING1A/RING1B/RNF2 (ring finger protein), hPC 1–3 (chromobox), hPH1–3 (Polyhomeotic), and YY1 (Pleiohomeotic). Whereas, the PRC2 contains three subunits; enhancer of zeste-2 (EZH2), suppressor of zeste-12 (SUZ12), and embryonic ectoderm development (EED) are PRC-2 subunit proteins collectively functions in maintaining the repressed gene state.[122, 123] These complexes trigger two significant functions of monoubiquitination of histone 2A at lysine 119 (H2AK119ub by PRC-1), and mono/di/tri-methylation of histone H3 at lysine residue 27 (H3K27me3 by PRC-2), respectively.[124] Functionally PRC2 subunit via histone methyltransferase activity initiates transcriptional repression, whereas the BMI-1/RING subunit of PRC1 functions to maintain the repression state as illustrated in Figure 1.3.[125] In neurogenic tissues, expression of

BMI-1 is required for the self-renewal in the peripheral and central nervous systems. Still, it does not impact the survival and differentiation in these tissues with canonical polycomb E3 ligase function.[126] The conditional depletion of the BMI-1 in the brain arises with the progeroid feature with cortical neuron apoptosis, p53 activation, and oxidative stress.[127] The neuroprotection against mitochondrial stress is one of the non-canonical functions of BMI-1 operates to reduce the cellular ROS level, and by triggers repression of antioxidant response genes (AOR).[128] Thus, abundant expression of BMI-1 regulating PRC-1 dependent epigenetic mechanism and drug-responsive PRC-1 independent function could be linked to the tolerance in neurodegenerative diseases.[129, 130] The polycomb protein 2 (pc2, also referred to as CBX4) component of the PRC-1 complex directly recognizes the H3K27me3 and triggers the SUMO E3 ligase function that alters the chromatin architecture at the time of transcriptional regulation.[131] This pc2 protein directly interacts with the α-SYN and induce the SUMOylation, which observed with an increased level of intracellular α-SYN aggregates.[132] The mechanism of polycomb switching associated with the neurogenesis also persists as a memory even in the adult brain. Multiple epigenetic modifications transiently linked to the disease occurrence, progression, and the non-canonical functions of the epigenetic machinery are implicated as promising neuropathological biomarkers and therapeutic targets.[133]

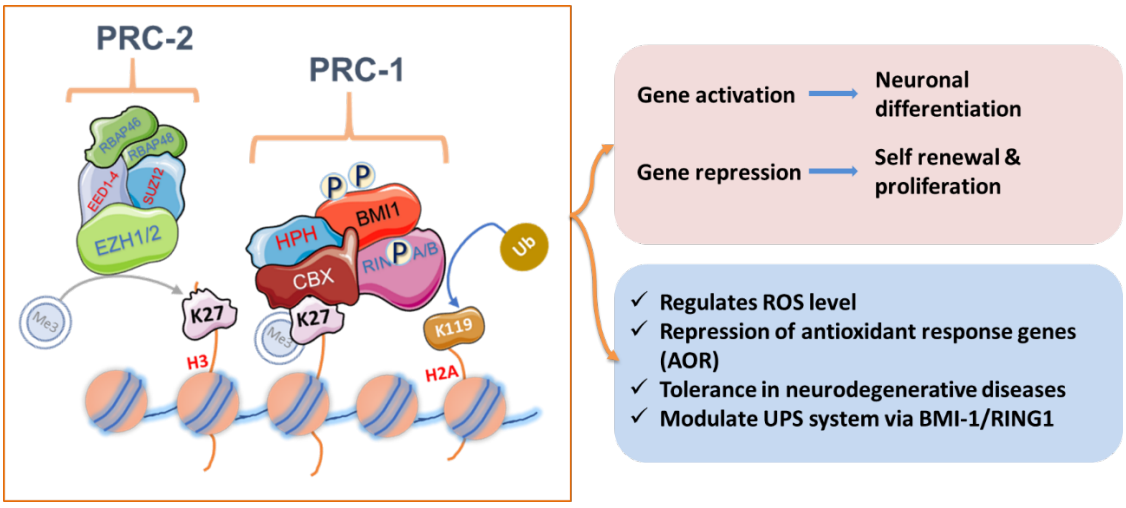

Figure 1.3 **Polycomb group of protein complexes and functions**

5. Nanotechnology in neuroscience

Nanotechnology is an approach of engineering materials to execute the wholly new or enhanced function at the nanometre scale (1 to ~10 nm).[134] Principally, it can be achieved by manipulation of either physical or chemical properties of the material in the nano dimension range, and functionally it would be surprisingly different than that of the exhibit by the bulk material.[135] The nanotechnology in the context of neuroscience is seen

to focus on the two significant aspects first to answer the significant scientific question, and second is to fulfill the therapeutic requirements.[136] Collectively it deals with manipulating the materials of any origin to near-atomic size range and endows a novel atomic, cellular, and molecular functions. At the nanoscale, these materials can be used for the understanding of the underlying neurological processes and formulating therapy of neurological diseases. At the nanoscale range, these materials owe extraordinary physical, chemical, and optical characteristics due to higher surface area to volume ratio, flexible surface functionality, site-specific targeting capacity, novel drug carrier capacity with the controlled time-lapse release of the molecule at the targeted disease site.[137] Major application of these nanomaterials are in developing stable nanocarriers for drug delivery to the brain, polymeric scaffold for brain tissue regeneration, and nanoplatforms for multimodal neuroimaging.[138] These drug-loaded nanostructures can retain in brain by penetrating blood-brain barrier (BBB) penetration and proved to be advantageous over conventional therapeutic approaches.[139] In addition, these nanostructures in the form of implantable devices provide advantages over sophisticated surgical processes and allow real-time monitoring of the neurological processes which may be used as electrodes for electrophysiological and optogenetics applications. Recent structural engineering of bio-inspired materials has innovated the field by designing biocompatible scaffolds of neurogenic and regenerative potential.[140] These materials upon interactions allow neuronal cell differentiation and dendritic growth.[141] The physicochemical and biological compatibility is one of the criteria for the selection of nanomaterials for wide neurological application of therapeutic delivery and nano-diagnostics platforms.

5.1 Nanobiomaterials as potential neurotherapeutics

The nanocarrier mediated drug delivery framework can circumvent the BBB, which restrict the bioavailability of most of the pharmacological agent during systemic administration. This approach is advantageous over invasive delivery of the therapeutics to the brain or by disruption of BBB. The lipid-based nanosized nano-liposomal vesicles (unilamellar and multilamellar) prepared from phospholipid monomers are functionalized with nicotine acetylcholine receptor-specific peptides for the targeted delivery of therapeutics in the brain. [142] A similar strategy has been used for multiple metallic nanostructures that were surface-functionalized with polyethylene glycol and targeted monoclonal antibodies or peptides for delivery. The magnetic iron oxide nanoparticles loaded with brain-derived neurotrophic factor (BDNF) delivery to the brain provided significant neuroprotection. [143] One of the criteria for choosing the nanocarrier is the chemical nature and solvent stability of the drug molecules. The amphiphilic noncarriers that possess hydrophobic core can effectively protect the drug and confer a stimuli-responsive controlled release of it on the

target site and can improve the pharmacokinetics. The hydrogels prepared by controlled crosslinking of ionic and non-ionic polymers based on chitosan, proteins, and dendrimers promote steady and prolong the release of the entrapped therapeutic molecules. Nano delivery of these neuroprotectant to brain mitigates the oxidative stress, mitochondrial dysfunction, activation of apoptotic cell death, and neuroinflammation. Most of these neuroprotectants regulate pathological sequences that are common in PD, AD, and traumatic brain injury (TBI). The number of dopamine and levodopa nanoformulation such as levodopa-α-lipoic acid (LD-LA), levodopa loaded in poly (lactide-co-glycolide) PLGA, dopamine loaded chitosan nanoparticles, dopamine in cellulose acetate phthalate nanostructures and many others have overcome the limitation associated with pharmacokinetics and pharmacodynamics of the dopamine and displayed collective symptomatic therapeutic effect on in-vivo PD models.[73] Similarly, dopamine agonists such as Rotigotine, Ropirinole, Bromocriptine, Apomorphine formulated with solid lipid nanoparticle, and PLGA with improved pharmacological function consequent the increased striatal dopamine buffering and also improve the motor function in PD mice models.[144] The phytochemicals such as curcumin, resveratrol, ginsenosides, quercetin, displayed antioxidant signaling, mitigated the loss of dopaminergic neurons, thus confer anti-PD effect in animal models. Recently, the fluorescence carbon dots with characteristics of enhanced biocompatibility, water dispersity, neuronal permeability, multimodal photonic characteristics, and ease of functionalization have been used for neuronal imaging and therapeutic agents. A number of carbon dots prepared from the biological precursors, including proteins, peptides, carbohydrates (D-Glucose), amino acids (aspartic acid, and glutamic acid) confer full wavelength fluorescence and characteristic brain tissue retention.[145]

6. Melatonin as potent neuroprotective

Melatonin (N-acetyl-5-methoxytryptamine) is an indoleamine based neurohormone, secreted from the pineal body in a rhythmic oscillation pattern. The melatonin synthesis in the pineal body is adapted to a rhythmic pattern of the day/night cycle. The retinohypothalamic, retinal ganglion cells containing pigments play a crucial role in the regulation of melatonin synthesis via β-adrenergic receptor–adenylyl cyclase–cyclic AMP singling. In addition to controlling diverse body functions such as circadian rhythm, development, and adaption, it proves to be a powerful free radical scavenger and potent antioxidant[12]. After scavenging several reactive oxygen species free radical and non-radical, it metabolizes 3-hydroxymelatonin, N1-acetyl-N2-formyl-5-methoxy kynuramine (AFMK) and N1-acetyl-5-methoxykynuramine (AMK). Reduced levels of MT1 and MT2 receptor expression in the amygdala and substantia nigra with reduced melatonin rhythm

amplitude indicated the role of the melatoninergic system in the pathophysiology of PD[9]. The recent molecular investigation demonstrated that it prevents dopaminergic neuronal cell death, maintain mitochondrial homeostasis, restore mitochondrial complex I, complex IV activity, restore mitochondrial membrane potential and cellular ATP level via any of the receptor-dependent and receptor-independent function in different Parkinson's model[146, 147]. Another neuro-epigenomics study reveals high doses of melatonin prevent glioblastoma stem-like cells growth via controlling AKT-EZH2-STAT3 signaling axis[148]. It impacts the DNA methylation, histone modifications and regulates the natural and disease-associated senescence. The *in-vivo* and *in-vitro* studies evident the regulation of MMP-9, NF-kB, HIF-1a, VEGF, Nestin, Bmi-1 and Sox2[149]. Melatonin triggers multiple signaling pathways, controlling a plethora of physiological and pathological functions with negligible side-effects. It has been found that it promotes the sirtuin 1(SIRT1) mediated α-secretase function, which reduced the Aβ accumulation and associated pathology. Melatonin controls glycogen synthase kinase 3 beta (GSK3β), and cyclin-dependent kinase 5 (Cdk5) mediated tau hyperphosphorylation and deposition of neurofibrillary tangles (NFT) in the AD. These phasic shifts in the melatonin secretion and associated enzymatic and non-enzymatic protective roles are continuously being explored for the new targets, disease modification mechanism, and therapeutic effects.

7. Objectives and outline of the thesis

It is hypothesized that multiple targets are involved in pathogenesis and progression of Parkinson's and Alzheimer's disease, which collectively moderate the heterogeneity in the neurodegeneration mechanism. The symptomatic cardinal non-motor and motor deficit, progressive degeneration of neurons, and deposition of protein-rich Lewy bodies (LWs in PD) and senile plaques (in AD) are clinically linked to the oxidative stress, mitochondrial dysfunction, ER stress, inflammation, apoptosis and excitotoxicity of the neurons. However, recent establishments indicates that disease-modifying nanotherapeutic delivery can provide collective regulation of these disease pathobiology. The exogenous systemic delivery of the dopamine and melatonin conferred a considerable therapeutic effect. However, the synergetic neuroprotection effect of these neurohormones with approaches of nanocarrier mediated neuroprotectant delivery are not yet explored. α-synuclein phosphorylation at serine 129 is an established biomarker of PD and associated with amyloidogenic transformation, oligomerization, aggregation and deposition as inclusions. However, the therapeutic approaches regulating this α-SYN associated posttranslational modification is not investigated. The polycomb repressor complex-1 (PRC-1) subunit BMI-1, altogether function as a polycomb E3 ligase to maintain the self-renewal of neurogenic tissues are linked to providing neuroprotection against mitochondrial stress, reduces the

cellular ROS level, triggers repression of antioxidant response genes upon neurodegeneration. However, whether this PRC-1 subunit BMI-1 plays any role in the regulation of the α-SYN pathobiology is largely unknown. In light of this information, there is a need to establish the approach which can prolong neuroprotectant bioavailability in the brain, could regulate the AD and PD associated pathobiology, and provides an understanding of the molecular mechanism of action, corroborated with parallel sensing of the disease biomarkers. However, the efforts have been made to establish this in the following objectives;

Chapter 3: To study the intrinsic reactivity of dopamine derived intermediates and Melatonin, upon co-abundance forming melatonin/polydopamine nanostructures

Chapter 4: Brain targeting of melatonin loaded polydopamine nanostructures (mPDAN) for collective neuroprotection in Parkinson ’s disease model

Chapter 5: Enriched melatonin facilitates Polycomb protein BMI-1 mediated ubiquitination and proteasomal degradation of alpha-synuclein In Parkinson’s Disease (PD) model.

Chapter 6a: Dopamine inspired quantum sized dots for multimodal fluorescence screening of the live and dead dopaminergic neuronal cell population

Chapter 6b: Developing stimuli-responsive Amyloid-beta anti-aggregation agent for neuroprotection in Alzheimer’s disease model

Chapter 6c: Protein-nanoparticles corona-based fluorescence biosensor for sensitive detection of Amyloid-β protein

To summarize, work has been presented in this thesis elucidated the existence of melatonin and dopamine derived highly biocompatible hybrid nanostructures confers precise synergistic multimodal therapeutic potential demonstrated in both Parkinson’s and Alzheimer’s disease models.

Chapter 2

Materials and methods

1. Reagents

3-Hydroxytyramine Hydrochloride (Dopamine HCl, 99%), Melatonin (≥ 98%, M5250), Rotenone (≥ 95%, R8875), DAPI (D9542), anti-Rabbit IgG-FITC (F9887), anti-mouse IgG-TRITC (F9887) and Polyethylene glycol 400 (PEG-400, 8.07485) were purchased from Sigma Aldrich (St. Louis, Missouri, United States), Sodium periodate, $NaIO_4$ (311448), Thioflavin-T (ThT, T3516), beta-amyloid peptide fragment 1-42 (A9810), Deuterium oxide, D_2O (99.9%, 151882), Retinoic acid (R2625) were purchased from Sigma Aldrich. The cell culture medium Dulbecco's Modified Eagle Medium (DMEM, AT186), Fetal bovine serum (FBS, RM9954), Antibiotic antimycotic solution 100x (A002) was received from Himedia lab. The beta-amyloid antibody, Cat. sc28365 purchased from Santacruz biotechnology, USA and anti-mouse IgG-TRITC secondary antibody, cat-T5393 were purchased from Sigma Aldrich. Lanthanum(III) acetate sesquihydrate (Alfa-Aesar), Sodium carbonate (Merck), cetyltrimethylammonium bromide (CTAB, Aldrich), sodium dodecyl sulfate (SDS, Himedia), lysozyme (Himedia), curcumin (Sigma), casein (Sigma), trisodium citrate dihydrate (Aldrich), citric acid (Aldrich), Tris base (Himedia), sodium bicarbonate (Himedia), Thioflavin T (Himedia), ethanol (Merck) were purchased commercially and used with mentioned purity specifications. In addition, all the reagents and solvents were used directly without further purification following the manufacturer protocol.

2. Preparations and purifications

2.1 Synthesis of melatonin/polydopamine hybrid nanostructures

The melatonin/polydopamine hybrid nanostructures were prepared following modified alkaline oxidation associated self-assembly method [150]. The basic reaction process was started with the variable molar ratio of dopamine and melatonin (2.5:1, 5:1, 10:1, 25:1 and 50:1 molar ratio) dissolved in the Milli-Q water in a glass vial and kept at the particular temperature on magnetic stirring. Next, 0.8 M sodium hydroxide (NaOH) was added into the mixture and further stirred for 24 h at 30 ºC. The appearance of the black colored product indicated the oxidation of dopamine leading to a black colored product at completion. These materials were collected in micro-centrifuge tubes and centrifuged at 32,000 x g, 15 min at room temperature. Following 2 times washing with Milli-Q water, products were again centrifuged at 5000 RPM, 10 min, room temperature and the supernatant were collected in the separate centrifuge tube. The supernatant was again centrifuged at 32,000 x g, 15 min at room temperature and final hybrid nanostructures (referred to as mPDAN and MEPN) were collected. The variant of the nanostructures was freeze by keeping at -20 ºC refrigerator, lyophilized and stored at 4 degrees for further treatments.

In another preparation, the dopamine and melatonin were mixed (2:1, 1:1 and 1:2) in the glass vial added with pre-optimized equimolar concentration (1 mM) of sodium periodate ($NaIO_4$) and stirred by keeping on the magnetic stirrer for 24 h at room temperature. The progressive appearance of the reddish-brown color indicated the reaction process and the reaction was processed at 24 h. The purification of these materials was performed by buffer exchange using amicon filters (MWCO 3 kDa, Millipore). The concentrated materials were washed in-column, collected and lyophilized for further use. The blank polydopamine nanoparticles (denoted as PDAN and PN), were prepared separately from 1 mM dopamine using 1 mM $NaIO_4$ as a catalyst and purified using buffer exchange column similar to the earlier procedures. The final product obtained by using dopamine and melatonin were referred to as dopamine/melatonin nanocomposites (DM-NCs).

The dopamine inspired quantum sized dots (referred as DI-10) was prepared by the thermally controlled alkaline oxidation process. The 1 mg/ml solution of 3-Hydroxytyramine hydrochloride stirred at 4° C for 15 min in glass vial and the oxidation reaction were triggered by adding 0.4 M sodium hydroxide and further stirred for 4 hours at 4° C. at completion of 4 hour the dark blackish solution was collected and passed through 3 kDa amicon filters (Millipore) and the concentrated supernatant was re-dispersed in filtered Milli-Q water. The purified material was further (10ml) added into the Teflon container (24 ml max volume) and inserted into stainless steel autoclave. The autoclave was heated by keeping in the hot air oven at 50° C to 180° C for various time periods under static conditions. The recovered products after hydrothermal treatment were lyophilized to get powder state.

2.2 Lanthanum carbonate nanospheres preparation

Lanthanum carbonate nanospheres (referred to as REM_{100}) were prepared by mix CTAB/SDS surfactant-assisted homogeneous precipitation methodology. For the first time, mix CTAB/SDS surfactant method were utilized for the preparation of $REM_{100\,w}$ with certain modification in the traditional homogeneous precipitation method. The CTAB (5 mM) and SDS (1 mM) were weighed and separately dissolved in the Milli-Q water at room temperature under magnetic stirring. These two-surfactant solutions were mixed and added with Lanthanum (III) acetate sesquihydrate (1 mM) and kept on stirring for 15 min at room temperature. The pH of the above solution was adjusted to 8.5 following drop by drop addition of sodium carbonate (100 µM) solution under continuous magnetic stirring and left for 2 h on stirring for complete synthesis. The obtained synthesis mixture was incubated for 30 min at 80°C via keeping in a water bath (Stuart instruments). The material was collected using centrifuge (Avanti jxn-26 centrifuge) at 30,220 X g (rotor, JS 14.05) for 20 min, washed two times with Milli-Q water, dried in vacuum over at 50°C.

3. Morphological and structural characterizations

3.1 Dynamic light scattering

Dynamic light scattering (DLS**)** measures the translational diffusion coefficient of the prepare nanostructures under free Brownian motion in the dispersion performed on the Malvern Nano ZS instrument (Malvern Instruments, and the UK) at scattering wavelength 632 nm, the temperature of the sample 25 ºC and scattering angle of 120º. The equilibration time for each measurement performed in triplicates was 180 sec. The mean hydrodynamic diameter was calculated based on the Stokes-Einstein equation and based on the fluctuations in the intensity of light scattering. The fitted autocorrelation data as cumulant analysis provided the z-average and the polydispersity index (PDI) of the sample. The same equipment measured the zeta potential based on the laser doppler electrophoresis principle, which is a gradient of electrophoretic mobility of the nanoparticles upon light illumination and presence of the electric field. The well-dispersed sample was taken in glass cuvette (PCS1115) and capillary cell with the gold-plated beryllium-copper electrode (DTS1070) for hydrodynamic diameter (d_h) and zeta potential measurement, respectively. The results are represented in the arithmetic mean ± standard deviation.

3.2 Transmission electron microscopy (TEM)

TEM were used for obtaining the nanoscale size and shape of the prepared nanostructures. Highly dispersed sample (2-5 µL) were dropped on pre-washed Carbon coated Cu TEM grid (300 meshes) and allowed for 5 min incubation. The left sample was wiped from the grid using Whatmann's filter paper and left to air dry for 15 min at room condition. The negative staining to the sample was performed with phospho-tungstic acid (PTA) and dried well by keeping inside the vacuumed desiccator. These grids were examined under JEOL JEM 2100, equipped with Tungsten filament, at an accelerating voltage of 120 kV and 200 kV. All the topographical and morphological data were imaged at best defocus value, exposure parameter and relatively analyzed for the representations.

3.3 Scanning electron microscopy- energy-dispersive X-ray spectroscopy (SEM-EDS)

The surface morphology and shape of the nanostructures were imaged under a scanning electron microscope (JEOL JSM IT300, Japan). The dispersed samples were prepared by drop-casting on the silicon wafer following vacuum drying by keeping inside the vacuumed oven at room temperature. The powdered samples were directly placed on the carbon tape and sputter-coated with the gold. The imaging was performed between an operational range of 5-20 kV and at a working distance of ~10 mm.

3.4 Steady-state fluorescence emission measurements

the steady-state fluorescence emission spectrum and endpoint intensity were collected on a spectrofluorometer (FS5, Edinburg Instruments), excitation ranged from 280-370 nm, 380-450 nm and 900-700 nm with the emission wavelength range of 400-850 nm, 450-850 and 300-690 nm for highly dispersed DI-10 sample.

However, the steady-state fluorescence emission spectral measurement of curcumin (λ_{ex}= 415 nm) was performed on a multimode plate reader (SYNERGY H1, Biotek). First, 3 μM curcumin was incubated with varying concentration of REM_{100} (20 μM- 800 μM) in 5 mM tris buffer (pH=7.0) for 30 min, and La^{3+} (20 μM- 800 μM) in 5 mM tris buffer (pH=7.0) for 30 min and added with 10 μg/mL casein protein in 96 well black microtiter plate with a measurement volume of 100 μL. The Cur-REM_{100} (3 μM curcumin + 20 μM REM_{100}) were first incubated with varying concentration of Casein, HSA, Lysozyme and BSA from 5 μM to 800 μM (20 μM, 50 μM, 100 μM, 200 μM, 300 μM, 400 μM, 500 μM and 800 μM) and fluorescence emission spectra were acquired for curcumin. The aggregation kinetics of the Aβ fibrillation was measured as endpoint fluorescence emission and individual spectrum of Thioflavin-T (ThT, 450/485) and compared with Cur-REM_{100} (415/500), respectively.

3.5 UV−Vis absorption spectroscopy measurement.

The underlying mechanism of nanostructures evolution was studied using UV-vis spectroscopy. The UV-vis spectra of dopamine and melatonin oxidation were recorded on a multimode plate reader (MPlex 200 pro, Tecan instrument) in a time-dependent manner. All the optical measurements were performed using HELLMA quartz cell cuvette within wavelength range was 190–850 nm. The UV-vis absorbance for examining the interaction of curcumin with REM_{100} was performed on UV-Vis spectrophotometer (Shimadzu UV-2600) and multimode plate reader (SYNERGY H1, BioTek Instruments). Curcumin stock (100 mM in absolute ethanol) was diluted into 5 mM Tris buffer (pH=7). The absorbance maxima at 430 nm and molar extinction coefficient value 53,000 $dm^3 \cdot mol^{-1} \cdot cm^{-1}$ were used to estimate the concentration of curcumin. Particular 1.2 mM REM_{100} incubated with varying curcumin concentration (25 μM, 80 μM, 130 μM, 180 μM and 250 μM and another preparation, where 120 μM curcumin were incubated with increasing amount of REM_{100} (240 μM, 480 μM, 720 μM, 960 μM, 1.2 mM, 1.4 mM, 1.6 mM, 1.9 mM, 2.2 mM and 2.4 mM) respectively were acquired for the spectrum within the wavelength range of 300 to 700 nm. The linear regression analysis of the absorbance versus concentration curve was performed and analyzed.

3.6 Fourier-transformed Infra-red spectroscopy measurement

The Fourier Transformed Infrared (FTIR) spectrum was recorded for powdered samples on Cary Agilent 660IR spectrophotometer, keeping the parameter 256 scans with 4 cm^{-1} resolutions over 400-4000 cm^{-1} range.

3.7 Thermogravimetric Analysis (TGA)

The equipment Perkin-Elmer STA 8000 was used for the thermogravimetric studies. The analytical grade pure nitrogen was purged with the flow rate of 150 mL/min to create an inert environment prior to start the measurement. The 5 mg pre-dried sample was subjected to the thermal decomposition with a heating rate of 10°C min^{-1}. The % weight loss was estimated using a resolution of 0.1 µg and analyzed.

3.8 X-ray photoelectron spectroscopy (XPS)

XPS was used to examining the elemental stoichiometry of the prepared DI-10. The spectrum was recorded using a Kratos Axis Ultra X-ray Photoelectron Spectroscopy system (Kratos Analytical Ltd, UK). The monochromatic Al Kα source at an operational power of 150 W, analyzer pass energy of 160 eV (wide spectrum), and 20 eV (element-specific lines) was used to obtain the biding energy referenced to carbon standard at 285 eV.

3.9 Nuclear Magnetic Resonance (NMR) Studies

The mPDAN synthesis via oxidation of dopamine in the presence of melatonin was followed by in-situ ^{1}H NMR (9.39 T, Avance-III, Bruker Biospin, Switzerland) at room temperature in D_2O. all the stock solutions of the reagents were prepared in 99.9% D_2O and 1H NMR spectrum was acquired on for 1 mM dopamine as reference, 1 mM dopamine with 1 mM $NaIO_4$ (polydopamine nanostructures); and 1 mM dopamine: 1mM melatonin, 1 mM $NaIO_4$ (1:1:1) (DM-NCs). The subsequent spectrum was collected at a difference of 30 min and analyzed.

4. Particle Stability, Integrity and drug release studies

The DM-NCs integrity and stability were tested by incubating in 5 mM phosphate buffer (pH 5 and pH 8), 5 mM tris buffer of pH 8.8, and hydrogen peroxide solution (5 mM and 10 mM). Further, particles were characterized using DLS and fluorescence emission intensity measurements. The amount of melatonin present into mPDAN was estimated using reversed-phase HPLC (Waters Corporation) based on the validated method. [151, 152] The hydrogen peroxide treatment at alkaline pH led to the complete degradation of mPDAN and was subjected to HPLC separately. The mobile phase, methanol and 0.1% trifluoroacetic acid in water (pH=3.0) (70:30 v/v) with 20 µL sample injected using autosampler at a flow rate of 1 mL min^{-1} were detected on photodiode array (PDA) detector at a wavelength of

278 nm. The standard curve of melatonin (R2 =0.9990, n=3) was prepared and entrapment efficiency of mPDAN was estimated using the following equation,

%EE = [(Total melatonin-melatonin in supernatant)/ Total melatonin] x 100.

The dialysis membrane technique was used to examine the in-vitro melatonin release. [153, 154] the preactivated dialysis membrane (MWCO 3kDa) filled with mPDAN and melatonin (equivalent to loaded concentration) were incubated in 40 ml sink buffer prepared using 1x PBS (pH 6.8 added with 0.4% SDS) at 37 ± 0.5ºC under dynamic shaking condition. 1 ml sink buffer was aliquoted and replaced with the fresh sink buffer at a certain time interval. The amount of melatonin present in different aliquots was estimated using both UV-visible spectrophotometer and HPLC. Furthermore, the melatonin release was fitted to Korsmeyer-Peppas, zero-order, and Hixson Crowell models and analyzed. [155]

5. Monolayer cell and three-dimensional organoid culture

The SH-SY5Y and IMR-32 human neuroblastoma cell line were procured from the National cell repository at Centre for Cell Science (NCCS), Pune, India. The culture was grown in Alanyl-L-Glutamine supplemented Dulbecco minimum essential medium (HiGlutaXL DMEM, AL007G, Himedia Labs) with 10% heat-inactivated fetal bovine serum (HiFBS, Gibco), Non-essential amino acids, 100 U mL^{-1} penicillin and 100 µg mL^{-1} streptomycin. The culture temperature 37 ºC and 5% (v/v) CO_2 atmosphere were maintained in the incubator. The multi-layered thee-dimension organoid culture of SH-SY5Y was prepared following a previously established protocol. First, SH-SY5Y cells were grown in 20% FBS containing DMEM culture medium were harvested at confluency and re-seeded ($2x10^6$ cells in 200 uL) on apical chamber of the Milli-cell membrane contain polycarbonate filters (16 mm diameter, 8 µm pore size, catalog number-PI8P01250, Millipore, Bedford, MA, USA) in a 24 well tissue culture plate. The distinct apical and basal chamber of the well partitioned by Milli-cell inserts has maintained the flow of nutrients among the multilayer culture. All the medium and treatment were added in the lower chamber of the insert with the preconditioned medium. The multi-layered SH-SY5Y cells in the inserts turn opaque and subjected to morphological test defined the number of cells > 3×10^5 cells cm^{-2} as criteria for further assessment.

6. Treatments

In the thesis, we considered two different experimental *in-vitro* neurodegenerative disease models of PD and AD developed by pharmacological doses of the rotenone and okadaic acid or amyloid-beta (A*β* fragments). Thus, the details of various treatments in these models are described as;

6.1 In-vitro Parkinson's disease model

The SH-SY5Y and IMR-32 cells resembling features of dopaminergic neurons were used for constructing the *in-vitro* experimental PD model. The established model was further used for estimation of the effective concentration of mPDAN, placebo PDAN and melatonin conferring maximum neuroprotection. First, these cells were seeded (10×10^3 cells) in 96 well plates were treated with rotenone (1 nM to 20 µM) for 72 h. For the treatment, the stock solution of rotenone was prepared in dimethyl sulphoxide (DMSO) and treated in order to prevent the maximum DMSO up to 0.025%. The dose-response curve and half-maximum inhibitory concentration (IC50) of rotenone were calculated based on the MTT results. The effective dose and percentage survival were estimated on 500 nM rotenone exposed cells co-treated with melatonin (2.3 ng mL^{-1}), mPDAN (5.1 ng mL^{-1}) and PDAN (5.1 ng mL^{-1}) in triplicates.

The cellular internalization study was performed on the SH-SY5Y cells (2 X 10^4 cells) were seeded on L-polylysine (PLL) coated coverslips inside a six-well culture plate. The mPDAN tagging with rhodamine-B was made following a reported procedure. In detail, well-dispersed 1 mg/mL mPDAN were incubated with 200 µM of rhodamine B for 24 h. The tagged nanoparticles were washed several times with Milli-Q water to remove unbound fluorophore and dialyzed against pure water for the next three days. The rhodamine tagged mPDAN (Rho-mPDAN) exposed to the cultured cell in concentration around 25 µg mL^{-1} per well, incubated for varying time point FBS containing a medium. These cells were carefully washed using 1x PBS with the use of pipette, added with 4% paraformaldehyde (PFA in 1x PBS) and incubated next 20 min. These fixed cells were further washed with chilled 1x PBS (3 times) to remove the residual of PFA and stained with DAPI (50 ng mL^{-1} in 1x PBS) for 10 min. After a quick wash with 1xPBS, these cells were mounted permanently and imaged under a confocal laser scanning microscope (CLSM).

The internalization capacity of mPDAN in 3D SH-SY5Y organoid culture was examined following the similar protocol used for monolayer culture. Briefly, Rho-mPDAN (25 µg mL^{-1}) were added to the lower chamber of the millcell insert containing 3D culture and incubated for 24 h. These cultures were carefully washed with 1x PBS by adding in the basal chamber and collecting it from the apical chamber (3 times), added with 4% PFA and incubated on 4ºC for 2 h. The DAPI (100 ng mL^{-1} in 1x PBS) was added to these cultures and incubated overnight at 4 ºC. The membrane containing 3D culture was cut and mounted permanently on the glass slide. The extent of mPDAN internalization in the 3D culture was observed using CLSM under 60 X objective and excitation laser of 405 nm and 565 nm. The cellular internalization was quantitatively estimated using cytofluorometric analysis on ImageJ software.

6.2 In-vitro Alzheimer's disease model

The *in-vitro* AD model was established in differentiated SH-SY5Y cells (1 x 10^5 cells/well). These cells were seeded in 6 well plates and exposed 1 µM Okadaic acid for 12 h in complete DMEM. Further, the medium containing DM-NCs (100 µg/mL) was added in triplicate sets and one set was irradiated with NIR. After exposure, these cells were further cultured for the next 48 h and processed for immunostaining. In separate experiments, the okadaic acid-induced SH-SY5Y cells (1x10^6 cells), treated with DM-NCs (100 µg/mL) and DM-NCs (100 µg/mL) + NIR irradiation were processed for flow cytometry-based reactive oxygen species (ROS) estimation.

The MTT (3-(4,5-dimethylthiazol-2-yl)-2,5-diphenyltetrazolium bromide) assay-based cytotoxicity profile of the prepared nanostructures was obtained on the SH-SY5Y cell adhered in 96 wells (1 x 10^4 cells/well). These cells were exposed to increasing concentration of DM-NCs (100 ng/mL, 1 µg/mL and 100 µg/mL) and irradiated with NIR (ON/OFF, 5 sec each) along with the unstimulated controls. At the endpoint, the treatment medium was removed from the assay plate well, washed with 1x PBS and added with MTT solution (0.5 mg/mL) and kept under incubation for the next 2 h. The isopropanol containing 0.04% HCl was added to dissolve the reduced formazan crystals, which were recorded by taking absorbance at 570 nm on a microplate reader (MPlex Pro 200, Tecan. Ltd.)

The SH-SY5Y cells resemble dopaminergic neurons that can form highly distinct neurite processes upon differentiation, as was reported in the earlier protocol.[156, 157] The fully differentiated SH-SY5Y cells were seeded into 6 well plates (800 cells/well) in 10% FBS enriched DMEM medium and incubated overnight by keeping inside CO_2 incubator. Furthermore, these differentiated cells were exposed to melatonin (1 µM) and DM-NCs (100 µg/mL + NIR) for the next 15 days and regularly imaged using a light microscope (EVOS XL, Thermo Scientific).

In addition, the biocompatibility and bioimaging studies of the DI-10 were conducted on the monolayer and three-dimensional culture of SH-SY5Y prepared following similar procedures mentioned in previous sections. These cultures were treated with DI-10 (25 µg/mL) in DMEM and incubated for 2, 4 and 6 h. Finally, these cells were washed with 1x PBS, fixed in PFA and mounted permanently. The CLSM was performed upon a combination of the excitation and emission channel and analyzed.

7. Mitochondrial membrane potential (ΔΨm) measurement

The fluorescence probe 5,5',6,6'-Tetrachloro-1,1',3,3'-tetraethylbenzimidazolylcarbocyanine iodide (JC1) were used to stain the treated 3D organoid culture. Briefly, these treated cultures were washed three times with 1xPBS for

5 min each and incubated with 500 nM JC1 dye for 1 hour. At endpoint, these cultures were washed using 1xPBS, immediately fixed by adding 4% PFA for 2 h at 4 ºC. The fixed organoid cultures were separated, stained with DAPI, mounted permanently and imaged under CLSM.

8. Immunofluorescence staining

The pre-treated SH-SY5Y cells were washed three times using 1xPBS, added with 4% PFA for 2 h and incubated at 4 ºC. The permeabilization of these fixed cells was performed by incubating in 0.1% Triton X-100 in 1xPBS by for 2 hours at 4º C. Next, these cells were added with 5% bovine serum albumin (BSA; Himedia lab) containing 0.1% Tween-20 for 2 hours at 4º C for blocking. After completion of the blocking step, these cells were incubated with primary antibodies included anti-amyloid beta antibody (1:1000, sc-28365, Santacruz Biotechnology, Dallas, TX, USA), anti-caspase-3 antibody (1:1000) overnight with gentle agitation on rocker platform at 4 °C. Following a few washing steps with blocking buffer, secondary anti-IgG antibody-TRITC (1:2000) was added for 2 hours and incubated at 4ºC. At completion, these cells were subjected to a quick wash, following DAPI (100 ng/mL) staining for 30 minutes. Finally, stained cells were mounted on the glass slides and imaged under CLSM (Zeiss LSM 880). The high-resolution imaging with optical sections was acquired in the respective fluorescence channel and analyzed on Zen software (Carl Zeiss, Jena, Germany), and Fiji (ImageJ, NIH). The studies comprised the expression of Aβ in SH-SY5Y cells that were subjected to the average intensity of the stacks for cytofluorometric quantifications. The relative fluorescence intensity (fold change) compared to the threshold (background) was estimated and plotted in Origin Lab (Northampton, MA, USA).

9. Intracellular reactive oxygen species (ROS) estimation

The intracellular ROS generation was estimated in SH-SY5Y cells (10,000 cells per well) seeded on 96-well plates were assayed following reported protocol. Briefly, seeded these cells were first stained with 10 μM dichlorodihydrofluorescein diacetate (DCF-DA) for 45 min in Hank's balanced salt solution (HBSS). With few intermittent items of washing of these cells with HBSS, these cells were treated with 1 μM rotenone, 1 μM rotenone + 2.3 ng mL^{-1} melatonin, 1 μM rotenone + 5.1 ng mL^{-1} mPDAN and 1 μM rotenone + 5.1 ng mL^{-1} PDAN in triplicates along with the unstimulated control. The DCF-DA Fluorescence (λex =485; λem =530) was measured on a multimode plate reader (Infinite M Plex, TECAN) in a time-dependent manner. The intracellular ROS level in AD induced SH-SY5Y cells was quantitated upon DM-NCs and DM-NCs+ NIR. The positive control cells were prepared by treating unstimulated cells with 0.1 mM H_2O_2 for 30 min. These cells were washed twice

with HBSS and incubated with DCF-DA (1 µM) for 30 min at 37 ºC. These cells were collected in HBSS by centrifuging it at 300 x g for 5 min, resuspended in HBSS and proceeded for flow cytometric estimation. The obtained cell population was specifically gated for ROS positive sub-population (ʎex= 488 nm & ʎem = 535 nm) in FlowJo software.

10. Apoptosis assay

The anti-apoptotic activity of the mPDAN was checked in the 3D organoid cultures model. These treated cultures were washed three times using 1x PBS (each 5 min) trypsinized to prepare the single-cell population and conditioned by adding 10% FBS containing DMEM. These cells were then collected and resuspended in 500 µL Annexin binding buffer. The double Annexin-V-PE and 7-AAD staining of these cells were performed following manufacturer protocol (PE Annexin V apoptosis kit, Catalog number-559763, BD Biosciences). After staining, these cells were subjected to acquisition on the BD-FACS ARIA III flow cytometer. The compatibility of the DI-10 against SH-SY5Y cells was examined using a double staining Annexin V-Cy3/6-CF kit following manufacturer protocol. First, these seeded SH-SY5Y cells were treated with DI-10 (10 µg /mL and 20 µg /mL for 48 h), washed with provided washing buffer and stained with annexin V-Cy3 (0.2 mg/ml) and 6-CF (0.05 mg/ml) for staining 20 min and were subjected to flow cytometric acquisition (FACS Aria, BD Biosciences).

11. Organotypic whole brain slice culture and immunostaining

The organotypic adult mice midbrain slice culture (MBSC) base PD and AD model were established using rotenone and okadaic acid. Prior to the construction of these models, the morphological and anatomical vitality of the culture should be maintained. Thus, for establishing MBSC, 8-week-old BALB/c wild type mice were rapidly sacrificed and decapitated. The intact brain of the mice was carefully isolated and immediately submerged in the dissection medium (2.5 mM potassium chloride, 1 mM magnesium chloride, 260 mM D-Glucose, 26 mM sodium bicarbonate, 1.25 mM dihydrogen sodium phosphate, 2 mM pyruvic acids, 2 mM Calcium chloride; pH= 7.4). The isolated brain was immediately chopped in ~ 400-500 µm thick sagittal sections using a vibrating microtome (Compresstome VF-300-0Z, Precision Instruments, North Carolina, USA). The operating parameter used was amplitude (2 mm), frequency (15 Hz), and velocity of 0.2 mm Sec^{-1}. These sliced brain sections were carefully transferred into membrane insert (0.4 µm, Millipore) with 1.2 ml/well-enriched culture medium contained 50% MEM/HEPES (Himedia), 25% heat-inactivated horse serum (Himedia), 25% Hanks' balanced salt solution (Himedia), 2 mM $NaHCO_3$ (Merck), 6.5 mg mL-1 glucose (Himedia), 2 mM glutamine (Merck pH 7.2)

and replaced on every alternate day. These MBSC were continuously observed until 7 days with time-dependent vitality tests.

The ex-vivo MBSC PD model was prepared by treating with 5 µM rotenone for 24 h in the low serum culture medium after confirming the vitality after 24 h, and the medium was replaced with fresh culture medium containing mPDAN, melatonin, and PDAN and further cultured for 72 h. upon completion of treatment, these MBSC were carefully washed using medium and proceed for the immunostaining following the procedure mentioned in 2.8. These MBSC were incubated with primary antibodies: anti-Caspase-3 (1:1000, overnight, 4º C), anti-pαSYN(S129) (1:1000, overnight, 4º C), anti-TH (1:1000, overnight, 4º C) and detected using fluorescence conjugated secondary antibody anti-Rabbit IgG-FITC (1:2500, 2 h, room temperature) and anti-mouse IgG-TRITC (1:2500, 2 h, room temperature). Similarly, upon confirming the vitality, these MBSC have proceeded with the establishment of the *ex-vivo* AD model with acute treatment of okadaic treatment (1 µM for 12 h). After confirming the establishment of the AD model, these AD induced MBSC were further exposed to DM-NCs (100 µg/mL), DM-NCs (100 µg/mL) + NIR (0.5 W/cm^2) irradiation incubated for another 7 days and proceeded for the immunostaining. The anti-amyloid beta (1:1000, sc-28365, Santacruz Biotechnology, Dallas, TX, USA) and CD-54 (1:1000, E-AB-70046, Elabscience, USA) primary antibodies were detected using anti-rabbit IgG-FITC (1:2500, 2 h, room temperature) and anti-mouse IgG-TRITC (1:2500, 2 h, room temperature) secondary antibodies. Furthermore, these MBSC were counterstained with DAPI, permanently mounted and imaged under CLSM.

12. Animals and Administrations

The Balb/c mice (female, 20-25 g) were housed under standard laboratory conditions and controlled environment and conditioned to acclimatize for at least 7days with proper availability of the food and water ad libitum. In addition, the 12 h light and the dark cycle was maintained during the acclimatization as well as the experimental procedures. All the experiments were duly approved by the institutional ethical and animal care committee and performed following provided guidelines. The twelve animals were sub-cutaneous (s.c.) injected with 2 mg/kg per day rotenone solution prepared in an equal volumetric ratio of polyethylene glycol-400 (PEG-400) and 1x PBS for total 7, 14 and 45 days. The vehicle of rotenone PEG-400/1x PBS (1:1; 100 µL per day) were injected s.c. in twelve mice as a control. The melatonin dissolved in PEG-400/1x PBS (4 mg/kg/day) was administered intraperitoneally (i.p.) in twelve mice along with previously mentioned rotenone (2 mg/kg/day in PEG-400/PBS 1:1, s.c.) injection. Similarly, the placebo PDAN was co-injected i.p. (7.5 mg/kg/day) with rotenone (2 mg/kg/day in PEG-400/PBS 1:1, s.c.) and mPDAN (8 mg/kg/day; i.p.) co-injected with rotenone (2 mg/kg/day in PEG-400/PBS 1:1,

s.c.). All the animals received the injections subjected to the behavioral assessment performed for alternate days post-injection. based on the behavioral results, the 4 animals from each group were sacrificed on day 7. These animals are anesthetized, perfused with PBS, and 4% PFA and proceed for further histochemical assessment. Furthermore, all the animals left were anesthetizing on the 45th day of the experiment and perfused with using 1x PBS. Out of these, the only four animals from each group were subjected to perfusion with 4% PFA and the brain was dissected for immunohistochemistry. The other four brains of all the groups perfused with PBS were isolated and subjected to western blotting.

13. In-vivo imaging and Biodistribution study

All the animal experimental procedures were approved and monitored by the institutional animal ethical committee and were followed in accordance with the guidelines. The whole-body bio-distribution profile of the mPDAN and DI-10 were performed in the BALB/c mice (four mice per group) via injecting this nanoformulation from the lateral tail vein and time-dependent imaging under IVIS Spectrum animal imager. First, the mPDAN was tagged with the NIR dye indocyanine green (ICG) based on the earlier reported procedures. Briefly, the mPDAN (27 mg) and ICG (2 mg) were taken in 5 mM acetate buffer (pH=4.8) dissolved well and mixed by keeping on a rotary shaker for 12 h at room temperature. The tagged mPDAN were collected by centrifuging at 16,000 rpm, 15 min, and washed well 3 times using 1x PBS. The collected nanoparticles were subjected to dialysis (3 days) in order to remove any loosely bound dye. The grouping of the animals was done as; only ICG injected group (1 mg/kg), ICG-mPDAN (5 mg/kg) intravenously (i.v.) injected and saline-injected group. In another set of imaging, where DI-10 was directly injected to animals via tail vein and imaged at variable fluorescence excitation/emission parameters. All the animals used in this study were cleaned with the ventral side fur to prevent the scattering and anesthetized by keeping in the vaporizer chamber maintain with the flow of 1.5.0% isoflurane flow along with oxygen gas. These anesthetized animals were quickly placed in the imaging chamber of the IVIS Spectrum 200 Imaging System (Xenogen) constantly maintained with a flow of 1.5 % isoflurane carried by oxygen gas. The imaging of the animals was performed from 15 min to 24 h time point after injection. The images acquired at the variable time point and exposure parameter were analyzed using Living Image software v4.0 (Xenogen) and represented as an average radiant efficiency (photons/second/centimeter/steradian). On observation of the whole-body distribution pattern of the nanostructures, these were re-injected in another set of animals for the particular time period and vital organs, including the kidney, liver, lung, and spleen and brain were excised and imaged for the presence of the nanostructures on the imager. For the histopathological studies, the mPDAN were injected in the Balb/c mice (5 mg/kg/day) for 15 days under laboratory condition. These

animals were sacrificed upon completion of the time point, and major organs, including the kidney, liver, lung, and spleen and brain were excised and immediately submerged in the 10% formalin. These issues were further embedded in paraffin resin and sectioned using ultra-microtome in 10-50 µm thick sections and subjected to Hematoxylin (S058, Himedia Lab) and Eosin (S007, Himedia Lab) (H&E) staining following an established procedure.

14. Brain Tissue Processing and Immunohistochemistry

The pre-fixed brain tissue was incubated with a range of sucrose (10%, 20% and 30%) solution prepared in 1xPBS. These intact brains were embedded in cytomatrix (Shandon Cryomatrix, Cat. No.-6769006, ThermoFisher Scientific, USA) and coronally 30 µm thick sections were obtained using freezing cryotome (HM525 NX, ThermoFIsher Scientific, USA). The collected midbrain tissue sections were transferred in PBST (1x PBS containing 0.05% tween 20 (pH=7.4)) and incubated at 80 ºC for 30 min for antigenic retrieval. Further, antibodies staining was performed following standard immunohistochemistry protocol mentioned in section 2.8 of the experimental section. The primary antibodies: anti-Caspase-3 (1:1000, overnight, 4º C), anti-pαSYN(S129) (1:1000, overnight, 4º C), anti-TH (1:1000, overnight, 4º C), 129, prepared in the blocking buffer (5% BSA+ PBS) were used to probe the particular protein of interest. These primary antibodies were further detected using anti-Rabbit IgG-FITC (1:2500, 2 h, room temperature) and anti-mouse IgG-TRITC (1:2500, 2 h, room temperature) secondary antibodies. These immune-stained midbrain sections were counterstained using DAPI, permanently mounted and subjected to CLSM imaging.

15. Total RNA extraction, cDNA synthesis, and Quantitative Real-Time PCR (qPCR)

The total RNA extraction from control and rotenone treated SH-SY5Y cells, co-exposed with melatonin, PDAN, mPDAN were performed using one of the procedures provided with PureLink RNA mini isolation Kit (Catalog number-12183018A, ThermoFisher Scientific,). Briefly, the cells collected in a sterile microcentrifuge tube were added with 350 µL lysis buffer containing 1% 2-mercaptoethanol. The obtained lysates were transferred to the provide spin mini-columns, subjected to fewer steps using washing buffer provided with the kit and subjected to in-column DNA digestion using DNase I reagent. Following contaminated DNA degradation, the column was washed repeatedly to inactivate the DNase I. Finally, the spin column containing RNA were transferred to fresh microcentrifuge collection tube, the 30 µl of RNase-free water was added in the middle of the membrane, incubated for 2 min and centrifuged at 3000 x g to elute the RNA stored at -80 ºC in aliquots. The purity and yield of RNA were quantified by measuring absorbance at 260 nm, and 260/280 nm ratio at NanoQuant (Tecan. Instruments).

Component	Volume (µL) Total (20 µL)
10X RT buffer	2 µL
10X RT Primers	2 µL
25X dNTP Mix (100 mM)	0.8 µL
MultiScribe Reverse Transcriptase	1 µL
RNAse Inhibitor	1 µL
mRNA	1 µL
Water (Nuclease free)	12.2

Table 2.1: The cDNA synthesis reaction mixture

The cDNA was prepared using the High capacity cDNA reverse transcription kit (catalog number-4368813, Thermo-Fisher Scientific). Briefly, ultra-pure ~ 1 µg mRNA in 1x reverse transcriptase reaction buffer (10x), 1x random primers (10x), 0.8 µL deoxynucleotides (dNTP) mix (100 mM, 25x),1 µL RNase inhibitor, 1 µL reverse transcriptase were taken in final reaction volume of 20 µL. The synthesis reaction was performed by incubating the mixture at 25 ºC (10 min), 37°C (120 min) and 85°C (5 min) step in a thermocycler (QuantStudio 3, Thermo Fisher Scientific). The samples were quantitated for the yield, purity and stored at −80°C until further use.The qPCR assays for gene expression analysis of Caspase-3, Interleukin-1β (IL-1β), Interleukin -6 (IL-6), Mitogen-activated protein kinases 3(3-pK or MAPKAPK3), Serine/threonine-protein phosphatase 2A (PP2A), Nuclear Factor Of Kappa Light Polypeptide Gene Enhancer In B-Cells 1 (NF-kB), AKT Serine/Threonine (Akt), Alpha-Synuclein (SNCA), Enhancer of Zeste homolog 2 (EZH2), Enhancer of Zeste Homolog 1 (EZH1) and B Lymphoma Mo-MLV Insertion Region 1 Homolog (BMI-1) were performed by adding 100-500 ng/reaction of cDNA template, 10 µL Maxima SYBR Green Mix (Catalog number-K0221, Thermo Fisher Scientific), 150-300 nM primers concentration (depending on amplification efficiencies) and nuclease-free water to a 20 µL total volume. The melting curve analysis was performed for each between 55 and 95 °C for amplification product evaluation. The analysis obtained with a higher presence of primer dimers; an additional acquisition step was added in each PCR cycle at 76 °C. The reaction condition of 94°C during 3 min followed by 40 cycles of a 15 s denaturation step at 94°C and a 30 s annealing and elongation step at 60°C were used.

Component	Total reaction concentration (20 µL)
Maxima SYBR Green/ROX qPCR Master mix (2x)	10 µL (1X)
Forward Primer	0.3 µM
Reverse Primer	0.3 µM
Template DNA	< 500 ng
Water (Nuclease free)	Up to 20 µL

Table 2.2: The qPCR reaction component

Gene (Human)	(5'-3') forward primer	(5'-3') reverse primer
EZH2	GCCAGACTGGGAAGAAATCTG	TGTGCTGGAAAATCCAAGTCA
Caspase-3	TTAATAAAGGTATCCATGGAGAA CACT	TTAGTGATAAAAA TAGAGTTCTTTTGTGAG
BMI-1	CTGGTTGCCCATTGACAGC	CAGAAAATGAATGCGAGCCA
GAPDH	GACTCATGACCACAGTCCATGC	AGAGGCAGGGATGATGTTCTG
IL-6	CCAGCTATGAACTCCTTCTC	GCTTGTTCCTCACATCTCTC
IL-1β	AATCTGTACCTGTCCTGCGTGTT	TGGGTAATTTTTGGGATCTACACTCT
α-Syn	GCCAAGGAGGGAGTTGTGGCTG C	CTGTTGCCACACCATGCACCACTCC
PP2A	TGCTGGGGAACTCTCACTCT	TTATCGGGATCAACTCCGG
3pK	AGGCTCAAAACTTGCCTCCT	GTGTGTCCATCTATGATCCCGG
EZH1	GCTTCCTTCACCCTTTTCATGCC ACCC	CGACGACCAGAGCACTTGGAG
NFkB	CCCCACGAGCTTGTAGGAAAG	CCAGGTTCTGGAAACTGTGGAT

Table 2.3. The primer set used for the qPCR studies

The primer sets used for the amplification were obtained from Integrated DNA Technology (IDT, Iowa, USA) considered based on their validation in previous reports. The reaction was conducted in Quant-Studio 3 Real-time PCR detection system (Thermo Scientific). The assay also included a non-template and no RT control (NTC, the sample was substituted by nuclease-free water; No-RT similar amount of mRNA directly used for amplification). Each amplification run was performed in the triplicates and measured for the threshold cycle (Ct) in the exponential phase. The Data analysis was performed on Quant Studio 3 design and analysis software (Thermo Scientific, Version 1.4.3). The Ct (ΔCt) and ΔΔCt were estimated based on Pfaffl's formula and represented as gene expression fold change.

16. Protein preparation and western-blot

The treated cells and tissues were washed twice with ice-cold phosphate buffer saline (pH=7.4) and scraped in modified radioimmunoprecipitation (RIPA) buffer (50 mM Tris-HCl pH 7.4, 1% NP-40, 0.25% Na-deoxycholate, 150 mM NaCl, and 1 mM EDTA) containing protease and phosphatase inhibitors (SIGMAFAST and PhosSTOP, Sigma Aldrich) to prepare the lysate. The lysate was subjected to ultrasonication, centrifuged at 14000 g for 10 min at 4º C, and the supernatant was used of the estimating yield using the Bradford reagent (ML106, Himedia labs). The 30 µg protein lysate was loaded in each well and resolved on sodium dodecyl sulfate-polyacrylamide gel electrophoresis (SDS-PAGE). The resolved protein bands were transferred to polyvinylidene fluoride (PVDF, 0.22 µm, Bio-Rad) membrane using a semi-dry transfer unit (Biorad. Ltd.) at room temperature. The blot containing transferred proteins were incubated in 5% bovine serum albumin prepared in Tris-buffered saline and Tween 20 (blocking and washing buffer) and incubated overnight at 4º C. The specific proteins were detected using the following primary antibodies: anti-Caspase-3 (1:1000), anti-pα-SYN(S129) (1:1000), Ubiquityl-Histone H2A (Lys119) (H2AK119ub, 1:1000), Bmi-1 (1:1000) anti-TH (1:1000), anti-β-Amyloid (1:1000, sc-53822, Santacruz Biotechnology, Dallas, TX, USA, overnight, 4º C) and anti-β-Actin (1:1000) by incubating overnight at the mild shaking condition. The blots were washed with washing buffer (3 times, 5 min each) and incubated with Horseradish peroxide tagged, m-IgGk BP-HRP (1:2000, 1 hour, room temperature) and anti-rabbit IgG-HRP (1:2000, 1 hour, room temperature), finally generated using chemiluminescence reagent (Bio-Rad) and imaged under ChemiDoc XRS+ imaging (Bio-Rad) and Azure C600 (Azure Instruments).

17. Immunoprecipitation assay

The 5% Cleared lysates obtained in RIPA buffer were incubated for 1 hr with anti- pα-SYN (S129) (0.2 µg) and anti-BMI-1(0.2 µg) antibodies for 1 hr at 4º C. These mixtures were incubated with Protein A/G agarose beads (sc-2003, SCBT, USA) overnight under mild

shaking condition. The beads were collected using centrifuge (3000 rpm, 10 min, 4º C) and washed five times with ice-cold lysis buffer. The obtained pellet was resuspended in SDS sample buffer heated at 95 ºC. The beads and proteins were separated at this step using spin at 5000 rpm for 5 min at room temperature. The recovered lysate was separated on SDS-PAGE and immunoblotted against anti-ubiquitin (1:1000) and anti-BMI-1(1:1000) antibodies. A similar experiment was performed for the lysate from 250 nmol rotenone and 2.3 ng/mL melatonin treated SH-SY5Y, immunoprecipitated using anti-BMI-1(0.2 µg) and immunoblotted with anti- *p*-Serine (1:1000) following the similar procedure detailed in section 2.16 of the experimental system.

18. Assessment of the photothermal effect

The photothermal effect of the nanostructures was estimated as the extent of change in the temperature of the aqueous dispersion of the DM-NCs (100 ng/mL, 1 µg/mL and 100 µg/mL) upon NIR exposure. The dispersion was taken in quartz cuvette irradiated with NIR (~0.5 W/cm^2 for 15 min) and simultaneous temperature change using a digital thermometer. The equivalent volume of the saline in the cuvette was considered as a control in the experiment. The DM-NCs (100 µg/mL) was subjected to alternate on/off the cycle of NIR each for 15 min with continuous measurement of change in the temperature. The NIR responsive melatonin release from DM-NCs was performed following the experimental setup reported earlier. [158] The nanomaterial was packed into activated dialysis membrane tube (MWCO 3 kDa), hermetically sealed, and dialyzed against a 40 ml sink buffer containing 1x PBS with 0.4% SDS at 37 ± 0.5ºC. One set of the dialysis tube was exposed to NIR (808 nm, 0.5 W/cm^2, for 15 min) and sample was collected quickly after exposure. The amount of the melatonin release was estimated by taking absorbance at 278 nm and calculated based on the standard.

19. Amyloid beta (Aβ) fibrillation and anti-aggregation assessment

.The stock of Aβ peptides was prepared following the reported protocol,[159] as 1 mg lyophilized peptide was dissolved adequately in hexafluoro-2-propanol (HFIP, 500 µM) to disaggregate the preformed fibrils. The solution containing HFIP was aliquoted and kept in a vacuum for evaporation and stored at −80° C until used. The aliquoted Aβ was dissolved in water containing 0.02% NH_3 and dissolved in the buffer to get the 100 µM concentration and used for experiments. The Aβ aggregate was prepared following a standard protocol [160]. Briefly, the Aβ to 10 µM in final concentration were incubated in 50cmM Tris buffer (pH=7.8) containing 100 mM NaCl and incubated at 37 °C for 24 h to achieve the Aβ aggregates.

To test the Aβ anti-aggregation characteristic of the DM-NCs, Aβ (10 μM in final concentration) solution was diluted in 20 mM Tris-HCl buffer (pH=7.4) containing 100 mM NaCl (Aggregation buffer) added with 20 μM ThT in final concentration within 100 μL of reaction volume at 37 °C and continuously measured for fluorescence emission intensity value. As a control experiment, preformed Aβ fibrils seed (0.2%, 1%, and 2%) v/v, were added to Aβ monomer (10 μM) and aggregation kinetics were measured using ThT fluorescence.

The Aβ monomer (10 μM), Aβ monomer (10 μM) + DM-NCs (1 μg/mL) and Aβ monomer (10 μM) + DM-NC (100 μg/mL) proceeded for aggregation reaction (n=3) in aggregation buffer and time-dependent fluorescence emission intensity of ThT was recorded. In next set of reaction, Aβ monomer (10 μM), Aβ monomer (10 μM) + DM-NCs (1 μg/mL) and Aβ monomer (10 μM) + DM-NCs (100 μg/mL) were irradiated with NIR (ON/OFF= 5 sec; 0.5 W/cm^2) after 2 h post-incubation in aggregation buffer. The ThT fluorescence emission intensity (λem = 480 nm; λex = 445 nm) was measured in kinetic mode. The aggregated Aβ fraction of Aβ monomer (10 μM), Aβ monomer (10 μM) + DM-NC (100 μg/mL) and Aβ monomer (10 μM) + DM-NCs (100 μg/mL) + NIR after 24 h were diluted and processed for TEM imaging following procedure mentioned in earlier section of the method.

20. Aβ- Protein Misfolding Cyclic Amplification (Aβ-PMCA) Assay

The Aβ-PMCA was performed following an earlier reported method. [161] Briefly, a 2% mixture of preformed Aβ fibrils was ultrasonicated for 30 sec (Amplitude 50%) and incubation with monomers at 37 °C for 24 h considered as one PMCA cycle. After 24 h, again 2% of the preformed seed was mixed with Aβ monomer and sonicated for 30 sec, kept under incubation for 24 h, next PMCA cycle and similarly continued till 20th cycle. The ThT based endpoint fluorescence emission intensity measurement of the Aβ at the end of each cycle was performed. Next set of an experiment performed by the addition of DM-NCs (100 μg/mL) following NIR laser (5 sec ON & 5 sec OFF) for 15 min, 2 h post-treatment. The Aβ aggregation state was examined using ThT fluorescence at the end of each PMCA cycle and TEM imaging at the completion of the 20th PMCA cycle.

21. In-vitro Aβ disaggregation studies

The preformed Aβ fibrils were collected by centrifuge, dispersed in PBS buffer. The 10 μM Aβ fibrils were incubated with DM-NCs (100 ng/mL, 1 μg/mL and 100 μg/mL) at 37 °C and subjected to NIR (5 sec ON & 5 sec OFF, for 15 min) exposure. The ThT endpoint fluorescence emission intensity was analyzed relative to the control for Aβ fibrils integrity.

22. Protein adsorption measurement and surface covering

The nanoparticle surface coverage (%) was estimated using the Langmuir isotherm model, which were used to estimate the protein adsorption over the Cur-REM$_{100}$ surface [162]. The fluorescence emission intensity recorded for different proteins was fitted to the Langmuir equation (Equation 1) [163, 164].

$$\Gamma = \frac{\Gamma_{max} \cdot C}{K \cdot C} \quad (1)$$

Where Γ is surface coverage of nanosphere, Γ_{max} represents the maximum surface coverage on nanosphere, C is bulk protein concentration, and K is the apparent binding/dissociation constant have been calculated by nonlinear regression analysis with least square fitting method [165]. Similarly, parameter K (dissociation constant) and Hill coefficient (h) were obtained by considering one site-specific binding with hill slop by fluorescence emission intensity versus protein concentration curve.

23. Steady-state fluorescence anisotropy measurement

The steady-state fluorescence anisotropy of curcumin was measured on a spectrofluorometer (FS5, Edinburgh Instruments)

The anisotropy (r) was calculated using the equation:

$$r = \frac{I_{vv} - GI_{vH}}{I_{vv} + 2GI_{vH}} \quad (2)$$

Where I_{vv} and I_{vH} are the observed fluorescence intensities, and subscript v (vertical) and H (horizontal) represents the orientation of excitation and emission polarizers. The instrument correction factor (G) was calculated by the expression[166]:

$$G = \frac{I_{HV}}{I_{HH}} \quad (3)$$

Where I_{HV} and I_{HH} are the measured fluorescence intensities by setting the Excitation polarizer/ Emission polarizer at horizontal/vertical and horizontal/horizontal signifying by subscript v (vertical) and H (horizontal). The anisotropy (r) measurement value is further corrected and analyzed.

24. Data processing and significance analysis

All the results variables are expressed as mean ± SEM in the results. The instrumental data were analyzed and plotted on Origin 8.5 (Northampton, USA) and GraphPad Prism 5 (GraphPad Software, La Jolla, CA, USA). The standard and equation fitting were performed using linear and non-linear regression analysis methods, particularly for calculation of the inhibitory concentration (IC50) and standard curve preparation. The one-way analysis of variance (ANOVA) with Tukey's and Bonferroni significance test were performed to

compare the statistical significance of the mean for the P-values (*P ≤ 0.05, **P ≤ 0.01, ***P ≤ 0.001) and (#P ≤ 0.05, ##P ≤ 0.01, ###P ≤ 0.001) relatively. [167].

Note:

* The due permission has been obtained from authors and corresponding author of the following published paper before adopting in the present thesis.

- Melatonin/Polydopamine Nanostructures for Collective Neuroprotection based Parkinson's Disease Therapy; Anup K. Srivastava, Subhasree R. Choudhry, and Surajit Karmakar; **Biomaterials Science**; Doi: 10.1039/C9BM01602C
- New insight into curcumin tethered lanthanum carbonate nanospheres and protein corona conferring fluorescence enhancement based sensitive detection of Amyloid-β aggregates. A. K. Srivastava; A. Dev; S.R. Choudhury; S. Karmakar **Sensors and Actuators B**: **Chemical**. 2018;262(1)
- Near-Infrared Responsive Dopamine/Melatonin Derived Nanocomposites Abrogating In-situ Amyloid Beta Nucleation, Propagation and Ameliorate Neuronal Function. Anup K. Srivastava; S.R. Choudhury; S. Karmakar; **ACS Applied Materials and Interface**. 2020, 12, 5, 5658-5670.

Chapter 3

Studying intrinsic reactivity of dopamine derived intermediates and melatonin upon co-abundance forming melatonin/ polydopamine nanostructures

1. Background

Polydopamine inspired hybrid nanostructures are obtained from the precursor dopamine (DA), and further integrating other polymers, small molecules, metals, and inorganic contents make it highly biocompatible for several biological applications. Polydopamine introduced a couple of decades ago, now frequently being used in the biocompatible thin film, [168] sensing platform, [169] active drug delivery vehicle [170], theranostics and tissue engineering. Dopamine is a catecholamine-based neurotransmitter localizes in the dopaminergic neurons in the brain and functionally regulates reward, cognition, body coordination, and motor functions. [14, 15] Due to unknown factors under oxidative and proteomic instability, dopamine deposited as insoluble black neuromelanin under physiological control.[171-173] This slow oxidation of dopamine proceeds with the chain of chemical reactions, which is highly dependent on the overall ionic and redox state in the local environment. [174-176]. Hastings et al. have demonstrated that dopamine upon oxidation can undergo one electron or two-electron oxidation reaction and produces semiquinone radical or dopamine-o-quinone (DQ), which is highly toxic, reactive and can easily couple with other radicals. [177] Further, *in-vivo* and *in-vitro* induction of the DQ induces the activation of microglial cells corroborates with enhanced cellular reactive oxygen species (ROS), oxidative nitrogen species (NOS), hydrogen peroxide (H_2O_2) and proinflammatory cytokines level. [178, 179] Transiently stable DQ undergoes intramolecular cyclization to form another reactive intermediate aminochrome (AC),[180] further rearrange to 5,6-indolequinone (DHI)[181] as the immediate precursor of protective neuromelanin/polydopamine. [182] DHI under oxidation forms a more stable indole 5,6-quinone, which as co-precursor self-assembled with DHI to form the polydopamine.[183]

In the past decades, the number of strategies has been employed to produce the multifunctional polydopamine nanostructures. The most trivial approach used for preparing polydopamine nanostructures is the oxidation of dopamine at higher pH under dissolved oxygen, using ammonium peroxodisulfate and sodium periodate as a chemical catalyst. [184] Recently, silica like reverse microemulsion methods with a controlled rate of ionization and polymerization in water/alcohol mix solvent were employed to prepare porous, hollow and highly stable polydopamine materials of ~50 nm diameter. The strategies further innovated with the template-assisted synthesis of the polydopamine capsules and core-shell nanostructures for multi-purpose drug delivery and catalytic applications. [185] The evolution mechanism of all these variants of polydopamine structures relied extensively on the rate of initial ionization induced by oxidants and intramolecular self-assembly of the intermediates produces polydopamine structure in nanosized range. The rate of dopamine oxidation is rationalized as one of the critical steps

for controlling the nanoparticle size and physicochemical properties. To date, there are very less information, whether the dopamine oxidation product can interact with melatonin (N-acetyl-5-methoxytryptamine) and consequent to form a new hybrid biomaterial. To probe this interaction for the first time, melatonin and dopamine has been used as a precursor to form a variant of hybrid nanostructures, which were characterized for their structural and morphological features, the exact mechanism of evolution and validated for their integrity and stability in a variable physiologically stressed environment. Hence, these two neurohormones regulate distinct neuroendocrine functions in the brain are used as precursors to fabricate the melatonin/polydopamine nanostructures (referred to as mPDAN and MEPN).

2. Results and discussions

2.1 Fabrication and Characterization of melatonin/polydopamine hybrid nanostructures

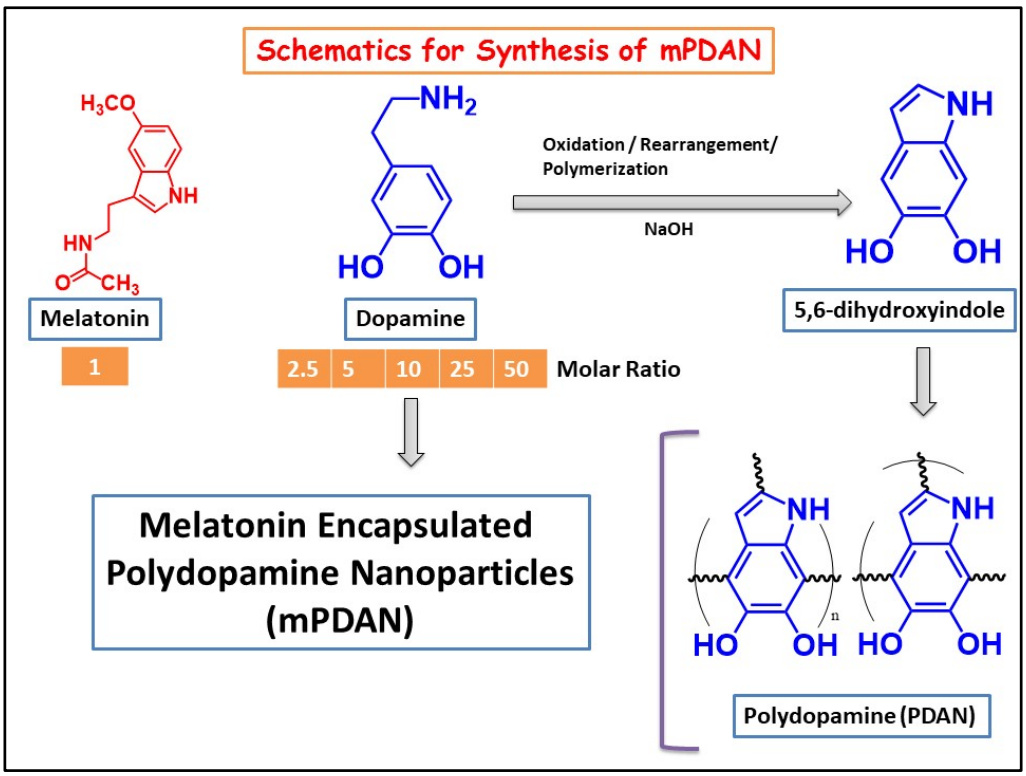

Figure 3.1. **The schematics are illustrating the steps for mPDAN preparation.**

The inspiration for preparing melatonin/polydopamine hybrid nanostructures has been taken from the process of natural accumulation of polydopamine/neuromelanin as self-assembled dopamine derived products in the midbrain region. [186] The vesicular monoamine transporter 1 (VMAT1) plays an essential role in the cellular dopamine homeostasis and functions to accumulate non-vesicular dopamine in the cytoplasm as neuromelanin. [187] This accumulated neuromelanin in the brain confer antioxidative and

neuroprotective role, terminally degraded via cytoplasmic peroxidation, and release the molecules encapsulated inside the neuromelanin. [156, 188] Considering this information, we conceptualized the synthesis of melatonin enriched polydopamine nanoformulation (mPDAN) following controlled oxidation based self-assembly of oxidative dopamine intermediates as represented in Figure 3.1.

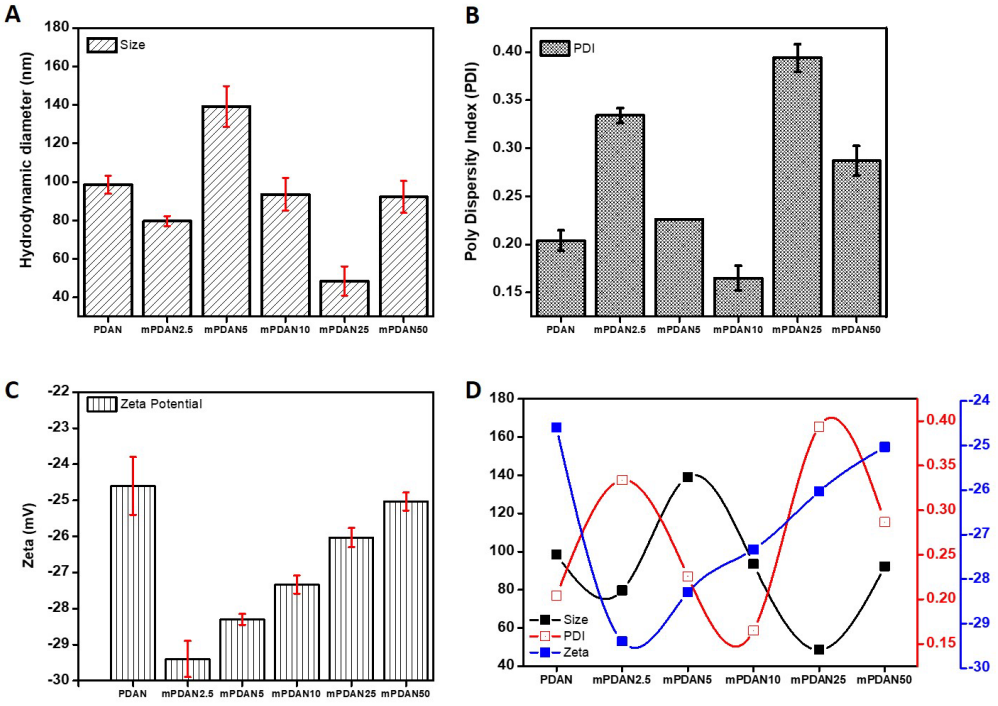

Figure 3.2. The photon correlation spectroscopic measurement of mPDAN variants; (A) The hydrodynamic diameter, (B) The polydispersity index (PDI), (C) The zeta potential, (D) Composite curve of the all these parameters.

The increasing variable concentration of dopamine and melatonin was used in such a way that ratio among dopamine/melatonin were ranged between 2.5:1, 5:1, 10:1, 25:1 and 50:1 and the obtained mPDAN were referred as mPDAN2.5, mPDAN5, mPDAN10, mPDAN25, and mPDAN50 as represented in Figure 3.1. The mPDAN prepared using 1:2.5 (molar ratio) of melatonin: dopamine displayed considerable physicochemical characteristics of the nanostructures. The mean hydrodynamic diameter of the mPDAN and PDAN was around 79 ±13 nm and 93 ±11 nm. The best-optimized parameter was estimated by monitoring of individual components includes concentration, temperature, and duration of the reaction in the synthesis process. The dynamic light scattering (DLS) and scanning electron microscope (SEM) imaging-based characterization provided uniform spherical morphology in the nano-dimensional range. The mean hydrodynamic diameter of the mPDAN variants (dh = 50-141 nm) the polydispersity index (PDI = 0.17-0.40) and zeta potential (-24.6 – 29.5 mV) were obtained using DLS measurement (Figure 3.2 A-D). The zeta potential value of -24.6 mV measured for PDAN estimated in more negative values for

maximum melatonin loading in mPDAN25. The gradual increase in the zeta potential value proportional to the dopamine/melatonin ratio can be seen in Figure 3.2C, and 3.2D suggested the drug and nanocarrier interaction, as well as the co-abundance, are the critical parameter determining the surface charge behavior of the nanoparticles. Furthermore, SEM imaging of the mPDAN variant displayed the uniform spherical structures with the extent of aggregation proportional to the added melatonin in the synthesis (Figure 3.3A).

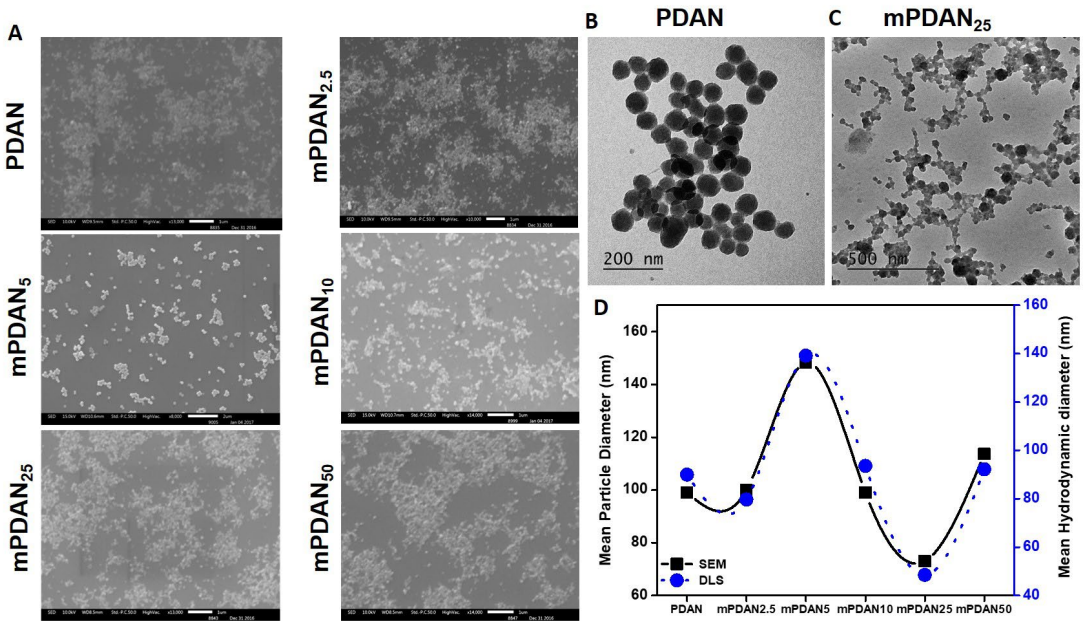

Figure 3.3. Morphological characterization of the mPDAN variants; (A) The scanning electron micrograph (SEM) of the mPDAN variants, (B and C) The transmission electron microscopic (TEM) image of the PDAN and mPDAN2.5, (D) The comparison of the hydrodynamic diameter obtained from DLS and mean particle diameter observed under SEM.

The mean nanoparticle diameters were precisely measured using the ImageJ software tool and compared to the hydrodynamic diameters of mPDAN variants obtained under DLS. The perfect correlation among the particle diameter distribution confirms the consistency among preparation, as displayed in Figure 3.3D. The morphology of the mPDAN and PDAN was observed under a transmission electron microscope (TEM). These nanoparticles had a spherical shape and narrow particle size distribution, as reflected in our DLS and SEM results (Figure 3.3B and 3.3C). These results further confirmed that the dopamine/melatonin ratio is the critical determinant of the morphology and physicochemical properties of mPDAN. Considering these results, mPDAN2.5 obtained at the highest precursor ratio displayed higher stability, and this characteristic makes it eligible to use in all further studies. Another synthesis proceeded with precursor dopamine/melatonin ratio of 1:1 formed sub 20 nm-sized small nanocomposites referred to as dopamine/melatonin nanocomposites DM-NCs. The preparation methodology has employed the controlled oxidation of the dopamine in the presence of an equimolar concentration of the melatonin,

triggered using chemical catalyst sodium periodate at 30 ºC. Dopamine under catalytic oxidation forms a range of reactive catechol and indole intermediates, which upon self-assembly forms a dark black colored end product polydopamine (PDANPs) elaborated in many earlier reports. [189] In the present work, for the first time, we used melatonin and dopamine as a precursor in synthesis, which is leading to a highly biocompatible nanocomposite of < 50 nm diameters. DM-NCs preparation is optimized by considering 1:1 and 2:1 ratio of dopamine and melatonin and added with an equal concentration of sodium periodate ($NaIO_4$). The DLS & TEM results provided the mean particle diameter of 16.7 ± 4.6 nm of DM-NCs obtained with a 1:1 precursor ratio. In contrast, it was 60.4 ±12.5 nm for the DM-NCs prepared by considering 2:1, dopamine/melatonin ratio (Figure 3.4).

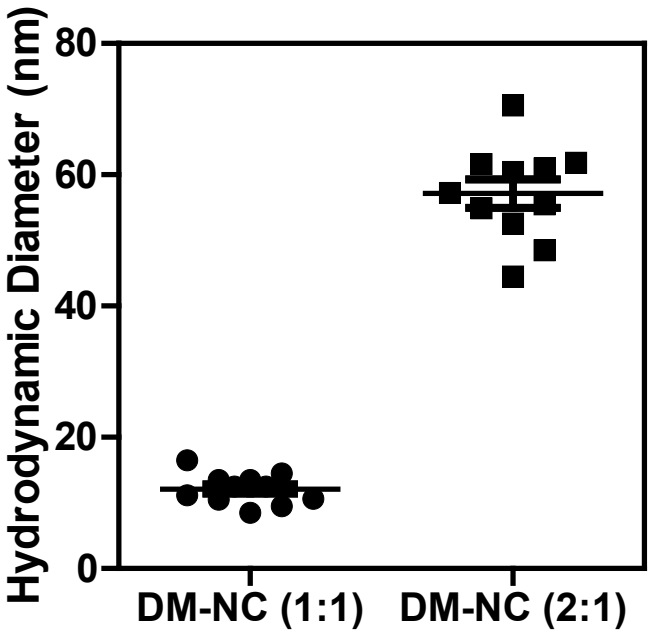

Figure 3.4. The mean hydrodynamic diameter of the DM-NCs obtained by dynamic light scattering (DLS) measurement

It is observed that dopamine/melatonin ratio confers maximum influence on the physicochemical characteristics of DM-NCs.The polydispersity index (PDI) of ~0.35 of variants suggests the narrow particle size distribution. Polydopamine nanostructures (referred to as PDANPs and PN) are used as control materials prepared from dopamine following a similar procedure. The physiological buffering of these neurohormones in nanomolar to picomolar concentration regulates wide neuroendocrine function in the brain. [190, 191] However, supporting previous studies, the equimolar concentration of dopamine and melatonin in the synthesis indicates that co-abundance of the melatonin and dopamine is one of the critical factors determine the physicochemical characteristics of DM-NCs. [192]

2.1 The hybrid nanostructures evolution mechanism and interactions

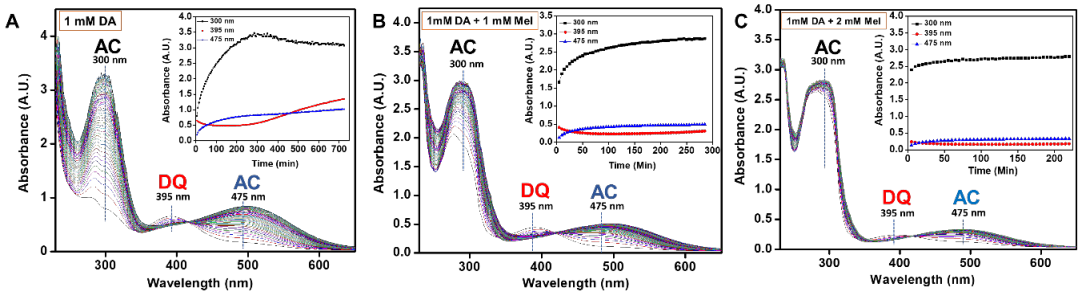

Figure 3.5. UV-vis spectroscopic analysis of DM-NCs synthesis; (A) The UV-vis absorbance spectrum of the dopamine (DA, 1 mM) under oxidation; **(B)** dopamine (1 mM) and melatonin (1 mM); **(C)** and dopamine (1 mM) and melatonin (2 mM). The major peaks assigned to dopamine-o-quinone (DQ, 395 nm, red), aminochorme (AC, 300 nm and 475 nm of black and blue). The DQ and AC specific kinetic curves are represented in the graph (inset).

The controlled dopamine oxidation to reactive intermediates using sodium periodate paved the way to study the effect of melatonin on dopamine oxidation kinetics. Thus, we have taken an optimized concentration of dopamine in the glass cuvette and induced the oxidation reaction by adding an equimolar concentration of the $NaIO_4$. This reaction was continuously observed by collecting the time-dependent UV-vis spectrum. The appearance of multiple peaks in the UV-Visible spectrum indicated the evolution of dopamine-o-quinone (λmax =395 nm), aminochrome (λmax =300 nm and 475 nm) are assigned based on earlier reports (Figure 3.5A). [192] The appearance of these peaks can be correlated with the appearance of intermediates mimicking the natural melanogenesis process in the solution phase. [193] The oxidation reaction with the equimolar ratio of dopamine and melatonin triggered with equimolar $NaIO_4$ under similar parameters displayed a time-dependent decrease in the dopamine-o-quinone and aminochrome UV-vis peak intensity (Figure 3.5B).

Furthermore, another oxidation reaction with 2 mM melatonin with 1 mM dopamine was induced with similar 1 mM concentration of the $NaIO_4$ displayed the further decrease in the intensities of the peak corresponds to DQ and aminochrome, suggested the existence of specific interactions between melatonin and dopamine derived intermediates during the reaction process as displayed in Figure 3.5C. The absorbance maxima of these peaks plotted as a function of time displayed the comparative kinetic curve of evolution in control reaction containing only dopamine, dopamine in the presence of 1 mM melatonin, dopamine in the presence of 2 mM melatonin. It can be seen that with increased concentration of added melatonin in the reaction, the slight decrease in the intensity and early saturation of dopamine-o-quinone and aminochrome specific curves has been observed, which further confirms the possible interactions which are influencing the dopamine oxidation kinetics (inset in Figure 3.5). Since both dopamine and melatonin have characteristic absorbance at ~280 nm, which makes it challenging to estimate the actual amount of these precursors

dynamically utilize in the reaction process. However, the differential absorption peak of the oxidative intermediates provides an estimate of melatonin and dopamine derived intermediates interactions during the reaction process.

The time-dependent ^{1}H Nuclear magnetic resonance (NMR) spectrum is acquired for dopamine, melatonin, an equimolar mixture of dopamine and melatonin (Figure 3.6). These spectra show the presence of the characteristic proton associated resonance peak is assigned based on chemical shift calculations and available references (Figure 3.7, 3.8).[192] The ^{1}H NMR spectrum shows characteristic resonance peaks of dopamine and melatonin are unambiguously visible in the spectrum dopamine/melatonin physical mixture confirms the absence of any interaction between these two small molecules in the native state (Figure 3.9 and Table 3.1 to 3.3).

The NMR spectrum recorded at an interval of every 30 min till 2 h time point of dopamine oxidation appears with the multiple resonance peaks assigned to the evolution of 5,6-indolequinone, dopamine, and aminochrome based on the earlier reports (Figure 3.10 and Table 3.4). However, following interaction of dopamine (1 mM) and melatonin (1 mM) during the synthesis phase indicated significant broadening, shifting, and complete deficiency in the resonance peak intensity of associated protons (Figure 3.11). The extended view of the particular region displayed the complete disappearance of the peaks assigned to 5,6-indolequinone and aminochrome within 2 h, with residual downfield shifted dopamine backbone proton resonance peak perfectly affirmed the transient reactivity of the melatonin towards these intermediates (Table 3.5). The integral peak values obtained after quantification suggested that multiple peaks may be associated with dynamically formed non-specific intermediates during the oxidative reaction process. However, integral peaks specific to the proton in melatonin were less affected attributes to the melatonin stability during the reaction process.

In essence, these results indicated the possible noncovalent interaction as the basis of the inherent reactivity of melatonin towards dopamine intermediates and the extent of this interaction regulates the physicochemical characteristics and structural stability of the obtained nanomaterials.

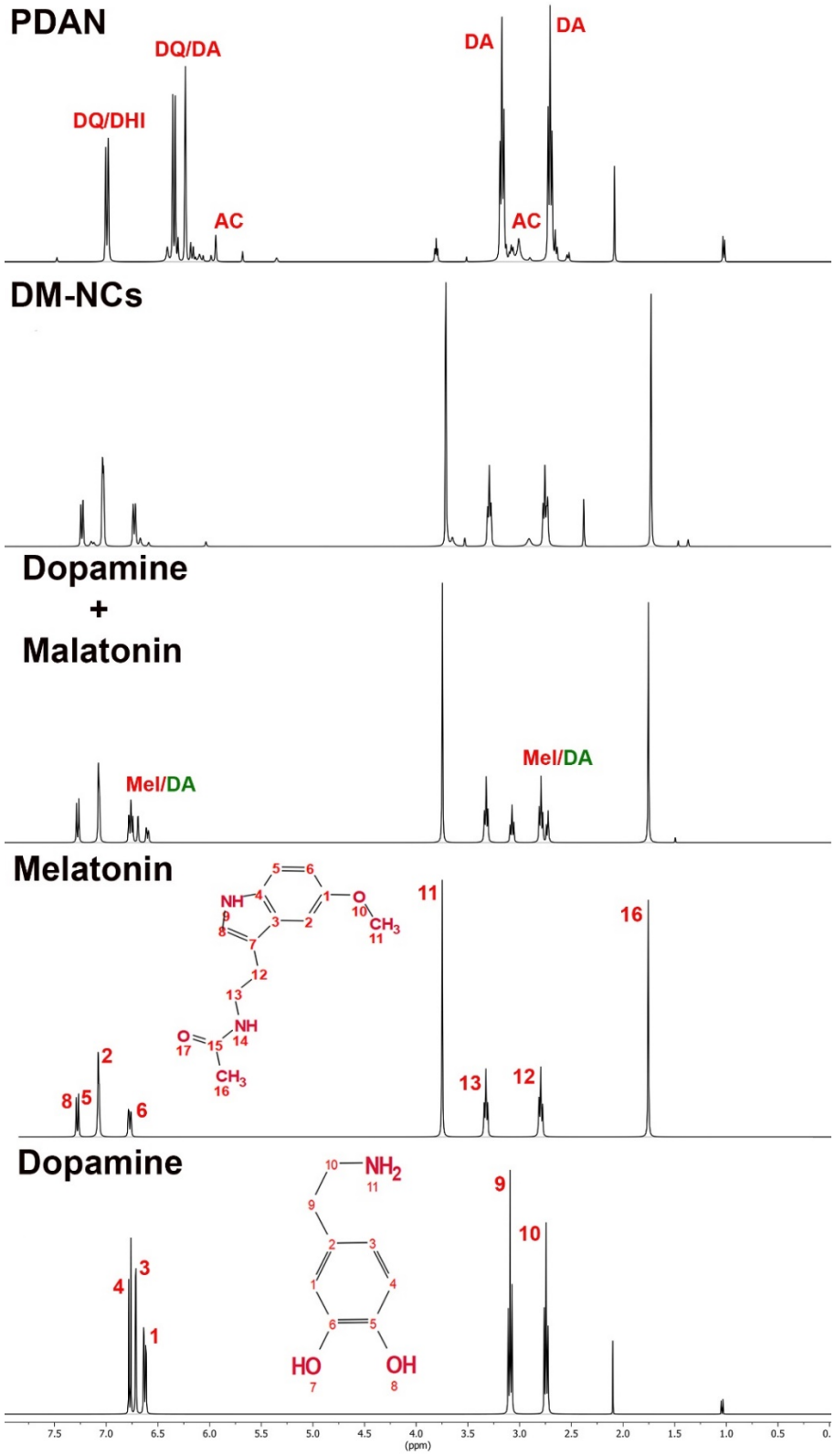

Figure 3.6. **^{1}H NMR study of DM-NCs synthesis**; the NMR spectrum of dopamine (DA), melatonin (Mel), dopamine + melatonin (DA+Mel), dopamine + melatonin upon oxidation (DM-NCs) and only dopamine upon oxidation forming polydopamine nanoparticles (PDAN).

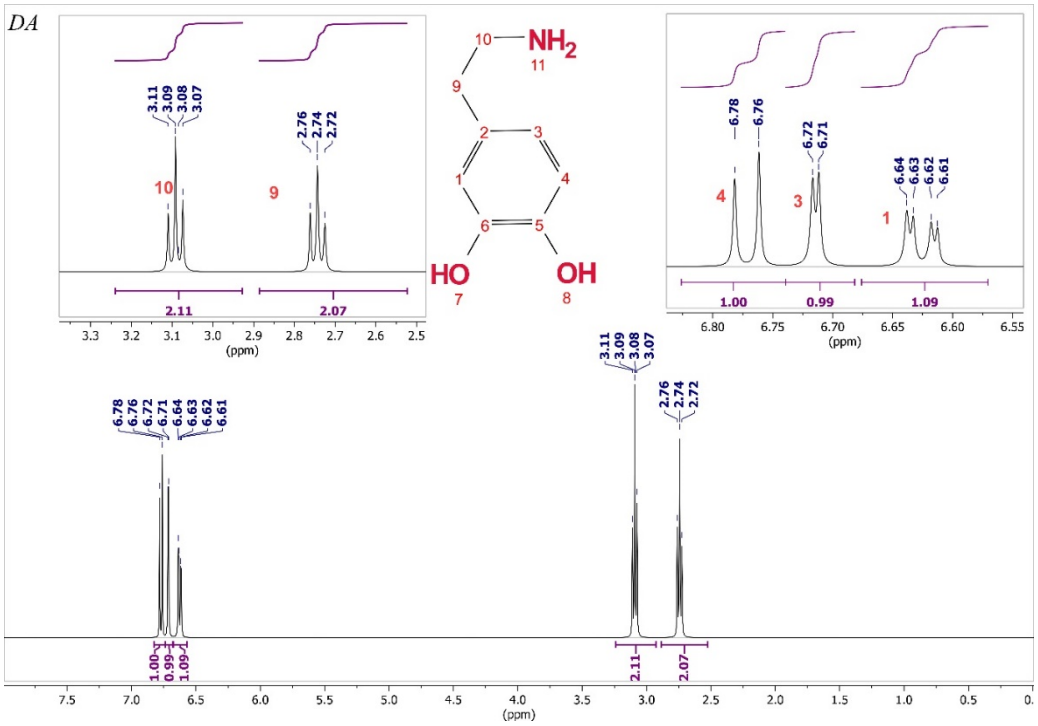

Figure 3.7. The 1H NMR spectrum acquired (0 ppm to 8 ppm, right to left) 1 mM Dopamine (DA) in deuterium dioxide (D_2O).

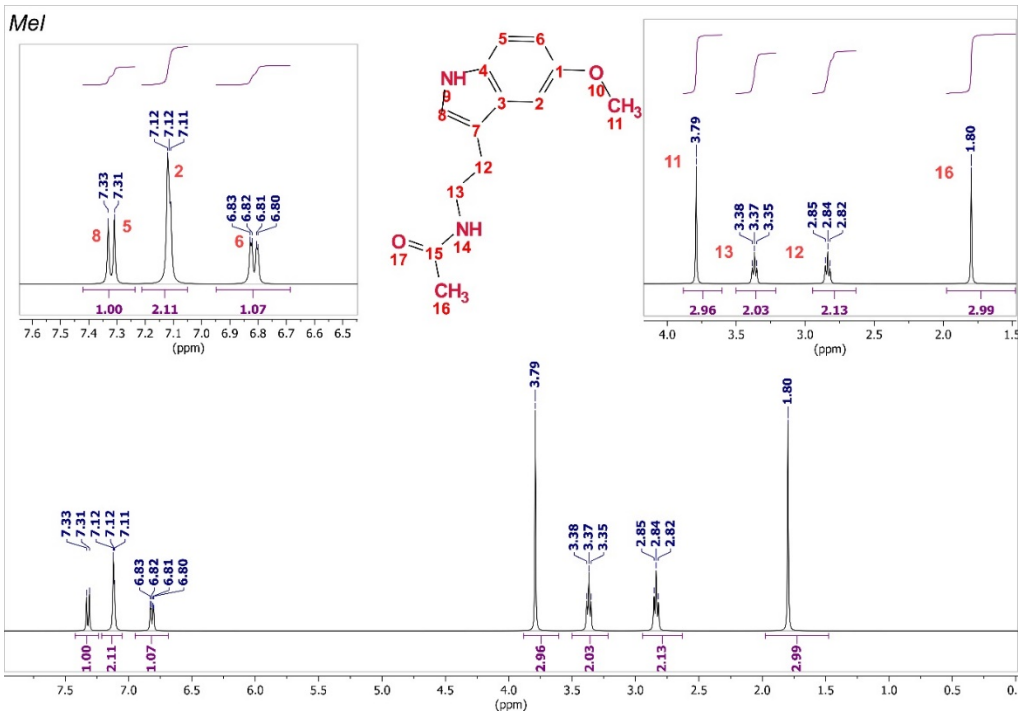

Figure 3.8 The 1H NMR spectrum acquired (0 ppm to 8 ppm, right to left) for 1 mM dissolved in Deuterium dioxide and dimethyl sulphoxide solvent mixture.

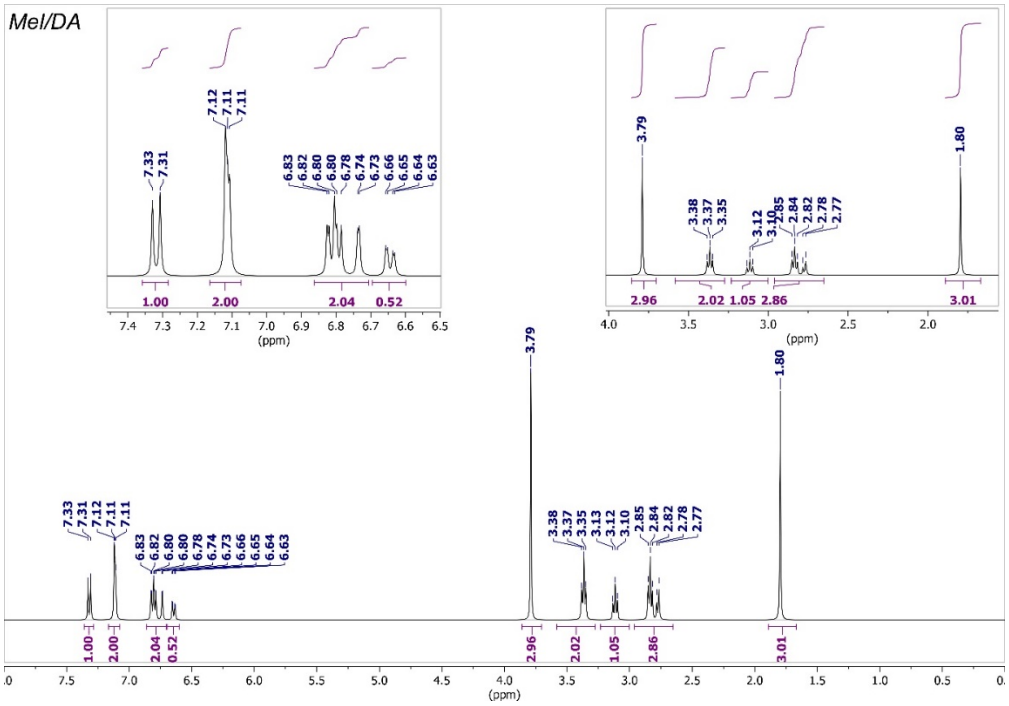

Figure 3.9 The 1H NMR spectrum acquired (0 ppm to 8 ppm, right to left) for 1mM melatonin with 1 mM dopamine in Deuterium dioxide and dimethyl sulphoxide solvent mixture.

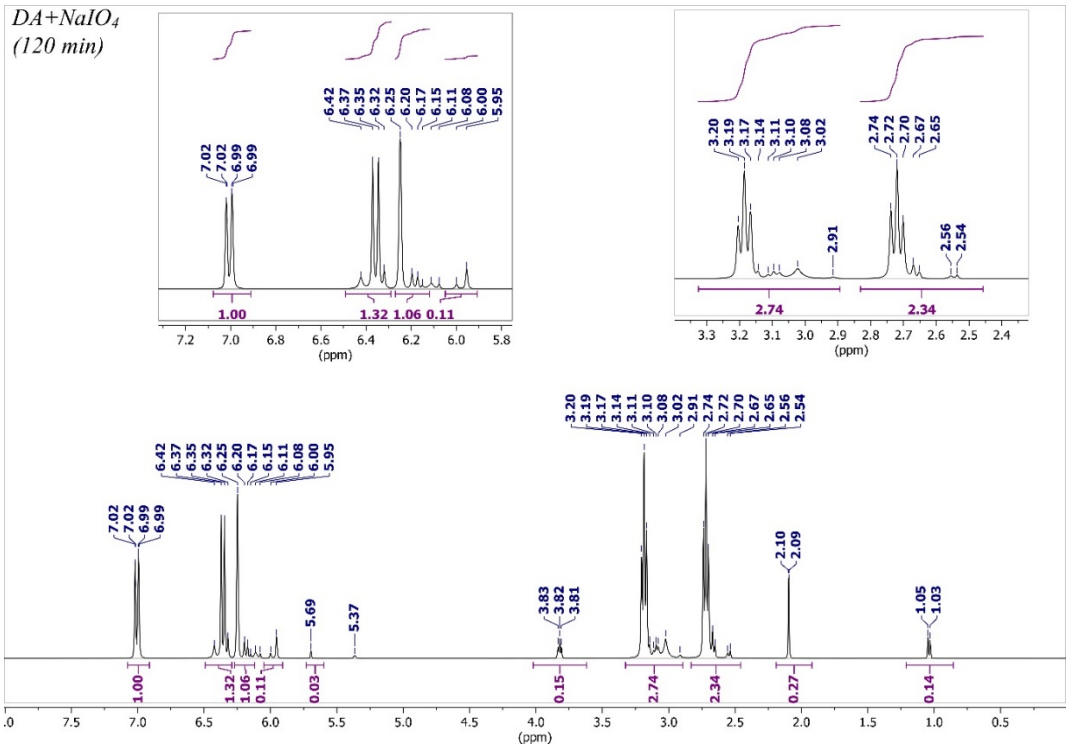

Figure 3.10. The 1H NMR spectrum acquired (0 ppm to 8 ppm, right to left) for dopamine, 120 min after addition of 1 mM $NaIO_4$.

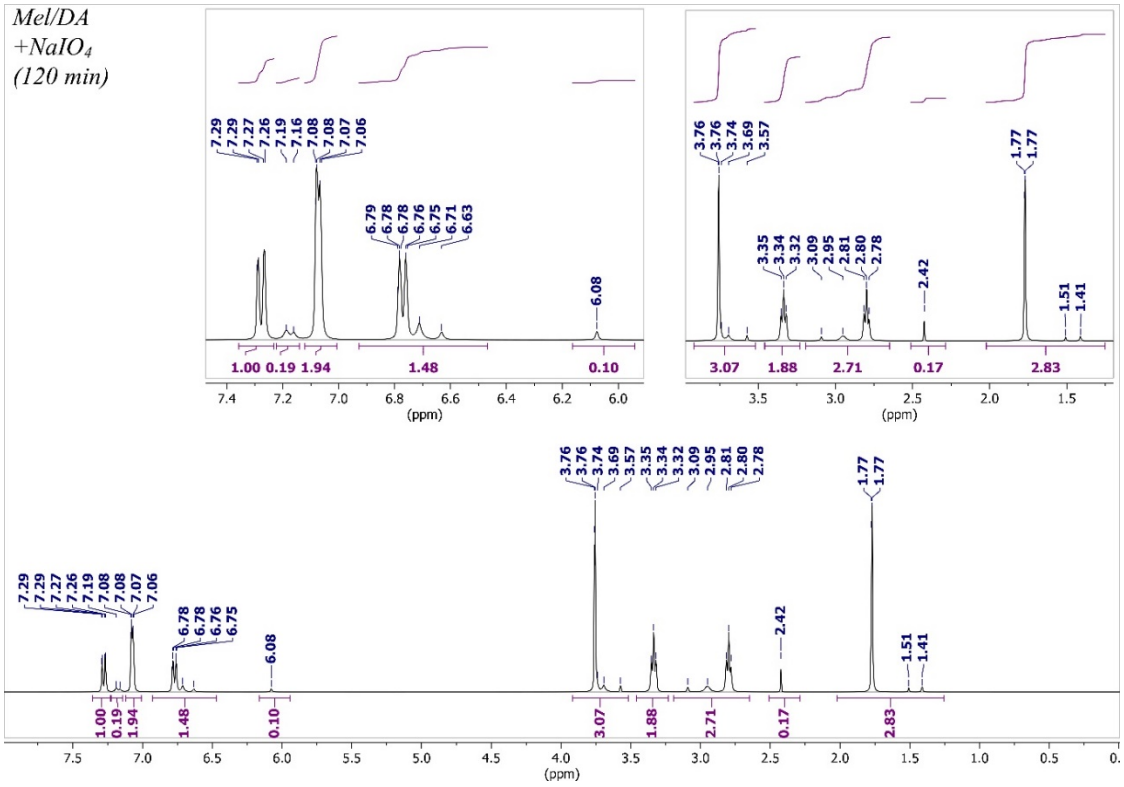

Figure 3.11. The 1H NMR spectrum acquired (0 ppm to 8 ppm, right to left) for 1 mM melatonin with 1 mM dopamine, 120 min after addition of 1mM $NaIO_4$ in Deuterium dioxide and dimethyl sulphoxide solvent mixture.

2.3 Stability and Integrity of nanostructures

In the context of future biomedical applications, the stability and integrity of these nanostructures in biological buffers as well under physiological stress condition are one of the potential criteria. [194] In this particular, the experiment measured the change in the hydrodynamic diameter of DM-NCs under variable pH, prolong NIR exposure and H_2O_2 treatment. The dispersed DM-NCs stock solution was diluted in the buffer solutions of pH=7.2, pH=5.0, and pH=8.8 and incubated for the prolonged-time period of at least 96 h. The hydrodynamic diameter of the DM-NCs incubated in the phosphate buffer of pH=7.2 displayed ~16 nm. In contrast, in the buffer of lower pH=5 the mean hydrodynamic diameter increases up to 21.9 ±6.9 nm suggested the slight aggregation leading to clustering of the DM-NCs (Figure 3.12A and 3.12C).

The mean hydrodynamic diameter <10 nm at alkaline pH indicated the degradation of the polydopamine matrix of DM-NCs, which is reported to be highly prone to alkaline degradation (Figure 3.12B). Next, the photostability of the dopamine has been assessed by exposing the DM-NCs dispersion under near-infrared (NIR) for 60 min and obtained with an unaffected hydrodynamic diameter of ~23 nm, which were significantly not different to the diameter of the control DM-NCs at **p ≤ 0.01 (Figure 3.12D). Thus, it confirms the stability

of DM-NCs at the biologically relevant condition, which makes it eligible for drug delivery applications.

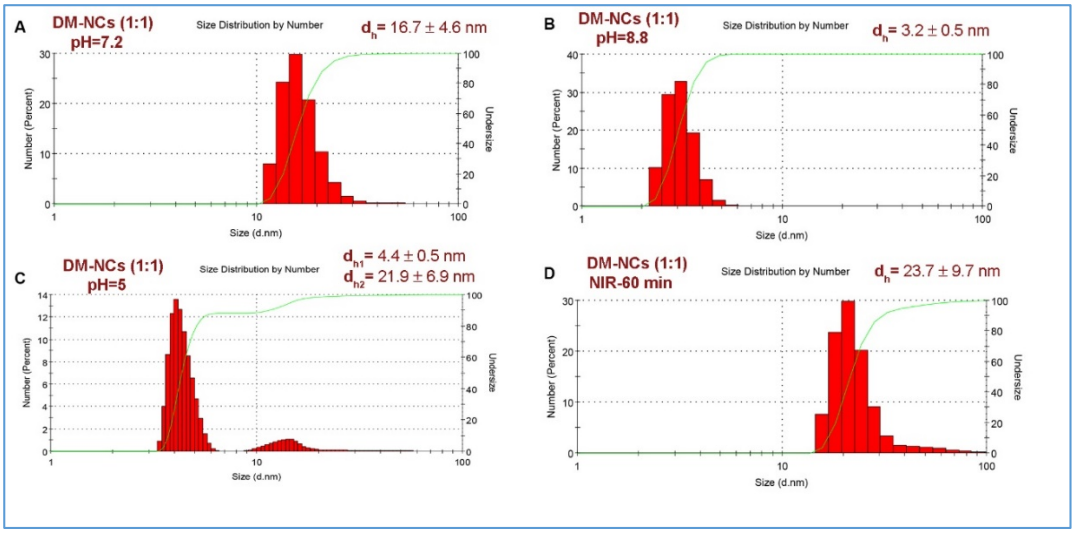

Figure 3.12. The hydrodynamic particle size distribution of DM-NCs (1:1); measured in (A) 5 mM Phosphate buffer (pH=7.2) centred at 16.7 ± 4.6 nm; (B) 5 mM Tris buffer (pH=8.8) centred at 3.2 ± 0.5 nm; (C) 5 mM phosphate buffer (pH=5) with particles of diameter 4.4 ± 0.5 nm and 21.9 ± 6.9 nm; (D) 5 mM phosphate buffer (pH=7.2) exposed to NIR (808 nm, 0.5 W/cm2) for prolong 60 min exposure.

The above results put an instructive view of DM-NCs stability at the physiological condition. Next, we checked the integrity of the DM-NCs against the hydrogen peroxide. The polydopamine matrix of the DM-NCs is highly prone to hydrogen peroxide (H_2O_2) mediated degradation, and it was interesting to investigate the degree of resistance our nanostructure can confer against H_2O_2.[195, 196] To assess the same, first, we incubated a similar concentration of the mock polydopamine nanoparticles (PDANPs) and DM-NCs in the two different concentrations of 5 mM and 10 mM hydrogen peroxide. The visual observation showed the progressive fading of the dark-colored nanostructures within 15 min for the PDANPs. In contrast, the light brownish color of the DM-NCs remained unchanged in appearance, primarily indicated the stability of DM-NCs against hydrogen peroxide (Figure 3.13C). Next, we have measured the hydrodynamic diameter of the particles present in the 10 mM H_2O_2, which were obtained distributed in less than 10 nm diameter range. However, DM-NCs remained unchanged with particle size distribution (Figure 3.13A and 3.13B).

One of the optical characteristic features of the polydopamine nanostructure is that it confers a weak fluorescence emission (λex = 405 nm; λem = 495 nm) in the visible range. Hence, change in the fluorescence emission intensity of the DM-NCs and PDANPs were measured within each 5 min interval till 15 min in 5 mM and 10 mM H_2O_2. As displayed in Figure 3.13 the fluorescence emission intensity of the PDANPs continuously decrease as a function of time indicated the progressive degradation. In contrast, no significant change

in the fluorescence emission intensity of the DM-NCs was seen in a similar period. Corroborating earlier results, the entrapped melatonin in the DM-NCs might be playing a crucial protective role by two of the following mechanism; first, by spatial masking of the polydopamine matrix due to non-covalent interaction as confirmed in our previous results; second, direct scavenging of the H_2O_2 by forming N1-acetyl-N2-formyl-5-methoxykynuramine (AFMK) as bi-product which is investigated in previous reports.[197, 198] conclusively, the DM-NCs with similar physicochemical characteristics and particle size diameter are more biocompatible and physiologically stable.

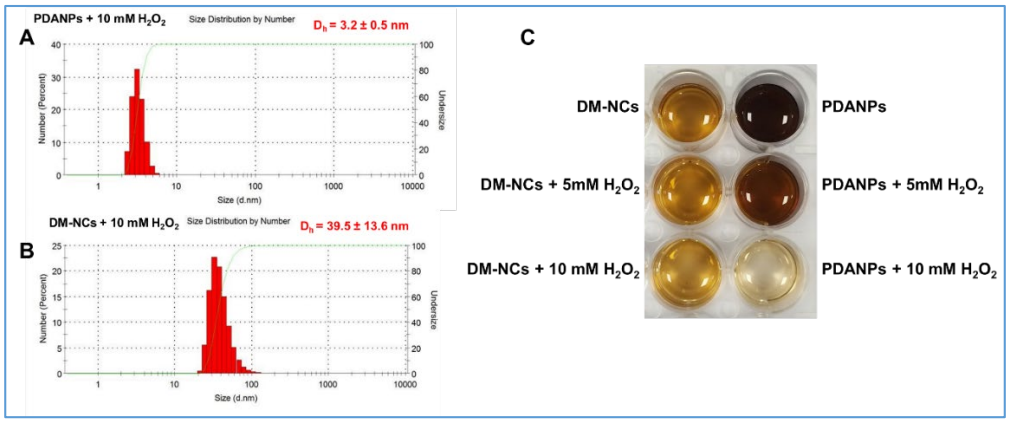

Figure 3.13. The DM-NCs stability and integrity studies; The DLS based mean particle size distribution of DM-NCs as (A) 3.2 ± 0.5 nm of PDANPs incubated in 10 mM H2O2; (B) 39.5 ±13.6 nm of DM-NCs incubated in 10 mM H2O2; (C) The progressive fading of the black color of PDANPs solution upon incubation with H2O2 (5 mM and 10 mM) indicated the susceptibility of PDANPs towards peroxide degradation but protected in DM-NCs.

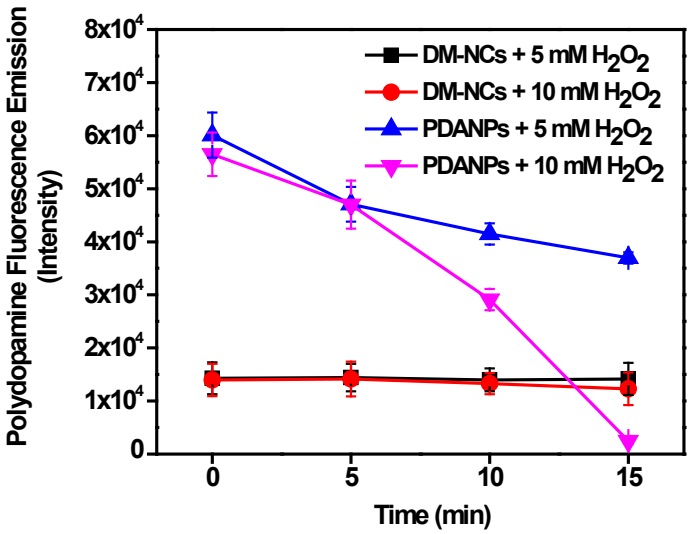

Figure 3.14. The fluorescence emission intensity of the DM-NCs and PDANPs incubated in hydrogen peroxide (5 mM and 10 mM). The results presented as mean ± SD and compared using one-way ANOVA with Tukey's test at **p≤0.01.

2.4 Melatonin cumulative release pattern

Next, we questioned the amount of melatonin entrapped in the polydopamine matrix in mPDAN. To check the same, first, we constructed the melatonin standard curve using UV-vis absorbance at 278 nm, and high-performance liquid chromatography (HPLC) based integrated peak area (Figure 3.14 A and 3.14B). The linearity obtained between concentration range of 0.2 mg/mL to 0.6 mg/mL and 5 µg/mL to 50 µg/mL on UV-Vis spectroscopy and HPLC, respectively. Based on these standard curves, the melatonin loading of 45.4 ± 1.9 w/w% was obtained at the highest dopamine/melatonin ratio 2.5:1.

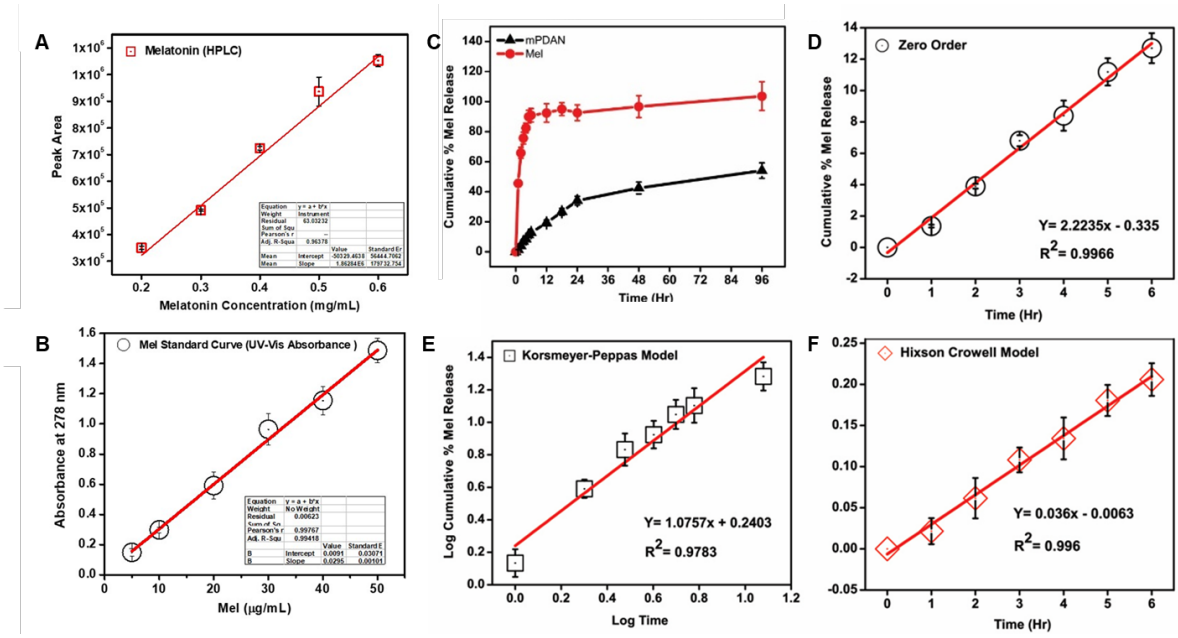

Figure 3.15. Estimation of melatonin loading and cumulative release (%); (A) The melatonin standard curve plot based on UV-vis absorbance intensity, **(B)** melatonin standard plotted using results from HPLC, **(C)** The percentage cumulative drug release, **(D)** The fitting of the release parameter to zero-order kinetics, **(E)** Korsmeyer-Peppas fitting, **(F)** Hixon-Crowell fitting of the release.

The mPDAN subjected to drug release studies considering only melatonin as control using the dialysis tube method. The cumulative percentage release of melatonin has been plotted against time (Figure 3.14 C) displayed sustained melatonin release from mPDAN for the prolonged-time period of 96h. The bare melatonin taken in the dialysis tube displayed a burst release of 70.4 % within 3 h than that of mPDAN, which only releases ~7% melatonin in the same time. The assessment provided that a total 54% melatonin has been released from mPDAN within 96 h. Understanding the mechanism of the melatonin release from the mPDAN and underlying dissolution process, we modeled the release parameter to different dissolution kinetics. The best fitting to zero-order kinetics with R^2 value of 0.996 (n=3) suggested the free melatonin release is independent of the concentration (Figure 3.14D). Furthermore, these release parameters were also fitted to Korsmeyer-Peppas (R^2 = 0.976,

n=3) and Hixson-Crowell (R^2 = 0.996, n=3) models (Figure 3.14 E and 3.14 F). The exponents (n=1) obtained for Korsmeyer-Peppas fitting suggested the controlled diffusion of the melatonin due to progressive swallowing of the polydopamine matrix. It has been observed that initially, the polydopamine matrix releases the melatonin without any dissolution and degradation. Thus, the melatonin release pattern and these dissolution models confirmed that structural attributes of mPDAN are highly favourable for future drug delivery applications.

3. Conclusion

In summary, we have successfully prepared the variant of melatonin/polydopamine nanostructures following alkaline oxidation or chemical oxidant mediated self-assembly method. The variable-ratio of the dopamine and melatonin from 1:1, 2.5:1, 5:1, 10:1, 25:1, and 50:1 after the synthesis forming range of the nanostructures of distinct structural and morphological characteristics. These results revealed that melatonin is playing a crucial role in determining the diameter of the particles and can divide the obtained nanostructures into two distinct domains. First, the particles at lower melatonin ratio leading to the particle size within range of ~43 to 150 nm (referred to as PDANPs) with uniform morphology and higher colloidal stability. Second, the nanocomposites of less than <50 nm (denoted as DM-NCs) obtained with higher melatonin concentration endows characteristic photostability, which is detailed in chapter 6b. The results unravel that the presence of melatonin as co-precursor can influence the dopamine oxidation kinetics due to crucial interactions with the reactive dopamine intermediates. The UV-vis and NMR studies confirmed the specific non-covalent interaction of melatonin with dopamine-o-quinone, aminochrome, and 5,6-indolequinone, which may be collectively retained in the obtained nanostructures. The presence of melatonin in polydopamine enhances the overall stability and integrity of these nanostructures and makes it resistant to peroxide degradation. The significant (~45%) amount of Melatonin is entrapped in the nanostructures, which characteristically release in a sustainable manner for a prolonged time period. Most importantly, these parts outlined the preparation of a range of highly stable melatonin/polydopamine nanostructures, where melatonin reconciled with the dopamine oxidation process and endows a nanocarrier feature and drug compatibility.

Note:

* The due permission has been obtained from authors and corresponding authors of the following published papers before adopting in the present thesis.

- Melatonin/Polydopamine Nanostructures for Collective Neuroprotection based Parkinson's Disease Therapy; Anup K. Srivastava, Subhasree R. Choudhry, and Surajit Karmakar; **Biomaterials Science**; Doi: 10.1039/C9BM01602C
- New insight into curcumin tethered lanthanum carbonate nanospheres and protein corona conferring fluorescence enhancement based sensitive detection of Amyloid-β aggregates. A. K. Srivastava; A. Dev; S.R. Choudhury; S. Karmakar **Sensors and Actuators B**: **Chemical**. 2018;262(1)
- Near-Infrared Responsive Dopamine/Melatonin Derived Nanocomposites Abrogating In-situ Amyloid Beta Nucleation, Propagation and Ameliorate Neuronal Function. Anup K. Srivastava; S.R. Choudhury; S. Karmakar; **ACS Applied Materials and Interface**. 2020, 12, 5, 5658-5670.

NMR Peak Assignments:

1H NMR (dopamine (1 mM), 400 MHz, Deuterium Oxide) δ = 6.77 (d, J=8.1, 1H), 6.71 (d, J=2.1, 1H), 6.63 (dd, J=8.1, 2.2, 1H), 3.09 (t, J=7.2, 2H), 2.74 (t, J=7.2, 2H).

	Name	Shift	Range	H's	Integral	Class	J's
1	E (t)	2.74	2.89-2.52	2	2.07	t	7.20, 7.20
2	D (t)	3.09	3.24-2.93	2	2.11	t	7.18, 7.18
3	C (dd)	6.63	6.68-6.57	1	1.09	dd	2.15, 8.12
4	B (d)	6.71	6.74-6.68	1	0.99	d	2.08
5	A (d)	6.77	6.83-6.74	1	1.00	d	8.08

Table 3.1. The NMR results of dopamine (1 mM).

1H NMR (Melatonin (1 mM), 400 MHz, Deuterium Oxide) δ = 7.32 (d, J=8.8, 1H), 7.21 – 7.05 (m, 2H), 6.81 (dd, J=8.8, 2.5, 1H), 3.79 (s, 3H), 3.37 (t, J=6.8, 2H), 2.95 – 2.63 (m, 2H), 1.80 (s, 3H).

	Name	Shift	Range	H's	Integral	Class	J's
1	G (s)	1.80	1.97-1.48	3	2.99	s	
2	F (m)	2.83	2.95-2.63	2	2.13	m	
3	E (t)	3.37	3.50-3.22	2	2.03	t	6.81, 6.81
4	D (s)	3.79	3.88-3.60	3	2.96	s	
5	C (dd)	6.81	6.95-6.69	1	1.07	dd	2.47, 8.80
6	B (m)	7.11	7.21-7.05	2	2.11	m	
7	A (d)	7.32	7.42-7.24	1	1.00	d	8.80

Table 3.2. The NMR results of Melatonin (1 mM).

1H NMR (Melatonin (1 mM), Dopamine (1 mM), 400 MHz, Deuterium Oxide) δ = 7.32 (d, J=8.8, 1H), 7.16 – 7.07 (m, 2H), 6.86 – 6.71 (m, 2H), 6.64 (dd, J=8.1, 2.1, 1H), 3.79 (s, 3H), 3.37 (t, J=6.8, 2H), 3.12 (t, J=7.2, 1H), 2.96 – 2.65 (m, 3H), 1.80 (s, 3H).

	Name	Shift	Range	H's	Integral	Class	J's
1	I (s)	1.80	1.89 -1.67	3	3.01	s	
2	H (m)	2.81	2.96 -2.65	3	2.86	m	
3	G (t)	3.12	3.23-3.00	1	1.05	t	7.22, 7.22
4	F (t)	3.37	3.58-3.27	2	2.02	t	6.78, 6.78
5	E (s)	3.79	3.86-3.70	3	2.96	s	
6	D (dd)	6.64	6.70-6.60	1	0.52	dd	2.11, 8.09
7	C (m)	6.79	6.86-6.71	2	2.04	m	
8	B (m)	7.11	7.16-7.07	2	2.00	m	
9	A (d)	7.32	7.36-7.28	1	1.00	d	8.85

Table 3.3. The NMR results of Melatonin (1 mM) with dopamine (1 mM).

1H NMR (dopamine (1 mM), sodium periodate (1 mM), 120 min, 400 MHz, Deuterium Oxide) δ = 7.01 (dd, J=10.2, 2.0, 1H), 6.36 (d, J=10.3, 1H), 6.25 (s, 1H), 5.95 (s, 0H), 5.69 (s, 0H), 3.82 (t, J=5.3, 0H), 3.33 – 2.89 (m, 3H), 2.83 – 2.46 (m, 2H), 2.10 (d, J=1.3, 0H), 1.04 (d, J=6.5, 0H).

	Name	Shift	Range	H's	Integral	Class	J's
1	J (d)	1.04	1.21-0.86	0	0.14	d	6.53
2	I (d)	2.10	2.19-1.92	0	0.27	d	1.26
3	H (m)	2.72	2.83-2.46	2	2.34	m	
4	G (m)	3.19	3.33-2.89	3	2.74	m	
5	F (t)	3.82	4.02-3.62	0	0.15	t	5.30, 5.30
6	E (s)	5.69	5.73-5.60	0	0.03	s	
7	D (s)	5.95	6.05-5.91	0	0.11	s	
8	C (s)	6.25	6.27-6.12	1	1.06	s	
9	B (d)	6.36	6.49-6.29	1	1.32	d	10.25
10	A (dd)	7.01	7.08-6.91	1	1.00	dd	2.01, 10.23

Table 3.4. The NMR results of dopamine (1 mM) in the presence of sodium periodate (1 mM) at 120 min.

1H NMR (Melatonin (1 mM), Dopamine (1 mM), sodium periodate (1 mM), 120 min, 400 MHz, Deuterium Oxide) δ = 7.28 (dd, J=9.0, 1.9, 1H), 7.17 (d, J=10.5, 0H), 7.07 (q, J=2.1, 2H), 6.93 – 6.47 (m, 1H), 6.08 (d, J=2.6, 0H), 3.76 (d, J=2.3, 3H), 3.34 (t, J=6.8, 2H), 3.19 – 2.65 (m, 3H), 2.42 (d, J=1.9, 0H), 1.77 (d, J=2.0, 3H).

	Name	Shift	Range	H's	Integral	Class	J's
1	J (d)	1.77	2.02-1.25	3	2.83	d	2.03
2	I (d)	2.42	2.51-2.29	0	0.17	d	1.89
3	H (m)	2.79	3.19-2.65	3	2.71	m	
4	G (t)	3.34	3.46-3.23	2	1.88	t	6.81, 6.81
5	F (d)	3.76	3.92-3.52	3	3.07	d	2.28
6	E (d)	6.08	6.16-5.94	0	0.10	d	2.64
7	D (m)	6.77	6.93-6.47	1	1.48	m	
8	C (q)	7.07	7.12-7.01	2	1.94	q	2.13, 2.13, 2.34
9	B (d)	7.17	7.22-7.14	0	0.19	d	10.53
10	A (dd)	7.28	7.36-7.23	1	1.00	dd	1.87, 8.97

Table 3.5. The NMR results of Melatonin (1 mM) with dopamine (1 mM) in the presence of sodium periodate (1 mM) at 120 min.

Chapter 4

Brain targeting of melatonin loaded polydopamine nanostructures (mPDAN) for collective neuroprotection in Parkinson's disease model

1. Background

The growing global burden of the Parkinson's disease (PD) with 10 million peoples worldwide is highly alarming in context of the prevention and therapy.[82-85] The symptomatic cardinal features of PD including deficit in motor function, resting tremor, bradykinesia, rigidity, posture instability, and parkinsonian gait make the person disable and dependent. The patient suffers even in executing daily life activities due to psychological fluctuations, inappropriate olfaction, insomnia, depression, and constipation. [88] These symptoms can be correlated with the pathophysiological changes in the dopaminergic neuron located in the substantia nigra (SN) and hippocampal (HIP) in brain observed with an intra-neuronal accumulation of protein-rich Lewy bodies (LWs). [3, 4] The degeneration of these neurons attributes the sequences with oxidative stress, mitochondrial dysfunction, ER stress, inflammation, apoptosis, excitotoxicity, loss of trophic factors, which is collectively linked to the clinical symptoms.[87] The highly investigated alpha-synuclein (α-SYN) protein of ~140 amino acid chains localized at synaptic terminals in neuronal cells which abruptly phosphorylate at serine 129 (pα-SYN(S129)) thereby misfold to produce the toxic oligomeric and fibrillar state investigated in both sporadic and familial PD.[5-8, 96, 97, 199] This modification affect essential cellular function including synaptic membrane binding, [200, 201] ion binding , interaction with cytoskeleton protein and nuclear translocation. [202-205] Presently, the anti-PD therapy rely on alleviating the dopaminergic motor functions either via systemic administration of levodopa (L-dopa) and dopamine agonist and the surgical brain stimulation to basal ganglia circuitry. [206] Progressively in most of the cases, it has been observed that L-dopa based therapies displayed partial and transient recovery with more severe motor and no-motor symptoms, thus cannot be categorized as ideal anti-PD therapy.[10] Therefore, the present therapeutic strategies focus a strong disease-modifying agent that can collectively regulate underlying pathophysiology as well as motor and non-motor symptoms in the PD.

Our interest in small neurohormone melatonin (N-acetyl-5-methoxytryptamine) (Mel), which is a powerful free radical scavenger and a potent antioxidant and alleviate the PD.[12] However, the hydrophobicity of the molecule, fast metabolism, lower retention in the brain tissue with irregular buffering in the brain upon systemic administration are major limitation associated with melatonin administration. This limitation can be overcome by using the nanocarrier based neuroprotection, which can be a superior druggable approach demonstrated for enhanced therapeutic potential.[207] The nanocarrier system from the biological origin can provide enhanced biocompatibility and biodegradability in the living system.[13] The polydopamine is demonstrated as one of the versatile drug delivery

systems that can penetrate the blood-brain barrier (BBB) and resides in diverse brain areas via steric protection to the encapsulated agent. [208]

The growing evidence of the underlying PD pathophysiology and the importance of the effective PD modifying treatment cues towards the druggable approach of targeting the key event occur at the early onset of the disease. Thus, our aim in the present chapter is to investigate the anti-PD efficacy of melatonin enriched polydopamine nanostructures (mPDAN), the preparation and characterization of which has been elaborated in the previous chapter 3. Present chapter details the superior neuroprotective effect of mPDAN in rotenone-induced *in-vitro* SH-SY5Y cell, three-dimensional culture, and *ex-vivo* organotypic mice brain slice culture and *in-vivo* PD mice model. mPDAN triggers anti-oxidative, anti-apoptotic, and anti-inflammatory pathways that attribute the collective neuroprotection in the PD model. mPDAN controls the pα-SYN(S129) level, as well as the cellular deposition of the high molecular weight (HMW) oligomeric state of pα-SYN(S129), validated for alleviating the effect of it even at early onset. These observations further corroborated with the resilience effect on dopaminergic neurons and lower processing of the pα-SYN(S129) in the hippocampal and SN region of the brain. Thus, targeting the PD associated pathophysiology via mPDAN could deliver a superior neuroprotection-based anti-PD effect.

2. Results and Discussion

2.1 In-vitro SH-SY5Y PD model preparation

The most widely used *in-vitro* system for the PD model is neuroblastoma cells established by controlled exposure of the rotenone (Rot), which via underlying molecular sequels of mitochondrial complex I damage, elicit the α-SYN processing and its cellular accumulation. In order to estimate the effective neuroprotective concentration of mPDAN, First, rotenone-induced neuroblastoma PD model was constructed by exposing a variable dose of rotenone, and neuronal survival was measured using MTT assay. The non-linear regression analysis of the cell neuroblastoma cell death value as a function of log-transformed rotenone concentration provided the half-maximum inhibitory concentration (IC50) of 559 ± 3 nM and 342 ± 4 nM for the SH-SY5Y cells and IMR-32 cells, estimated for 72-hour chronic rotenone exposure (Figure 4.1A).

2.2 Estimation of the effective neuroprotective concentration

The dose-response curve allowed us to use the 500 nM of rotenone, which maintained 61.1 ± 1% (n=3) SH-SY5Y cell viability, whereas 52 ± 2 % (n=3) cell viability estimated in IMR-32 cells treated with 250 nM rotenone. For obtaining effective neuroprotective dose, the cells were first treated with rotenone (500 nM in SH-SY5Y cells and 250 nM in IMR-32 cells)

following nanoformulation treatment with in 2 h. Treatment of mPDAN in increasing concentration of 2.5 ng mL-1, 5.1 ng mL-1 and 25.7 ng mL-1 given 79± 3%, 92 ± 4% and 75 ± 2% SH-SY5Y and 79 ± 4%, 91 ± 3% and 86± 5% IMR-32 cell viability, respectively (Figure 4.1B and 4.1C). The mPDAN at an optimum and effective concentration of 5.1 ng mL^{-1} confers maximum protection of neuroblastoma cells against rotenone-induced cell death. The 1.1 ng mL^{-1}, 2.3 ng mL^{-1} and 11.6 ng mL^{-1} bare melatonin induced 65± 2%, 75± 2% and 64± 1% SH-SY5Y and 65± 2%, 75± 2% and 79± 1% IMR-32 cells viability. The equivalent dose of PDAN has not shown any significant change in the viability of SH-SY5Y and IMR-32 cells. Thus, dose-response analysis of these multiple concentrations revealed that the 5.1 ng mL^{-1} mPDAN effectively loaded with 2.3 ng mL^{-1} (~100 nM) melatonin can provide enhanced survival capacity against rotenone. The results indicate that a single effective dose of mPDAN provided a prolonged neuroprotection may eliminate the conventional steps involve multiple systemic administration of the neuroprotectant for PD therapy.

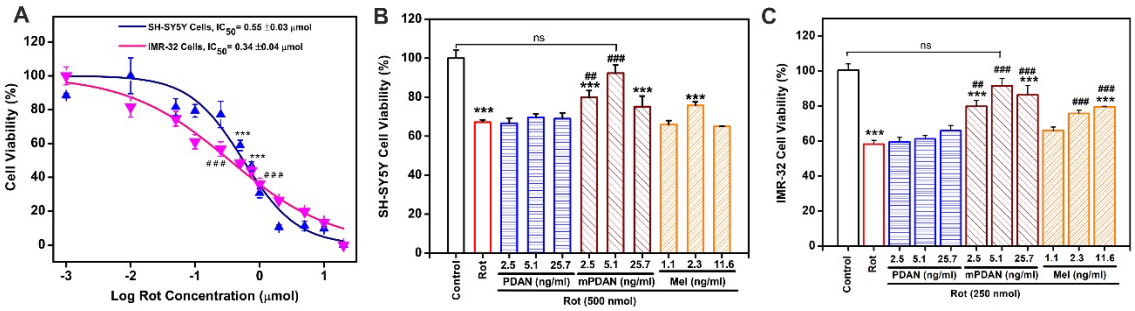

Figure 4.1. Rotenone induced in-vitro model preparation and estimation of effective neuroprotection dose; (**A**) The dose-response curve of the rotenone and IC50 estimated in SH-SY5Y cells and IMR-32 cells, (**B**) The 5.1 ng mL^{-1} mPDAN as an effective dose with maximum cell viability (92 ±4 %) against rotenone in SH-SY5Y cells, (**C**) Maximum cell viability (91 ±3 %) obtained for 5.1 ng mL^{-1} against rotenone giving 58±2% IMR-32 cell viability. The one-way ANOVA with Bonferroni significance test performed for mean comparison with Control (*p≤0.05, **p≤0.01 and ***p≤0.001) and rotenone (#p≤0.05, ##p≤0.01 and ###p≤0.001)

2.3 Internalization in Monolayer and three-dimensional organoid

The rhodamine B tagged mPDAN (Rho-mPDAN) is incubated with adhere SH-SY5Y cells shows a strong cytoplasmic localization within the four hours (Figure 4.2A). The Caveolae, Arf6 dependent endocytosis, or Rab34 mediated micropinocytosis could be the collective passage for mPDAN internalization into the neuroblastoma cells[209]. Rho-mPDAN can easily retain in a three-dimensional neuroblastoma model resembling nervous tissue with morphologically differentiated cells. Altogether, these results displayed the efficient mPDAN internalization into the monolayer and three-dimensional neuroblastoma culture (Figure 4.2B).

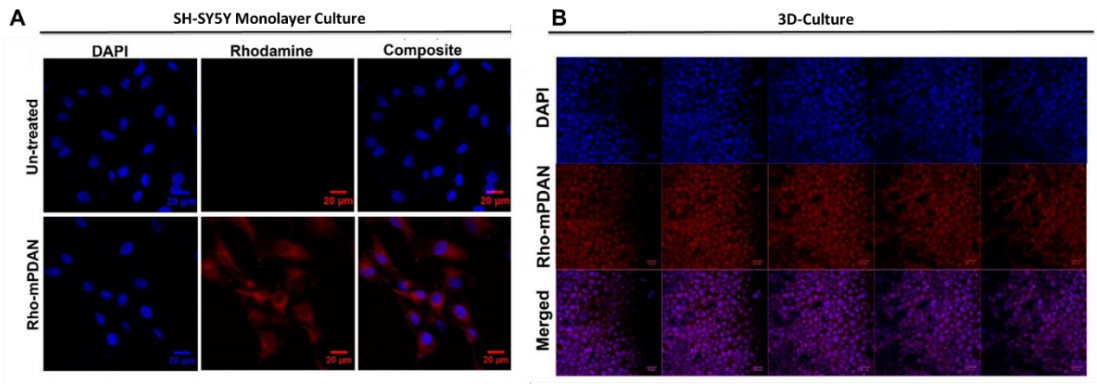

Figure 4.2. Cellular internalization of mPDAN in monolayer and three-dimensional neuroblastoma culture; (A) The rhodamine tagged mPDAN (25 µg mL^{-1}) accumulated in the cytoplasm of SH-SY5Y cells (Red); DAPI (Blue); Scale bar = 20 µm; **(B)** SH-SY5Y organoid culture model displayed mPDAN retention in 24 h treatment in optical sections (left to right); Scale bar = 20 µm.

2.4 Anti-oxidant potential measurement

ROS active fluorescence compound DCFH-DA was used to estimate the intracellular ROS generation. The SH-SY5Y cells were respectively incubated with 1 µM rotenone and separately co-treated with 2.3 ng/mL melatonin, 5.1 ng/mL PDAN, and 5.1 ng/mL mPDAN and real-time change in the green signal were measured using a multimode plate reader. The 1 µM rotenone-induces 1.2 ±0.1, 2.6 ±0.1, 2.9 ±0.2 and 2.9 ±0.2-fold increase in the cellular ROS level in initial 2, 4, 8 and 12 h, respectively (Figure 4.3A). The effective 5.1 ngmL-1 mPDAN treatment regulates intracellular ROS generation and maintains it equivalent to ROS level present in untreated controls, whereas 2.3 ng mL-1 melatonin and 5.1 ng mL-1 PDAN treatment have not shown any regulatory impact on intracellular ROS generation. (Figure 4.3B). Thus, effective 5.1 ng mL^{-1} mPDAN is effective in regulating the rotenone-induced ROS generation in SH-SY5Y cells. Thus, the anti-oxidant characteristic of the mPDAN is one of the attributes of collective neuroprotection therapy.

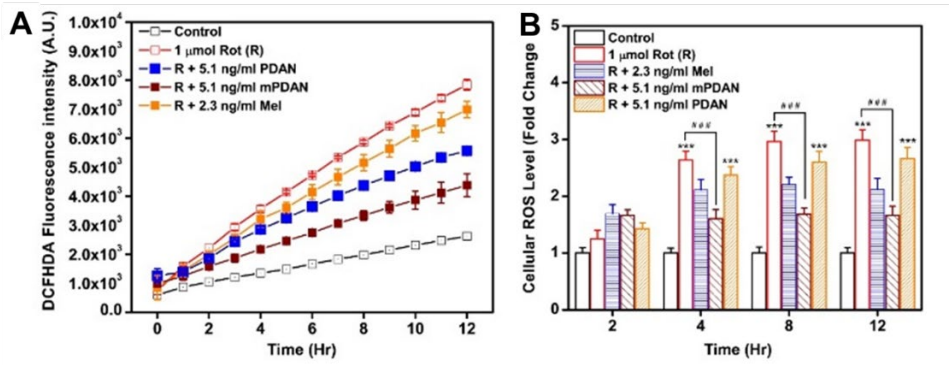

Figure 4.3. Measurement of intracellular ROS scavenging ability of mPDAN; (A) DCFH-DA fluorescent dye-based time-dependent estimation of cellular ROS up to 12 h were obtained for rotenone, melatonin, mPDAN and PDAN (n=3); **(B)** The quantification of cellular ROS level based on the fluorescence intensities compared for mean using one-way ANOVA following Bonferroni statistical test (*p≤0.05, **p≤0.01 and ***p≤0.001).

2.5 Anti-Apoptotic activity estimation

The anti-apoptotic and anti-necrotic effect of mPDAN, PDAN, and melatonin are studied by double staining dispersed treated SH-SY5Y 3D culture by Annexin V-PE (Red) and 7-AAD (green) reagent. Rotenone exposure in these organoid models generates PD like cellular damage with 45 ± 0.5 % cell population under apoptosis compared to the control cell population in the Q2 quadrant (Figure 4.4A and 4.4B). The exposure of melatonin and PDAN in the rotenone-induced 3D culture limits 32.5 ± 0.3 % and 35.6 ± 0.6 % populations double-positive in Q2 (Figure 4.4C and 4.4D). mPDAN co-treatment displayed markedly fewer double-stained population compared to only the rotenone treated group, which indicates significantly reduced rotenone associated apoptotic induction within the cells (Figure 4.4E). Furthermore, the quantitating apoptotic and necrotic cell population confirmed that rotenone-induced significant apoptosis within the SH-SY5Y cell population. however, mPDAN co-treatment completely suppresses this apoptotic induction in SH-SY5Y cells. (Figure 4.4F).

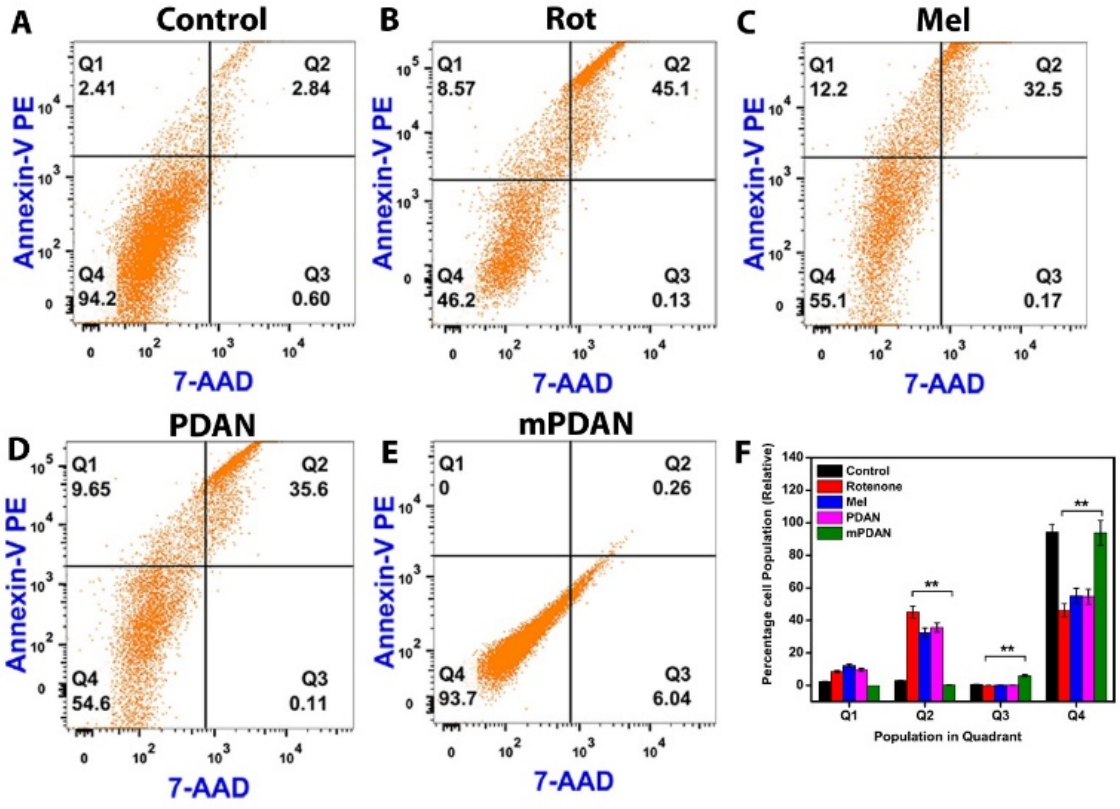

Figure 4.4 Annexin V-PE and 7-AAD based apoptosis measurement; (A-E) The PD induced 45.1 ± 3 % apoptotic cell population, whereas 5.1ng mL^{-1} mPDAN cotreatment revert the effect of rotenone. The 2.3 ng mL^{-1} melatonin and 5.1 ng mL^{-1} PDAN co-treatment resist the apoptotic activation. (F) Quantification of the apoptotic population and mean were compared using One-way ANOVA with Tukey's significance test (*p≤0.05, **p≤0.01 and ***p≤0.001).

2.6 Mitochondrial membrane potential measurement

The rotenone is a specific inhibitor of mitochondrial complex I, induces intracellular ROS generation, decouple the mitochondrial membrane transporters, thereby hampers mitochondrial membrane potential. The cationic fluorescent dye JC-1 was used to probe change in mitochondrial membrane potential (Δψm). SH-SY5Y 3D culture exposed to 500 nM rotenone and cotreated 5.1 $ngmL^{-1}$ PDAN, 2.3 $ngmL^{-1}$ melatonin and 5.1 $ngmL^{-1}$ mPDAN for 72 h and proceeded with the JC-1 staining. The mitochondrial membrane pore opening, transmembrane depolarization, release of apoptogenic factor (Cytochrome c and apoptotic inducing factors), and loss of oxidative phosphorylation are the cellular perturbation observed in the PD. This JC-1 can easily accumulate (J-aggregates) on the mitochondrial membrane in unstimulated cells with high Δψm and gives a distinct fluorescence emission at 585 nm. Confocal laser scanning microscope (CLSM) imaging displayed rotenone treatment to SH-SY5Y 3D culture leads to the transition of J-aggregates (mitochondrial membrane) into monomers (mitochondrial matrix) appears with a shift in fluorescence emission from red to green region corroborates mitochondrial membrane depolarization or loss of Δψm. The 500 nM rotenone exposure to this culture induces JC-1 monomers with increasing intensity of green fluorescence than that of mPDAN cotreated culture, which displayed the dominating red fluorescence intensity of JC-1 identical to control (Figure 4.5A). The fluorescence intensity-based quantitation of JC-1 aggregate (Red)/ JC-1 monomer (Green) ratio (Δψm) vs treatment group displayed minimum value 0.35 ± 0.05 (###p≤0.001) in 500 nM in rotenone exposed group and highest 0.98 ±0.05 in 5.1 ng mL^{-1} mPDAN treated group (ns at ***p≤0.001) (Figure 4.5B). Notably, the 5.1 ng mL^{-1} PDAN and 2.3 ng mL^{-1} melatonin treated cultures displayed no increase in this ratio (Δψm), thus failed to protect mitochondrial damage induced by rotenone (ns at ***p≤0.001). Thus, these results confirm that mPDAN can protect the mitochondrial dysfunction on the *in-vitro* PD model.

2.7 Estimation of Caspase-3 level

The caspase-3 activation in the three-dimensional SH-SY5Y culture PD model was estimated using immunofluorescence of caspase-3. The 500 nM exposure of rotenone to these 3D cultures displayed 3.9 ± 0.04 (n=3, ###p≤0.001) fold increase in the caspase-3 compared to the unstimulated control group (Figure 4.5C and 4.5D). 5.1 ng mL^{-1} mPDAN exposure maintain the caspase-3 level to 0.98 ± .01, which were similar to observed in the unstimulated control (***p≤0.001 and ns at ###p≤0.001). This result corroborates activation of p38/JNK MAPK pathway induces Bcl-2 family pro-apoptotic proteins recruitment in mitochondria leads to cytochrome c release to the cytoplasm thereby activation of procaspase-9, and caspase-3 occurs which starts the cascade of apoptotic cell death. The

overall results indicated that mPDAN pursue strong anti-apoptotic characteristics by inhibiting both caspase-dependent and caspase-independent apoptotic pathway activation in the PD model.

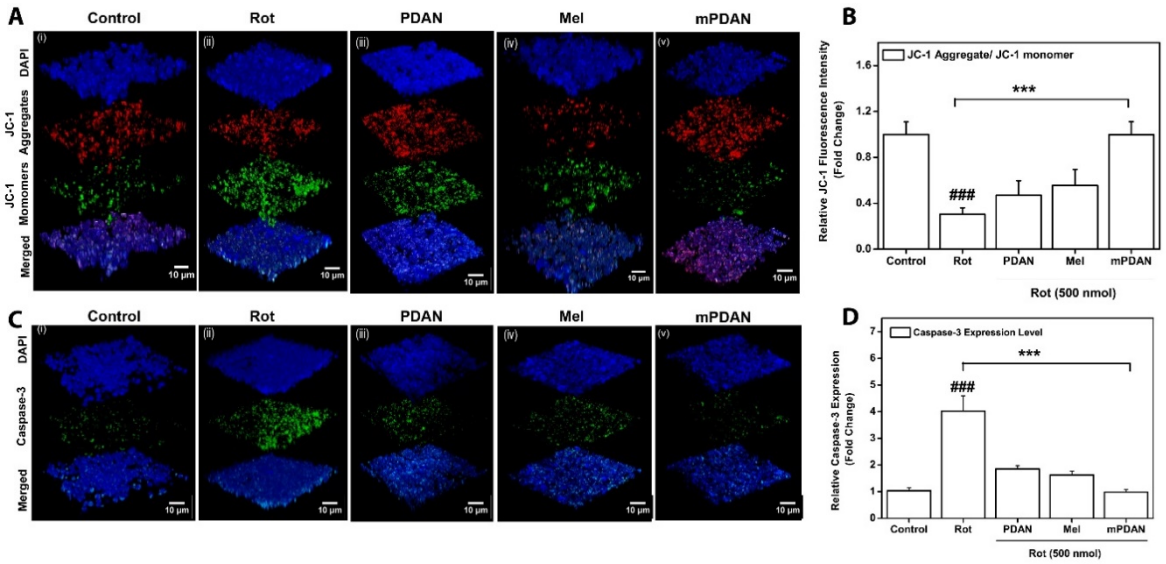

Figure 4.5. Confocal microscopy analysis of mitochondrial membrane potential and caspase-3 level in three-dimensional neuroblastoma PD model; (A) The JC-1 (Aggregates, red fluorescence) and (monomer, green fluorescence) estimating the mitochondrial membrane potential of SH-SY5Y cells in thee dimension culture model 500, for PDAN, melatonin and mPDAN; (B) The cytofluorimetric quantitation of the Red and Green fluorescence, the ratio of JC-1 aggregates(red)/JC-1 monomer (Green) were plotted.(C) The Immunofluorescence of caspase-3 in the SH-SY5Y 3-D PD model was performed with the treatment mentioned above; (D) The fluorescence intensity-based quantitation and mean were statistically significant at (***P < 0.001; n=3). Scale bar = 10 µm

2.8 Anti-inflammatory effect

More than 10 % population of brain microglial cells are densely populated in the SN region and responsible for the pronounce neuroinflammatory effect leading to dopaminergic cell death. Neuronal cells in the SN region displayed increased expression of pro-inflammatory cytokines that includes tumor necrosis factor-α (TNF-α), interleukin-1β (IL-1β) and interferon-gamma (INF-γ) in PD [105, 210]. Based on this information, we proceeded to check the level of PD related gene SNCA, apoptosis-related caspase-3, neuroinflammation related IL-1β, IL-6, NF-kB, and cellular phosphatase PP2A, and Kinase 3pK in the rotenone-induced PD model using qPCR. The rotenone triggered overexpression, estimated as fold change for caspase-3 (~4, n=3,***p≤0.001), IL-1B (~4.5, n=3,***p≤0.001), NF-kB (~2, n=3,***p≤0.001), Akt (~2.9, n=3,***p≤0.001), 3pK (~2.3, n=3,***p≤0.001), whereas downregulated PP2A and not responsive for Il-6 and alpha-synuclein gene (Figure 4.6A and 4.6B).

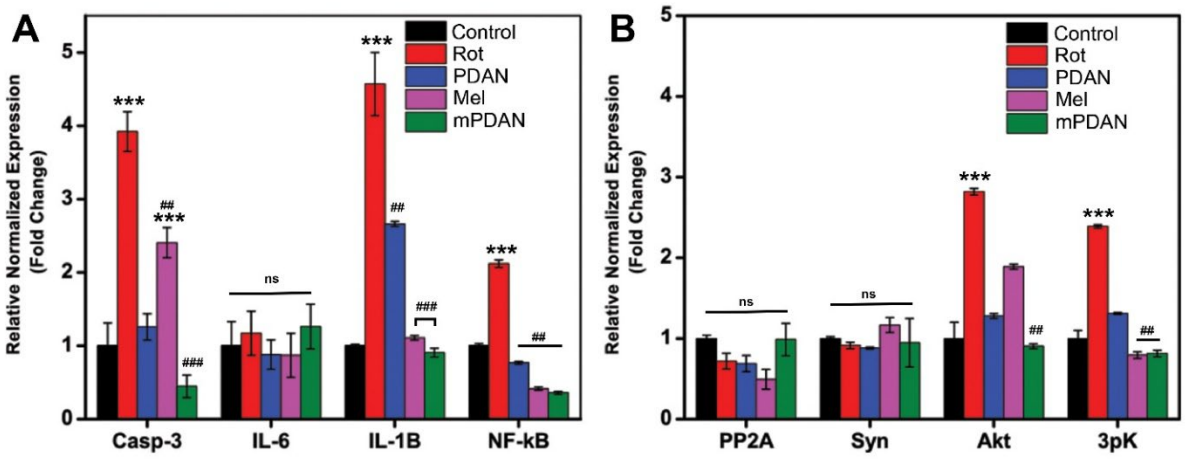

Figure 4.6. qPCR based gene expression analysis of inflammation and apoptosis-associated genes; (A) the qPCR based gene expression profile of delta Ct method were used to calculate the gene expression of caspase-3, IL-1B, NFkB was overexpressed under rotenone exposure are regulated upon nanoformulation exposure (*p≤0.05, **p≤0.01 and ***p≤0.001). The IL-6 gene found unresponsive to the treatment; (B) mPDAN reverts rotenone induce Akt (2.9 fold; ***P< 0.001; n=3) and 3pK (2.3 fold; ***P< 0.001; n=3) gene expression, promotes slight over-expression of PP2A and not responsive towards alpha-synuclein at gene expression level. The fold change values between treatment groups were analyzed using a one-way analysis of variance (ANOVA) with Tukey's significance test.

The protective effect of the 5.1 ng mL^{-1} mPDAN, 2.3 ng mL^{-1} melatonin and 5.1 ng mL^{-1} PDAN has been estimated against the rotenone exposure. The expression level of housekeeping glyceraldehyde 3-phosphate dehydrogenase (GAPDH) gene was used as a control for the calculation of relative Ct values. Co-treatment of 5.1 ng mL^{-1} mPDAN significantly resist the rotenone-induced overexpression of the Caspase-3, IL-1B, NFkB genes and limit the expression level up to the untreated control (ns at ***p≤0.001) could be due to prolong bioavailability elicits the cytoprotective activity and reduces neuronal expression of these markers[211]. Melatonin regulates p53 phosphorylation by PI3K/Akt pathway [212], p38 signaling, extracellular signal-regulated kinase (ERK), Jun N-terminal kinase (JNK) and mitogen-activated protein kinase [213], which collectively confer the cytoprotective signaling. The PD is associated with activation of 3pK, promoting p38 signaling and inhibits PP2A expression reflected in our qPCR results. Nonetheless, unchanged alpha-synuclein gene expression indicates that it may not respond at early PD stages or may not be associated with the progression of the PD. [214] Hence, the mPDAN triggers the regulatory pathways associated with the anti-inflammatory and anti-apoptotic activity.

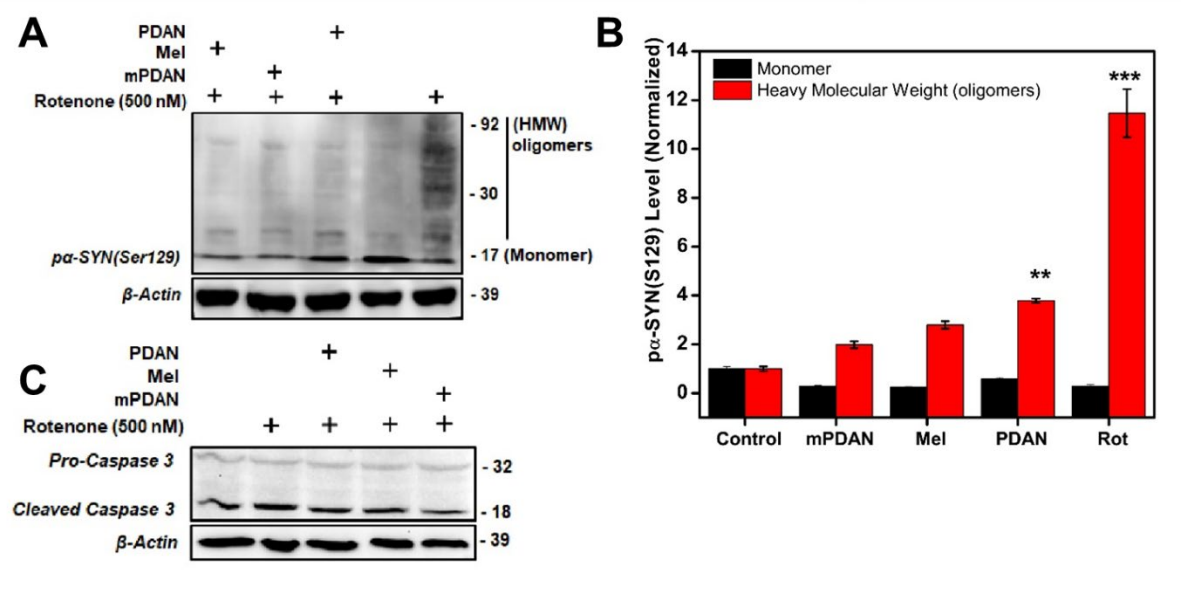

Figure 4.7. The western blot examination of pα-SYN(S129) and caspase-3 protein on *in-vitro* PD model; (A) The pα-SYN(S129) level (monomer) and oligomers (Heavy Molecular Weight, HMW) in PD induced SH-SHY5Y cell lysates exposed to PDAN, melatonin and mPDAN. The densitometric quantitation of monomer (Black bar) and high molecular weight aggregates (Red bar); (C) The level of pro-caspase-3 and cleaved caspase-3 upon these treatments are shown on the blot. β-Actin protein was used as an endogenous reference protein.

2.9 mPDAN controls the alpha-synuclein phosphorylation associated oligomerization

It has been proposed that more than 90% of alpha-synuclein protein deposits as inclusion in PD brains are phosphorylated at the Serine-129 position.[215] This post-translational modification as pα-SYN(S129) altered the conformational stabilities and may contribute to the toxicity, which is markedly manifested in the PD progression [216]. Rotenone induced SH-SY5Y PD model displayed pα-SYN(S129) modification with an increased level of both monomeric and high molecular weight (HMW) oligomeric states appear on the immunoblot. The densitometric quantitation revealed 11.6 ± 0.5 (n=3, ***p≤0.001) fold increase in the pα-SYN(S129) HMW oligomers upon rotenone exposure. In contrast, the mPDAN cotreatment deferred the accumulation of these HMW deposits in the cells (Figure 4.7A and 4.7B). The role of melatonin in the regulation of the phosphorylation state of α-SYN is not yet explored. However, the intermediate level of pα-SYN(S129) monomers and HMW were seen in PDAN and melatonin treated cells. The rotenone exposure to SH-SY5Y cells triggered proteolytic cleavage of cellular aspartate-specific cysteine protease -3 (caspase-3), which is observed by the appearance of the p17 fragment along with total caspase-3 on the blot (Figure 4.7C). Corroborating the earlier immunofluorescence results, it can be speculated that caspase-3 is activated by proteolytic cleavage of its 32 kDa precursor and generate catalytically active p12/p17 complex. The proteolytic cleavage of the caspase-3 attribute to apoptotic activation in the cells, which may activate PKCδ and with subsequent

nuclear translocation, confers the oxidative induced neuronal cell death [217]. The least proteolytic cleavage of caspase-3 is obtained in the mPDAN co-treated group. Thus, mPDAN treatment not only regulates the major neuroprotective pathways but also regulates the cellular pα-SYN(S129) level in the PD model.

2.10 In-vivo and ex-vivo distribution of the mPDAN

The in-vivo studies in the mice through intravenous injection, which provided the distribution of the fluorescently tagged mPDAN. The time-dependent localized fluorescence of the mPDAN was observed following the imaging of animals at 1, 3, 6, 12, and 24 h time points. Intense fluorescence of ICG-mPDAN within 1 h post-injection associated with retention in the liver tissue follows accumulation in the kidneys between 2 h to 6 h, which indicates systemic clearance function via hepatic and nephric route. Importantly, significant retention of mPDAN in the brain has been observed at ~ 12 h post-injection. More widespread distribution of the mPDAN was seen in ex-vivo imaging with significant accumulation of mPDAN in the brain even at the more extended time point of 24 h (Figure 4.8B). A majority of mPDAN accumulated in the liver may be phagocytosis by the resident macrophages attribute the clearance mechanism of the nanomaterial from the animal system. The histopathological evaluation of the major organs, including the brain, heart, kidney, liver, and spleen, showed that at present, concentration mPDAN had not induced any histological lesions (Figure 4.8C). Therefore, these biodistribution studies confirm that a significant amount of mPDAN can retain in the brain via circumventing BBB without inducing any non-specific toxicity in other visceral organs.

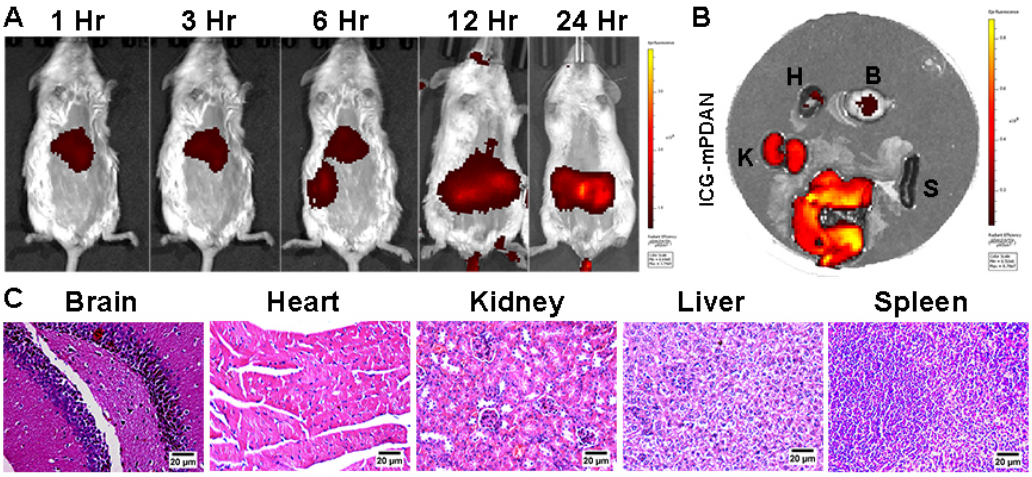

Figure 4.8. The *in-vivo and ex-vivo* biodistribution and histopathological analysis; (A) The whole-body imaging of ICG-mPDAN injected mice acquired at the different time point of 1 h, 3 h, 6 h, 12 h, and 24 h; (B) the ex-vivo imaging of the organs isolated from ICG-mPDAN treated mice showing Liver (L), Brain (B), Kidney (K), Spleen (S) and Heart (H) at 24 h post-injection; (C) The H&E histopathological staining of Liver, Kidney, Heart, Brain, and Spleen tissue section of animals injected with mDPAN. Scale bar = 20 μm

2.11 Neuroprotective effect on *ex-vivo* PD model

Recently, the organotypic midbrain slice culture (MBSC) model of PD became a useful tool to study the physiological tissue characteristics and to screen the acute and chronic effects of the therapeutics. This MBSC based PD model has been developed and used to study the neuroprotective therapeutic efficacy of mPDAN. The details of the MBSC establishment have been mentioned in the experimental section of Chapter 2. Immediately after confirming the morphological vitality of MBSCs, these were treated with 5 μM of rotenone for induction of the PD and further exposed to melatonin, mPDAN, PDAN and investigated using immunofluorescence of key protein markers. The CLSM images provided 1.34 ±0.2 (n=3, *p<0.05) fold increase in pα-SYN(S129) level in PD induced MBSC, whereas mPDAN co-treatment limits pα-SYN(S129) level to 0.38 ±0.15 (n=3, ###p<0.001 wrt rotenone). The equivalent dose of melatonin fails to control the increase in pα-SYN(S129) level (Figure 4.9A and 4.9B).

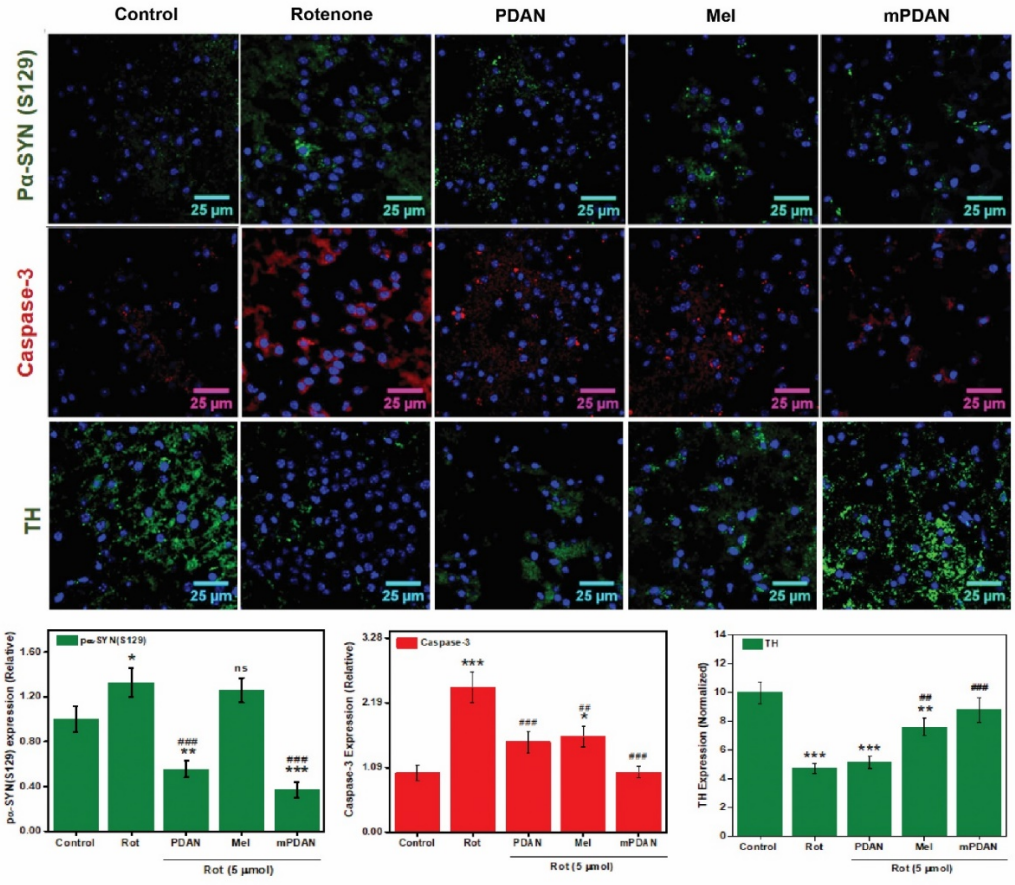

Figure 4.9. The therapeutic assessment of mPDAN in organotypic adult mice brain slice culture; The Immunofluorescence of pα-SYN(S129) (Green); Caspase-3 (Red) and Tyrosine Hydroxylase, TH (Green) counterstained with DAPI in untreated control, rotenone, PDAN, melatonin, and mPDAN treated midbrain slice culture (MBSC). The cytofluorimetric quantitation is represented in histograms. The means were compared using one-way ANOVA and Tukey's significance test represented as control (*p≤0.05, **p≤0.01 and ***p≤0.001) and rotenone (#p≤0.05, ##p≤0.01 and ###p≤0.001).

Tyrosine hydroxylase (TH) is a rate-limiting enzyme for the synthesis of dopamine and its level in the brain provides an estimate of dopaminergic neurons. Using cytofluorimetric quantitation ~ 58% loss in the TH positive neurons has been estimated in the PD induced MBSC than that of mPDAN, which significantly protected the loss of TH positive cell populations (ns at ***p<0.001 wrt to control) (Figure 4.9A and 4.9C). Further, we checked the level of caspase-3 in rotenone-induced MBSC, which were estimated to 2.4 ±0.3-fold than in the unstimulated control. As previous corroborating results, the mPDAN strongly resist the increase in caspase-3 level and limit to basal level (ns at ***p<0.001 wrt control; ###p<0.001 wrt to rotenone) (Figure 4.9A and 4.9B). It is interesting to see that bare melatonin and PDAN failed to regulate the caspase-3 level. The collective suppression of pα-SYN(S129), inactivation of caspase-3, and maintained TH-positive cell populations indicate the multi-targeted resilience effect of mPDAN in ex-vivo organotypic midbrain slice culture-based PD model.

2.12 Therapeutic efficacy on *in-vivo* PD mice model

PD is associated with lower expression of the dopamine synthesizing enzyme tyrosine hydroxylase (TH) and degeneration of the dopaminergic neuronal cells. Clinically, these cells accompany parallel pathological processing and accumulation of pα-SYN(S129). Thus, the therapeutics restoring or preventing these processes and prevent the TH positive neuron loss in the brain could significantly regulate the PD progression. A precise dose of rotenone has been used to develop the experimental PD model, which recapitulates specific molecular events of PD pathology and characteristic features, which is precisely demonstrated in most of the chemically induced experimental PD mice models.[218] Immunofluorescence imaging of the TH in the contralateral side of the midbrain section displayed severe loss in TH positive cells. Quantitatively, 39±2 % (n=4, **p< 0.0062) loss in the TH+ cells have been estimated in hippocampal (HIP) and SN brain region compared to present in healthy control mice brain. Considering earlier studies, the continuous exposure of the rotenone for seven days led to ~39% TH^+ dopaminergic neuronal loss in HIP and SN regions of the brain (Figure 4.10A and 4.10C).[219] These rotenone-induced PD mice show 1.5 ± 0.3 (n=4, ***p<0.001) fold increase in the pα-SYN(S129) accumulates at the nerve ending in the brain (Figure 4.10A and 4.10B). The change in endogenous expression of α-SYN is also associated with the accumulation of truncated membrane-associated insoluble alpha-synuclein in the hippocampal region, contributes to the hippocampal neurogenic deficit and linked with reduced hippocampal TH and dopamine level.[220] [221] The change in the thickness of hippocampal subfield CA1 is closely linked

to the episodic memory impairment in PD patients, whereas the CA2-CA3 is clinically implemented in α-SYN pathology.[222, 223] The mPDAN co-injected (intraperitoneally) along with rotenone (subcutaneous) was estimated with 81±1% (n=4) TH^+ population and reduced level of pα-SYN(S129). The equivalent dose of melatonin and PDAN cotreated with rotenone failed to confer any insignificant protective effect on TH+ cell population and pα-SYN(S129) level. Nonetheless, melatonin and PDAN induced significant regulation of the pα-SYN(S129) level, and its distribution inside the brain might be controlled via any alternative pathways. Thus, these results concluded that mPDAN with a collective resilience effect regulates α-SYN phosphorylation, its amyloidogenic transformation and deposition in the diverse brain area and prevents PD associated dopaminergic cell death.

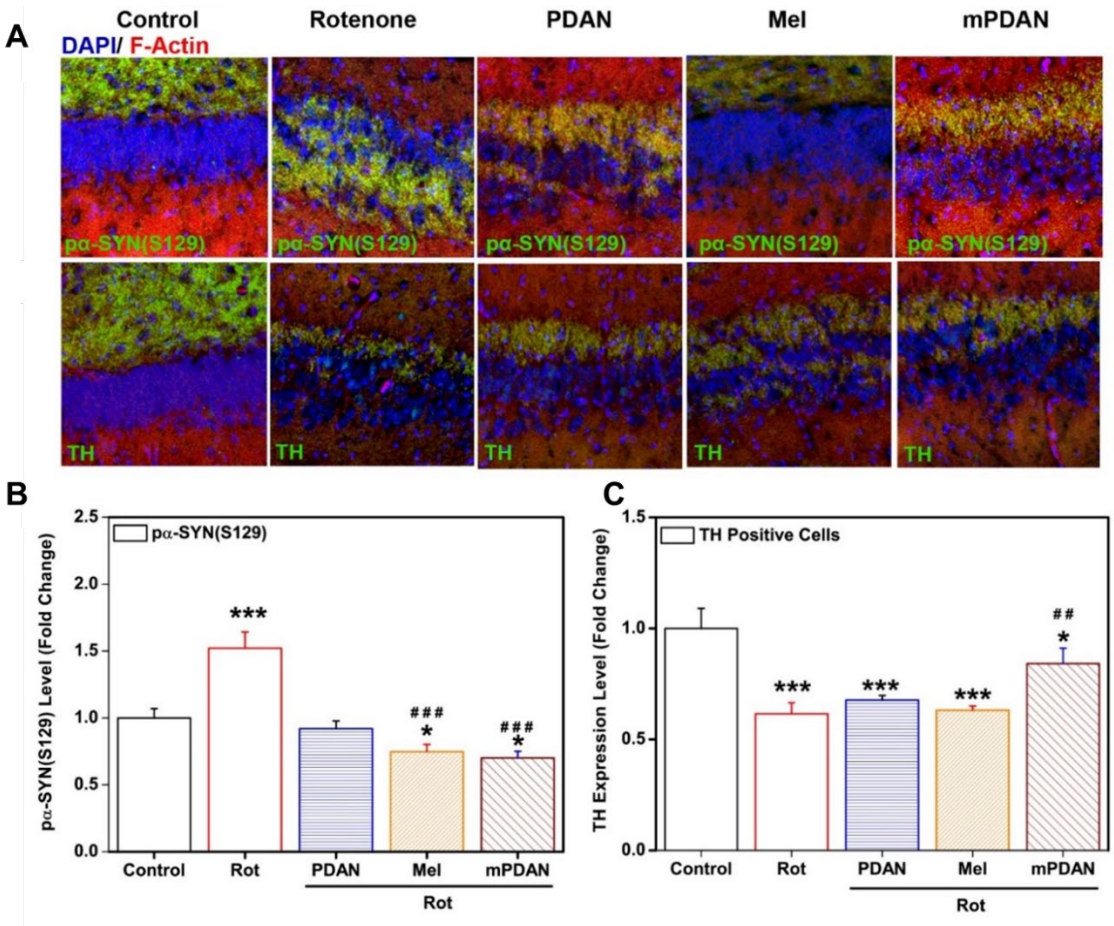

Figure 4.10 The immunofluorescence-based examination pα-SYN(S129) and tyrosine hydroxylase (TH) on in-vivo PD mice model midbrain section; (A and B) The immunofluorescence of pα-SYN(S129) level in the hippocampal region of PD bearing mice (rotenone) injected with PDAN, mPDAN and melatonin. The quantitation in histogram, shows 1.5 ± 0.3 (n=4, ***p< 0.001) fold increase in pα-SYN(S129) regulated at basal level (###p< 0.001) on mPDAN co-injected; **(A and C)** The immunofluorescence of TH in rotenone and co-injection of PDAN, mPDAN and melatonin, displayed 81±1% (n=4) TH+ populations significantly higher compared to rotenone (##p< 0.001). The F-actin and nuclear region were stained with phalloidin-PE (Red) and DAPI (Blue). Scale bar = 50μm

The accumulating amount of research indicates that phosphorylation of the α-SYN at S129 is marginally associated with the pathological transformation, aggregation, and deposition as Lewy body.[95] Controlling the pα-SYN(S129) level at early onset could be developed as a promising disease-modifying therapy in PD. In the present approach, mPDAN collectively regulating both, loss of the dopaminergic neurons and also resist the increase in cellular pα-SYN(S129) level. The prolonged and sustained release of melatonin in the tissue continuously triggers the anti-oxidation, anti-inflammatory, and anti-apoptotic mechanisms established as the basis of the therapeutic effect. Recently, intravenous or intranasal administration of exogenous melatonin controlled the PD symptoms but observed with equal partitioning among cerebrospinal fluid (CSF) and plasma, which decrease its adequate abundance in the brain compared to other drugs. It has also been observed that higher systemic melatonin can exert undesirable calcium signaling, uncontrolled DAergic buffering, and motor response. [11] Thus, mPDAN nanoformulation is overcoming the many limitations associated with melatonin and demonstrates a superior therapeutic value via protecting dopaminergic neurons and regulating α-SYN associated pathophysiology in PD.

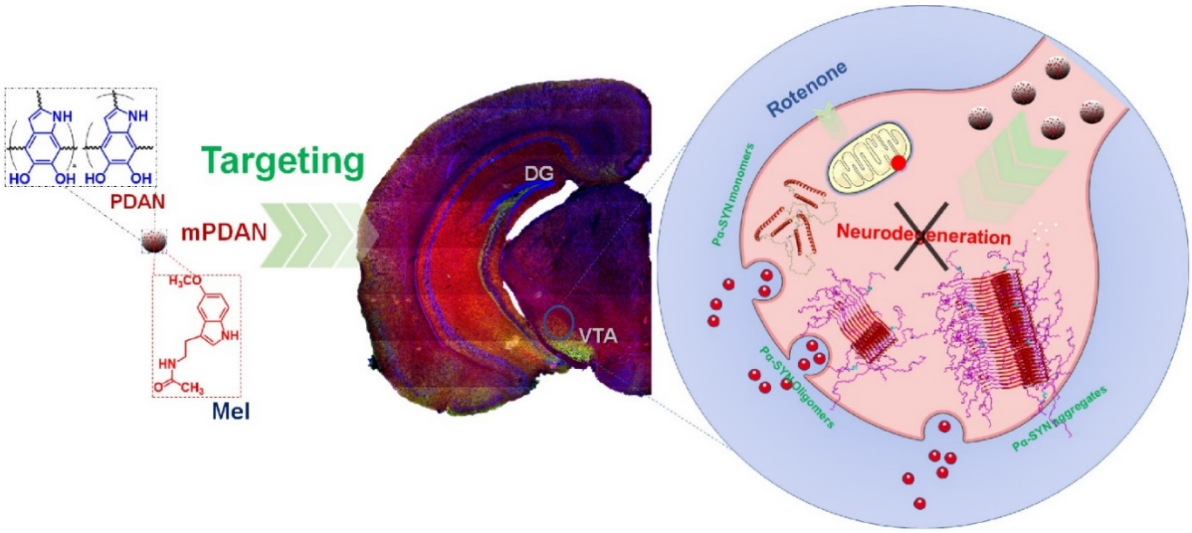

Scheme 1. The illustration of mPDAN targeting to the brain regulating alpha-synuclein processing and confers collective neuroprotection in Parkinson's disease

3. Conclusion

In the present work, melatonin/polydopamine nanoformulation (mPDAN) is demonstrated for a superior neuroprotection-based PD therapy. The mPDAN prolongs the release of encapsulated melatonin, and 5.1 ng/mL of mPDAN displayed the most effective therapeutic potential in rotenone-induced SH-SY5Y and IMR-32 cells-based PD models. mPDAN can quickly internalize in the cells and confer superior antioxidant and anti-apoptotic effects.

The mPDAN exposure can alleviate the PD associated mitochondrial damage and prevent the caspase-dependent and independent apoptosis activation. mPDAN triggers the activation of neuroprotective molecular signaling pathways and regulates expression of apoptosis and inflammation-associated genes. The mPDAN abrogate rotenone-induced α-SYN phosphorylation at serine 129 and significantly prevent amyloidogenic transformation and deposition of high molecular weight oligomer deposition on *in-vitro*, *ex-vivo* and *in-vivo* PD model. In, addition via underlying neuroprotective pathways, it protects the dopaminergic neuronal cells in the hippocampal and SN region of the PD bearing mice brain. The single effective dose of mPDAN, which overcomes the repeated dosing, can confer the prolonged neuroprotection during long-lasting symptoms of the PD. Thus, this nanoformulation based neuroprotectant delivery system offers collective neuroprotection against the PD pathophysiology and confers a regulatory effect on the alpha-synuclein phosphorylation, which revealed its enormous potential use in disease-modifying PD therapy.

Note:

* The permission has been obtained from authors and corresponding author of the following published paper before adopting in the present thesis.

- Melatonin/Polydopamine Nanostructures for Collective Neuroprotection based Parkinson's Disease Therapy; Anup K. Srivastava, Subhasree R. Choudhry, and Surajit Karmakar; **Biomaterials Science**; Doi: 10.1039/C9BM01602C

Chapter 5

Enriched melatonin facilitates polycomb protein BMI-1 mediated ubiquitination and proteasomal degradation of alpha-synuclein in Parkinson's disease (PD) model

1. Background

Polycomb group (PcG) proteins is an evolutionary conserved group of protein complexes that regulate chromatin structure via cell-specific gene repression. [224] PcG is composed of mainly two canonical polycomb repressive complex 1/2 (PRC1 and PRC2) among which PRC-2 consists main catalytic subunit enhancer of zeste 2 (EZH2) or its homolog EZH1 as histone methyltransferase and catalyzes mono-, di- or trimethylation of histone H3 at lysine 27 (H3K27me3).[225] H3K27me3 on the genomic site serves as a mark for docking of chromo box-domain (CBX) subunit of polycomb repressive complex 1 (PRC1). This PRC1 complex subunit BMI-1 catalyzes the mono-ubiquitination of H2A at lysine 119 (H2AK119ub) via polycomb E3 ligase activity.[224, 226] The expression of BMI-1 is required for the self-renewal in the peripheral and central nervous system but play an insignificant role in the survival and differentiation of these tissues. [18] In the recent investigation, BMI-1 has been studied for its role in neuroprotection, particularly in the regulation of mitochondrial stress and cellular ROS level, which is regulated by polycomb mediated repression of antioxidant response genes (AOR) in the nervous tissues. [227-231] BMI-1 is not only fucntions as PRC1 dependent epigenetic E3 ligase but also linked with drug-responsive and PRC-1 independent functions associated with tolerance in neurodegenerative diseases.[232] The emerging concept in neuro-epigenetics indicates that the mechanism of chromatin remodeling associated with the neurogenesis persists as a memory even in the adult brain.[233] Multiple epigenetic modifications transiently linked to the disease occurrence, progression, and the non-canonical functions of the epigenetic machinery are implicated as promising neuropathological biomarkers and therapeutic targets.[234, 235] Accumulation of α-SYN is characterisitics feature of Parkinson's disease (PD) creates a burden on cellular proteolytic degradation machinery which fails to degrade these α-SYN protein deposits. [236]. In order to overcome this burden a number of E3 ligase activator gain a promising interest, which prominently ubiquitinate α-SYN and promote its proteasomal degradation.[237] However, there is no information about the regulatory function of these polycomb repressor complex subunits on the phosphorylation and associated pathological transformation of alpha-synuclein. Downregulation of PRC-1 subunit BMI-1 is observed in the PD models and linked with neurodegeneration, but the exact mechanism of the BMI-1 in such regulatory functions is still unexplored. Thus, it is essential to understand the underlying neuro-epigenetic mechanism which may leads to finding of novel pathways in regulation of neurodegeneration process. The lower buffering of melatonin (N-acetyl-5-methoxytryptamine, Mel) and associated MT1 and MT2 receptor expressions were implicated in the PD progression.[9] Melatonin regulates expression of multiple genes such as MMP-9, NF-kB, HIF-1a, VEGF, Nestin, BMI-1, and Sox2 signaling

on in-vitro and in-vivo models.[149] The exogenous melatonin provides a promising resilience in neurodegeneration, regulates multiple signaling pathways. Moreover, several strategies have been used to concentrate the melatonin inside biomaterial/nanomaterial to improve the effect via maintaining constant bioavailability.[238, 239] Active pharmacological nanocarriers capability and biocompatibility of polydopamine nanostructures are already demonstrated but preparation and use of polydopamine nanostructures enriched melatonin for targeted brain delivery is not yet demonstrated.[240, 241]

The present chapter details the regulatory role of polycomb repressor complex 1 subunit BMI-1 on melatonin mediated neuroprotection in rotenone-induced *in-vitro* and *in-vivo* Parkinson's disease models. Our results revealed a crucial interaction between BMI-1 and pα-SYN (S129), implicated in the ubiquitin-dependent proteasomal clearance of the pathological pα-SYN (S129) in PD models.

2. Results and Discussions

2.1 Alpha-synuclein hyperphosphorylation (pα-SYN (S129)) and cellular accumulation substantiates PD model

The Post-translational modifications (PTMs) of pα-SYN protein in PD is one of the highly dynamic and modulatory processes determining its structure, function, degradation, and toxicity. The primary phosphorylation site at serine 129 within the C-terminal domain emerged as a dominant pathogenic modification that occurs within the brain and positively correlated with PD progression.[8, 242] The hallmark of the hyperphosphorylated α-SYN confirmed PD phenotype in rotenone-induced SH-SY5Y cells, which were achieved via a dose-dependent rotenone (0, 10, 50, 100 and 250 nmol) exposure for 96 hours, and examined by immunoblot analysis. The lowest dose of 10 nmol has no impact, while 50 nmol rotenone could cause a significant increase in pα-SYN (S129) monomer and high molecular weight (HMW) oligomers in neuroblastoma cells. The maximum fold increase in pα-SYN (S129) monomer, as well as HMW oligomers, were observed at 100 nmol rotenone exposure and unchanged up to 250 nmol rotenone treatment (Figure 5.1A, 1D and 1E). These results indicated that rotenone dose >100 nmol led to established PD phenotype in SH-SY5Y cells and confirmed that hyperphosphorylated α-SYN exist as a monomer and heavy molecular weight oligomers/aggregates in PD condition were similar as previously observed in the brain tissue of the PD patient.

2.2 Implication of decreased polycomb repressor complex 1 subunit BMI-1 and H2AK119ub in PD

The polycomb repressor complex 1 subunit BMI-1 overexpression in the brain tissue promotes oligodendrocyte differentiation and plays a vital role in spatial learning and memory [243]. We have verified the PD associated downregulation of BMI-1 and monoubiquitylation of the histone H2A subunit at lysine 119 (H2AK119ub) level in SH-SY5Y cells following exposure with variable 0, 10, 50, 100 and 250 nmol rotenone for 96 hr. The 10 and 50 nmol rotenone minimally alter the BMI-1 and H2AK119ub expression levels in neuroblastoma cells. However, 100 nmol and 250 nmol rotenone exposure significantly downregulated the BMI-1 in the SH-SY5Y cells (Figure 5.1A-C). The considerable reduction of ~38% BMI-1 and ~75% H2AK119ub upon 250 nmol rotenone exposure within 96 hours, indicates lower polycomb E3 ligase activity of the PRC-1 subunit under progressive neurodegeneration.

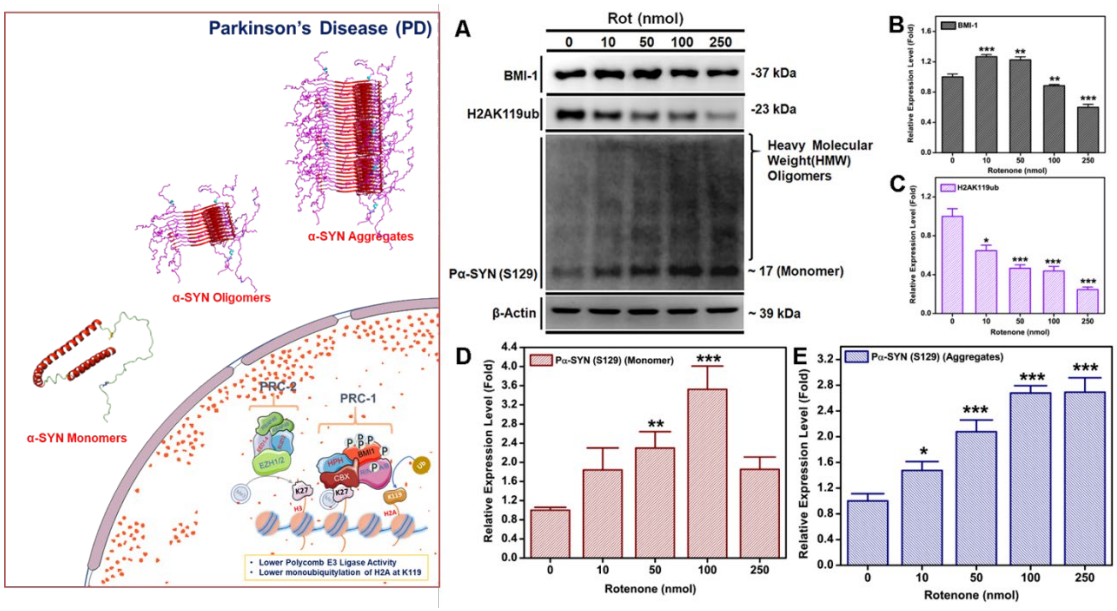

Figure 5.1. The rotenone triggers α-synuclein hyperphosphorylation and downregulates polycomb repressor complex 1 (PRC1) function in SH-SY5Y cells; (A) The protein level of BMI-1, H2AK119ub, phosphorylated α-synuclein at serine 129 (pα-SYN (S129)) with the monomer (~17kDa) and high molecular weight (HMW) oligomers, examined by western blotting. The beta-actin was used as control; The densitometric quantitation of the blot is represented as bar diagram for (B) BMI-1; (C) H2AK119ub; (D) pα-SYN (S129) monomers; (E) pα-SYN (S129) HMW oligomers. The data are represented as Mean ± SEM (n=3). The one-way ANOVA was used to compared the means using Tukey's significance test respect to control (***p≤0.001; **p≤0.01; *p≤0.05).

2.3 Melatonin enrichment suppresses rotenone-induced Bmi-1 phosphorylation

Post-translational modification, such as phosphorylation of BMI-1 is relevant to its functional diversity in transcriptional repression. The MAPKAP kinase 3 (3pK), AKT and CK2α phosphorylate BMI-1 at serine 316, 251, 253, 255 and 110 positions confer de-repressed state and dissociate from chromatin binding site [244, 245]. Hence, we estimated the

collective serine phosphorylation level of BMI-1 using immunoprecipitation and subsequent immunoblotting using anti-p-Ser antibody (Figure 5.2A). The 250 nmol rotenone treatment-induced hyperphosphorylated serine in BMI-1 was significantly reduced to ~ 40% of the total following 2.3 ng/mL melatonin co-treatment (Figure 5.2B). Posttranslational modification such as phosphorylation of BMI-1 at multiple serine residues regulates its cellular function. [244, 245]. However, restoration of BMI-1 activity through pharmaceutical approaches is one of the therapeutic strategies that are used in the regulation of fo neurodegenerative diseases.[246] Thus, melatonin exposure can resist the rotenone-induced phosphorylation of BMI-1 at serine residues and ameliorate the canonical PRC1 function.

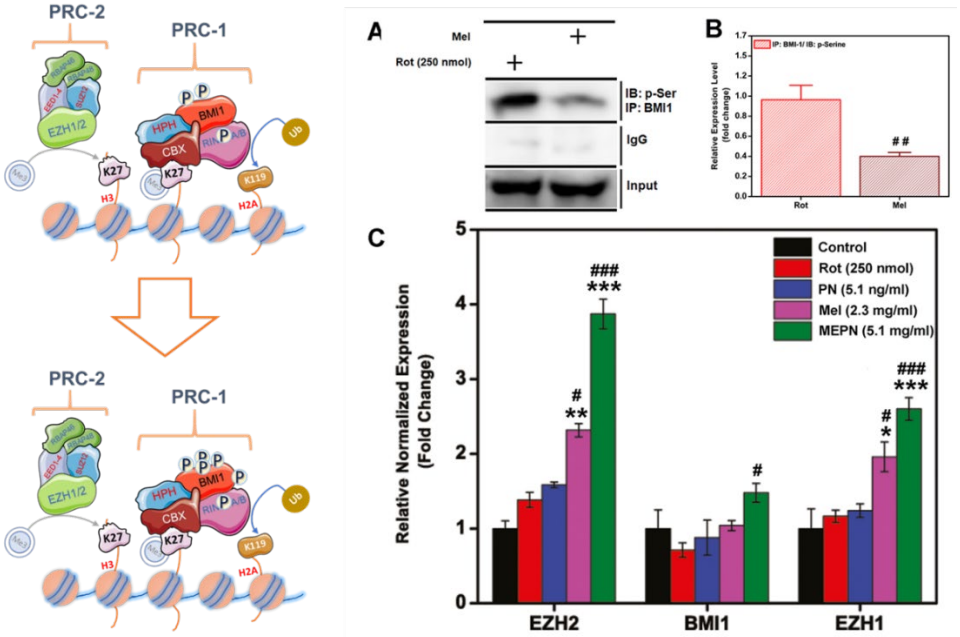

Figure 5.2 Rotenone and melatonin are differently regulating BMI-1 phosphorylation and expression of polycomb repressor complex (PRC) subunit genes; (A) The immunoprecipitation (BMI-1) and Immunoblotting (p-Serine) were performed for the lysate treated with rotenone and melatonin; (B) The densitometric quantitation is represented in bar diagram as Mean ± SEM (n=3) and statistically compared using paired t-test ($^{\#\#}p\leq0.01$); (C) The gene expression of PRC2 subunit EZH2, EZH1, and PRC1 subunit BMI-1 was estimated using qRT-PCR. The fold change was calculated from the ΔΔCt values and represented (n=3), The one-way ANOVA used for statistical analysis with Tukey's test against control (***p≤0.001; **p≤0.01; *p≤0.05) and rotenone ($^{\#\#\#}p\leq0.001$; $^{\#\#}p\leq0.01$; $^{\#}p\leq0.05$).

2.4 BMI-1 and pα-SYN (S129) are reciprocally regulated upon melatonin enrichment

The rotenone exposure is establishing PD phenotype, severely altering PRC subunits gene expression and protein level. The qRT-PCR results indicated that melatonin enrichment triggered significant overexpression of PRC-2 associated EZH2, EZH1, and PRC-1 associated BMI-1 compared to unstimulated control and rotenone treated SH-SY5Y cells (Figure 5.2C). The downregulated BMI-1 level (0.4±0.09%, ***p<0.001) were maintained

(0.76 ±0.09-fold) upon 2.3 ng/mL melatonin exposure, while the polydopamine nanostructures considered as the vehicle (Abbreviated as PN) fails to exert any recovery in BMI-1 expression. The co-treatment of 5.1 ng/mL MEPN (melatonin enriched in PN vehicle) with 250 nmol rotenone prevented the reduction in BMI-1 protein (0.84±0.1-fold (ns at ***p<0.001)).

The rotenone treatment significantly downregulated the H2AK119ub (0.24 ±0.03) whereas co-treatment of PN, melatonin, and MEPN maintained 0.76 ±0.06, 0.6 ±0.2, and 1.5 ±4-fold increase in H2AK119ub level, respectively (Figure 5.3A and 5.3C). The rotenone triggers a 1.6 ±0.2-fold increase in pα-SYN (S129) monomer and 1.7 ±0.3-fold increase in the HMW oligomeric state, compared to present in control (***p≤0.001). Rotenone induction has recapitulated the PD phenotype similar to a precise pathological transformation event with a 1.6 to 4-fold increase in α-SYN achieved on *in-vivo* and *in-vitro* models.[247] Rotenone treatment promotes the influx of extracellular Ca(2+) in SH-SY5Y cells and moderate phosphorylation of PP2Ac at Tyr307, thereby decrease the cellular PP2A activity.[248-250] Decrease in both pα-SYN (S129) monomer (0.72 ±0.2) and HMW (0.56 ±0.4) were observed in MEPN treated PD model, which were significant compared to control (***p≤0.001; **p≤0.01) and rotenone treated group (###p≤0.001) (Figure 5.3A, 5.3D and 5.3E). The melatonin regulates circadian and seasonal rhythms confers a strong antioxidant and neuroprotective effect by preventing oxidative injury in the nigrostriatal dopaminergic system, increasing phosphorylated TH (TH-pSer40) enzyme, enhancing alpha-SYN ubiquitination, reducing mitochondrial dysfunction and preventing alpha-SYN aggregation. [251-255] melatonin block α-SYN fibril formation as well as destabilize preformed fibrils, inhibit protofibril formation, oligomerization, secondary structure transitions and protect the neuronal cell population.[256] Interestingly, the biomaterial characteristics of the polydopamine matrix enriched with melatonin regulate a constant and control bioavailability of active melatonin within cellular compartments. Thus, these results demonstrated that rotenone exposure downregulates BMI-1 and reduces the associated polycomb E3 ubiquitin ligase activity measured as H2Ak119ub level. Interestingly, equivalent rotenone induces pα-SYN (S129) monomers and HMW oligomers deposition also downregulates PRC-1 subunits protein and associated E3 ligase function in SH-SY5Y cells. Overall, the collective downregulation of the PcG function associated with PD was rescued upon melatonin enrichment observed for significant overexpression of the PRC2 (EZH1 and EZH2) and PRC1 (BMI-1) genes.

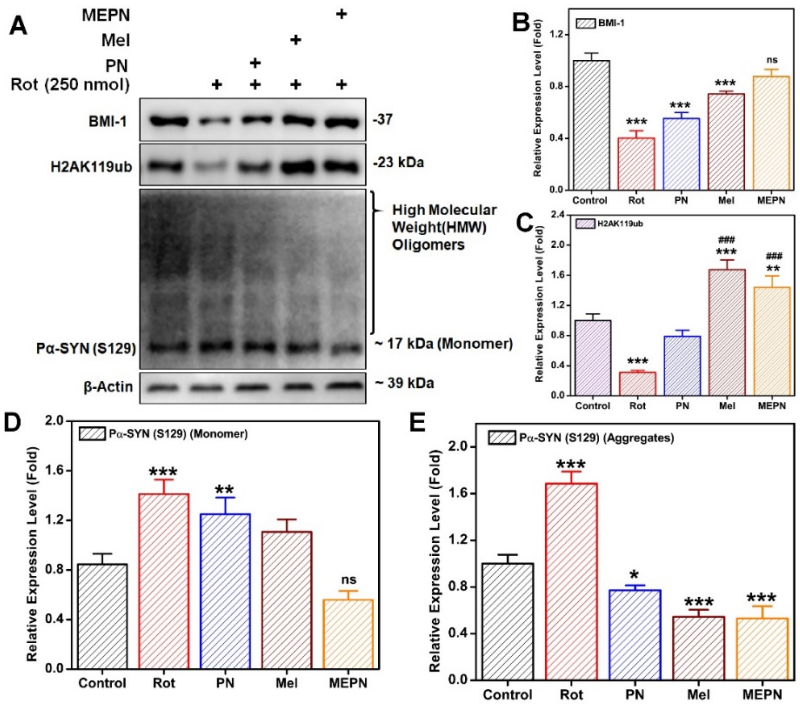

Figure 5.3. BMI-1 and pα-SYN (S129) are reciprocally regulated upon melatonin enrichment in SH-SY5Y PD model; (A) The protein level of BMI-1, H2AK119ub, phosphorylated α-synuclein at serine 129 (pα-SYN (S129)) with the monomer (~17kDa) and high molecular weight (HMW) oligomers, examined by western blotting. The beta-actin was used as indigenous control; The densitometric quantitation of the blot is represented as bar diagram for (B) BMI-1; (C) H2AK119ub; (D) pα-SYN (S129) monomers; (E) pα-SYN (S129) HMW oligomers. The data are represented as Mean ± SEM (n=3). The one-way ANOVA were used to compared the means using Tukey's significance test respect to control (***p≤0.001; **p≤0.01; *p≤0.05) and rotenone ($^{###}$p≤0.001; $^{##}$p≤0.01; $^{#}$p≤0.05).

2.5 BMI-1 mediates ubiquitin-dependent proteasomal degradation of pα-SYN (S129) in PD

The PRT4165 is a specific inhibitor of E3 ligase function and BMI-1 mediated monoubiquitylation of H2A at K119, which at variable inhibitory concentrations of IC25 (~6.5 µmol), IC50 (~10 µmol) and IC75 (~18.5 µmol) shows significant downregulation of BMI-1 protein but induces up to ~4.6 ±0.2-fold increase in pα-SYN (S129) (***p≤0.001) in SH-SY5Y cells upon highest 18.5 µmol PRT4165 treatment. (Figure 5.4A, 5.4D and 5.4E). The result emphasizes that BMI-1 is reciprocally associated with pα-SYN (S129) level in PD. To further evaluate the mechanism of BMI-1 mediated reduction of pα-SYN(S129), the role of proteasomal machinery was investigated. Cells were treated with IC25 (0.65 µmol), IC50 (1 µmol) and IC75 (1.43 µmol) doses of proteasome inhibitor MG132 which fails to clear BMI-1 (1.7 ±0.2-fold) and pα-SYN (S129) (2.2 ±0.2-fold) and promoted their accumulation at the cellular level (Figure 5.4A, 5.4B, and 5.4C). Furthermore, the BMI-1 protein level was not much affected by Betulinic acid (BA) induced proteasomal activation, whereas it critically affects the pα-SYN (S129) level even at minimum IC25 (22.5 µmol) concentration (Figure 5.4A, 5.4F and 5.4G). Altogether, these results represent that BMI-1

inhibition led to an increase in cellular pα-SYN (S129) level and is firmly dependent on proteasome function in SH-SY5Y cells. The suspected association of the BMI-1 and pα-SYN (S129) were confirmed by pharmacological downregulation of the BMI-1 appeared in reduced H2AK119ub activity. Noticeably downregulation of H2AK119ub and BMI-1 increases both pα-SYN (S129) monomer and HMW oligomers deposition.

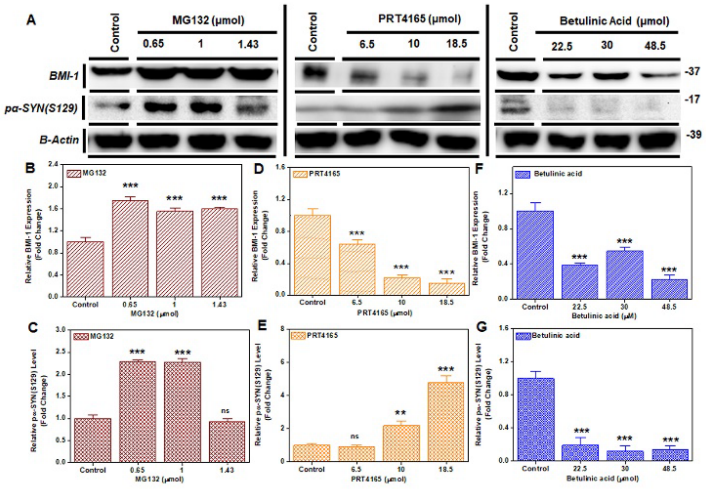

Figure 5.4. Role of proteasomal degradation machinery and BMI-1 in pα-SYN (S129) regulation; (A) The requisite dose of proteasomal inhibitor MG132, BMI-1 inhibitor PRT4165, and Proteasomal activator Betulinic acid (BA) were determined after treating respective IC25, IC50, and IC75. The BMI-1 and pα-SYN (S129) monomer protein was examined using western blot against B-actin as indigenous control. The densitometric quantitation of the band was plotted as bar diagram for MG132 (B, BMI-1, and C, pα-SYN (S129)); PRT4165 (D, BMI-1, and E, pα-SYN (S129)); and BA (F, BMI-1, and G, pα-SYN (S129)).

2.6 Melatonin enrichment mediates BMI-1 dependent regulation of pα-SYN (S129) level in PD

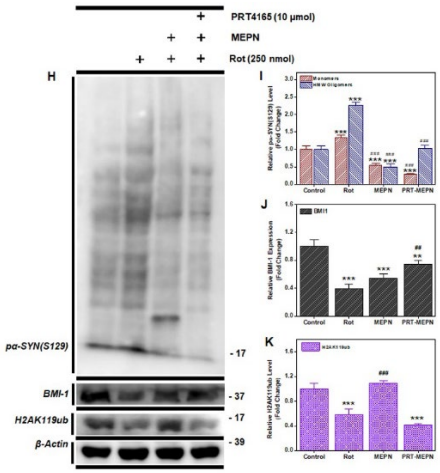

Figure 5.5. Melatonin enrichment mediates BMI-1 dependent regulation of pα-SYN (S129) level in PD; (H) The pα-SYN (S129), BMI-1 and H2AK119ub protein were examined after rotenone, rotenone+MEPN and rotenone+MEPN+PRT4165 exposed cells; The quantitated protein level was represented (I) pα-SYN (S129) monomer and HMW oligomers; (J) BMI-1; and (K) H2AK119ub. The measured values are represented as Mean ± SEM (n=3) and statistically compared using one-way ANOVA with Tukey's test against control (***p≤0.001; **p≤0.01; *p≤0.05) and rotenone ($^{###}$p≤0.001; $^{##}$p≤0.01; $^{#}$p≤0.05).

The 5.1 ng/mL MEPN rescues the rotenone-induced downregulation of BMI-1 and H2AK119ub, while it fails to control the cellular deposition of pα-SYN (S129) HMW oligomer upon 10 μmol PRT4165 co-treatment. The significantly reduced level of H2AK119ub confirmed the effect of PRT4165 in suppressing the E3 ligase activity of the PRC1 complex. Altogether, the result indicates BMI-1 mediated loss of pα-SYN (S129) upon MEPN exposure is mechanistically the basis of neuroprotection in PD (Figure 5.5H-5.5K). Almost 0.4 ±0.1-fold decreases in pα-SYN (S129) HMW were estimated in MEPN treated cells. However, co-exposure of 1 μmol MG132 with MEPN withdraws such an inhibitory effect of MEPN on pα-SYN (S129). (Figure 5.6A and 5.6D). Conversely, complete clearance of the pα-SYN (S129) monomer and HMW states were observed upon co-exposure of 30 μmol BA with MEPN in the PD model. These results indicate that MEPN exposure rescues BMI-1 expression and PRC-1 function and is requisite for proteasomal degradation of pα-SYN (S129) in the PD model. (Figure 5.6A-5.6D). In particular relevance of PD, both ubiquitin-dependent proteasomal system (UPS) and autophagy are involved in pathological pα-SYN (S129) clearance. Earlier reports detail that failure of the proteasomal degradation machinery consequent the intracellular aggregation and accumulation of alpha-SYN in the PD model. [257] Moreover, rotenone treatment leads to mitochondrial dysfunction triggers the direct oxidative modification of proteasome subunit and other cellular proteins.[258] The immunoprecipitation and anti-ubiquitin immunoblotting results confirmed the increased association of the Ub with pα-SYN (S129) following MEPN cotreatment shows that MEPN regulates UPS pathway to eliminate cellular pα-SYN (S129). Moreover, another immunoblotting experiment confirmed the association of BMI-1 protein with pα-SYN (S129) under MEPN exposure (Figure 5.6E-5.6G). The finding indicates that BMI-1 directly interact with pα-SYN (S129) on MEPN stimulation and directs the ubiquitin-dependent proteasomal degradation of pα-SYN(S129). The abrogated cellular proteasomal function promotes the pα-SYN (S129) accumulation; conversely the proteasomal activation significantly clears deposited pα-SYN (S129). Furthermore, BMI-1 depletion in the cells compromised the effect of melatonin to reduce the the pα-SYN (S129) HMW oligomers. However, MEPN associated BMI-1 overexpression promotes ubiquitination of pα-SYN(S129) and proteasomal degradation. The BMI-1 as a positive feedback loop in the multi-regulatory network reclassified as a polycomb member distinctly regulating the PD progression. Notably, the two crucial observations confirmed the non-canonical function of PRC1 in the regulation of the pα-SYN(S129). First, the BMI-1 may directly interact with the pα-SYN (S129) and significantly modulates the UPS system via PRC1 E3 ligase complex BMI-1/RING1 via a similar mechanism by which it ubiquitinates chromatin-associated proteins on promotor site before entering in G1 cell cycle phase.[259] Second, the pα-SYN (S129) undergoing increased ubiquitination upon melatonin enrichment is prominently associated

with BMI-1. Thus, our study reveals enriched melatonin is a pleiotropic signaling molecule that can suppress neuronal pα-SYN (S129) level by promoting its proteasomal degradation.

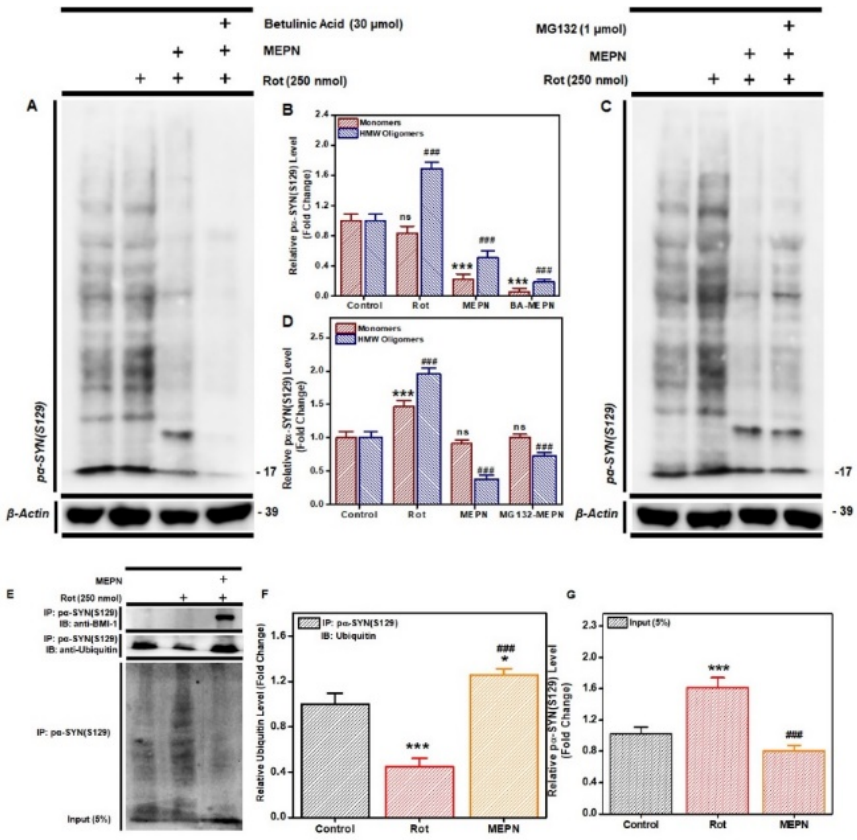

Figure 5.6. BMI-1 mediates ubiquitin-dependent proteasomal degradation of pα-SYN (S129) in PD; The pα-SYN (S129) monomer and HMW oligomers were examined using western blot, following exposure of, (A) rotenone, rotenone+ MEPN, rotenone+ MEPN+ Betulinic acid (BA); and (C) rotenone, rotenone+ MEPN, rotenone+ MEPN+ MG132. (B and D) The densitometric quantitation of pα-SYN (S129) monomer and HMW oligomers were represented as a bar diagram. (E) The immunoprecipitation (IP) with pα-SYN (S129) and Immunoblotting (IB) with anti-BMI-1; IP- pα-SYN (S129) and IB-anti-ubiquitin were represented. The 5% input of the isolates were examined using western blot. (F and G) the associated ubiquitylation of the pα-SYN (S129) was quantitated and represented In bar diagram along with the quantitation of pα-SYN (S129) in input sample; The measured values are expressed as Mean ± SEM (n=3) and statistically compared using one-way ANOVA with Tukey's test against control (***p≤0.001; **p≤0.01; *p≤0.05) and rotenone ($^{###}$p≤0.001; $^{##}$p≤0.01; $^{#}$p≤0.05).

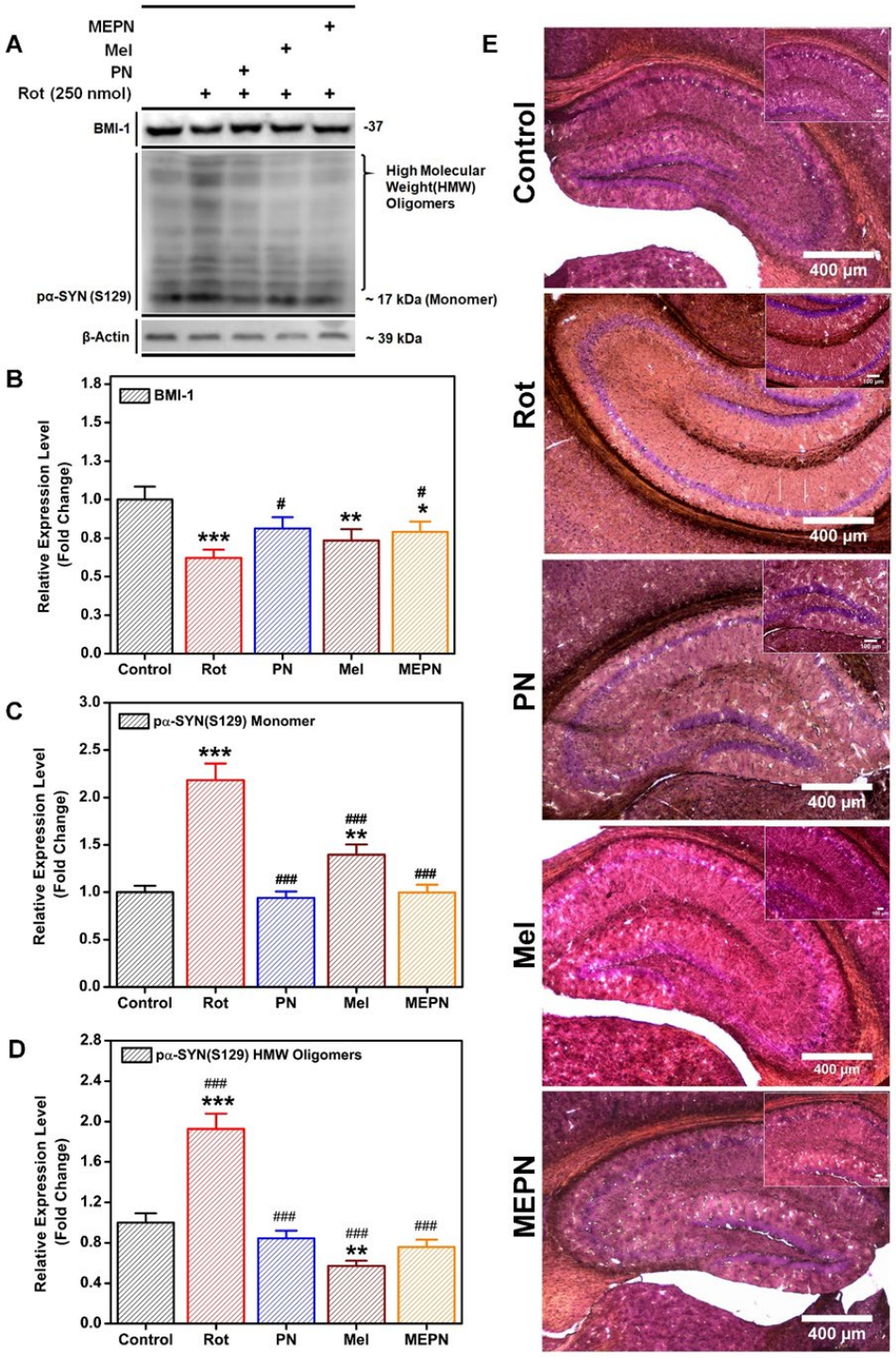

Figure 5.7..mPDAN induces superior neuroprotection on in-vivo PD model; (A) The western blot analysis of pα-SYN (S129) monomer and HMW oligomers, BMI-1 was performed for 45 days rotenone induced mice, whole-brain isolates; The densitometric quantitation of (B) BMI-1; (C) pα-SYN (S129) monomer and (D) HMW oligomers were represented as bar diagram. The measured values are expressed as Mean ± SEM (n=3) and statistically compared using one-way ANOVA with Tukey's test against control (***p≤0.001; **p≤0.01; *p≤0.05) and rotenone (###p≤0.001; ##p≤0.01; #p≤0.05); (E) The Hematoxylin and Eosin (H&E) staining of midbrain section of 45 days rotenone, PN, melatonin, and MEPN injected (i.p) mice showing comparative sign of PD associated damage. Scale bar = 400 µm.

2.7 Enriched melatonin induces superior neuroprotection on *in-vivo* PD model

The 2.2 ±0.3-fold pα-SYN (S129) monomer and 1.9 ±0.3-fold pα-SYN (S129) HMW oligomer level was estimated in rotenone-induced PD mice brain (***p≤0.001). In contrast, MEPN co-injection significantly resists the rotenone-induced pα-SYN (S129) change (###p≤0.001) (Figure 5.7A, 5.7C and 5.7D). The reduced BMI-1 expression (0.62 ±0.3) in PD were recovered upon MEPN co-injection (0.81 ±0.2%, #p≤0.05) (Fig. 5.7A and 5.7B). The localized morphological damage seen in the Hippocampal (HIP) tissue area of the PD brain, were absent in MEPN co-injected brain (Fig. 5.7E). The differential expression pattern of the pα-SYN (S129) and BMI-1 in midbrain revealed increased (1.7 ± 0.2-fold, n=3) and scattered deposition of the pα-SYN (S129) in the cortex (Ctx), HIP and SN region. At the same time, melatonin and MEPN injected mice brains were devoid of any distinct and significant change in the expression as well as distribution (ns= *p<.05) (Figure 5.8).

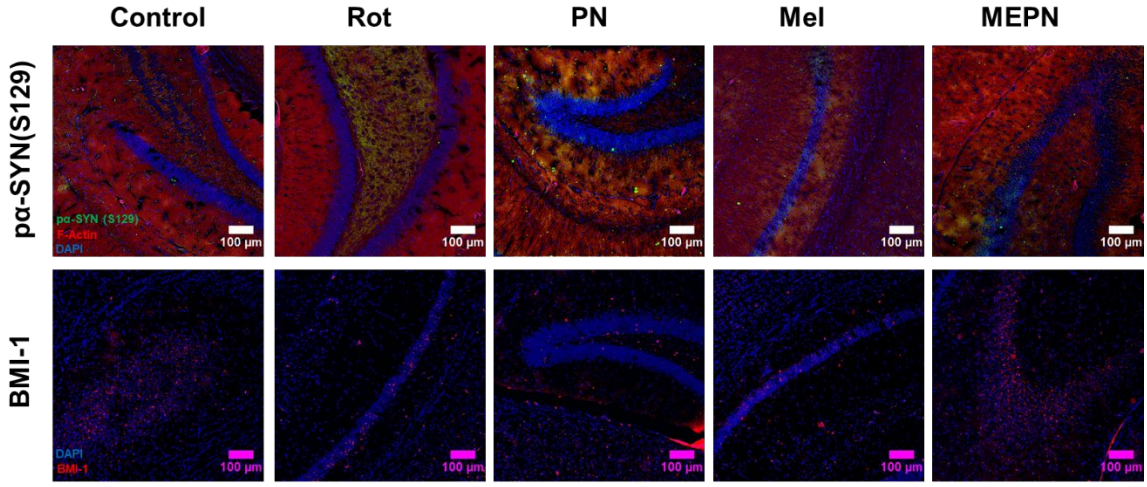

Figure 5.8 The immunofluorescence studies in brain section of PD mice model; The pα-SYN (S129) and BMI-1 fluorescence (Green) in Control, rotenone, PN, melatonin and MEPN injected mice midbrain section were represented. The F-actin were stained with phalloidin-PE (Red). The nucleus was stained with DAPI (Blue). Scale bar = 400 µm.

The BMI-1 (0.52 ±0.06-fold, n=3) level is significantly decreased in HIP and SN, but less protein level change is seen in the cortical region in the PD brain. Interestingly, the reciprocal expression pattern of the pα-SYN (S129) and BMI-1 are observed in HIP and SN in the contralateral side of the midbrain. Furthermore, the distinct pα-SYN (S129) and BMI-1 expression in whole mice brain corroborate in-*vitro* results, rather the differential expression of α-SYN in SN and dorsal motor nucleus of vagus at early onset and in the HIP, neocortex and frontal cortex at later stages of PD, marked as a most vulnerable brain area.[260] The increased level of pα-SYN (S129) expression was seen in these highly susceptible HIP and SN regions on the contralateral brain side accompanying lower BMI-1 but no such changes in the expression have appeared in the thalamus and frontal cortical area. Conversely, downregulated BMI-1 expression is closely associated with brain region-

specific pα-SYN (S129) positive neurons, and collectively restored upon melatonin exposure.

3. Conclusion

The α-synuclein (α-SYN) is a presynaptic protein, undergoes abnormal aggregation and accumulates in the diverse area of the brain underlie Parkinson's disease (PD) pathogenesis. The post-translational modification, specifically phosphorylation at serine 129 of α-syn (pα-SYN (S129)) was linked to pathological transformation and established as a hallmark of the PD. In a multi-regulatory environment, the pathways controlling phosphorylation and in-situ proteolysis of the α-syn were modulated using the molecular therapeutic intervention. It has been suggested that epigenetic polycomb repressor protein BMI-1, which plays a crucial role in the repression of key regulatory genes in neurogenic tissues, may be linked to alpha-synuclein associated synucleinopathy. The present study elucidates the role of BMI-1 in neuroprotection in rotenone-induced neuroblastoma cell and PD mice model (chronic; 45 days). Here, we report BMI-1 as a critical negative regulator of α-SYN phosphorylation at Serine 129 (pα-SYN (S129)) and its aggregation in neuroblastoma cells in-vitro, hippocampal (HIP) and Substantia nigra (SN) of the PD bearing mice. Melatonin as a neuroprotectant, upregulates BMI-1 expression and its E3 ligase activity, whereas it significantly downregulates pα-SYN (S129) level in HIP and SN neurons in the brain. Furthermore, immunocytochemistry results confirmed that BMI-1 can directly interact with pα-SYN (S129) and regulates the pathological processing under melatonin exposure. However, pharmacological depletion of the BMI-1 compromises the neuroprotective function of melatonin. The BMI-1 facilitates the ubiquitination and proteasomal degradation of pα-SYN (S129), which is confirmed by inhibition of both the BMI-1 function and cellular proteasomal machinery. Thus, this brain region-specific crucial regulatory interaction between BMI-1 and pα-SYN (S129) elucidates the non-canonical function of BMI-1 and could emerge as a potential epigenetic therapeutic target in PD.

Chapter 6a

Dopamine inspired quantum sized dots for multimodal fluorescence screening of the live and dead neuronal cell population

1. Background

In the last couple of decades, the carbon dots (CD) are preferred for *in-vitro* and *in-vivo* applications due to its low cost, low non-specific toxicity, more robust optical properties, higher thermal and photo-stability.[261] The sub-nanometer size range, broad adsorption from ultraviolet to green region, and tunable full wavelength fluorescence emission are the characteristics that enable it for fluorescence-based multiplex imaging and guided therapy.[262, 263] Recently, enormous effort has been made to prepare CDs using precursors from biological sources such as proteins, carbohydrates, and small molecules.[264] Despite the origins, exogenous doping of nitrogen and sulfur are performed to get desirable emission characteristics in CDs, which compromise the biocompatibility and targetability of prepared CDs.[261] There are rare reports for the evolution of such fluorescent dots from catecholamine, i.e. Dopamine (DA) and its oxidation products. Dopamine is a biogenic amine-based neurotransmitter in the central nervous system (CNS) that controls reward, addiction, control of coordinated movement, metabolism, and hormonal secretion.[265-267] Naturally, dopamine is derived from tyrosine amino acid with two of the following reaction process, first tyrosine hydroxylase catalyzes the synthesis of dihydroxyphenylalanine (DOPA), which further decarboxylated into dopamine in the presence of enzyme DOPA decarboxylase.[268] However, exogenous L-DOPA undergoes decarboxylation reaction in the brain tissue upon systemic administration gives a natural fluorescence emission in the brain region.[269]

In contrast, the dopamine exhibits natural fluorescence in the UV region, which progressively changes under the alkaline condition and can be linked to chemical instability leading to oxidation of dopamine into quinone intermediates and aminochromes.[270] pH-induced controlled oxidative polymerization of dopamine leads to polydopamine nanostructures (PDANPs).[271] The molecular chemistry and intrinsic chemical reactivity of PDA confer widespread application in bio-mineralization, single-cell encapsulation, sensors, catalysis and attenuation of *in-vivo* toxicity.[272] Initially, PDA was suspected as a disordered organic semiconductor, identical to melanin, but its inherent chemical heterogeneity extended its absorption in the UV-Vis-NIR region and under UV excitation, it exhibits a weak fluorescence between 400-550 nm.[273] However, the fluorescent dots are already prepared from chemical degradation of polydopamine, but no efforts have been made to fabricate these fluorescence dots from dopamine derived early oxidative intermediates. The conventional preparation method, such as laser ablation, pyrolysis, and electrochemical oxidation, hydrothermal treatment, and microwave-assisted syntheses are commonly used for preparing fluorescence dots.[274, 275] The controlled catalysis following the mild solvothermal treatment providing the enhanced photostability

and optical characteristics are among the rare strategies employed for the fabrication of these nanoprobes.

In the present chapter, we detailed a highly facile methodology for preparing a biocompatible, quantum-sized dots (DI-10) using a thermally controlled oxidation condition that immediately produces dopamine derived intermediates, which were further stabilized by hydrothermal treatment. DI-10 is characterized for physicochemical and optical properties using multiple morphological, structural, and optical measurement tools. These nanostructures were demonstrated as a promising imaging agent that can distinctly separate the live and dead neuroblastoma cell population.

2. Results and discussion

2.1 Preparation of DI-10

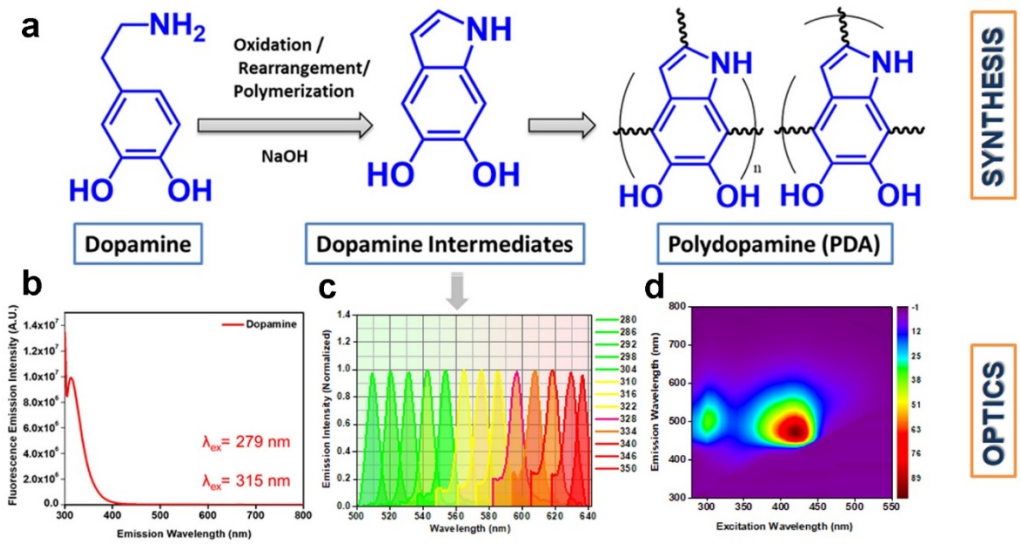

Figure 6.11. Synthesis and optical characterization of DI-10; (a) Controlled melanogenesis pathway of dopamine (DA) as the precursor, dopamine early oxidation intermediates give polydopamine (PDA) as final product. (b) The precursor dopamine confers a weak fluorescence emission in UV region. (c) The quantum sized dots (abbreviated as DI-10) recovered from thermal processing of the early dopamine oxidation intermediates shown full-wavelength emission. (d) comparably under similar processing, polydopamine confer broad fluorescence emission in the green region.

The presence of an aromatic ring, hydroxyl moieties, and an amine group in the structure of dopamine motivated us to consider dopamine oxidation products as a precursor for the synthesis of DI-10.[273, 276] These multiple functionalities in dopamine derived structures offer a versatile interaction that allows them to use as a coating material in many applications.[277] In our procedure, pre-optimized dopamine concentrations, alkaline pH conditions, reaction time, and temperature are used to prepare DI-10.[273] The product obtained by using a dopamine concentration of 1 mg/mL and dopamine: NaOH (1:0.4) was

giving the strongest fluorescence emission (Figure 6.11). The post-synthesis hydrothermal processing provides enormous structural and optical stability measured as a function of change in fluorescence emission. The purified DI-10 gives a characteristic full wavelength fluorescence from blue to red spectral region, which is similar to the fluorescence emission pattern of quantum dots or carbon dots. In contrast, the material prepared in the aprotic nonpolar solvent phase exhibited more pronounced excitation dependent fluorescence emission in full spectral regions, characterized by excitation wavelength-dependent emission mapping. The fluorescence intensity and quantum yield estimated showed a direct relationship with the degree of oxidation of dopamine.

2.2 Morphological and structural characterization

The transmission electron microscopy (TEM) images revealed that DI-10 was uniform with a mean particle size distribution of 11 ±5 nm (Figure 6.12). The High-resolution TEM (HR-TEM) images represented identical well-resolved lattice spacing of 0.22 nm correspond to (100) lattice spacing, attributed to the lattice parameter of conventional quantum sized materials.[275] X-ray photoelectron spectroscopy (XPS) findings provided the elemental composition and elemental speciation within the DI-10. The wide spectrum represented three characteristic peaks corresponds to C 1s (285 eV), N 1s (400 eV), and O 1s (531 eV) (Figure 6.13c(i)). In the high-resolution spectra, the C 1s band deconvoluted into five peaks in Figure 6.13a(ii), corresponding to sp2 carbons (C=C, 284.7 eV), sp3 carbons (C−O/C−N, 286.5 eV), carbonyl carbons (C=O, 287.4 eV) and (π-π, 297 ev). The N 1s band can be deconvoluted into three peaks at X_3–N (403.6 eV, X = C, N, or P), X_2–N (pyridinic- and pyrrolic-N, 400.1 eV, X = C, N or P) and N–H (398.2 eV), respectively (Figure 6.13a(iii)). The O 1s band contains two peaks at 531.4 and 541.3 eV for C=O and -OH, respectively (Figure 13a(iv)). The P_2p XPS spectrum shows two peaks at 132.4 eV, and 133.3 eV, which can be assigned to P–X aromatic (X = C or N) and P–O groups coming from the buffer component as the material has been dissolved in phosphate buffer saline before sample preparation. The Fourier transform infrared (FTIR) spectra revealed that DI-10 possessed several hydrophilic groups O−H (3350 cm^{-1}), CN (3160 cm^{-1}) and NH (3052 cm^{-1}) on their surfaces are similar to the functional groups present on dopamine, thereby ensuring their good dispersity in water (Figure 6.12b(i)). Moreover, small peaks in the range of 2778-2170 cm^{-1}, attributes to different CH vibrations of aryl or aliphatic C-H bond. The higher transmittance band at 1494 cm^{-1} and 1252 cm^{-1} corresponds to the bending vibration of C-H and aryl oxygen stretching vibrations (Figure 6.13b(ii)). A comparison of the FTIR spectra of the dopamine, poly-dopamine, and DI-10 reveals this critical information.

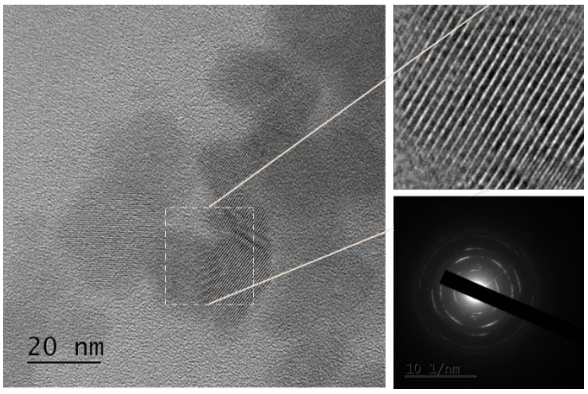

Figure 6.12. Morphological characterization of DI-10; High-resolution TEM, showing dots appearance with clearly visible single-phase lattice width and electron diffraction pattern

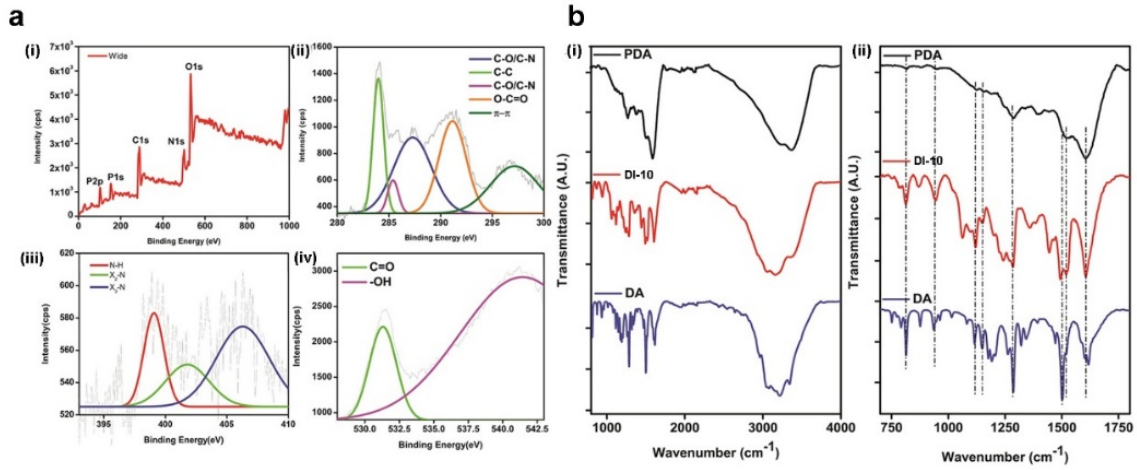

Figure 6.13 The structural characterization of DI-10; (a(i)), Wide survey of X-ray photoelectron spectroscopy representing the presence of C, N, O element. (ii-iv), binding energy corresponds to Carbon, Nitrogen & Oxygen. (b(i)) FTIR pattern of the precursor dopamine (blue) and PDA (Black) and DI-10 (red). (ii), the enlarged region between 750-1750 cm-1 showing functional group involved in the preparation of DI-10.

2.3 Multimodal optical characteristics of DI-10

The polydopamine nanostructures are achieved by oxidation of dopamine at elevated temperatures. Characteristically, the preparation of DI-10 using solvothermal reaction in water leads to the co-formation of polydopamine (PDA) nanostructures along with DI-10. The native PDANPs shows characteristics fluorescence emission peaks confined between 480 nm to 510 nm even after multiple excitation wavelengths. Here, our primary goal was to modify the preparation method to remove the contribution of PDANPs within DI-10 (Figure 6.14a). Thus, seven different solvents were selected as the preparation medium, namely chloroform, carbon tetrachloride, acetonitrile, dimethyl sulphoxide, methanol, n-butyl alcohol, and n-hexane.[278, 279] The DI-10 prepared in absolute acetonitrile was utterly devoid of the PDANPs contamination. The fluorescence spectra of DI-10 excited

from 280 nm to 350 nm, shown in Figures 6.14a. Overall observation demonstrated that the fluorescence emission spectra could be seen into four different domains (Figure 6.14a); the normalized enlarged green band region shows excitement wavelength-dependent emission shift from 500 nm to 650 nm (Figure 6.14b and 6.14c).

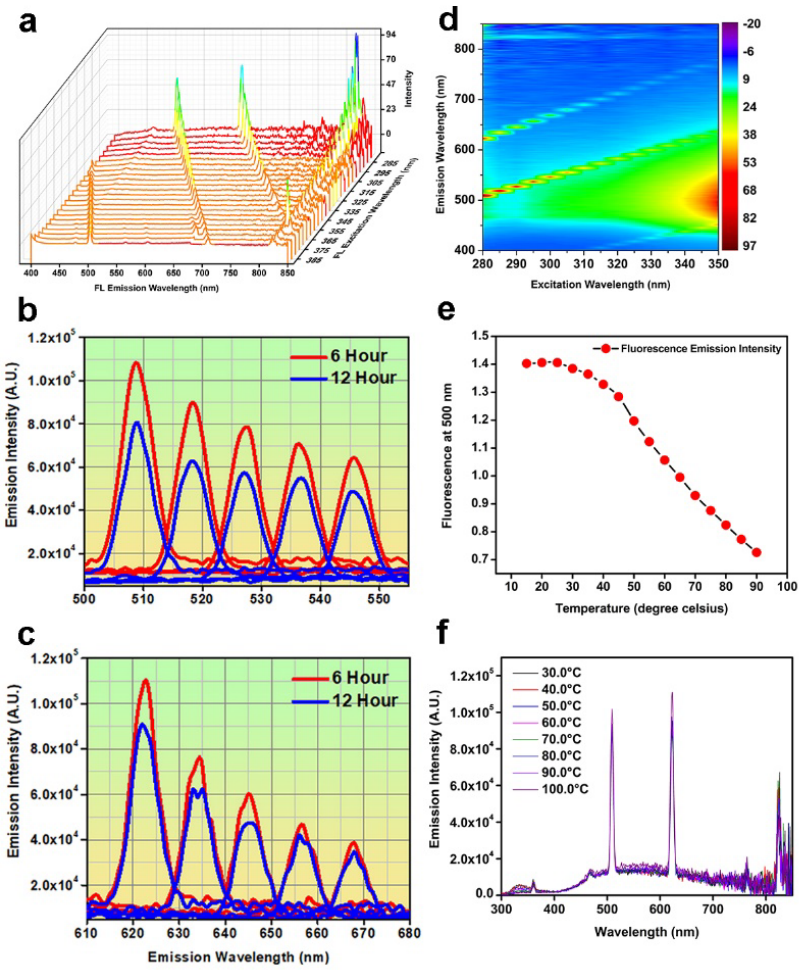

Figure 6.14. Photonic characteristics and thermal stability; (a) Excitation dependent emission intensity shifting of the DI-10 giving fluorescence in Blue, Green, and Red. (b & c) the fluorescence emission in the green and red regions. (d) DI-10 giving fluorescence components of PDA as noise in the Ex/Em map. (e) The DI-10 without hydrothermal processing displayed thermal instability. (f) purified and stabilized DI-10 is showing enhanced thermal stability.

Though DI-10 was optimally prepared at low-temperature conditions and its stability at physiological temperature can be questionable. Thus, the stability of DI-10 was estimated by measuring the change in fluorescence emission as a function of temperature. The DI-10 obtained in the first synthesis product displayed continuous fluorescence quenching with an increase in the temperature from 20 ˚C to 90 ˚C (Figure 6.14e). However, DI-10 recovered post-hydrothermal shows stable fluorescence emission and thermal stability up to 90 °C (Figure 6.14f).

2.4 Cellular compatibility of DI-10

The biocompatibility of DI-10 assessed to make sure that as-synthesized DI-10 possesses low cytotoxicity and is suitable for biomedical applications. MTT based cellular cytotoxicity measurement was performed over neuroblastoma and healthy cells (293-T) as test cell lines. Compared to the untreated control group, the viability of the cells exceeds ~80% after incubation with DI-10 for 48 h at six different concentrations (10 to 200 µg/mL) (Figure 6.15).

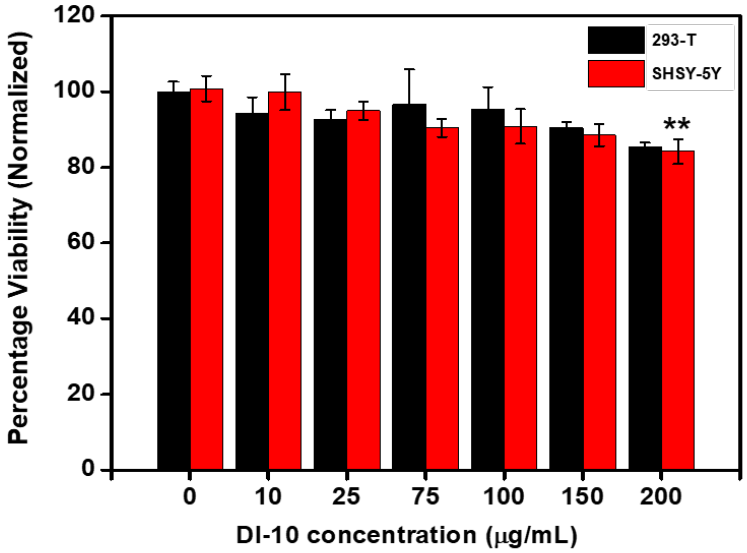

Figure 6.15, Cellular viability MTT assay performed to observe the cytotoxicity of DI-10 over SH-SY5Y(Neuroblastoma) and 293T (fibroblast) showing ~75% maximum even at maximum concentration. The assay performed in independent triplicates and tukey's significant test was performed at $p \leq 0.01$.

Results indicated that up to optimum treatment dose DI-10 does not inhibit the proliferation of the cells and confirms its compatibility for biomedical applications. Laser confocal scanning microscopy (LCSM) was used to demonstrate further the bioimaging applications of DI-10. DI-10 incubation for 2, 4 and 6 h show cellular internalization emitted intense blue, green, and red fluorescence. DI-10 shows rapid cellular accumulation with the partitioned distribution in subcellular space. As for the initial 2 h uptake, the characteristics blue fluorescence appear from the perinuclear space in the cytoplasm, whereas green and red fluorescence was distributed into the cytoplasm (Figure 6.16a). Long-term treatment of DI-10 in SH-SY5Y 3D organoid culture given uniform accumulation into the nucleus and cytoplasm (Figure 6.16b). The excellent biocompatibility, broad tunability, and remarkably high photostability are incredibly beneficial for bioimaging and sensing applications.

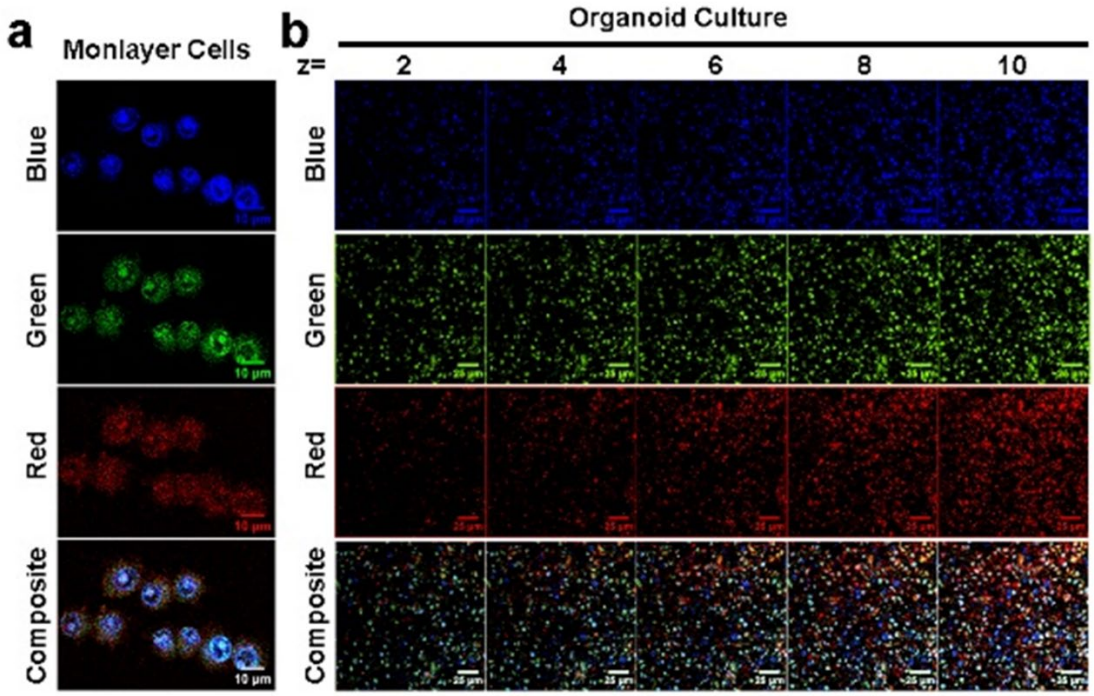

Figure 6.16 Multiplex bioimaging property of DI-10; (a) Cellular uptake of the DI-10 showing fluorescence in Blue, Green and Red represented. (b) DI-10 penetrating and localizing into the 3-dimensional multicellular culture giving characteristic fluorescence in the blue, green and red regions.

2.5 In-vivo biodistribution and histopathological effect of DI-10

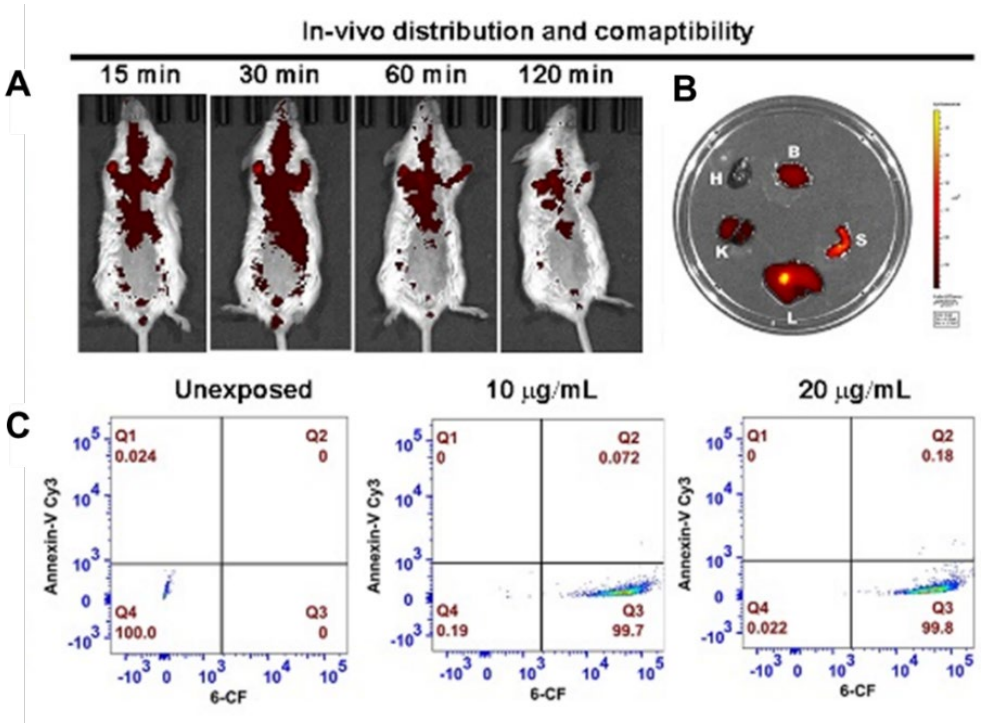

Figure 6.17. the *in-vivo* and *ex-vivo* whole-body distribution and anti-apoptotic assay of DI-10. mice representing the time-lapsed distribution of the DI-10, which is maximum at the 30 minutes after tail vein injection. (d) ex-vivo imaging shown the presence of the DI-10 in major organs. (e) the anti-apoptotic FACS based assay representing higher biocompatibility of the material up to 20 µg/ml DI-10 treatment.

Furthermore, *In vivo* whole-body biodistribution in the mice was conducted by using an in vivo imaging system (IVIS Spectrum, Caliper, USA). The dispersed solution of DI-10 was injected in the mice via lateral tail vein, and time-dependent imaging displayed progressive accumulation in the brain suggested that DI-10 can circumvent the blood-brain barrier (BBB) and retain in the brain tissue. The highest fluorescent intensity of DI-10 was observed at 30 min post-injection followed a gradual decrease in the intensity indicated systemic clearance of the DI-10. (Figure 6.17A). In another set of experiments, the major organs of mice injected with DI-10 were isolated and imaged. In reference to the uninjected control group, significant accumulation of DI-10 was found in the liver, kidney, spleen, and brain (Figure 6.17B). Annexin V-Cy3/6CF staining in combination with flow cytometry shown in Figure 6.5C, after 24 h treatment with 10 µg/mL & 20 µg/ mL, there was no significant apoptosis or necrosis occurred in the treated SH-SY5Y cells. (Figure 6.17C)This result was consistent with the MTT results, Altogether representing higher compatibility with the biological systems and proved to be excellent candidates for bioimaging and diagnostics applications.

2.6 FACS based screening of the live and dead population

The intracellular partitional distribution of DI-10 led us to investigate the basis of its inherent interaction with the biomolecules. Further, we suspected differentiation fluorescence of DI-10 in viable and non-viable cells, thus treated neuroblastoma cells with DI-10 and subjected to flow cytometry measurement. The excitation and emission channel parameters were set at 348/496, 405/510, 407/602 and 496/612 (excitation/emission). While untreated live cells are optically neutral, the ~50.1 and ~96.2 % positive live cell population has given fluorescence in the 407/602 and 496/612 channels (Figure 6.18). The DI-10 exposed to the non-viable cells displayed no fluorescence signal in 405/510, 407/602 and 496/612 channels, whereas characteristics ~92% positive population have appeared in 348/496 channel. The comparison of the viable and non-viable quadrants provided that ~52.5 % population emits at 602 nm and 612 nm than that of the non-viable population, which strictly emitted at 496 nm. Thus, this differential selectivity of DI-10 towards the viable and non-viable cells displayed distinct characteristics that can be used for FACS based analysis of viable/non-viable cells among the mixed population. However, we suspected cell surface charge as a major driving factor regulates the dynamic interaction and internalization of DI-10 within cells. The exact mechanism of such selectivity can be investigated using detailed cellular and molecular studies in the future. Conclusively, DI-10 can differentially stain viable and non-viable cell populations and could be utilized as a sensitive probe for FACS based live/dead assay.

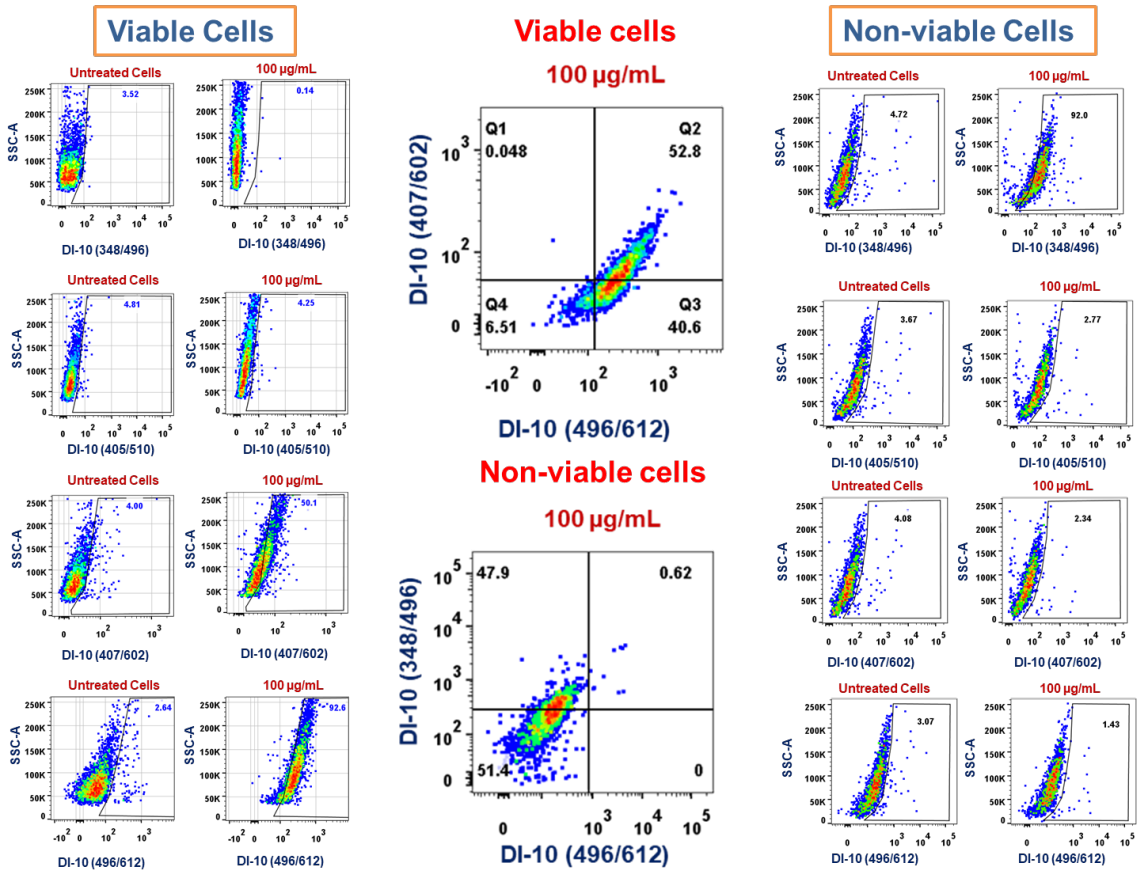

Figure 6.18 **DI-10 for live/dead FACS based assy;** the dot-plot of the unstimulated, exposed to maximum 100 µg/mL DI-10 to viable cells and non-viable cells displayed the positive fluorescence at the range of excitation and emission channel of 348/496, 405/510, 407/602 and 496/612 nm.

3. Conclusion

The fluorescence dots are highly photostable nanoprobes used in a range of biomedical applications, from detection to the real-time monitoring of the biomolecular cascades. Despite enormous innovation, these probes suffer from the issue of biocompatibility, non-specificity and poor photo/thermal stability. The present work reports the development of highly biocompatible quantum sized dots (DI-10) from dopamine derived intermediates under thermally controlled oxidation coupled with solvothermal treatment which displayed full-wavelength excitation dependent fluorescence emission, robust photo, and thermal stability. DI-10 can readily visualize in monolayer, three-dimensional organoid, and in-vivo mice model under unique excitation dependent full wavelength fluorescence from blue to NIR. The differential subcellular partitioning of the DI-10 inside the cells following internalization can differently label the viable and nonviable cell population. This work reports the bottom-up approach to produce the bioinspired, highly biocompatible quantum sized dots as cocktail components for bioimaging and FACS based live/dead assay.

Chapter 6b

Developing stimuli-responsive Amyloid-beta anti-aggregation agent for neuroprotection in Alzheimer's disease model

1. Background

Alzheimer's disease (AD), is age-associated and highly prevalent neurodegeneration and cause of dementia, characterized by deposition of senile plaque and intraneuronal neurofibrillary tangles in the diverse area of the patient brain.[30, 280, 281] The amyloid-beta (Aβ) fragment generated during amyloidogenic processing of amyloid precursor protein (APP) turns into soluble oligomer, insoluble aggregates, prominent fibrils hampers synaptic plasticity and leads to neuronal cell death.[41] The pharmacological and multimodal combinatorial strategy of targeting in-situ A*β* processing, nucleation, seeding, and aggregation proves to be beneficial in controlling the AD progression.[282] A number of nanostructures loaded with Aβ inhibitors that can circumvent the blood-brain barrier (BBB) have been utilized.[283] Dopamine (DA) and melatonin (Mel) plays a crucial role in the etiology of AD. Dopamine is a catecholamine-based neurotransmitter deposit as neuroprotective polydopamine (PDA) or neuromelanin in brain tissues.[182] The polydopamine nanostructures (PDANPs) displayed excellent biocompatibility and NIR responsive photothermal effect.[16] The melatonin (*N*-acetyl-5-methoxytryptamine) shows pharmacological inhibition of major AD-associated pathobiology via regulating the catalytic activity of protein phosphatase 2A (PP2A),[284] structure-dependent inhibition of A*β* fibrillation,[285, 286] reduced APP processing by regulating *β*-secretase function,[287] activating anti-apoptotic and anti-oxidative signaling.[288, 289] Considering these facts, we hypothesized that melatonin polydopamine nanocomposites (DM-NCs) formed by self-assembly of dopamine derived intermediates and melatonin, may confer a superior multimodal neuroprotective regime in AD. Recently, near-infrared radiation-based photo-biomodulation are accounted considerable therapeutic effect by reducing Aβ plaque formation, inflammation and oxidative stress in AD models.[290] Hence, the present rationale for developing highly biocompatible agent confers combined photothermal and pharmacological therapeutic effects may be highly potent in controlling Aβ pathophysiology.

The dopamine/melatonin nanocomposites (denoted as DM-NCs) were prepared and characterized for the physicochemical characteristics, stability and integrity (Please see chapter 2 and chapter 3 for the details). The present chapter details the NIR responsive photothermal effect of DM-NCs triggers NIR responsive release of the entrapped melatonin due to the inherent photothermal conversion (PTC) effect. The photothermal effect of DM-NCs prevents the ex-situ A*β* fibrillation, propagation and disrupt preformed A*β* fibrils. Highly biocompatible DM-NCs can accumulate on in-vitro AD induced cells, scavenge intracellular ROS and prevents in-situ Aβ processing. Further, it has been observed that DM-NCs can suppress the cellular A*β* processing and associated pathology

in mice midbrain slice culture (MBSC) based AD model. Therefore, in present work, a nano-therapeutic agent is demonstrated that can confer synergistic photothermal and pharmacological inhibition of Aβ associated AD pathology.

2. Results and Discussions

2.1 NIR Responsive Photothermal Effect of DM-NCs

The concentration-dependent increase in the temperature upon NIR illumination is one of the ways to estimate the photothermal effect of active material. Highly dispersed aqueous solution of DM-NCs on the increasing concentration of 100 ng/mL, 1 *μ*g/mL and 100 *μ*g/mL showed immediate increased in the temperature up to ~ 36 °C, ~39 °C and 45 °C, upon NIR illumination (808 nm, 0.5 W/cm^2 for 15 min) (Figure 6.21A). An equal volume of saline considered as reference control displayed no significant increase in the temperature. These results indicated that the presence of melatonin in DM-NCs had not compromised the PTC effect of polydopamine.

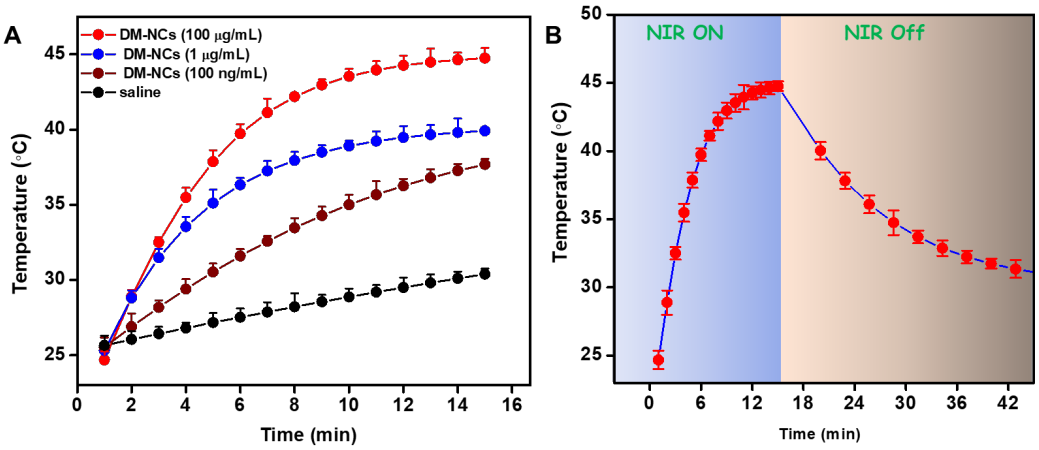

Figure 6.21. The NIR responsive photothermal effect of DM-NCs; (A) The temperature increases of DM-NCs dispersion (100 ng/mL, 1 μg/mL and 100 μg/mL) upon NIR illumination (808 nm, 0.5 W/cm^2, 15 min) were represented as function of time. The saline sample is considered as the control in the experiment; (B) The temperature increases and recovery phase pattern of DM-NCs (100 μg/mL) + NIR illumination for 15 min (ON) and 15 min (Off) cycle.

Photothermal conversion (PTC) capability is one of the characteristic features of the polydopamine, which upon absorption of the electromagnetic radiations in the NIR region, converts this radiation energy into heat energy.[291] PTC capability of polydopamine nanostructures expands its use as coating/component of another nanomaterial or as a core component for chemo/photothermal therapeutic agents.[16, 292-294] Moreover, the stability of the photothermal agent is one of the criteria of its translational potential during the multimodal application.[295] DM-NCs (100 μg/mL) under intermittent ON/Off NIR exposure cycle of 15 min each displayed continuous increase in the temperature up to ~46°C during ON cycle and spontaneously decrease down to ~35°C at the end of OFF

cycle. (Figure 6.21B). Meanwhile, the imaging of the DM-NCs dispersion in the NIR region further supports NIR responsiveness. Therefore, these observations confirmed that DM-NCs could exhibit a considerable photothermal effect in response to NIR illumination. The combined photodynamic (PD) and photothermal (PT) effect of the polydopamine matrix are well demonstrated in multiple disease models, but there is rare information whether the polydopamine matrix can trigger the release of the encapsulated drug upon NIR illumination. .[170, 241, 296] Based on the UV-vis results, it has been estimated that DM-NCs constituted ~53 % melatonin, which sustainably released it in the solution phase (cumulative percentage release = 58 %). While NIR illumination to DM-NCs packed in the dialysis tube triggered burst release with a total ~82% melatonin release in the solution (Figure 6.22). Thus, DM-NCs could exhibit both photothermal effect and NIR responsive release of the melatonin.

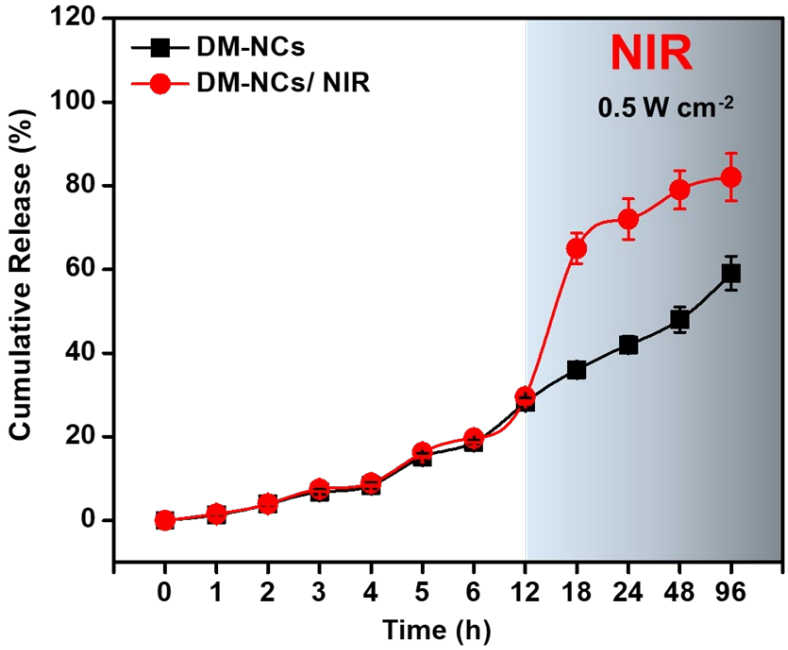

Figure 6.22. The NIR responsive melatonin release pattern showing the cumulative release of melatonin from DM-NCs without NIR and NIR irradiation.

2.2 Aβ anti-aggregation effect

Thioflavin-T (ThT) is a benzothiazole based fluorescent dye that has been widely used for probing amyloid fibrillation process in biophysical studies. It interacts explicitly at the quaternary beta rich amyloid fibrillar structure and emits strongly around ~490 nm upon excitation with ~440 nm light. The unbound ThT in aqueous buffer shows a weak fluorescence in the blue region around ~440 nm at an excitation wavelength of 350 nm. Based on these characteristics, this amyloid binding fluorescence dye has been used to

measure the aggregation kinetics of Aβ (1-42) peptide provided characteristic lag, exponential and stationary phase corresponds to nucleation, growth and saturated aggregation states.[297] Hence, the inhibitory effect of DM-NCs and DM-NCs + NIR on Aβ aggregation kinetics are studied using ThT assay. First, the control aggregation reaction was set up by incubating 10 μM Aβ with ThT in an aggregation buffer and monitored for time-dependent fluorescence emission intensity change. Unlike characteristic sigmoidal aggregation kinetic curve of unseeded Aβ (10 μM), Aβ (10 μM) monomer seeded with 0.2%, 1%, and 2% preformed Aβ fragments displayed seed concentration-dependent loss of lag phase with early saturation and fast Aβ aggregation kinetics. (Figure 6.23). These results validated that Aβ aggregation pathway can be recapitulated in cell-free environment using Aβ peptides, and self-seeding of Aβ monomers triggers the aggregation process. In the similar setup, the incubation of increasing concentration of DM-NCs of 1 *μ*g/mL and 100 *μ*g/mL drastically inhibited the exponential growth phase of the A*β* aggregation kinetics, which suggested that DM-NCs may interact with the A*β* oligomers and prevent the self-assembly process leading to early saturation (Figure 6.23B). However, only DM-NCs fail to stop the A*β* nucleation that may correspond to the A*β* oligomeric structure. The A*β* aggregation in the presence of DM-NCs and preoptimized single cycle of pulsed NIR (ON/OFF, 5 sec; 0.5 W/cm^2) exposure for 15 min appears with a significant reduction in the ThT fluorescence emission intensity. It can be seen that NIR induction completely abrogated the A*β* aggregation with loss of typical sigmoidal curve of A*β* aggregation kinetics (Figure 6.23C). This strong inhibitory efficacy of the DM-NCs may be due to synergistic melatonin associated inhibition of the peptide self-assembly and PTC effect of polydopamine triggering the disaggregation of preformed Aβ seeds. Importantly, under an optimized set of parameters DM-NCs and NIR exposure, we confirmed that ThT fluorescence remained unaffected in the multi-component environment. To confirm the inhibitory effect of DM-NCs, we further performed the TEM imaging of the Aβ fractions aliquoted at 24 h from control Aβ aggregation reaction displayed prominent and highly confined Aβ fibrils. (Figure 6.23D). The Aβ fraction incubated with DM-NCs was devoid of any intact fibrillar structure and showed amorphous deposits of A*β* oligomers under TEM. (Figure 6.23E). The DM-NCs exposure following NIR illumination to Aβ aggregation reaction leads to small clusters of Aβ peptide that appeared in the TEM micrograph (Figure 6.23F). Therefore, corroborating the ThT fluorescence emission results, these TEM observations further confirm that DM-NCs + NIR illumination can confer a superior Aβ anti-aggregation effect.

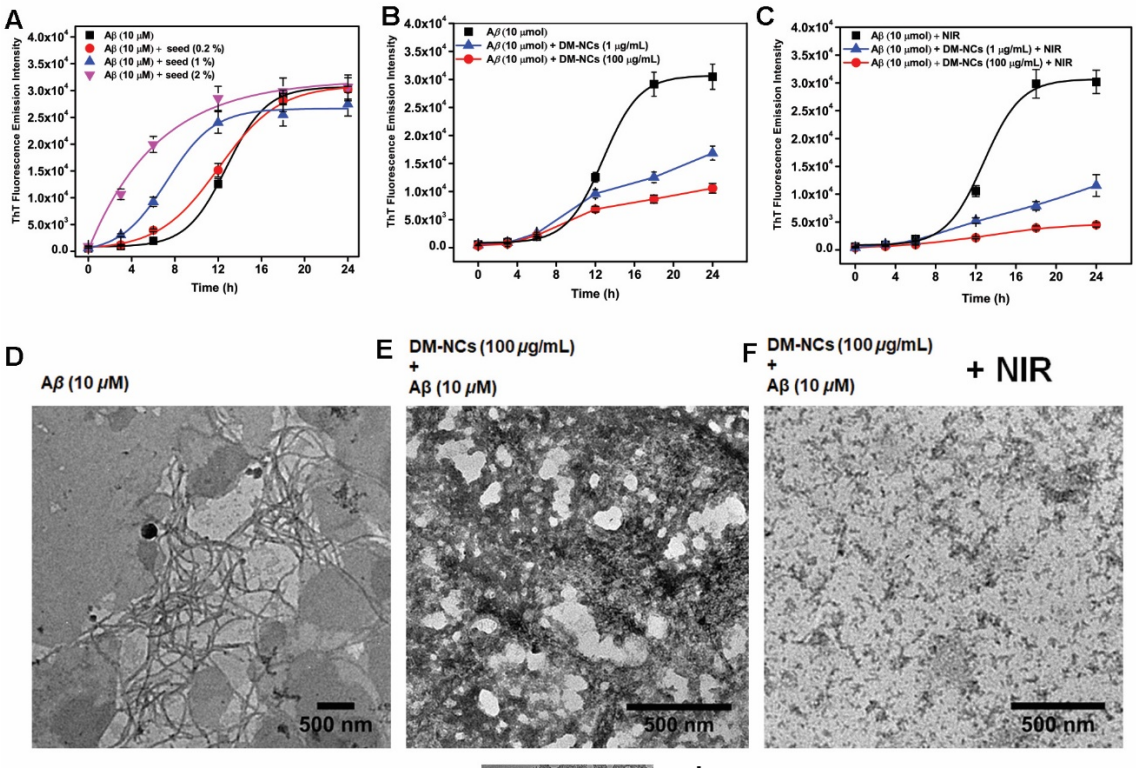

Figure 6.23. The NIR responsive Aβ anti-aggregation effect of DM-NCs; (A) The typical Aβ aggregation kinetics of Aβ1-42 recombinant peptide and seeded aggregation with 0.2%, 1 %, and 2% preformed Aβ fibrils incubation; (B) The Aβ aggregation kinetics in the presence of 1 μg/mL and 100 μg/mL DM-NCs; (C) The 1 μg/mL and 100 μg/mL DM-NCs changing the Aβ aggregation kinetics upon NIR irradiation. The aggregation Aβ aggregation kinetics were obtained by measuring the steady-state fluorescence emission intensity of the Thioflavin-T (ThT) dye; (D) TEM imaging of typical Aβ1-42 recombinant peptide fraction at 24 h of aggregation (E) in the presence of DM-NCs (100 μg/mL) and F) DM-NCs (100 μg/mL) +NIR illumination.

2.3 A*β* disaggregation effect

The A*β* fibrillation was achieved by diluting the A*β* monomer stock in the aggregation buffer for 48 h. The fibrillation was confirmed using relative ThT fluorescence of the aliquots. Next, we aimed to determine the in-vitro disaggregation effect of DM-NCs + NIR, that was performed considering the preformed A*β* fibrils and quantitated using ThT fluorescence emission intensity. The ThT results show that DM-NCs from 100 ng/mL and 1 *μ*g/mL displayed no significant disaggregation of these fibrils. In contrast, the highest concentration of 100 *μ*g/mL triggered a slight but insignificant decrease in the A*β* fibril content (Figure 6.21A). In next set of measurement, the DM-NCs with NIR illumination induced 20% of the A*β* fibrils disaggregation at 1 *μ*g/mL and ~ 40 % disaggregation of A*β* fibrils at highest 100 *μ*g/mL DM-NCs incubation (Figure 6.24B). Thus, DM-NCs photothermal effect can dis-integrate the preformed A*β* fibrils in cell-free conditions.

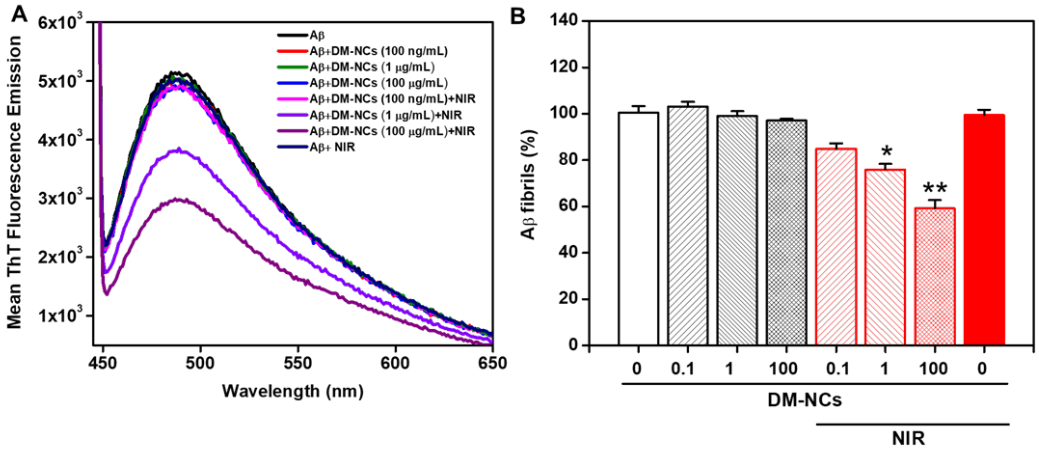

Figure 6.24. **The Aβ fibrils disaggregation by DM-NCs**s; (A) using ThT fluorescence emission spectrum for Aβ, Aβ in the presence of DM-NCs (100 ng/mL, 1 μg/mL and 100 μg/mL) and Aβ in presence of DM-NCs (100 ng/mL, 1 μg/mL and 100 μg/mL) +NIR in 50 mM Phosphate buffer (pH=7.2);(B) The ThT fluorescence emission intensity based quantitation of Aβ fibrils percentage were represented in bar diagram as mean ± SD and statistically compared using one way ANOVA following Tukey's test for mean comparison at **p<0.01 and * p< 0.05.

2.4 Aβ-Protein Misfolding Cyclic Amplification (Aβ-PMCA) Assay

In the last decade, the protein misfolding cyclic amplification (PMCA) assay emerged as a versatile and robust method in amyloid and prion biology in the aspect of both basic and clinical studies. This assay has the advantage of ultrasensitive screening of amyloids in biological samples. Aβ-PMCA assay was used for examining the effect of DM-NCs on the Aβ self-seeding and amyloidogenic propagation, where minute amount of preformed Aβ incubated in a cyclic manner with intermittent sonication step and proceeds for subsequent PMCA cycles.[298] This assay replicates relapsed nucleation based self-propagation of the Aβ is the cell-free condition as an economical and fast method to screen the impact of DM-NCs on Aβ propagation as depicted in Figure 6.25A-D. [299] Next, the ThT based quantitation upon DM-NCs incubation with Aβ following NIR exposure for 15 min (in each PMCA cycle) displayed a significant decrease in self-seeding and propagation of Aβ. Aβ -PMCA reaction seeded with 2 % Aβ + DM-NCs in each PMCA step displayed higher ThT fluorescence intensity compared to unseeded reaction (negative control), but significantly lower than that of seeded Aβ-PMCA (positive control). The TEM imaging of the Aβ recovered at 20th PMCA cycle displayed oligomeric and networked structure with no intact fibrillar Aβ indicates the complete abolishment of the self-propagation capability upon DM-NCs + NIR exposure (Figure 6.25B). The TEM imaging of Aβ sample collected at the end of 20th Aβ-PMCA cycle, displayed presence of weak and delicate fibrils of the Aβ could be due to considerable inhibitory effect of the DM-NCs alone (Figure 6.25C). Thus, Aβ-PMCA assay provided the compelling results confirms that DM-NCs+ NIR can effectively abolish the self-seeding capability and propagation of the Aβ.

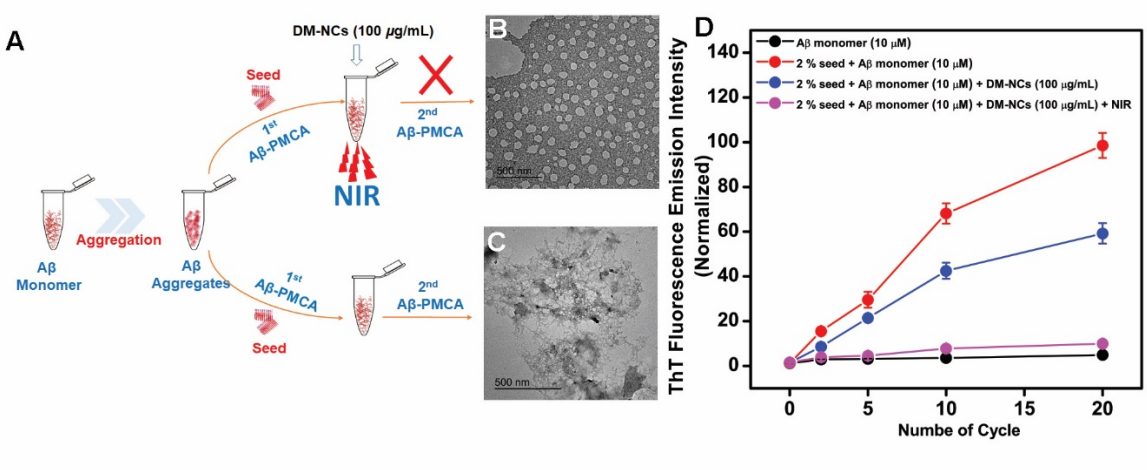

Figure 6.25. **Aβ-protein misfolding cyclic amplification (Aβ-PMCA) assay (A)**; (B) The TEM micrograph of the aggregates at 20th Aβ-PMCA cycle upon DM-NCs (100 μg/mL) +NIR illumination; (C) The TEM micrograph for typical Aβ-PMCA at 20th cycle; (D) The ThT fluorescence emission intensity measured at completion of each Aβ-PMCA cycle are represented.

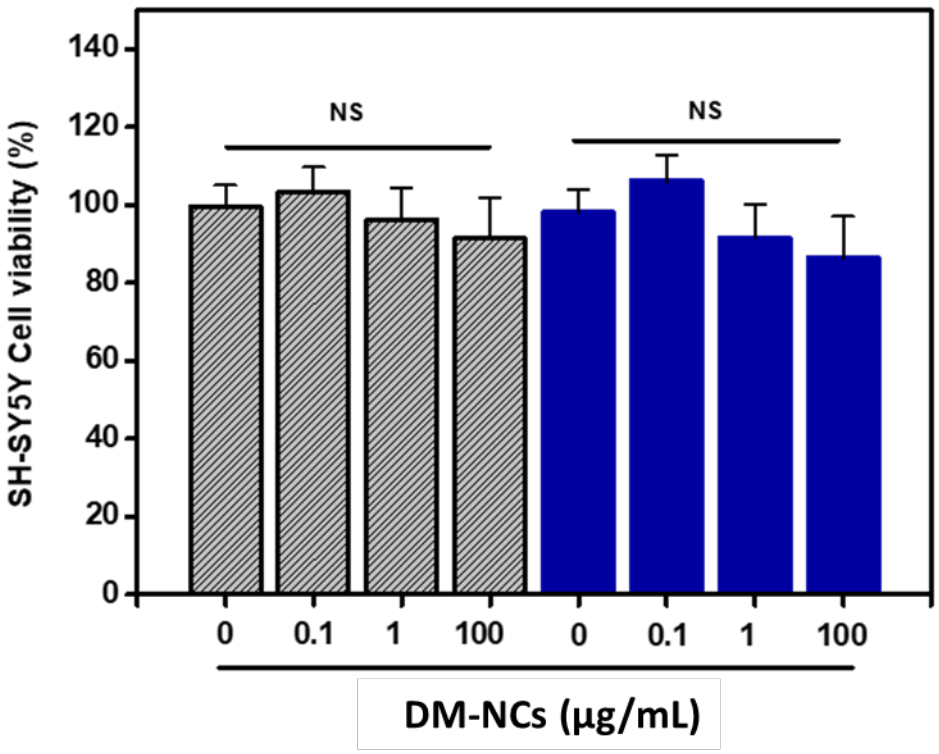

Figure 6.26. The SH-SY5Y cell viability measured using MTT assay; following exposure with DM-NCs (100 ng/mL, 1 μg/mL and 100 μg/mL) and DM-NCs (100 ng/mL, 1 μg/mL and 100 μg/mL) + NIR. The relative viability compared to untreated control is represented in bar diagram as mean ± SD and statistically compared using one-way ANOVA following Tukey's test for mean comparison.

2.5 Cell viability assay

The SH-SY5Y neuroblastoma cell line derived from neuronal lineage resembles phenotypic and differentiation characteristics of neuronal cells. This cell line has been frequently used for screening of the neurotoxins, and also established as a robust in-vitro AD model. The cell viability of SH-SY5Y cells was measured using MTT assay against DM-NCs and DM-NCs with NIR (On/OFF; 5 sec), only NIR (On/OFF; 5 sec) and phosphate buffer saline (PBS) exposure at a concentration ranging from 100 ng/mL to 100 μg/mL. The cell viability of SH-SY5Y cells against only NIR was evaluated to omit out the potential inhibitory or modulatory effect. The results showed no marked cytotoxicity induced by DM-NCs without and upon NIR illumination (NS at $^{**}p \leq 0.01$) (Figure 6.26). Thus, these results show higher biocompatibility of the DM-NCs to the SH-SY5Y cells may be due to NIR responsive intracellular release of encapsulated melatonin, providing cytoprotective effect in the cellular environment.

2.6 DM-NCs scavenge Intracellular ROS

The reactive oxygen species (ROS) play a central role in cellular oxidative homeostasis regulation, signaling cascades activation, and counterbalanced by the cellular antioxidant system.[300] The Number of investigations shows that the generation of multiple reactive oxygens and reactive nitrogen radicals produces cellular oxidative stress, which promotes neuroinflammation and leading to neurodegeneration.[301] The extent of ROS generation in the neuronal cells is used to evaluate the oxidative stress, which is playing a central role in AD pathogenesis and related etiology.[29] The intracellular ROS level can be estimated using fluorescence redox-active DCFH dye, which upon oxidation generates a highly fluorescent dichlorofluorescein emit at 530 nm. The flow-cytometry results displayed ~26 % increase in the ROS positive cells upon induction of AD pathology in SH-SY5Y cells (Figure 6.27A). The ROS positive population in DM-NCs + NIR exposed group was significantly lower (~8%) than that of only DM-NCs (~16%) and AD induced model (positive control) (Figure 6.27B-D). It is noteworthy that the weak fluorescence emission of DM-NCs in a similar channel was referenced to minimize the potential impact on DCFH fluorescence and redox stability. These results suggested that DM-NCs and DM-NCs following NIR exposure could significantly inhibit the AD-associated intracellular ROS generation. The NIR illumination at 808 nm may trigger the immediate intracellular release of the melatonin, which can robustly scavenge highly toxic hydroxyl radical (·OH), superoxide anion radical ($O_2^{\cdot -}$), peroxy radicals (ROO·), nitrogen-based free radicals and metabolize in N^1-acetyl-N^2-formyl-5-methoxykynuramine (AFMK), 3-hyroxymelatonin and 6-hydroxymelatonin.[302] Thus, consistent with our earlier DM-NCs integrity analysis, the enhanced ROS scavenging ability of DM-NCs upon NIR illumination demonstrates a neuroprotective potential against AD associated cellular damage.

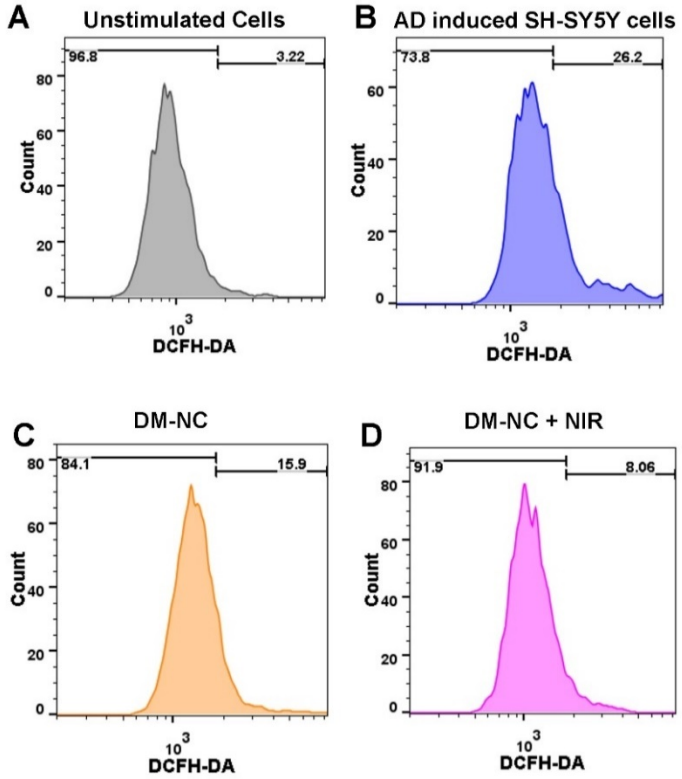

Figure 6.27. FACS based estimation of intracellular reactive oxygen species (ROS) on *in-vitro* AD model; (A) The flow cytometric measurement of the cellular ROS level by using H_2DCFA fluorescence for unstimulated control, okadaic acid (OA, 1 μM) induced SH-SY5Y cells, OA (1 μM) + DM-NCs (100 μg/mL) and OA (1 μM) + DM-NCs (100 μg/mL)+ NIR.

2.7 Compatibility to Neurite processes

The axon processes with multiple neurites outgrowth in the brain are for the precise connectivity among the cells for functional navigation. However, degeneration of these processes in the AD pathogenesis is the critical underlying cause of the behavior and cognitive deficit.[303] The differentiated human SH-SY5Y neuroblastoma cells represent a well-established model that has been used to screen the acute or chronic effects DM-NCs.[304] The well-differentiated axonal process was achieved upon retinoic acid (RA) exposure, which regulates the gene transcription nuclear retinoic acid receptor and promotes the neuronal differentiation. The complete loss of the axonal morphology was observed within 96 h of A*β* peptide exposure substantiated AD phenotype. Notably, DM-NCs confers negligible adverse effect on axonal processes observed for 15 days (Figure 6.28A). The mean axon length of the differentiated SH-SY5Y cells were reduced by 41±5 % and 64±7 % within 7 and 15 days upon DM-NCs exposure which is significantly more than that of measured for negative control group (Figure 6.28B). This result clearly shows the biocompatibility of the DM-NCs towards axonal processes of the neuronal cells.

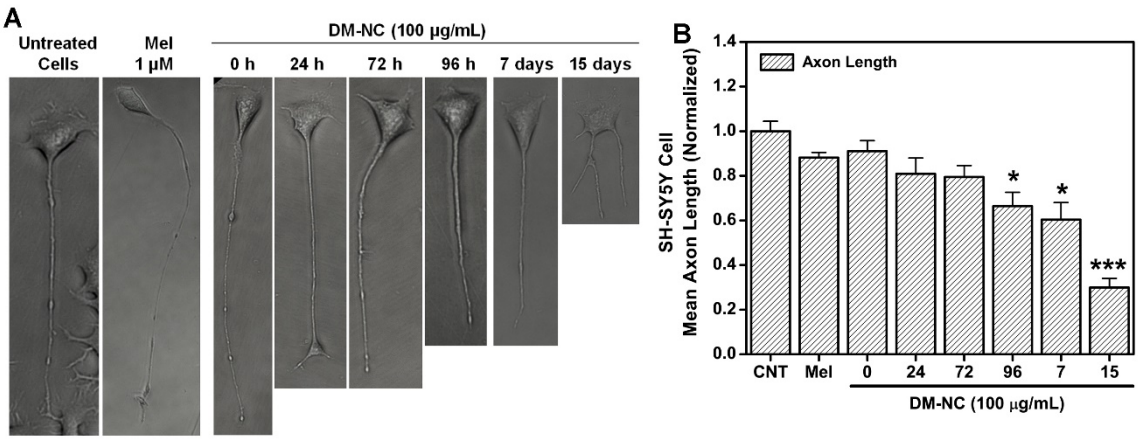

Figure 6.28. Axonal Differentiation Assay; (A) The differentiated SH-SY5Y cells with prominent axonal processes showing compatibility with DM-NCs (100 µg/mL) for 15 days; (B) The mean axonal length of the differentiated SH-SY5Y cells at different time point were represented as mean ± SD.

2.8 Estimation of *in-situ* Aβ Processing

Next, the impact of DM-NCs + NIR illumination on intracellular Aβ processing and accumulation in AD induced SH-SY5Y cells was examined using immunofluorescence studies. Consistent with the previous result, neuronal ROS is linked with the cellular processing of the amyloid precursor protein (APP), enhances the *β*-secretase activity, promotes oligomeric A*β* level and its localized deposition in the diverse brain region.[305] The confocal microscopic imaging shows enhanced intracellular processing of the Aβ protein and its cytoplasmic depositions in AD induced SH-SY5Y cells. The AD induced cells exposed with DM-NCs with and without NIR illumination shows a significant decrease in cellular Aβ level. Minimum cellular Aβ was evident in DM-NCs + NIR illuminated cells indicate that photothermal stimulation is critical for inhibitory effect. In contrast, DM-NCs without NIR fails to stop the cellular Aβ deposition (Figure 6.29). Thus, corroborating the earlier results, DM-NCs + NIR exposure can also regulate the intracellular A*β* processing and accumulations. It can probably be referred to two mutually exclusive processes of intracellular disintegration of DM-NCs releasing melatonin for collective anti-AD effect and PTC associated disruption of A*β* cytoplasmic inclusions present in close proximity of polydopamine matrix. Thus, neuro-compatible DM-NCs following NIR illumination could confer coupled in-situ A*β* anti-aggregation and disintegration associated with combined chemo-inhibitory, and photothermal effect collectively demonstrates a smart and multimodal strategy for AD therapy.

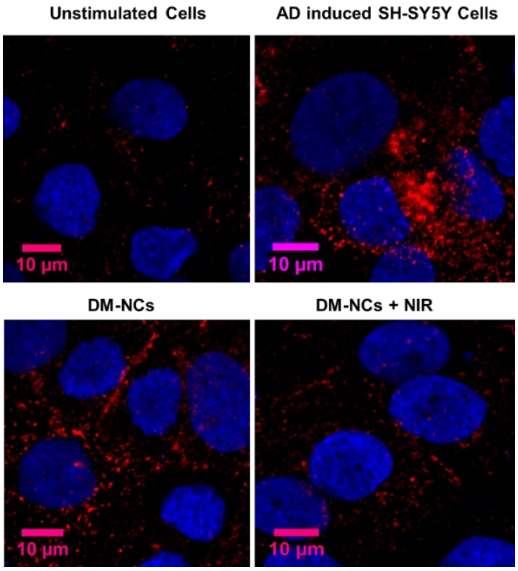

Figure 6.29. Lower Aβ processing in AD cellular model; The confocal image displaying immunofluorescence of cellular Aβ in unstimulated control cells, OA (1 µM) induced AD model, OA (1 µM) + DM-NCs (100 µg/mL) and OA (1 µM) + DM-NCs (100 µg/mL) + NIR irradiation. Scale bar = 10 µm.

2.9 Therapeutic assessment in mice mid-brain slice culture AD model

First, we established the *ex-vivo* adult mice midbrain slice culture (MBSC) based AD model following a previously reported protocol.[306] After 7 days of MBSC growth, it represented considerable morphological vitality and proceeded with exposure of okadaic acid (1 *µ*M, 12 h) for induction of AD phenotype. Following incubation, AD-induced MBSC was immunostained and imaged under a confocal laser scanning microscope (CLSM) showed increased A*β* positive cells with localized deposition of A*β* in the brain slice. The induction of AD in MBSC was obtained through okadaic acid associated PP2A inhibition, which suppresses the cellular phosphatase activity and promotes the tau associated A*β* deposition.[307, 308] This ex-vivo model has been used for the therapeutic assessment of potential drugs due to the ease of establishment, comparative results, and precise temporal observation. It recapitulates the pathological features of AD, such as deposition of senile plaque of transmembrane amyloid precursor protein A*β* and neurofibrillary tangles of axon specific microtubules associated tau proteins.[306, 309] The AD induced MBSC treated with DM-NCs for 96 h displayed significantly reduced A*β* processing and deposition. However, this inhibitory effect was more profound upon post-NIR illumination (Figure 6.30A). The AD induced MBSC displayed an increased association of intercellular adhesion molecule-1 (ICAM-1, also known as CD54) with deposited A*β* that can be linked to AD-associated microglial recruitment in the brain upon early onset.[310] However, the DM-NCs treatment following NIR illumination significantly reduced CD-54 expression that can relate to lesser microglial associated pathophysiology.[311]

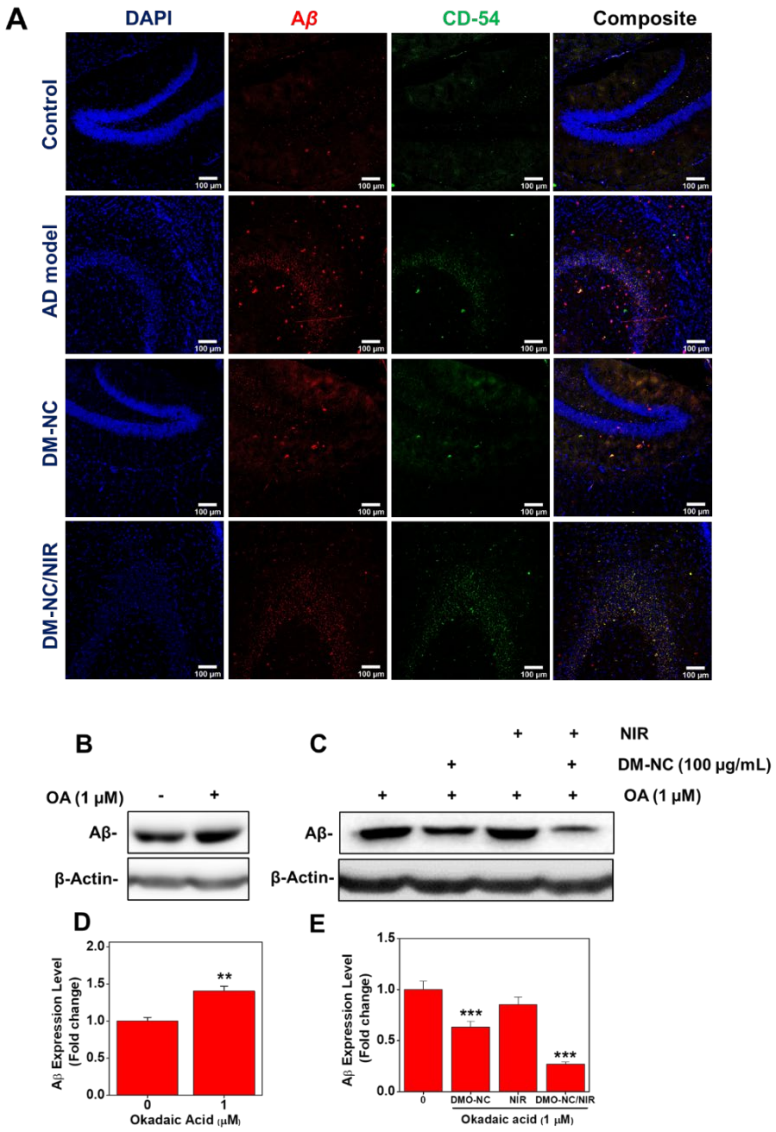

Figure 6.30. Therapeutic assessment in ex-vivo adult mice midbrain slice culture AD model; (A) The confocal image showing hippocampal region of adult mice midbrain slice culture, with immunofluorescence of DAPI (Blue, nuclear region), cellular Aβ (Red) and CD-54 (Green); Okadaic acid (OA, 1 μM) induced adult mice midbrain slice culture based AD model; cotreated with DM-NCs (100 μg/mL); and DM-NCs (100 μg/mL)+ NIR (808 nm, 0.5 W/cm^2) illumination. Scale bar = 100 μm. (B) The Western blot-based examination of the cellular Aβ protein upon OA (1 μM) exposure, (C) quantitatively showing a significant increase in the cellular Aβ level. D) The change in the Aβ protein in OA (1 μM) induced SH-SY5Y cells cotreated with DM-NCs (100 μg/mL), only exposed with NIR (808 nm, 0.5 W/cm^2) and DM-NCs (100 μg/mL) + NIR (808 nm, 0.5 W/cm^2) illumination.

Furthermore, the western blot-based protein examination confirms the increased cellular *β*-secretase activity and generation of A*β* fragments upon okadaic acid (1 *μ*M) exposure, which were 1.4± 0.1 (**p ≤ 0.01) times more than the unstimulated group (Figure 6.30B and 6.30D). The protein lysates from DM-NCs, NIR, and DM-NCs+NIR treated AD induced MBSC shows 36 ± 8 %, 14 ± 2 % and 73 ± 7 % decrease in the cellular A*β* level, respectively (Figure 6.30C and 6.30E). The DM-NCs treatment reduced the cellular A*β* level, but this decrease was significantly more profound upon post-NIR exposure (***p ≤

0.001). Control NIR exposure has not conferred any significant modulation in the A*β* level. Thus, the establishment of the *in-vitro* and *ex-vivo* experimental AD model advantageously validated the combined chemo-inhibitory and photothermal therapeutic efficacy of DM-NCs. Interestingly, DM-NCs conferred considerable therapeutic homogeneity both on *in-situ* and cell-free conditions via multimodal inhibition of A*β* associated pathophysiology. Therefore, DM-NCs with a combined pharmacological and photothermal modality demonstrates a potential for superior anti-AD therapy.

3. Conclusions

The dopamine/melatonin derived nanocomposites (DM-NCs), which was prepared by self-assembly of the dopamine derive intermediates and melatonin characterized for the morphology, structure, and integrity (Please see Chapter-3). In continuation, the present chapter detailed the DM-NCs as near-infrared (NIR) responsive photothermal agent. The photoconversion capability of the constituent polydopamine exhibits a highly stable photothermal effect. DM-NCs trigger burst release of the melatonin upon NIR induction and exhibits characteristic of the stimuli-responsive drug release system. DM-NCs with photothermal effect can prevent the A*β* aggregation, disintegrate preformed A*β* fibrils and halt A*β* propagation estimated using Thioflavin-T (ThT) and A*β*-protein misfolding cyclic amplification (PMCA) assay. These DM-NCs are highly biocompatible to the neuroblastoma cells and do not affect the neuronal cell survival and the neurite's processes. DM-NCs can regulate the in-situ amyloidogenic processing and reduce the intracellular A*β* depositions. Furthermore, the midbrain slice culture (MBSC) AD model confirms the therapeutic potential of DM-NCs, which upon NIR illumination control the AD-associated processing and accumulation of A*β* with lower recruitment of CD54 microglial cells in the hippocampal region. The anti-AD therapeutic efficacy is achieved by an underlying coupled mechanism that includes NIR responsive melatonin release in the proximity for multi-targeted pharmaco-inhibition synergize by photomodulatory photothermal conversion effect of matrix polydopamine. Thus, a new class of NIR responsive nanocomposites has been demonstrated for combined photothermal and chemo-inhibition based anti- AD therapy.

Note:

* The due permission has been obtained from authors and corresponding authors of the following published papers before adopting in the present thesis.

Near-Infrared Responsive Dopamine/Melatonin Derived Nanocomposites Abrogating In-situ Amyloid Beta Nucleation, Propagation and Ameliorate Neuronal Function. Anup K. Srivastava; S.R. Choudhury; S. Karmakar; **ACS Applied Materials and Interface**. 2020, 12, 5, 5658-5670.

Chapter 6c

Protein-nanoparticle corona-based fluorescence biosensor for sensitive detection of Amyloid-β protein

1. Background

The use of nanotechnology for developing the targeted drug-delivery vehicle, biosensing platforms, and diagnosis platforms became a reality within the last couple of decades. [312-314][315-318] It has a straightforward control perspective by which the physicochemical characteristics can be manipulated as a function of surface area and particle size diameter. Based on the fact these nanostructures with the active surface can interact with the surrounding entities, especially during drug delivery applications, their interaction with biological fluids is evident. It has been observed that many nanostructures undergo a complex interaction with biological components when administered in the bloodstream. Immediately upon interactions, these biological entities form a continuous layer on nanoparticle surface known as protein corona (PC).[319] The formation of PC changes the identity of functionalized nanostructures, which might lead to aggregation during circulation and change circulation time, affect the clearance rate, and further changes the *in-vivo* targeting efficacy. In the depth of PC, the Van der wals interaction, hydrophobic interaction, electrostatic interaction, hydrogen bonding, and pi-pi stacking control the layer composition on the surface of nanostructures.[320] Principally PC accompany multiple layers of proteins, the first layer bind with higher affinity as the hard corona, whereas the further protein-protein interaction accommodates the soft corona.[321, 322] One of the major contributions of surface charge, surface functionality, size, shape, surface roughness, curvature, and hydrophobicity of the nanostructures offer the compositional dynamics to protein corona.[317] Although the existence of the PC can be categorized as an interfacial phenomenon that more or less dependent on the affinity area. Whether pathological protein also forms the corona structure on the nanoparticle surface and misfolded conformations of these proteins affect the dynamics of corona structures that remain unanswered. Amyloid beta(Aβ) is a disordered protein implicated in Alzheimer's Disease (AD) exhibit as the monomer, soluble oligomer, aggregates and deposits as a senile plaque in the brain.[323] The fluorescent probe Thioflavin T (ThT) is often used for the detection of Aβ, conformations, rather has been found that it is ineffective in discriminating prefibrillar and fibrillar Aβ aggregates. [324] Recent advances have been made to quantify these Aβ conformations based on the small nanosized probes. Curcumin (1,7-bis(4-hydroxy-3-methoxyphenyl)-1, 6-heptadiene-3,5-dione) (Cur) is a chemically active small molecule, which can interact with multivalent metals, non-metals and other biomolecules with characteristic H-bond donating and accepting capacity of the β-dicarbonyl group, a terminal phenylic hydroxyl moiety and methoxy functional groups. [325] Lanthanum carbonate has been considered for its therapeutic potential of dietary phosphate- binding, thus used in the treatment of hyperphosphatemia,[326, 327] secondary hyperparathyroidisms,[328] and

chronic kidney diseases.[329, 330] The trivalent lanthanum ion interacts with curcumin and form a highly stable conjugate with enhanced photophysical characteristics, but there is no investigation has been made for interfacial interaction of lanthanum carbonate nanostructures (referred as REM_{100}) with curcumin. [331]

The present chapter details the construction of a hybrid Cur-REM_{100} fluorescent probe, which is formed by interfacial interaction of curcumin as hard corona on the REM100 surface. Cur-REM_{100} upon interaction with Casein, HSA, Lysozyme, and BSA, forms a long-lived soft corona on Cur-REM_{100} surface, giving a robust steady-state fluorescence enhancement of curcumin which can positively correlate the amount of adsorbed protein. The maximum surface coverage and apparent binding provided the factor to facilitate the protein adsorption on the developed probe. Further, we have estimated constrain in the dynamics of curcumin (hard corona) and protein (soft corona) in the Cas-Cur-REM_{100} complex. Cur-REM_{100} has shown differential interaction with Aβ conformations corroborated with a fluorescence emission intensity of Cur and it has been found that based on the fluorescence emission intensity, Aβ monomer and Aβ aggregates states can be quantitatively delineated. Thus, a nanoparticle corona based sensitive fluorometric tool has been demonstrated that can detect and delineate pathological Aβ conformations.

2. Results and Discussion

2.1 Synthesis and characterization of Lanthanum carbonate nanospheres (REM_{100})

As illustrated in Scheme 6.3**,** the Cur-REM_{100} comprises two parts, lanthanum carbonate nanospheres as the substrate and curcumin as fluorescence probe. The REM_{100} is the primary component that has been prepared using mixed sodium dodecyl sulfate (SDS) and cetyltrimethylammonium bromide (CTAB) surfactant-directed homogeneous precipitation method. It was essential to understand the mechanism and stability of the nano-spherical morphology, which was studied via precise monitoring of the surfactant concentration, pH, and water-surfactant ratio during the synthesis process. Unlike conventional homogenous precipitation, where carbonate ion and lanthanum precursor react immediately, give a turbid precipitate due to the fast nucleation process. However, in the present method, the rate of nucleation and precipitation can be dynamically controlled.

Importantly in our method, SDS/CTAB mix-surfactant is functioning as a structure-directing agent that controls the rate of nucleation and growth of the materials during the reaction process.

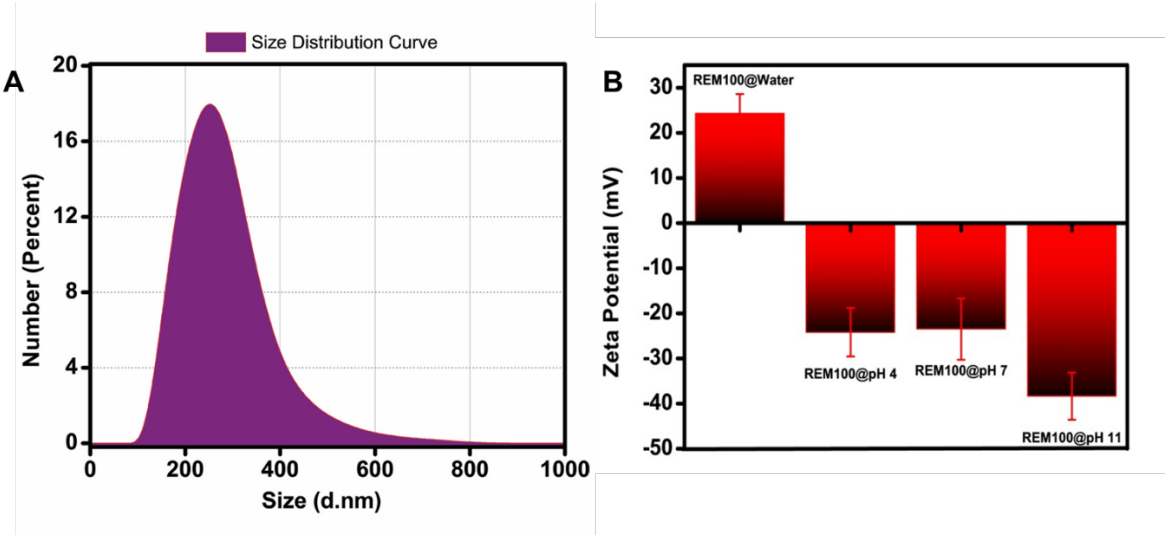

Figure 6.31. The particle size distribution and zeta potential of REM_{100}; (A) mean hydrodynamic size distribution cantered at ~250 nm; (B) The zeta potential value of REM_{100} in milliQ water, pH 4, pH 7 and pH 11.

The powdered REM_{100} was resuspended in ultrapure mill-Q water and subjected to mean hydrodynamic diameter measurement, which was centered around ~250 nm in the particle size distribution. (Figure 6.31A). The nano-bio complexion is an interfacial phenomenon which heavily dependent on the surface charges, thus surface zeta potential of REM_{100} was measured in milliQ and at variable pH. ζ potential value of REM_{100} in water was 24.3± 4.3 mV indicated the presence of a positive surface charge. This values were -24.2± 5.3 mV, -23.5± 6.8 mV and -38.4± 5.2 mV in 5 mM citrate buffer (pH 4), 5 mM Tris buffer (pH 7) and 5 mM bicarbonate buffer (pH 11), respectively (Figure 6.31B). REM_{100} contains both positive and negative surface charge gives a flexible surface charge characteristic which may be neutralized by the counterions present in the buffer of different pH and responsible for the drastic reversal of the surface ζ potential value.[332]

Lanthanum trivalent ion interacts with specific amino acids in protein via electrostatic bonding and leads to precipitation of whole protein. [333, 334] The analysis of the dispersed nanospheres under scanning electron microscopy (SEM) displayed the spherical and highly uniform morphology in the ~200-250 nm particle size diameter range (Figure 6.32A). The X-ray diffraction pattern (XRD) of REM_{100} showed that nanospheres predominantly composed of orthorhombic with kozoit like crystal parameter. The obtained major diffraction peaks at 20.40°, 23.76°,29.92°, 33.47°, 38.09°, 43.36° and 44.76° (±0.2°) were in good agreement with the deposited diffraction data (JCPDS Card No: 00-049-0981) The major diffraction intensity peak at 20.40°, and 23.76° 2θ suggested the surfactant-assisted growth of the single crystal in <110> and <111> direction (Figure 6.32B).

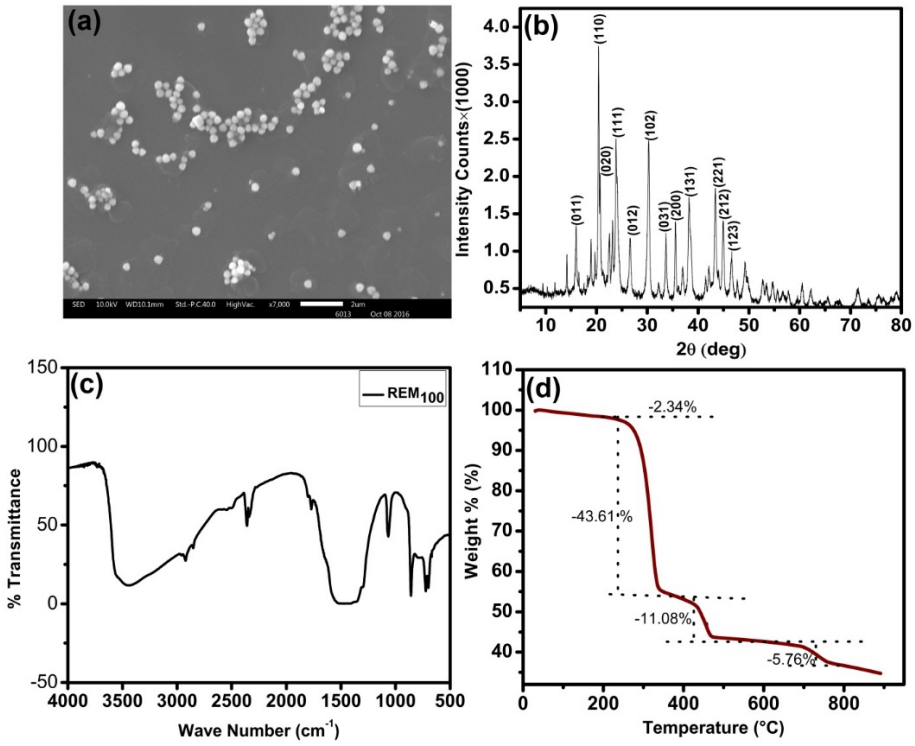

Figure 6.32. Morphological and structural characterization of REM_{100}; (A) Scanning electron micrograph; (B) The X-ray diffraction pattern; (C) The Fourier Transformed Infra-Red spectroscopic results; (D) The thermogravimetric analysis (TGA) curve of REM_{100}.

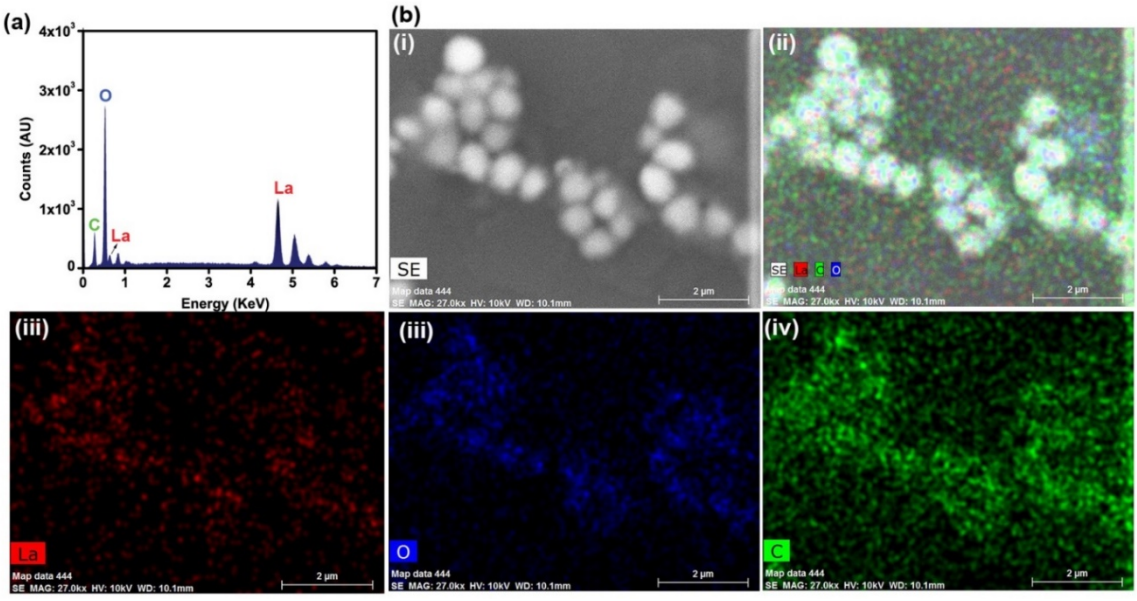

Figure 6.33. The energy-dispersive X-ray spectroscopy of REM_{100}; (A) Elemental spectrum with the corresponding peak of Carbon, Oxygen, and Lanthanum; (B) The elemental imaging of lanthanum (red), oxygen (blue) and carbon (green).

The thermostat step used in the preparation of REM_{100} was mainly to eliminate the surfactant content, and it was necessary to identify the purity of the prepared material for any residual presence of these surfactant moieties. Thus, functional group analysis was conducted using Fourier transformed infrared spectroscopy (FTIR) on the powdered REM_{100} samples. The results displayed the transmittance band at 860 cm^{-1} and 1088 cm^{-1} corresponds to an out of plane bending of (υ_2, $\pi(CO_3)$) and symmetric $\upsilon_s(CO)$, respectively. The characteristic broadening in the transmittance band in the range of 3100-3400 cm^{-1} can be linked to the stretching mode of $\upsilon(H_2O)$ (Figure 6.32C). It is imperative to define the stoichiometry and stability of the REM_{100}, thus thermal gravimetric analysis (TGA) has been performed taking powdered REM_{100}. TGA of REM_{100} showed the percentage weight loss in four steps ca 30-240 °C (Weight loss =2.34%), ca 240-400 °C (Weight loss =43.61%), ca 400-605 °C (Weight loss =11.08%) and ca 605-790 °C (Weight loss =5.76%) (Figure 6.32D). The structural directing agents of complementary ionic nature used in REM_{100} synthesis may undergo precipitation and can contaminate the obtained $RM_{100.}$ Thus, the elemental composition of the REM_{100} has been verified using semi-quantitative elemental analysis using energy-dispersive X-ray spectroscopy (EDX) given stoichiometry of Lanthanum, Oxygen, and Carbon with the mass percentage of 61.90, 30.55 and 7.54 that were in good agreements to lanthanum carbonate materials (Figure 6.33A and 6.33B).

2.2 REM_{100} and curcumin interaction

The previous section detailed the preparation and characterization of $REM_{100,}$ which is a component used as a substrate in the present work. Here, the interaction between curcumin and REM_{100} were analysed using the component concentration-dependent change in the absorbance of curcumin, which was measured using UV-vis spectrum. The aqueous solution of curcumin displayed the characteristic spectrum with maximum absorbance intensity at λ_{max}= 430 nm, whereas only REM_{100} displayed no absorbance either in UV or visible range (Figure 6.34D). 1.2 mM REM_{100} incubated with increasing concentration of curcumin (25 µM to 250 µM) obtained with a gradual increase in absorbance maxima (λ_{max}) of curcumin. (Figure 6.34A and 6.34B). The linear regression curve fit of the absorbance at 430 nm shows the nonlinear increase in the absorbance of curcumin in Cur-REM_{100} compared to the only Cur, which primarily suggests the interaction of Cur with REM_{100} (Figure 6.34C). The concentration of the curcumin in the present experiment has been considered based on the absorbance maxima range of 0.2 to 1.2 achieved with the 25 µM to 250 µM concentration, respectively. On the other hand, the fixed concentration of 120 µM curcumin incubated with varying 240 µM to 2.20 mM REM_{100} displayed the progressive concentration-independent linear increase in the absorbance of curcumin (Figure 6.34E and 6.34F). These results indicate that the surface area of REM_{100} is a crucial factor, which can

accommodate the particular concentration of the Cur. The interaction between Cur and REM_{100} was further confirmed using the FTIR study. The characteristic $–CO_3$ associated transmittance band such as v_1 symmetric CO_3 (1060 cm^{-1}), v_3 asymmetric CO_3 (1406 cm^{-1}) and v_4 symmetric CO_3 (744 cm^{-1}) observed with slight shifts may be due to non-covalent interaction of curcumin with these functional groups (Figure 6.35A). These interactions also appeared in the zeta potential change, where the REM_{100} displayed the positive values, which were negative for the pure curcumin. However, a similar concentration of REM_{100} and Cur in mixed state exhibited comparatively less negative zeta potential. Therefore, these results support the interfacial interaction of Cur with REM_{100} that were stabilized by both electrostatic and non-covalent interactions.

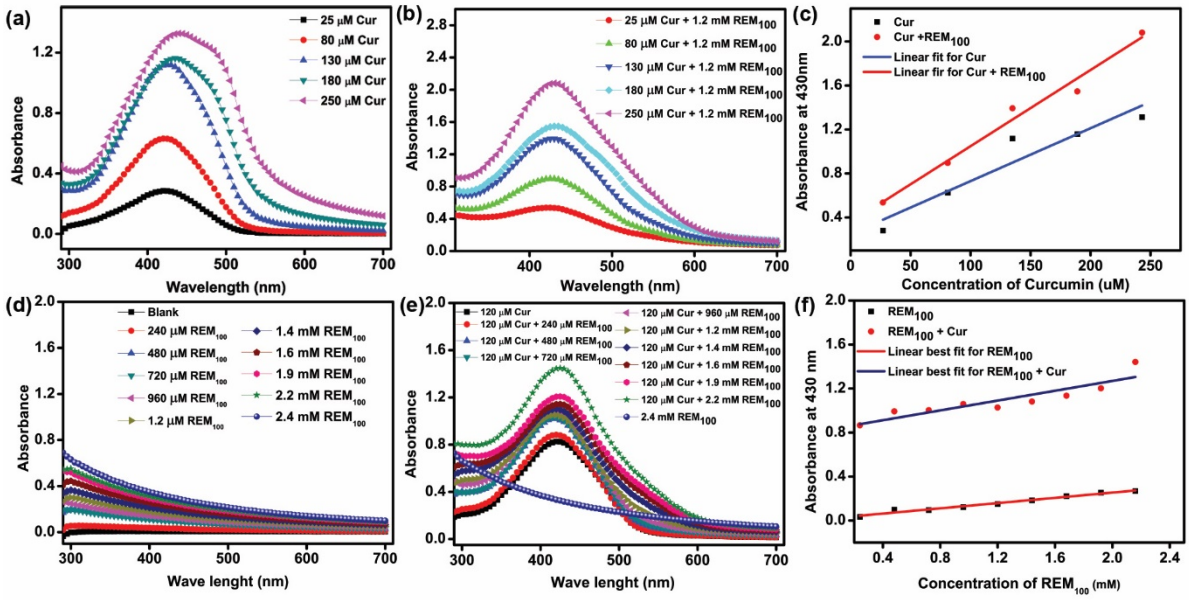

Figure 6.34 The UV-vis studies of curcumin- REM_{100} interaction; **(A)** The absorbance of Cur (λ_{max}= 430 nm) from 25 µM to 250 µM concentration; **(B)** 25 µM to 250 µM Cur incubated with REM_{100} (1.2 mM); **(C)** Absorbance intensity versus Cur concentration plot at fixed REM_{100}; **(D)** No absorbance peak of REM_{100} from 240 µM to 2.4 mM; **(E)** Absorbance peak change of 120 µM Cur incubated with REM_{100} from 240 µM to 2.4 mM; **(F)** Absorbance intensity versus Cur concentration plot at fixed Cur.

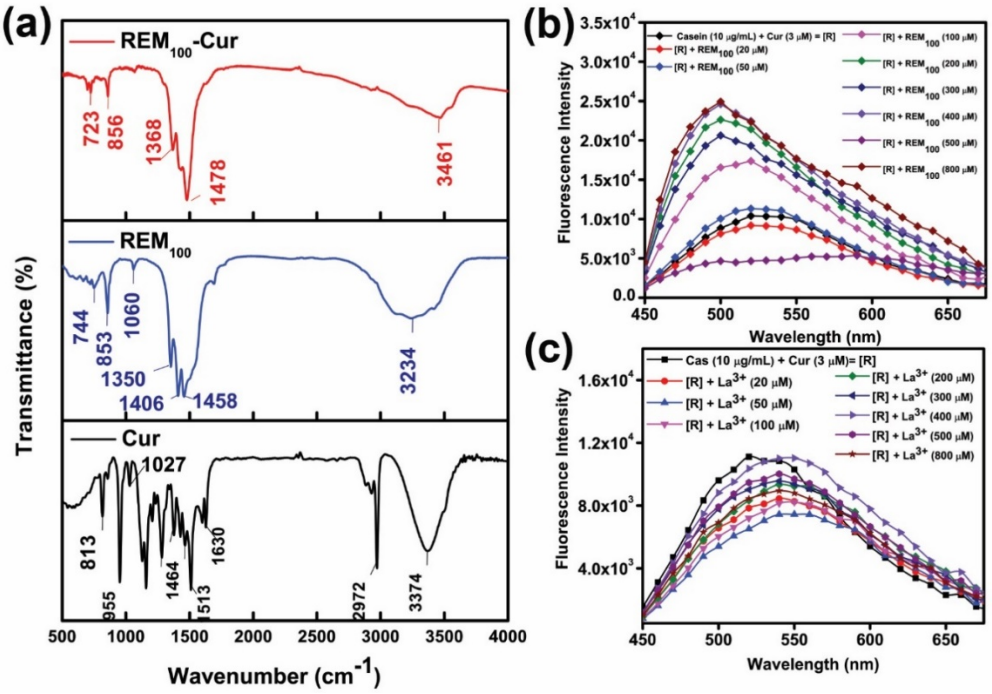

Figure 6.35 The Fourier Transformed Infra-Red (FTIR) and fluorescence emission spectroscopic results for Cur and REM_{100} interaction; (A) The FTIR transmittance peaks of Cur-REM_{100}, REM_{100} and Cur; (B) fluorescence emission spectrum of Casein-Cur-REM_{100} (C) Casein-Cur-La^{+3}

The steady-state fluorescence emission measurement of curcumin was performed for Cur-REM_{100} and Cur-La+3 with fixed Cur and increasing REM_{100} and La3+ concentration. The results displayed that the nanomaterials characteristics and surface properties are a major factor for the fluorescence enhancement of curcumin in casein-curcumin-REM_{100}, which has not been observed in casein-curcumin-La^{3+}. The fluorescence emission intensity versus REM_{100}/ La^{+3} plot displayed the continuous increase in the fluorescence intensity was saturated at a particular concentration of the materials. This result supports our hypothesis of the formation of a uniform, long-lived, and stable layer of curcumin over REM_{100}, which can be referred as the hard corona. The slight blue shift in the fluorescence emission peak of Cur with increasing concentration of REM_{100} suggests the change in solvent microenvironment promotes H-aggregation of the curcumin on the REM_{100} surface, which can be linked to the negative solvatochromism and hypsochromic shift from 550 nm to 500 nm. [325]

2.3 Protein adsorption on Cur-REM_{100}

As in the previous section, the formation of the hard corona of the curcumin on the REM_{100} was estimated in the presence of a residual concentration of the protein, where the concentration of the nanosphere played a critical role. Next, the capability of Cur-REM_{100} probe to accommodate the range of protein on the surface were estimated using the steady-state fluorescence emission of the Cur upon increasing concentration (5 μg/mL to 800

μg/mL) of Casein, HSA, Lysozyme, and BSA in Protein-Cur-REM_{100} complex (Figure 6.36A-D). The distinct fluorescence emission peak of the Cur-REM_{100} with the continuous increase in the intensity was obtained as a function of incubated protein concentration. The maximum fluorescence intensity (λ_{em}=500 nm) of these peaks was plotted as a function of the equilibrium concentration of the proteins and fitted to the Langmuir adsorption model. These plots suggested the occurrence of two major probable phenomena the appearance of the initial steep of the curve may be due to stronger protein to Cur-REM_{100} surface affinity, and the plateau phase appears in the curve suggests the saturation of the nanosphere surface due to formation of a continuous monolayer of protein over the Cur-REM_{100}.

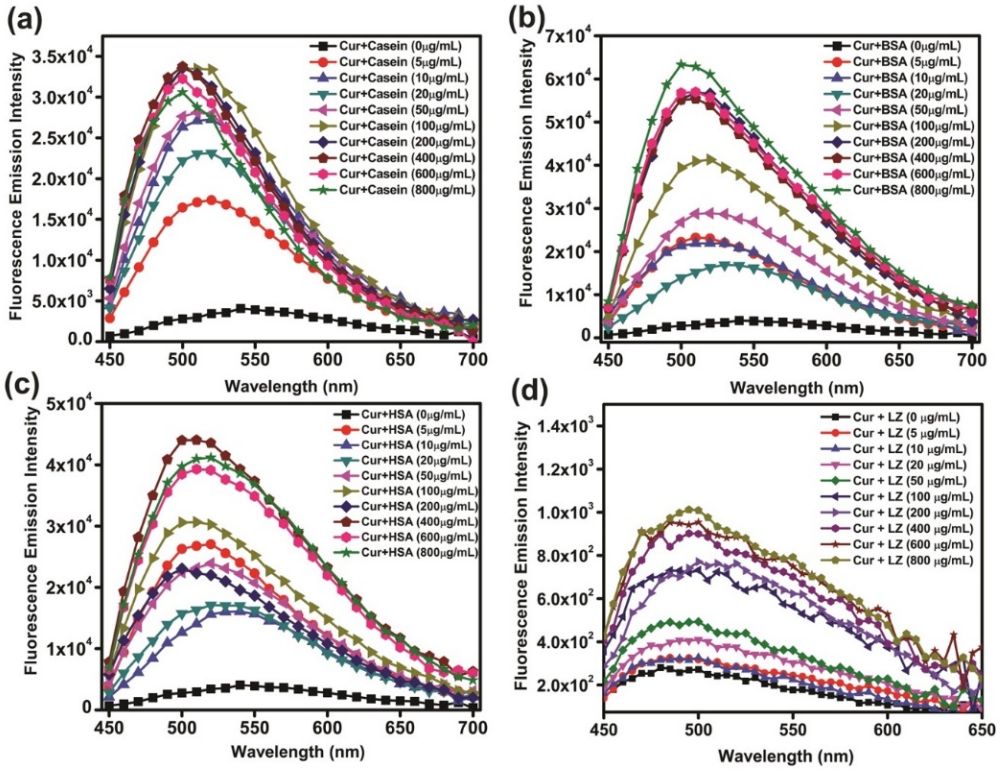

Figure 6.36 The steady-state fluorescence spectrum measurement of Protein-Cur-REM_{100}. (A) Casein, (B) BSA, **(C)** HSA **(D)** Lysozyme. The protein concentration from 5 μg/mL to 800 μg/mL in protein-cur-REM_{100}. The excitation wavelength 415 nm (λ_{ex}= 415 nm) and emission collected from 450 nm to 700 nm.

Based on the fitting parameter, maximum surface coverage (Γ_{max}) was estimated for 99.14 μg/m^2, 123.80 μg/m^2, 98.11 μg/m^2 and 105.10 μg/m^2 for casein, HSA, Lysozyme, and BSA respectively (Figure 6.37A). The apparent dissociation constant (K) of the 6.05 μg/ml, 112.5 μg/ml,85.12 μg/ml and 85.7 μg/ml were obtained for casein, HSA, Lysozyme, and BSA respectively (Figure 6.37A). The possibility of change in the native protein structures that may be due to local unfolding of the secondary structures cannot be ignored. However, our assumption for Langmuir adsorption model fitting omits the effect of such lateral

alterations. Next, the plot represented in Figure 6.37B obtained by fitting the fluorescence emission intensity of the protein from a minimum 5 µg/ml to a maximum of 800 µg/ml concentration. The Hill coefficient estimated for these proteins suggested positive cooperativity with h value of 0.83, 1.02 and 0.87 for Casein, Lysozyme, and HSA, respectively. The hill plot of BSA with a coefficient of 0.47 displayed the negative cooperativity. These results suggested the existence of protein monolayer on Cu-REM$_{100}$ surface with the possibility of crowding and concomitant steric hindrance may also occur at higher protein concentrations.[335]

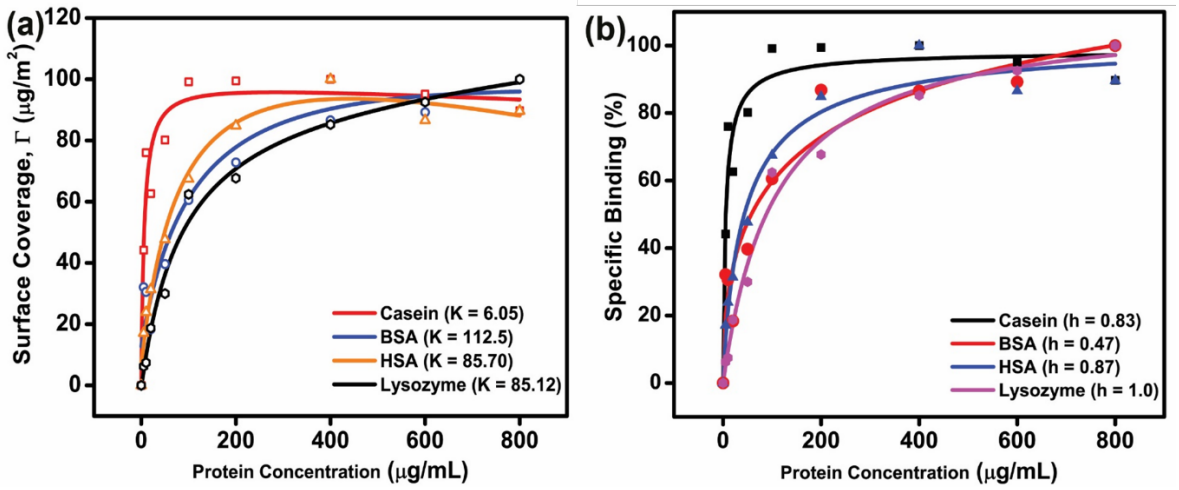

Figure 6.37. The maximum surface coverage and specific biding of proteins on Cur-REM$_{100}$. (.A) The Langmuir model shows maximum surface coverage and apparent dissociation constant; (B) Hill plot with Hill coefficient for each protein. The Casein (red), BSA (blue), HSA (orange) and Lysozyme (Black) from 5µg/mL to 800 µg/mL concentration in Protein-Cur-REM$_{100}$.

2.4 Confirmation of Protein-Cur-REM$_{100}$

Our earlier result strongly supports the existence of the hard corona of Cur on REM$_{100}$ (Cur-REM$_{100}$) and further accommodates the soft corona layer of protein (protein-cur-REM$_{100}$). Among the range of protein considered in the study, casein demonstrated highest, and BSA offered the least interaction in Protein-Cur-REM$_{100}$. Furthermore, spatial and conformational dynamics of curcumin and casein in the Protein-Cur-REM$_{100}$ system were measured using steady-state fluorescence anisotropy. Fluorescence anisotropy (r) is a direct estimate of the angular correlation between the excitation and emission transition dipoles. In general principle, under constraint dynamics, the fluorophore fails to get excited and observed with a change in the anisotropy value within a range of 0.4 to -0.2 corresponds to the collinear and orthogonal excitations. In our results, the increase in fluorescence anisotropy (r) value from 0.05± 0.01 to 0.14± 0.02 was seen for casein in free aqueous state and casein-REM$_{100}$

(Figure 6.38), compared to free translational motion of casein protein in solution phase. It undergoes spatial constraints upon REM_{100} surface binding. The increase in the anisotropy(r) value of Cur in Casein-Cur-REM_{100} and Cur-REM_{100} was observed, which suggests that Cur undergo constraint for translational and angular displacements.

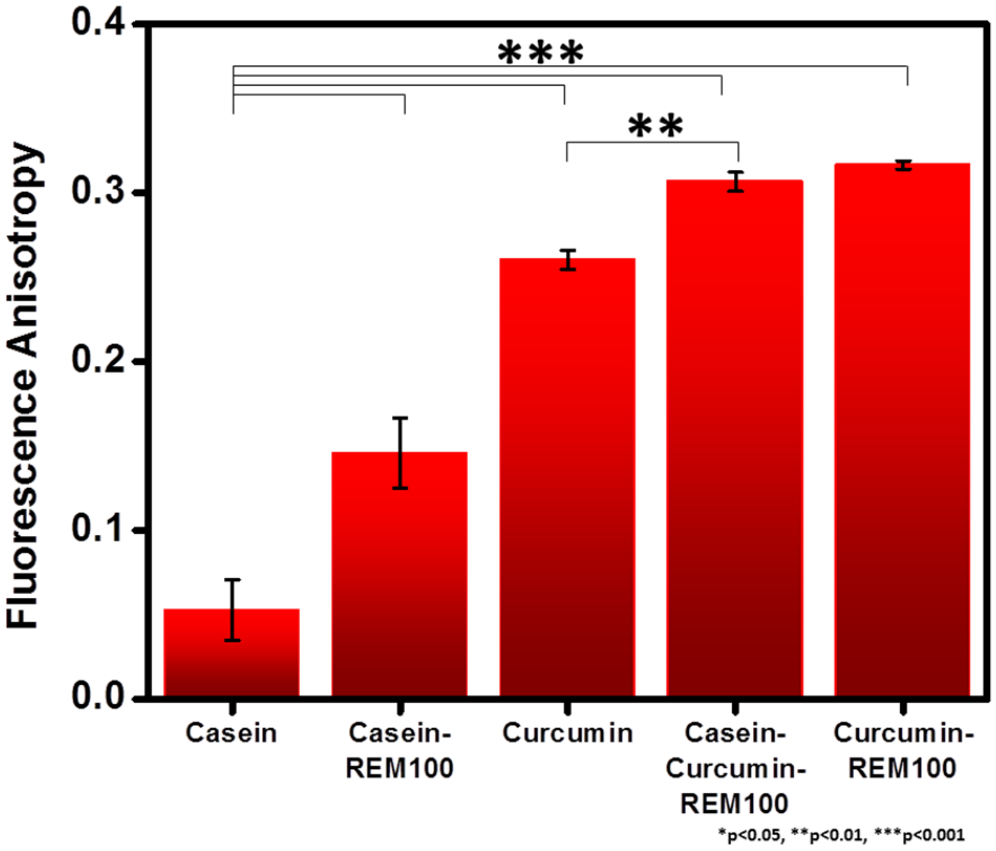

Figure 3.38. The steady-state fluorescence anisotropy measurement. The fluorescence anisotropy value (r) represented as mean ±SD for Casein and Casein-REM100; for Cur, Casein-Cur-REM_{100} and Cur-REM_{100}. The mean was compared for significance using one-way ANOVA with Tukey's test.

Thus, these results confirm that Cur and Casein protein undergoing spatial binding on the REM_{100} surface. Corroborating our earlier results, it can be concluded that the synchronous strong ionic and non-covalent interactions between Cur and REM_{100} in Cur-REM_{100} allow the formation of a hard corona layer of Cur on the REM_{100} surface. Furthermore, the non-covalent and hydrophobic interactions between casein and Cur-REM_{100} in Casein-Cur-REM_{100} accommodates this protein on the Cur-REM_{100} surface as highly dynamic soft corona layer. Based on overall results, it can be emphasized that Casein-Cur-REM_{100} comprises the hard corona layer of Cur tethering between protein and nanoparticles and also emerged as PC based fluorescence probe can be further developed as biosensors for multiple biomedical applications.

2.5 Detection of Aβ conformations

The pathophysiology of the AD implicates the deposition of Aβ as senile plaque, which has been observed in the AD patient brain during the histopathological investigation. The progressive process of the Aβ pathology makes early detection cumbersome, and existing practices involve the symptomatic test associated with a cognitive response, memory and behavioral changes of the afflicted patients.[336] Presently, the positron emission tomography (PET) and another variant of the nuclear imaging employed at the symptomatic stage, thus an approach of detecting this disease at early onset, is warranted.[337] The Aβ binding probes such as chrysamine G, pinacynaol and Thioflavin-T have been used to detect and image the Aβ dynamics, suffers from low signal/background ratio and insufficiency of detecting all the Aβ conformational states.[338] Based on this information, we further expected that Cur-REM_{100} might also interact with Aβ protein and provide similar outcomes as investigated for other proteins, but it was interesting to use this probe for discriminating monomer and aggregated Aβ state. The Aβ monomer and Aβ fibrillar state was prepared separately and quantitated. Next, increasing concentration of these proteins in different states form 10 nM to 10 μM were incubated with the prepared Cur-REM_{100} probe and the steady-state fluorescence emission intensity of Cur has been recorded for all the concentration**.** It can be seen that at highest concentration of 10 μM, Aβ aggregates in $Aβ_{agg}$-Cur-REM_{100} displayed ~18 times more intensity compared equal concentration of Aβ monomer $Aβ_{mono}$-Cur-REM_{100} (Figure 6.39A). It my be possible that Aβ encounters slight unfolding or aggregation upon nanostructures surface interactions which may alters exact estimation during fluorescence emission intensity measurement. In the control experiment, we observed a negligible change in the Aβ conformations on REM_{100} might be due to higher surface curvature and nanoparticle diameter, which comply the earlier theoretical and experimental validation that particle size in 70 – 200 nm diameter range confers minimum effect on the native structures of adsorbed proteins.[339] Our earlier FTIR and zeta potential results support the electrostatic and non-covalent interactions among Cur and REM_{100}, mask the possibility of nanoparticle and Aβ protein interaction and the exposed hydrophobic region of the Cur possibly the major interactions between adsorbing protein and Cur in the Aβ-Cur-REM_{100} system. Indeed, the highest fluorescence enhancement of $Aβ_{agg}$-Cur-REM_{100} may be due to transient hydrophobic interaction between $Aβ_{agg,}$ and Cur mediates non-polar environment or intermolecular energy transfer in $Aβ_{agg}$-Cur-$REM_{100.}$ [340] The thioflavin-T (ThT) has been recognized with the most frequently used fluorescent probe for quantification of Aβ which heavily dependent on the protein/probe ration, optimal concentration and the condition that do not alter the conformational state of the Aβ. Thus, robustness and sensitivity of the Cur-REM_{100} were compared to the ThT in Aβ-Cur-REM_{100}

and Aβ-ThT system in such a way that the concentration of both ThT and Cur remained 3 μM upon incubation with a range of $Aβ_{agg}$ and $Aβ_{mono}$ concentrations. It has been found out that at optimal parameter a ~30-fold sensitivity of Cur-REM_{100} towards $Aβ_{agg}$ with a limit of detection (LOD) of 0.2 ±0.045 μM was estimated compared to ThT (Figure 6.39B). Thus, protein-Cur-REM_{100} is a small molecule tethered nanoparticle corona-based fluorescence biosensor which can detect and delineate the pathological states of the Aβ protein at early onset of AD.

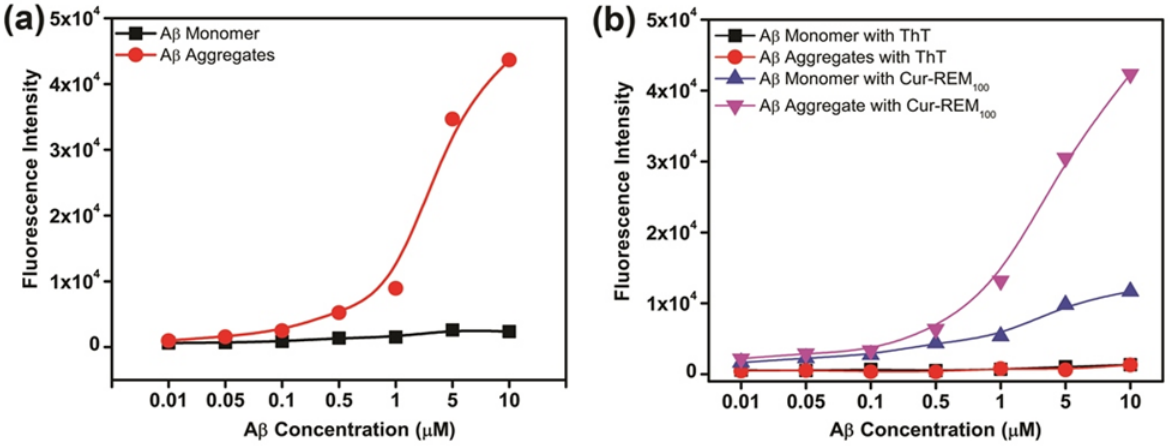

Figure 3.39 Fluorescence-based detection of the Aβ monomer and Aβ aggregates. (A) The fluorescence emission intensity of varying concentration of Aβ aggregates and Aβ monomer with Cur-REM_{100}, (B) the fluorescence emission intensity of Aβ aggregates and Aβ monomer incubated with Cur-REM_{100} and thioflavin-T (ThT).

3. Conclusion

In the present chapter, we have shown the preparation of the lanthanum carbonate nanosphere (REM_{100}) using a new mix surfactant-assisted synthesis methodology. The prepared REM_{100} has been characterized for the mean particle size, the spherical and highly uniform morphology, flexible surface charge behavior, stoichiometry and elemental composition. REM_{100} displayed robust binding to the small molecule curcumin (Cur) and based on the UV-vis, steady-state fluorescence and steady-state fluorescence anisotropy results, it was confirmed that Cur forms a hard corona layer over the REM_{100} surface (Cur-REM_{100}). Cur-REM_{100} as the stable fluorescent probe can interact and allow other proteins such as Casein, BSA, HSA and Lysozyme to form a soft corona (Protein-Cur-REM100) on the surface. The fluorescence enhancement of curcumin in Protein-Cur-REM_{100} complex was correlated with the concentration of protein adsorb in the soft corona layer, and based on it, the maximum surface coverage and specific binding have been estimated using Langmuir model. For the first time, Protein-Cur-REM_{100} based protein nanoparticle corona system is demonstrated for diagnostics of pathological proteins. The robust design of this

probe allows it to differentially interact with amyloid-beta (Aβ) conformations and distinctly offered ~30-fold sensitivity compared to commonly used fluorescence dye.

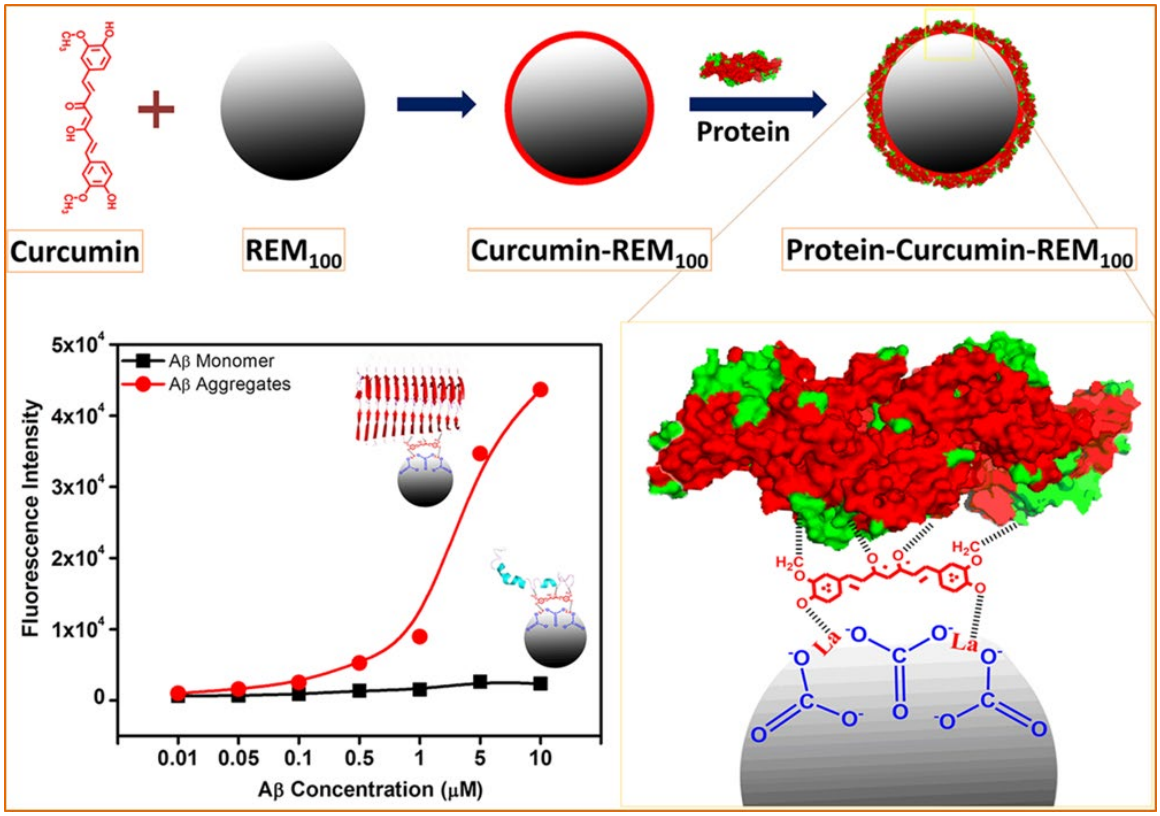

Scheme 6.3 The illustration represents the fabrication of Cur-REM$_{100}$ as a protein nanoparticle corona-based biosensor for the detection of the Aβ monomer, and Aβ aggregated states.

Note:

* The due permission has been obtained from co-authors and corresponding authors of the following published paper before adopting in the present thesis.

- New insight into curcumin tethered lanthanum carbonate nanospheres and protein corona conferring fluorescence enhancement based sensitive detection of Amyloid-β aggregates. A. K. Srivastava; A. Dev; S.R. Choudhury; S. Karmakar **Sensors and Actuators B**: **Chemical**. 2018;262(1)

Summary

Summary

Parkinson's disease (PD) and Alzheimer's disease (AD) associated neurodegeneration are start with slow but progressive loss of neuroanatomical structures and functions in the elderly population hampering the healthy livelihood of people.[20] The causal factor of these diseases are best investigated using amyloid hypothesis, where two proteins alpha-synuclein (in PD) and amyloid-beta (Aβ) (in AD) abruptly change structural conformations and with cascade of oligomeric, protofibrils, fibrillar structure, deposit as Lewy body (PD) and senile plaques (AD) in brain. [54, 55, 96, 97] The pathobiology of both the neurodegenerative diseases involves the typical sequel of reactive oxygen species generation, oxidative stress, mitochondrial damage, induction of apoptosis and inflammation and neuronal cell death. [102] In-depth reviews of the literature, detailed the regulation of key pathways controlling progression of these devastating diseases. The pharmacological targeting of the BACE-1 mediated amyloidogenic pathway provides promising response and rescue the AD-associated cognition and behaviour changes. [59] The complex Aβ aggregation cascades of nucleation, aggregation and propagation are one of the prime targets to control the progression of this debilitating disease. Multiple anti-aggregation agents and beta-sheet breakers demonstrated the therapeutic efficacy in AD. [71] The alpha-synuclein (α-SYN) phosphorylation at serine 129 position is clinically associated with the disease severity and established as one of the biomarkers of PD. [99, 100] The pathobiology of α-SYN involves the molecular sequel of neuroinflammation, ER stress, loss of unfolded protein response system, dysfunctional ubiquitin-mediated proteasomal degradation pathway and damaged autophagy-lysosomal pathway. [106, 109-111] The risk factor of PD is largely unknown; however the role of epigenetic polycomb group of protein (PcG) subunit BMI-1 has been investigated for the neuroprotective signaling in neurodegeneration.[126] The polycomb repressor complex-1 subunit BMI-1 regulates oxidative and mitochondrial stress and anti-oxidant response gene repression in neuronal cells. [128] However, lower expression and canonical E3 ligase function of PRC-1 subunit BMI-1 have been linked to PD, but whether BMI-1 is directly or indirectly regulates α-SYN associated pathobiology is not yet investigated. [132] The nanocarrier mediated neurotherapeutic delivery and diagnostics platform have innovated this area, however recent efforts are made for developing these nanocarriers from biological origins.[139]

Dopamine derived polydopamine nanostructures exhibit excellent biocompatibility and nanocarrier characteristics. [16] Considering these information variants of melatonin/polydopamine nanostructures prepared by considering the variable ratio of dopamine and melatonin. The physicochemical, morphological and structural characterization suggests that the relative abundance of melatonin plays a crucial role in

determining the characteristics of the obtained nanostructures. These melatonin/polydopamine structures are categorized in; melatonin loaded polydopamine nanoparticles (referred as mPDAN or MEPN), melatonin/dopamine nanocomposites (DM-NCs) and quantum sized dots (DI-10). These nanostructures constitute a significant amount of melatonin that released in a sustainable and prolonged pattern. The crucial non-covalent interaction between melatonin and dopamine oxidative intermediates during the oxidation reaction is the underlying evolution mechanism that also stabilizes these nanostructures. These nanostructures can withstand a physiologically stressed environment without any change in integrity.

The mPDAN confers significant neuroprotection efficacy and rescues the neuroblastoma cell death on *in-vitro* PD models. It can frequently internalize in the neuroblastoma monolayer and three-dimension culture and can confer superior anti-oxidant function, protect mitochondrial membrane potential loss, prevent caspase-3 dependent apoptosis pathways activation and induce an anti-inflammatory response. mPDAN after exposure to *in-vitro, ex-vivo and in-vivo* PD models suppresses the level of pα-SYN(S129) monomer and its cellular oligomerization as high molecular weight (HMW) oligomers. These observations indicate the superior neuroprotection efficacy of the mPDAN that specifically reduce the cellular level of pα-SYN(S129) in multiple PD model. The time-dependent accumulation of mPDAN in the mice brain indicates that it can retain in the brain tissue without any marked morphological damage and non-specific toxicity to the other organs. It prevents the pathological accumulation of the pα-SYN(S129) in hippocampal (HIP) of the brain and also protects the PD associated dopaminergic neuronal cell loss. Thus, in these assessments, mPDAN proves to be superior therapeutics which can easily localize in the brain and protect the dopaminergic neuronal loss with a reduced level of pα-SYN(S129).

Next, the induction of PD substantiates the lower expression of PRC-1 complex subunit BMI-1, thus observed with lower monoubiquitinates at histone 2A at the K119 position (H2AK119ub). PD associated hyperphosphorylation of BMI-1 at serine residues could downregulate the canonical functions. The polycomb E3 ligase function regulated by BMI-1 is severely affected in PD with lower H2AK119ub modification. Our nanoformulation provided a protective role and maintained the cellular level of both BMI-1 and H2AK119ub with a reduced level of pα-SYN (S129) on *in-vitro* and *in-vivo* PD models. Interestingly, we find that the neuroprotective function of our treatment turns ineffective upon cellular BMI-1 depletion and failed to clear the oligomeric alpha-synuclein indicates that BMI-1 is critical for therapeutic efficacy. The increased ubiquitination of pα-SYN (S129) and ubiquitin-dependent proteasomal degradation is the mechanism of clearance which surprisingly associated with the BMI-1. These results provide a significant understanding and the role

of epigenetic BMI-1 in the therapeutic regulation pα-SYN (S129) that can develop as a therapeutic target in PD.

The increased vulnerability of the dopaminergic neurons in the devastating pathobiology of the neurodegeneration requires the precise monitoring of the cellular and molecular components. To screen the neuroblastoma cell status, a highly biocompatible, dopamine-based quantum sized dot referred as DI-10 has been used. DI-10 demonstrates for full wavelength fluorescence emission is used for bio-imaging applications and confers higher cellular biocompatibility and distribution on *in-vivo*. The preoptimized concentration of DI-10 can easily discriminate against the healthy neuroblastoma and non-viable neuronal cell in mixed populations. Thus, DI-10 as a bioimaging agent can be used as a flow cytometry fluorescence probe.

The dopamine/melatonin nanocomposites (DM-NCs) displayed a characteristic of a stable photothermal agent and a smart NIR responsive drug delivery system. NIR responsive DM-NCs confers significant Aβ anti-aggregation and dis-aggregation characteristics in both cell-free system and in-situ experimental AD model. It can also prevent the self-propagation and reseeding capability of Aβ. Upon NIR pulsed response DM-NCs reduces the AD associate cellular ROS level and the intracellular processing of Aβ. It is highly compatible to neuronal cells with no inhibitory effect on the cellular processes. Furthermore, it displayed a strong anti-AD effect on the *ex-vivo* AD model with decreased recruitment of the microglial population in the brain area. The NIR responsive DM-NCs confers combined photothermal and chemo-inhibitory regulation of AD pathophysiology.

The highly complicated process of the Aβ pathology makes the diagnosis of disease cumbersome and requires a highly promising tool to detect it at on early onset. However, lower signal/background ratio and incompatibility to Aβ conformational dynamics are associated limitations of presently used approaches. Thus, in our approach, the Cur-REM_{100} has been prepared based on the interfacial non-covalent interaction between the lanthanum carbonate substrate and curcumin. The curcumin as stable hard corona layer over REM_{100} surface can further accommodate the layers of proteins as the soft corona and extent of protein in soft corona can be detected via relative fluorescence emission of the curcumin. The Cur-REM_{100} fluorescence probe conferred higher sensitivity towards Aβ protein and can delineate the monomer and the aggregated states of Amyloid-β. Thus, the nano-bio complexion-based fluorescence biosensor can easily discriminate the Aβ conformational state in Alzheimer's disease.

Taken together, this thesis outlines the newer approach of developing range of bioinspired nanostructures, displayed superior neurotherapeutic efficacy and also demonstrated for

biosensing potential in neurodegenerative diseases. Exploring the epigenetic pathways in neurodegeneration, we feel that further newer targets may be identified for understanding of the underlying pathways. Addition to, present knowledge of the neurodegeneration pathology, therapeutic efficacy and diagnostics approach, understanding of these fundamental interplays has revealed the new epigenetic target to move forward in the field of Neurobiology.

References

References

1. Lebouvier, T., et al., *The second brain and Parkinson's disease.* European Journal of Neuroscience, 2009. **30**(5): p. 735-741.
2. Nichols, E., et al., *Global, regional, and national burden of Alzheimer's disease and other dementias, 1990-2013;2016: a systematic analysis for the Global Burden of disease Study 2016.* The Lancet Neurology, 2019. **18**(1): p. 88-106.
3. Spillantini, M.G., et al., *Alpha-Synuclein in Lewy bodies.* Nature, 1997. **388**(6645): p. 839-40.
4. McCann, H., et al., *alpha-Synucleinopathy phenotypes.* Parkinsonism Relat Disord, 2014. **20 Suppl 1**: p. S62-7.
5. Sato, H., T. Kato, and S. Arawaka, *The role of Ser129 phosphorylation of alpha-Synuclein in neurodegeneration of Parkinson's disease: a review of in vivo models.* Rev Neurosci, 2013. **24**(2): p. 115-23.
6. Oueslati, A., *Implication of alpha-Synuclein phosphorylation at S129 in Synuclein opathies: What have we learned in the last decade?* J Parkinsons Dis, 2016. **6**(1): p. 39-51.
7. Fujiwara, H., et al., *alpha-Synuclein is phosphorylated in Synucleinopathy lesions.* Nat Cell Biol, 2002. **4**(2): p. 160-4.
8. Okochi, M., et al., *Constitutive phosphorylation of the Parkinson's disease associated alpha-Synuclein .* J Biol Chem, 2000. **275**(1): p. 390-7.
9. Alghamdi, B.S., *The neuroprotective role of melatonin in neurological disorders.* J Neurosci Res, 2018. **96**(7): p. 1136-1149.
10. Ferrazzoli, D., et al., *Dopamine replacement therapy, learning and reward prediction in parkinson's disease: Implications for rehabilitation.* Frontiers in behavioral neuroscience, 2016. **10**: p. 121-121.
11. Peters, J.L., et al., *Modulation of intercellular calcium signaling by melatonin in avian and mammalian astrocytes is brain region-specific.* The Journal of comparative neurology, 2005. **493**(3): p. 370-380.
12. Chuang, J.I., et al., *Melatonin prevents the dynamin-related protein 1-dependent mitochondrial fission and oxidative insult in the cortical neurons after 1-methyl-4-phenylpyridinium treatment.* J Pineal Res, 2016. **61**(2): p. 230-40.
13. Liu, X., et al., *Mussel-inspired polydopamine: a biocompatible and ultrastable coating for nanoparticles in vivo.* ACS Nano, 2013. **7**(10): p. 9384-95.
14. Haber, S.N., *The place of dopamine in the cortico-basal ganglia circuit.* Neuroscience, 2014. **282**: p. 248-257.
15. Kiehn, O., *Decoding the organization of spinal circuits that control locomotion.* Nature reviews. Neuroscience, 2016. **17**(4): p. 224-238.
16. Tiwari, A.P., et al., *Polydopamine-based implantable multifunctional nanocarpet for highly efficient photothermal-chemo therapy.* Sci Rep, 2019. **9**(1): p. 2943.
17. Wang, Y., et al., *Phosphorylated α-Synuclein in Parkinson's disease.* Science translational medicine, 2012. **4**(121): p. 121ra20-121ra20.
18. Molofsky, A.V., et al., *Bmi-1 dependence distinguishes neural stem cell self-renewal from progenitor proliferation.* Nature, 2003. **425**(6961): p. 962-967.
19. Wyss-Coray, T., *Ageing, neurodegeneration and brain rejuvenation.* Nature, 2016. **539**(7628): p. 180-186.
20. Chakrabarti, S. and K.P. Mohanakumar, *Aging and Neurodegeneration: A Tangle of Models and Mechanisms.* Aging and disease, 2016. **7**(2): p. 111-113.
21. Cespedes, M.I., et al., *Comparisons of neurodegeneration over time between healthy ageing and Alzheimer's disease cohorts via Bayesian inference.* BMJ Open, 2017. **7**(2): p. e012174.

22. Moya-Alvarado, G., et al., N*eurodegeneration and Alzheimer's disease (ad). What can proteomics tell us about the Alzheimer's brain?* Molecular & cellular proteomics : MCP, 2016. **15**(2): p. 409-425.
23. Hague, S.M., S. Klaffke, and O. Bandmann, *Neurodegenerative disorders: Parkinson's disease and Huntington's disease.* Journal of Neurology, Neurosurgery & Psychiatry, 2005. **76**(8): p. 1058.
24. Bano, D., et al., *Neurodegenerative processes in Huntington's disease.* Cell death & disease, 2011. **2**(11): p. e228-e228.
25. Cluskey, S. and D.B. Ramsden, *Mechanisms of neurodegeneration in amyotrophic lateral sclerosis.* Molecular pathology : MP, 2001. **54**(6): p. 386-392.
26. Salas-Vargas, J., et al., *Spinocerebellar ataxia type 7: A neurodegenerative disorder with peripheral neuropathy.* European Neurology, 2015. **73**(3-4): p. 173-178.
27. Mukherjee, S., et al., *A microglial signature directing human aging and neurodegeneration-related gene networks.* Frontiers in Neuroscience, 2019. **13**(2).
28. Galvan, A. and T. Wichmann, *Pathophysiology of parkinsonism.* Clinical neurophysiology : official journal of the International Federation of Clinical Neurophysiology, 2008. **119**(7): p. 1459-1474.
29. Cheignon, C., et al., *Oxidative stress and the amyloid beta peptide in Alzheimer's disease.* Redox biology, 2018. **14**: p. 450-464.
30. Murphy, M.P. and H. LeVine, 3rd, *Alzheimer's disease and the amyloid-beta peptide.* Journal of Alzheimer's disease : JAD, 2010. **19**(1): p. 311-323.
31. Braskie, M.N. and P.M. Thompson, *Understanding cognitive deficits in Alzheimer's disease based on neuroimaging findings.* Trends in cognitive sciences, 2013. **17**(10): p. 510-516.
32. Zhao, Q., et al., *Cognitive decline in patients with Alzheimer's disease and its related factors in a memory clinic setting, Shanghai, China.* PLOS ONE, 2014. **9**(4): p. e95755.
33. Du, X., X. Wang, and M. Geng, *Alzheimer's disease hypothesis and related therapies.* Translational neurodegeneration, 2018. **7**: p. 2-2.
34. Edwards, F.A., *A unifying hypothesis for Alzheimer's disease: from plaques to neurodegeneration.* Trends in Neurosciences, 2019. **42**(5): p. 310-322.
35. Yang, H.D., et al., *History of Alzheimer's disease.* dementia and neurocognitive disorders, 2016. **15**(4): p. 115-121.
36. Nicoll, J.A.R., et al., *Cerebral amyloid angiopathy plays a direct role in the pathogenesis of Alzheimer's disease: Pro-CAA position statement.* Neurobiology of Aging, 2004. **25**(5): p. 589-597.
37. Criscuolo, C., et al., *Entorhinal Cortex dysfunction can be rescued by inhibition of microglial RAGE in an Alzheimer's disease mouse model.* Scientific Reports, 2017. **7**(1): p. 42370.
38. Grace, E.A., C.A. Rabiner, and J. Busciglio, *Characterization of neuronal dystrophy induced by fibrillar amyloid β: implications for Alzheimer's disease.* Neuroscience, 2002. **114**(1): p. 265-273.
39. Kashyap, G., et al., *Synapse loss and progress of Alzheimer's disease -A network model.* Scientific Reports, 2019. **9**(1): p. 6555.
40. Stefan, F.L., *Alpha-secretase cleavage of the amyloid precursor protein: proteolysis regulated by signaling pathways and protein trafficking.* Current Alzheimer Research, 2012. **9**(2): p. 165-177.
41. Selkoe, D.J. and J. Hardy, *The amyloid hypothesis of Alzheimer's disease at 25 years.* EMBO Molecular Medicine, 2016. **8**(6): p. 595-608.
42. Das, B. and R. Yan, *Role of BACE1 in Alzheimer's synaptic function.* Translational neurodegeneration, 2017. **6**: p. 23-23.

43. Cole, S.L. and R. Vassar, *The Alzheimer's disease β-secretase enzyme, BACE1.* Molecular Neurodegeneration, 2007. **2**(1): p. 22.

44. Ruiz-Riquelme, A., et al., *Prion-like propagation of β-amyloid aggregates in the absence of APP overexpression.* Acta neuropathologica communications, 2018. **6**(1): p. 26-26.

45. Sardar Sinha, M., et al., *Alzheimer's disease pathology propagation by exosomes containing toxic amyloid-beta oligomers.* Acta neuropathologica, 2018. **136**(1): p. 41-56.

46. Sowade, R.F. and T.R. Jahn, *Seed-induced acceleration of amyloid-β mediated neurotoxicity in vivo.* Nature Communications, 2017. **8**(1): p. 512.

47. Tycko, R., *Molecular structure of aggregated amyloid-β: insights from solid-state nuclear magnetic resonance.* Cold Spring Harbor perspectives in medicine, 2016. **6**(8): p. a024083.

48. Chen, G.-f., et al., *Amyloid beta: structure, biology and structure-based therapeutic development.* Acta Pharmacologica Sinica, 2017. **38**(9): p. 1205-1235.

49. Rezaei-Ghaleh, N., et al., *Interaction between amyloid beta peptide and an aggregation blocker peptide mimicking islet amyloid polypeptide.* PLOS ONE, 2011. **6**(5): p. e20289.

50. Swerdlow, R.H., *Mitochondria and mitochondrial cascades in Alzheimer's disease.* Journal of Alzheimer's disease : JAD, 2018. **62**(3): p. 1403-1416.

51. Kinney, J.W., et al., *Inflammation as a central mechanism in Alzheimer's disease.* Alzheimer's & dementia (New York, N. Y.), 2018. **4**: p. 575-590.

52. Pocernich, C.B. and D.A. Butterfield, *Elevation of glutathione as a therapeutic strategy in Alzheimer disease.* Biochimica et Biophysica Acta (BBA) - Molecular Basis of disease, 2012. **1822**(5): p. 625-630.

53. Grant, B.D. and J.G. Donaldson, *Pathways and mechanisms of endocytic recycling.* Nature reviews. Molecular cell biology, 2009. **10**(9): p. 597-608.

54. El-Amouri, S.S., et al., *Neprilysin: an enzyme candidate to slow the progression of Alzheimer's disease.* The American journal of pathology, 2008. **172**(5): p. 1342-1354.

55. Qiu, W.Q. and M.F. Folstein, *Insulin, insulin-degrading enzyme and amyloid-β peptide in Alzheimer's disease: review and hypothesis.* Neurobiology of Aging, 2006. **27**(2): p. 190-198.

56. Jiang, L., et al., *Exosomes in pathogenesis, diagnosis, and treatment of Alzheimer's disease.* medical science monitor : international medical journal of experimental and clinical research, 2019. **25**: p. 3329-3335.

57. Xiao, T., et al., *The role of exosomes in the pathogenesis of Alzheimer' disease.* Translational neurodegeneration, 2017. **6**: p. 3-3.

58. Vassar, R., *The β-secretase, BACE.* Journal of Molecular Neuroscience, 2001. **17**(2): p. 157-170.

59. Amakiri, N., et al., *Amyloid beta and micrornas in Alzheimer's disease.* Front Neurosci, 2019. **13**: p. 430.

60. MacLeod, R., et al., *The role and therapeutic targeting of α-, β- and γ-secretase in Alzheimer's disease.* Future science OA, 2015. **1**(3): p. FSO11-FSO11.

61. Marcade, M., et al., *Etazolate, a neuroprotective drug linking GABAA receptor pharmacology to amyloid precursor protein processing.* Journal of Neurochemistry, 2008. **106**(1): p. 392-404.

62. Nelson, T.J., et al., *Bryostatin effects on cognitive function and pkcε in Alzheimer's disease phase iia and expanded access trials.* Journal of Alzheimer's disease : JAD, 2017. **58**(2): p. 521-535.

63. Devi, L., J. Tang, and M. Ohno, *Beneficial effects of the β-secretase inhibitor GRL-8234 in 5XFAD Alzheimer's transgenic mice lessen during disease progression.* Current Alzheimer research, 2015. **12**(1): p. 13-21.

64. Chang, W.-P., et al., *In vivo inhibition of Aβ production by memapsin 2 (β-secretase) inhibitors.* Journal of Neurochemistry, 2004. **89**(6): p. 1409-1416.

65. Fukumoto, H., et al., *A noncompetitive BACE1 inhibitor TAK-070 ameliorates Abeta pathology and behavioral deficits in a mouse model of Alzheimer's disease.* The Journal of neuroscience : the official journal of the Society for Neuroscience, 2010. **30**(33): p. 11157-11166.

66. May, P.C., et al., *The potent BACE1 inhibitor LY2886721 elicits robust central Aβ pharmacodynamic responses in mice, dogs, and humans.* The Journal of neuroscience : the official journal of the Society for Neuroscience, 2015. **35**(3): p. 1199-1210.

67. Ma, T., et al., *Inhibition of AMP-activated protein kinase signaling alleviates impairments in hippocampal synaptic plasticity induced by amyloid β.* The Journal of neuroscience : the official journal of the Society for Neuroscience, 2014. **34**(36): p. 12230-12238.

68. Giorgetti, S., et al., *Targeting amyloid aggregation: an overview of strategies and mechanisms.* International journal of molecular sciences, 2018. **19**(9): p. 2677.

69. Lu, J., et al., *Structure-based peptide inhibitor design of amyloid-β aggregation.* Frontiers in Molecular Neuroscience, 2019. **12**(54).

70. Viet, M.H., et al., *Inhibition of aggregation of amyloid peptides by beta-sheet breaker peptides and their binding affinity.* The Journal of Physical Chemistry B, 2011. **115**(22): p. 7433-7446.

71. Hoyer, W., et al., *Stabilization of a beta-hairpin in monomeric Alzheimer's amyloid-beta peptide inhibits amyloid formation.* Proceedings of the National Academy of Sciences of the United States of America, 2008. **105**(13): p. 5099-5104.

72. Sevigny, J., et al., *The antibody aducanumab reduces Aβ plaques in Alzheimer's disease.* Nature, 2016. **537**(7618): p. 50-56.

73. de Araújo, D.P., et al., *Behavioral and neurochemical effects of alpha-lipoic Acid in the model of Parkinson's disease induced by unilateral stereotaxic injection of 6-ohda in rat.* Evidence-based complementary and alternative medicine : eCAM, 2013. **2013**: p. 571378-571378.

74. Perchiacca, J.M., et al., *Structure-based design of conformation- and sequence-specific antibodies against amyloid β.* Proceedings of the National Academy of Sciences of the United States of America, 2012. **109**(1): p. 84-89.

75. Palhano, F.L., et al., *Toward the molecular mechanism(s) by which EGCG treatment remodels mature amyloid fibrils.* Journal of the American Chemical Society, 2013. **135**(20): p. 7503-7510.

76. Feng, Y., et al., *Resveratrol inhibits beta-amyloid oligomeric cytotoxicity but does not prevent oligomer formation.* NeuroToxicology, 2009. **30**(6): p. 986-995.

77. Thapa, A., S.D. Jett, and E.Y. Chi, *Curcumin attenuates amyloid-β aggregate toxicity and modulates amyloid-β aggregation pathway.* ACS Chemical Neuroscience, 2016. **7**(1): p. 56-68.

78. Boespflug, E.L., et al., *Targeted assessment of enlargement of the perivascular space in Alzheimer's disease and vascular dementia subtypes implicates astroglial involvement specific to Alzheimer's disease.* Journal of Alzheimer's disease : JAD, 2018. **66**(4): p. 1587-1597.

79. Sokolowski, J.D. and J.W. Mandell, *Phagocytic clearance in neurodegeneration.* The American journal of pathology, 2011. **178**(4): p. 1416-1428.

80. Kanekiyo, T. and G. Bu, *The low-density lipoprotein receptor-related protein 1 and amyloid-β clearance in Alzheimer's disease.* Frontiers in aging neuroscience, 2014. **6**: p. 93-93.

81. Bruno, M.A., et al., *Increased matrix metalloproteinase 9 activity in mild cognitive impairment.* Journal of Neuropathology & Experimental Neurology, 2009. **68**(12): p. 1309-1318.

82. de Roos, P., et al., *A consensus set of outcomes for parkinson's disease from the international consortium for health outcomes measurement.* Journal of Parkinson's disease, 2017. **7**(3): p. 533-543.

83. Goldman, J.G., et al., *Cognitive impairment in Parkinson's disease: a report from a multidisciplinary symposium on unmet needs and future directions to maintain cognitive health.* npj Parkinson's disease, 2018. **4**(1): p. 19.

84. E. RayDorsey, et al., *Global, regional, and national burden of Parkinson's disease, 1990–2016: a systematic analysis for the Global Burden of Disease Study 2016.* THE LANCET Neurology 2018. **17**(11): p. 939-953.

85. Rocca, W.A., *The burden of Parkinson's disease: a worldwide perspective.* Lancet Neurol, 2018. **17**(11): p. 928-929.

86. Goubault, E., et al., *Cardinal motor features of parkinson's disease coexist with peak-dose choreic-type drug-induced dyskinesia.* Journal of Parkinson's disease, 2018. **8**(2): p. 323-331.

87. Maiti, P., J. Manna, and G.L. Dunbar, *Current understanding of the molecular mechanisms in Parkinson's disease: Targets for potential treatments.* Translational Neurodegeneration, 2017. **6**(1): p. 28.

88. Cooper, J.F., et al., *Delaying aging is neuroprotective in Parkinson's disease: a genetic analysis in C. elegans models.* Npj Parkinson's Disease, 2015. **1**: p. 15022.

89. German, D.C., et al., *Midbrain dopaminergic cell loss in parkinson's disease: Computer visualization.* Annals of Neurology, 1989. **26**(4): p. 507-514.

90. Alexander, G.E., *Biology of Parkinson's disease: pathogenesis and pathophysiology of a multisystem neurodegenerative disorder.* Dialogues in clinical neuroscience, 2004. **6**(3): p. 259-280.

91. Canerina-Amaro, A., et al., *Differential aggregation and phosphorylation of alpha Synuclein in membrane compartments associated with parkinson disease.* Front Neurosci, 2019. **13**: p. 382.

92. Oueslati, A., M. Fournier, and H.A. Lashuel, *Chapter 7 - Role of post-translational modifications in modulating the structure, function and toxicity of α-Synuclein : Implications for Parkinson's disease pathogenesis and therapies*, in *Progress in Brain Research*, A. Björklund and M.A. Cenci, Editors. 2010, Elsevier. p. 115-145.

93. Fiske, M., et al., *Contribution of alanine-76 and serine phosphorylation in α-Synuclein membrane association and aggregation in yeasts.* Parkinson's disease, 2011. **2011**: p. 392180-392180.

94. Hara, S., et al., *Serine 129 phosphorylation of membrane-associated α-Synuclein modulates dopamine transporter function in a G protein-coupled receptor kinase-dependent manner.* Molecular biology of the cell, 2013. **24**(11): p. 1649-S3.

95. Oueslati, A., *Implication of alpha-Synuclein phosphorylation at S129 in Synuclein opathies: What have we learned in the last decade?* Journal of Parkinson's disease, 2016. **6**(1): p. 39-51.

96. Polymeropoulos, M.H., et al., *Mutation in the alpha-Synuclein gene identified in families with Parkinson's disease.* Science, 1997. **276**(5321): p. 2045-7.

97. Kruger, R., et al., *Ala30Pro mutation in the gene encoding alpha-Synuclein in Parkinson's disease.* Nat Genet, 1998. **18**(2): p. 106-8.

98. Sato, H., et al., *Authentically phosphorylated α-Synuclein at Ser129 accelerates neurodegeneration in a rat model of familial Parkinson's disease.* The Journal of neuroscience : the official journal of the Society for Neuroscience, 2011. **31**(46): p. 16884-16894.

99. Foulds, P.G., et al., *A longitudinal study on α-Synuclein in blood plasma as a biomarker for Parkinson's disease.* Scientific reports, 2013. **3**: p. 2540-2540.

100. Hilton, D., et al., *Accumulation of α-Synuclein in the bowel of patients in the pre-clinical phase of Parkinson's disease.* Acta Neuropathologica, 2014. **127**(2): p. 235-241.

101. Wang, X. and E.K. Michaelis, *Selective neuronal vulnerability to oxidative stress in the brain.* Frontiers in aging neuroscience, 2010. **2**: p. 12-12.

102. Perfeito, R., T. Cunha-Oliveira, and A.C. Rego, *Revisiting oxidative stress and mitochondrial dysfunction in the pathogenesis of Parkinson disease—resemblance to the effect of amphetamine drugs of abuse.* Free Radical Biology and Medicine, 2012. **53**(9): p. 1791-1806.

103. Chavarria, C., et al., *Nitroalkylation of alpha-Synuclein by Nitro-Oleic Acid: Implications for Parkinson's disease.* Adv Exp Med Biol, 2019. **1127**: p. 169-179.

104. Muñoz, Y., et al., *Parkinson's disease: The Mitochondria-Iron Link.* Parkinson's disease, 2016. **2016**: p. 7049108-7049108.

105. Leal, M.C., et al., *Interleukin-1β and tumor necrosis factor-α: reliable targets for protective therapies in Parkinson's disease?* Frontiers in cellular neuroscience, 2013. **7**: p. 53-53.

106. Wang, Q., Y. Liu, and J. Zhou, *Neuroinflammation in Parkinson's disease and its potential as therapeutic target.* Translational neurodegeneration, 2015. **4**: p. 19-19.

107. Mercado, G., et al., *ER stress and Parkinson's disease: Pathological inputs that converge into the secretory pathway.* Brain Research, 2016. **1648**: p. 626-632.

108. Pukaß, K. and C. Richter-Landsberg, *Inhibition of UCH-L1 in oligodendroglial cells results in microtubule stabilization and prevents α-Synuclein aggregate formation by activating the autophagic pathway: implications for multiple system atrophy.* Frontiers in cellular neuroscience, 2015. **9**: p. 163-163.

109. Fornai, F., et al., *Fine structure and biochemical mechanisms underlying nigrostriatal inclusions and cell death after proteasome inhibition.* The Journal of neuroscience : the official journal of the Society for Neuroscience, 2003. **23**(26): p. 8955-8966.

110. Han, Y.H., et al., *The effect of MG132, a proteasome inhibitor on HeLa cells in relation to cell growth, reactive oxygen species and GSH.* Oncol Rep, 2009. **22**(1): p. 215-21.

111. McNaught, K.S.P., et al., *Systemic exposure to proteasome inhibitors causes a progressive model of Parkinson's disease.* Annals of Neurology, 2004. **56**(1): p. 149-162.

112. Dokladny, K., O.B. Myers, and P.L. Moseley, *Heat shock response and autophagy--cooperation and control.* Autophagy, 2015. **11**(2): p. 200-213.

113. Klucken, J., et al., *A single amino acid substitution differentiates Hsp70-dependent effects on α-Synuclein degradation and toxicity.* Biochemical and Biophysical Research Communications, 2004. **325**(1): p. 367-373.

114. Weinhold, B., *Epigenetics: the science of change.* Environmental health perspectives, 2006. **114**(3): p. A160-A167.

115. Chen, Z., et al., *Epigenetic regulation: a new frontier for biomedical engineers.* Annual Review of Biomedical Engineering, 2017. **19**(1): p. 195-219.

116. Mastrototaro, G. and A. Sessa, *Chapter 9 - Emerging role of epigenetics in human neurodevelopmental disorders*, in *Epigenetics in Human disease (Second Edition)*, T.O. Tollefsbol, Editor. 2018, Academic Press. p. 269-304.

117. Cutter, A.R. and J.J. Hayes, *A brief review of nucleosome structure.* FEBS letters, 2015. **589**(20 Pt A): p. 2914-2922.

118. Arents, G., et al., *The nucleosomal core histone octamer at 3.1 A resolution: a tripartite protein assembly and a left-handed superhelix.* Proceedings of the National Academy of Sciences, 1991. **88**(22): p. 10148.

119. Eickbush, T.H. and E.N. Moudrianakis, *The histone core complex: an octamer assembled by two sets of protein-protein interactions.* Biochemistry, 1978. **17**(23): p. 4955-4964.

120. Di Croce, L. and K. Helin, *Transcriptional regulation by Polycomb group proteins.* Nature Structural & Molecular Biology, 2013. **20**(10): p. 1147-1155.

121. Simon, J.A., *Polycomb group proteins.* Current Biology, 2003. **13**(3): p. R79-R80.

122. Chittock, E.C., et al., *Molecular architecture of polycomb repressive complexes.* Biochemical Society transactions, 2017. **45**(1): p. 193-205.

123. Margueron, R. and D. Reinberg, *The Polycomb complex PRC2 and its mark in life.* Nature, 2011. **469**(7330): p. 343-349.

124. Vidal, M. and K. Starowicz, *Polycomb complexes PRC1 and their function in hematopoiesis.* Experimental Hematology, 2017. **48**: p. 12-31.

125. Buchwald, G., et al., *Structure and E3-ligase activity of the Ring–Ring complex of Polycomb proteins Bmi1 and Ring1b.* The EMBO Journal, 2006. **25**(11): p. 2465-2474.

126. Huang, Y., et al., *Evolution and conservation of polycomb repressive complex 1 core components and putative associated factors in the green lineage.* BMC Genomics, 2019. **20**(1): p. 533.

127. Chatoo, W., et al., *The polycomb group gene BMI1 regulates antioxidant defenses in neurons by repressing p53 pro-oxidant activity.* The Journal of Neuroscience, 2009. **29**(2): p. 529-542.

128. Liu, J., et al., *Bmi1 regulates mitochondrial function and the DNA damage response pathway.* Nature, 2009. **459**(7245): p. 387-392.

129. Alchanati, I., et al., *The E3 ubiquitin-ligase BMI1/RING1a controls the proteasomal degradation of TOP2α cleavage complex – a potentially new drug target.* PLOS ONE, 2009. **4**(12): p. e8104.

130. Ismail, I.H., et al., *A small molecule inhibitor of polycomb repressive complex 1 inhibits ubiquitin signaling at DNA double-strand breaks.* The Journal of biological chemistry, 2013. **288**(37): p. 26944-26954.

131. Kagey, M.H., T.A. Melhuish, and D. Wotton, *The Polycomb Protein Pc2 Is a SUMO E3.* Cell, 2003. **113**(1): p. 127-137.

132. Oh, Y., et al., *Human Polycomb protein 2 promotes α-Synuclein aggregate formation through covalent SUMOylation.* Brain Research, 2011. **1381**: p. 78-89.

133. Xylaki, M., B. Atzler, and T.F. Outeiro, *Epigenetics of the synapse in neurodegeneration.* Current Neurology and Neuroscience Reports, 2019. **19**(10): p. 72.

134. Pampaloni, N.P., et al., *Advances in nano neuroscience: From nanomaterials to nanotools.* Frontiers in Neuroscience, 2019. **12**(953).

135. Jeevanandam, J., et al., *Review on nanoparticles and nanostructured materials: history, sources, toxicity and regulations.* Beilstein journal of nanotechnology, 2018. **9**: p. 1050-1074.

136. Ambesh, P. and D.G. Angeli, *Nanotechnology in neurology: Genesis, current status, and future prospects.* Annals of Indian Academy of Neurology, 2015. **18**(4): p. 382-386.

137. Al-Jawad, S.M.H., A.A. Taha, and A.M. Redha, *Studying the structural, morphological, and optical properties of CuS:Ni nanostructure prepared by a hydrothermal method for biological activity.* Journal of Sol-Gel Science and Technology, 2019. **91**(2): p. 310-323.

138. Re, F., R. Moresco, and M. Masserini, *Nanoparticles for neuroimaging.* Journal of Physics D: Applied Physics, 2012. **45**(7): p. 073001.

139. Kim, K.-T., et al., *Nanodelivery systems for overcoming limited transportation of therapeutic molecules through the blood–brain barrier.* Future Medicinal Chemistry, 2018. **10**(22): p. 2659-2674.

140. Sardoiwala, M.N., et al., *Nanostructure endows neurotherapeutic potential in optogenetics: Current development and future prospects.* ACS Chemical Neuroscience, 2019. **10**(8): p. 3375-3385.

141. Fathi-Achachelouei, M., et al., *Use of nanoparticles in tissue engineering and regenerative medicine.* Frontiers in Bioengineering and Biotechnology, 2019. **7**(113).

142. Shi, N., et al., *Brain-specific expression of an exogenous gene after i.v. administration.* Proceedings of the National Academy of Sciences of the United States of America, 2001. **98**(22): p. 12754-12759.

143. Pilakka-Kanthikeel, S., et al., *Targeted brain derived neurotropic factors (BDNF) delivery across the blood-brain barrier for neuro-protection using magnetic nano carriers: an in-vitro study.* PloS one, 2013. **8**(4): p. e62241-e62241.

144. Bunten, S. and S. Happe, *Rotigotine transdermal system: a short review.* Neuropsychiatric disease and treatment, 2006. **2**(4): p. 421-426.

145. Zheng, M., et al., *Self-targeting fluorescent carbon dots for diagnosis of brain cancer cells.* ACS Nano, 2015. **9**(11): p. 11455-11461.

146. Diaz-Casado, M.E., et al., *Melatonin rescues zebrafish embryos from the parkinsonian phenotype restoring the parkin/PINK1/DJ-1/MUL1 network.* J Pineal Res, 2016. **61**(1): p. 96-107.

147. Chuang, J.I. and T.H. Chen, *Effect of melatonin on temporal changes of reactive oxygen species and glutathione after MPP(+) treatment in human astrocytoma U373MG cells.* J Pineal Res, 2004. **36**(2): p. 117-25.

148. Chen, X., et al., *Melatonin inhibits tumorigenicity of glioblastoma stem-like cells via the AKT-EZH2-STAT3 signaling axis.* J Pineal Res, 2016. **61**(2): p. 208-17.

149. Yi, C., et al., *Melatonin enhances the anti-tumor effect of fisetin by inhibiting COX-2/iNOS and NF-kappaB/p300 signaling pathways.* PLoS One, 2014. **9**(7): p. e99943.

150. Batul, R., et al., *Synthesis of polydopamine nanoparticles for drug delivery applications.* Microscopy and Microanalysis, 2018. **24**(S1): p. 1758-1759.

151. Peniston-Bird, J.F., et al., *HPLC assay of melatonin in plasma with fluorescence detection.* Clinical Chemistry, 1993. **39**(11): p. 2242-2247.

152. Zagajewski, J., et al., *Conversion L-tryptophan to melatonin in the gastrointestinal tract: the new high performance liquid chromatography method enabling simultaneous determination of six metabolites of L-tryptophan by native fluorescence and UV-VIS detection.* J Physiol Pharmacol, 2012. **63**(6): p. 613-21.

153. Singh, P., et al., *Design and development of Amphotericin B bearing polycaprolactone microparticles for macrophage targeting.* J Biomed Nanotechnol, 2011. **7**(1): p. 50-1.

154. Guzzarlamudi, S., et al., *Synergistic chemotherapeutic activity of curcumin bearing methoxypolyethylene glycol-g-linoleic acid based micelles on breast cancer cells.* J Nanosci Nanotechnol, 2016. **16**(4): p. 4180-90.

155. Zhang, Y., et al., *DDSolver: an add-in program for modeling and comparison of drug dissolution profiles.* The AAPS journal, 2010. **12**(3): p. 263-271.

156. Meiser, J., D. Weindl, and K. Hiller, *Complexity of dopamine metabolism.* Cell Commun Signal, 2013. **11**(1): p. 34.

157. Nicolini, G., et al., *Retinoic acid differentiated SH-SY5Y human neuroblastoma cells: an in vitro model to assess drug neurotoxicity.* Anticancer Res, 1998. **18**(4A): p. 2477-81.

158. Yan, F., et al., *NIR-laser-controlled drug release from DOX/IR-780-loaded temperature-sensitive-liposomes for chemo-photothermal synergistic tumor therapy.* Theranostics, 2016. **6**(13): p. 2337-2351.

159. Stine, W.B., Jr., et al., *In vitro characterization of conditions for amyloid-beta peptide oligomerization and fibrillogenesis.* J Biol Chem, 2003. **278**(13): p. 11612-22.

160. Jan, A., D.M. Hartley, and H.A. Lashuel, *Preparation and characterization of toxic Abeta aggregates for structural and functional studies in Alzheimer's disease research.* Nat Protoc, 2010. **5**(6): p. 1186-209.

161. Jung, B.C., et al., *Amplification of distinct α-Synuclein fibril conformers through protein misfolding cyclic amplification.* Experimental & molecular medicine, 2017. **49**(4): p. e314-e314.

162. Du, Z., et al., *Isolation and pre-concentration of basic proteins in aqueous mixture via solid-phase extraction with multi-walled carbon nanotubes assembled on a silica surface.* Analyst, 2008. **133**(10): p. 1373-9.

163. Eren, N.M., G. Narsimhan, and O.H. Campanella, *Protein adsorption induced bridging flocculation: the dominant entropic pathway for nano-bio complexation.* Nanoscale, 2016. **8**(6): p. 3326-36.

164. Iafisco, M., et al., *Adsorption and spectroscopic characterization of lactoferrin on hydroxyapatite nanocrystals.* Dalton Trans, 2011. **40**(4): p. 820-7.

165. Hulme, E.C. and M.A. Trevethick, *Ligand binding assays at equilibrium: validation and interpretation.* British Journal of Pharmacology, 2010. **161**(6): p. 1219-1237.

166. Ladha, S., A.R. Mackie, and D.C. Clark, *Cheek cell membrane fluidity measured by fluorescence recovery after photobleaching and steady-state fluorescence anisotropy.* J Membr Biol, 1994. **142**(2): p. 223-8.

167. Cameron, W.D., et al., *Apollo-NADP(+): a spectrally tunable family of genetically encoded sensors for NADP(+).* Nat Methods, 2016. **13**(4): p. 352-8.

168. Richardson, J.J., et al., *Innovation in Layer-by-Layer Assembly.* Chemical Reviews, 2016. **116**(23): p. 14828-14867.

169. Fan, D., et al., *Polydopamine nanotubes as an effective fluorescent quencher for highly sensitive and selective detection of biomolecules assisted with exonuclease III amplification.* Analytical Chemistry, 2016. **88**(18): p. 9158-9165.

170. Poinard, B., et al., *Polydopamine nanoparticles enhance drug release for combined photodynamic and photothermal therapy.* ACS Appl Mater Interfaces, 2018. **10**(25): p. 21125-21136.

171. Haining, R.L. and C. Achat-Mendes, *Neuromelanin, one of the most overlooked molecules in modern medicine, is not a spectator.* Neural regeneration research, 2017. **12**(3): p. 372-375.

172. Zecca, L., et al., *The protective and toxic role of neuromelanins in brain aging and Parkinson's disease.* SpringerPlus, 2015. **4**(Suppl 1): p. P56.

173. Zecca, L., et al., *Substantia nigra neuromelanin: structure, synthesis, and molecular behaviour.* Molecular pathology : MP, 2001. **54**(6): p. 414-418.

174. Sun, Y., et al., *Kinetic modeling of pH-dependent oxidation of dopamine by iron and its relevance to parkinson's disease.* Frontiers in Neuroscience, 2018. **12**(859).

175. Iuga, C., J.R. Alvarez-Idaboy, and A. Vivier-Bunge, *ROS initiated oxidation of dopamine under oxidative stress conditions in aqueous and lipidic environments.* The journal of physical chemistry. B, 2011. **115**(42): p. 12234-12246.

176. Santiago-López, D., et al., *Oxidative stress, progressive damage in the substantia nigra and plasma dopamine oxidation, in rats chronically exposed to ozone.* Toxicology Letters, 2010. **197**(3): p. 193-200.

177. LaVoie, M.J. and T.G. Hastings, *Dopamine quinone formation and protein modification associated with the striatal neurotoxicity of methamphetamine: evidence against a role for extracellular dopamine.* The Journal of Neuroscience, 1999. **19**(4): p. 1484-1491.

178. Galzigna, L., A. De Iuliis, and L. Zanatta, *Enzymatic dopamine peroxidation in substantia nigra of human brain.* Clinica chimica acta; international journal of clinical chemistry, 2000. **300**(1-2): p. 131-138.

179. Block, M.L., L. Zecca, and J.-S. Hong, *Microglia-mediated neurotoxicity: uncovering the molecular mechanisms.* Nature Reviews Neuroscience, 2007. **8**: p. 57.

180. Segura-Aguilar, J., et al., *Protective and toxic roles of dopamine in Parkinson's disease.* Journal of Neurochemistry, 2014. **129**(6): p. 898-915.

181. Muñoz, P., et al., *DT-diaphorase prevents aminochrome-induced alpha-Synuclein oligomer formation and neurotoxicity.* Toxicological sciences : an official journal of the Society of Toxicology, 2015. **145**(1): p. 37-47.

182. Herrera, A., et al., *Are dopamine oxidation metabolites involved in the loss of dopaminergic neurons in the nigrostriatal system in parkinson's disease?* ACS Chemical Neuroscience, 2017. **8**(4): p. 702-711.

183. Solano, F., V.J. Hearing, and J.C. García-Borrón, *Neurotoxicity due to o-Quinones: Neuromelanin formation and possible mechanisms for o-Quinone detoxification.* Neurotoxicity Research, 1999. **1**(3): p. 153-169.

184. Wei, Q., et al., *Oxidant-induced dopamine polymerization for multifunctional coatings.* Polymer Chemistry, 2010. **1**(9): p. 1430-1433.

185. Liu, R., et al., *Core–shell Fe_3O_4 polydopamine nanoparticles serve multipurpose as drug carrier, catalyst support and carbon adsorbent.* ACS Applied Materials & Interfaces, 2013. **5**(18): p. 9167-9171.

186. Dreyer, D.R., et al., *Elucidating the structure of poly(dopamine).* Langmuir, 2012. **28**(15): p. 6428-6435.

187. Liu, Y., et al., *Preferential localization of a vesicular monoamine transporter to dense core vesicles in PC12 cells.* J Cell Biol, 1994. **127**(5): p. 1419-33.

188. Sulzer, D., et al., *Neuromelanin biosynthesis is driven by excess cytosolic catecholamines not accumulated by synaptic vesicles.* Proc Natl Acad Sci U S A, 2000. **97**(22): p. 11869-74.

189. Ryu, J.H., P.B. Messersmith, and H. Lee, *Polydopamine Surface Chemistry: A Decade of Discovery.* ACS applied materials & interfaces, 2018. **10**(9): p. 7523-7540.

190. Tan, D.-X., et al., *Significance of high levels of endogenous melatonin in Mammalian cerebrospinal fluid and in the central nervous system.* Current neuropharmacology, 2010. **8**(3): p. 162-167.

191. Gottås, A., et al., *Determination of dopamine concentrations in brain extracellular fluid using microdialysis with short sampling intervals, analyzed by ultra high performance liquid chromatography tandem mass spectrometry.* Journal of Pharmacological and Toxicological Methods, 2015. **74**: p. 75-79.

192. Bisaglia, M., S. Mammi, and L. Bubacco, *Kinetic and structural analysis of the early oxidation products of dopamine: analysis of the interactions with alpha-Synuclein .* J Biol Chem, 2007. **282**(21): p. 15597-605.

193. Jimenez, M., et al., *Chemical intermediates in dopamine oxidation by tyrosinase, and kinetic studies of the process.* Archives of Biochemistry and Biophysics, 1984. **235**(2): p. 438-448.

194. Wu, L., J. Zhang, and W. Watanabe, *Physical and chemical stability of drug nanoparticles.* Advanced Drug Delivery Reviews, 2011. **63**(6): p. 456-469.

195. Bettinger, C.J., et al., *Biocompatibility of biodegradable semiconducting melanin films for nerve tissue engineering.* Biomaterials, 2009. **30**(17): p. 3050-3057.

196. Liu, Y., et al., *Dopamine-melanin colloidal nanospheres: an efficient near-infrared photothermal therapeutic agent for in vivo cancer therapy.* Advanced Materials, 2013. **25**(9): p. 1353-1359.

197. Tan, D.-X., et al., *Melatonin directly scavenges hydrogen peroxide: a potentially new metabolic pathway of melatonin biotransformation.* Free Radical Biology and Medicine, 2000. **29**(11): p. 1177-1185.

198. Tan, D.-X., et al., *Melatonin suppresses autoxidation and hydrogen peroxide-induced lipid peroxidation in monkey brain homogenate.* Neuro endocrinology letters, 2000. **21**(5): p. 361-365.

199. Oueslati, A., M. Fournier, and H.A. Lashuel, *Role of post-translational modifications in modulating the structure, function and toxicity of alpha-Synuclein : implications for Parkinson's disease pathogenesis and therapies.* Prog Brain Res, 2010. **183**: p. 115-45.

200. Nubling, G.S., et al., *Modelling Ser129 phosphorylation inhibits membrane binding of pore-forming alpha-Synuclein oligomers.* PLoS One, 2014. **9**(6): p. e98906.

201. Visanji, N.P., et al., *Effect of Ser-129 phosphorylation on interaction of alpha-Synuclein with synaptic and cellular membranes.* J Biol Chem, 2011. **286**(41): p. 35863-73.

202. Liu, L.L. and K.J. Franz, *Phosphorylation-dependent metal binding by alpha-Synuclein peptide fragments.* J Biol Inorg Chem, 2007. **12**(2): p. 234-47.

203. Burre, J., et al., *Alpha-Synuclein promotes SNARE-complex assembly in vivo and in vitro.* Science, 2010. **329**(5999): p. 1663-7.

204. Schell, H., et al., *Nuclear and neuritic distribution of serine-129 phosphorylated alpha-Synuclein in transgenic mice.* Neuroscience, 2009. **160**(4): p. 796-804.

205. Zhou, R.M., et al., *Molecular interaction of alpha-Synuclein with tubulin influences on the polymerization of microtubule in vitro and structure of microtubule in cells.* Mol Biol Rep, 2010. **37**(7): p. 3183-92.

206. Löhle, M. and H. Reichmann, *Clinical neuroprotection in Parkinson's disease — Still waiting for the breakthrough.* Journal of the Neurological Sciences, 2010. **289**(1): p. 104-114.

207. Karlsson, A.M., et al., *Melatonin-induced organelle movement in melanophores is coupled to tyrosine phosphorylation of a high molecular weight protein.* Cell Signal, 2000. **12**(7): p. 469-74.

208. Huang, Y., et al., *Mimicking melanosomes: Polydopamine nanoparticles as artificial microparasols.* ACS Cent Sci, 2017. **3**(6): p. 564-569.

209. Ding, L., et al., *Intracellular fate of nanoparticles with polydopamine surface engineering and a novel strategy for exocytosis-inhibiting, lysosome impairment-based cancer therapy.* Nano Letters, 2017. **17**(11): p. 6790-6801.

210. Koprich, J.B., et al., *Neuroinflammation mediated by IL-1beta increases susceptibility of dopamine neurons to degeneration in an animal model of Parkinson's disease.* Journal of neuroinflammation, 2008. **5**: p. 8-8.

211. Cardinali, D.P., et al., *Melatonin therapy in patients with Alzheimer's disease.* Antioxidants (Basel), 2014. **3**(2): p. 245-77.

212. Kilic, U., et al., *Particular phosphorylation of PI3K/Akt on Thr308 via PDK-1 and PTEN mediates melatonin's neuroprotective activity after focal cerebral ischemia in mice.* Redox Biol, 2017. **12**: p. 657-665.

213. Meng, X., et al., *Dietary Sources and Bioactivities of Melatonin.* Nutrients, 2017. **9**(4).

214. Su, X., et al., *Alpha-Synuclein mRNA is not increased in sporadic PD and alpha-Synuclein accumulation does not block GDNF signaling in parkinson's disease and disease models.* Molecular therapy : the journal of the American Society of Gene Therapy, 2017. **25**(10): p. 2231-2235.

215. Arawaka, S., et al., *Mechanisms underlying extensive Ser129-phosphorylation in α-Synuclein aggregates.* Acta neuropathologica communications, 2017. **5**(1): p. 48-48.

216. Samuel, F., et al., *Effects of Serine 129 Phosphorylation on alpha-Synuclein Aggregation, Membrane Association, and Internalization.* J Biol Chem, 2016. **291**(9): p. 4374-85.

217. Aoki, R. and Y.R. Li, *α-Synuclein promotes neuroprotection through NF-κB–mediated transcriptional regulation of protein kinase Cδ.* Science Signaling, 2011. **4**(195): p. jc6-jc6.

218. Zhang, X., et al., *Therapeutic effects of baicalein on rotenone-induced Parkinson's disease through protecting mitochondrial function and biogenesis.* Scientific Reports, 2017. **7**(1): p. 9968.

219. Thakur, P., et al., *Modeling Parkinson's disease pathology by combination of fibril seeds and α-Synuclein overexpression in the rat brain.* Proceedings of the National Academy of Sciences, 2017. **114**(39): p. E8284-E8293.

220. Schlachetzki, J.C.M., et al., *Dopaminergic lesioning impairs adult hippocampal neurogenesis by distinct modification of α-Synuclein .* Journal of Neuroscience Research, 2016. **94**(1): p. 62-73.

221. Goldsmith, S.K. and J.N. Joyce, *Dopamine D2 receptor expression in hippocampus and parahippocampal cortex of rat, cat, and human in relation to tyrosine hydroxylase-immunoreactive fibers.* Hippocampus, 1994. **4**(3): p. 354-373.

222. La, C., et al., *Hippocampal CA1 subfield predicts episodic memory impairment in Parkinson's disease.* NeuroImage: Clinical, 2019. **23**: p. 101824.

223. Pang, C.C.-C., et al., *Ammon's Horn 2 (CA2) of the Hippocampus: A long-known region with a new potential role in neurodegeneration.* The Neuroscientist, 2018. **25**(2): p. 167-180.

224. Di Croce, L. and K. Helin, *Transcriptional regulation by Polycomb group proteins.* Nat Struct Mol Biol, 2013. **20**(10): p. 1147-55.

225. Margueron, R., et al., *Ezh1 and Ezh2 maintain repressive chromatin through different mechanisms.* Mol Cell, 2008. **32**(4): p. 503-18.

226. Cao, R., Y. Tsukada, and Y. Zhang, *Role of Bmi-1 and Ring1A in H2A ubiquitylation and Hox gene silencing.* Mol Cell, 2005. **20**(6): p. 845-54.

227. Abdouh, M., et al., *Bmi1 is down-regulated in the aging brain and displays antioxidant and protective activities in neurons.* PLoS One, 2012. **7**(2): p. e31870.

228. Abdouh, M., et al., *Bmi1 is down-regulated in the aging brain and displays antioxidant and protective activities in neurons.* PloS one, 2012. **7**(2): p. e31870-e31870.

229. Barabino, A., et al., *Loss of Bmi1 causes anomalies in retinal development and degeneration of cone photoreceptors.* Development, 2016. **143**(9): p. 1571-1584.

230. Chatoo, W., et al., *The polycomb group gene Bmi1 regulates antioxidant defenses in neurons by repressing p53 pro-oxidant activity.* The Journal of neuroscience : the official journal of the Society for Neuroscience, 2009. **29**(2): p. 529-542.

231. Stapels, M., et al., *Polycomb group proteins as epigenetic mediators of neuroprotection in Ischemic tolerance.* Science Signaling, 2010. **3**(111): p. ra15-ra15.

232. Shen, J., et al., *The E3 ligase ring1 targets p53 for degradation and promotes cancer cell proliferation and survival.* Cancer Research, 2018. **78**(2): p. 359-371.

233. Lardenoije, R., et al., *The epigenetics of aging and neurodegeneration.* Progress in Neurobiology, 2015. **131**: p. 21-64.

234. Li, J., et al., *EZH2-mediated H3K27 trimethylation mediates neurodegeneration in ataxia-telangiectasia.* Nat Neurosci, 2013. **16**(12): p. 1745-53.

235. Yadav, R. and H.R. Weng, *EZH2 regulates spinal neuroinflammation in rats with neuropathic pain.* Neuroscience, 2017. **349**: p. 106-117.

236. Rott, R., et al., *α-Synuclein ubiquitination and novel therapeutic targets for Parkinson's disease.* CNS and Neurological Disorders - Drug Targets, 2014. **13**(4): p. 630-637.

237. Park, H.J., et al., *The ER retention protein RER1 promotes alpha-Synuclein degradation via the proteasome.* PLoS One, 2017. **12**(9): p. e0184262.

238. Hoffmeister, C.R., et al., *Hydrogels containing redispersible spray-dried melatonin-loaded nanocapsules: a formulation for transdermal-controlled delivery.* Nanoscale Res Lett, 2012. **7**(1): p. 251.

239. Komninou, E.R., et al., *Effects of two types of melatonin-loaded nanocapsules with distinct supramolecular structures: Polymeric (NC) and lipid-core nanocapsules (LNC) on bovine embryo culture model.* PLoS One, 2016. **11**(6): p. e0157561.

240. Yang, L., et al., *Polydopamine particle-filled shape-memory polyurethane composites with fast near-infrared light responsibility.* Chemphyschem, 2018. **19**(16): p. 2052-2057.

241. Ambekar, R.S. and B. Kandasubramanian, *A polydopamine-based platform for anti-cancer drug delivery.* Biomater Sci, 2019. **7**(5): p. 1776-1793.

242. El Turk, F., et al., *Exploring the role of post-translational modifications in regulating alpha-Synuclein interactions by studying the effects of phosphorylation on nanobody binding.* Protein Sci, 2018. **27**(7): p. 1262-1274.

243. Zhang, J., et al., *Ezh2 regulates adult hippocampal neurogenesis and memory.* J Neurosci, 2014. **34**(15): p. 5184-99.

244. Banerjee Mustafi, S., et al., *BMI1, a new target of CK2α.* Molecular Cancer, 2017. **16**(1): p. 56.

245. Liu, Y., et al., *Akt phosphorylates the transcriptional repressor bmi1 to block its effects on the tumor-suppressing ink4a-arf locus.* Science signaling, 2012. **5**(247): p. ra77-ra77.

246. Flamier, A., et al., *Modeling late-onset sporadic Alzheimer's disease through bmi1 deficiency.* Cell Reports, 2018. **23**(9): p. 2653-2666.

247. Sugeno, N., et al., *Serine 129 phosphorylation of alpha-Synuclein induces unfolded protein response-mediated cell death.* J Biol Chem, 2008. **283**(34): p. 23179-88.

248. Arawaka, S., et al., *Mechanisms underlying extensive Ser129-phosphorylation in alpha-Synuclein aggregates.* Acta Neuropathol Commun, 2017. **5**(1): p. 48.

249. Wang, Y., et al., *The novel mechanism of rotenone-induced alpha-Synuclein phosphorylation via reduced protein phosphatase 2A activity.* Int J Biochem Cell Biol, 2016. **75**: p. 34-44.

250. Perfeito, R., et al., *Linking alpha-Synuclein phosphorylation to reactive oxygen species formation and mitochondrial dysfunction in SH-SY5Y cells.* Mol Cell Neurosci, 2014. **62**: p. 51-9.

251. Ishido, M., *Melatonin inhibits maneb-induced aggregation of alpha-Synuclein in rat pheochromocytoma cells.* J Pineal Res, 2007. **42**(2): p. 125-30.

252. Lin, A.M., et al., *Melatonin attenuates arsenite-induced apoptosis in rat brain: involvement of mitochondrial and endoplasmic reticulum pathways and aggregation of alpha-Synuclein .* J Pineal Res, 2007. **43**(2): p. 163-71.

253. Klongpanichapak, S., et al., *Melatonin inhibits amphetamine-induced increase in alpha-Synuclein and decrease in phosphorylated tyrosine hydroxylase in SK-N-SH cells.* Neurosci Lett, 2008. **436**(3): p. 309-13.

254. Chang, C.F., et al., *Melatonin attenuates kainic acid-induced neurotoxicity in mouse hippocampus via inhibition of autophagy and alpha-Synuclein aggregation.* J Pineal Res, 2012. **52**(3): p. 312-21.

255. Sae-Ung, K., et al., *Melatonin reduces the expression of alpha-Synuclein in the dopamine containing neuronal regions of amphetamine-treated postnatal rats.* J Pineal Res, 2012. **52**(1): p. 128-37.

256. Ono, K., et al., *Effect of melatonin on alpha-Synuclein self-assembly and cytotoxicity.* Neurobiol Aging, 2012. **33**(9): p. 2172-85.

257. Bentea, E., L. Verbruggen, and A. Massie, *The proteasome inhibition model of Parkinson's disease.* Journal of Parkinson's disease, 2017. **7**(1): p. 31-63.

258. Shamoto-Nagai, M., et al., *An inhibitor of mitochondrial complex I, rotenone, inactivates proteasome by oxidative modification and induces aggregation of oxidized proteins in SH-SY5Y cells.* Journal of Neuroscience Research, 2003. **74**(4): p. 589-597.

259. Arora, M., et al., *RING1A and BMI1 bookmark active genes via ubiquitination of chromatin-associated proteins.* Nucleic acids research, 2016. **44**(5): p. 2136-2144.

260. Taguchi, K., et al., *Brain region-dependent differential expression of alpha-Synuclein .* Journal of Comparative Neurology, 2016. **524**(6): p. 1236-1258.

261. Tang, L., et al., *Deep ultraviolet to near-infrared emission and photoresponse in layered n-doped graphene quantum dots.* ACS Nano, 2014. **8**(6): p. 6312-6320.

262. Qu, D., et al., *Tailoring color emissions from N-doped graphene quantum dots for bioimaging applications.* Light: Science & Applications, 2015. **4**(12): p. e364-e364.

263. Zheng, M., et al., *One-pot to synthesize multifunctional carbon dots for near infrared fluorescence imaging and photothermal cancer therapy.* ACS Applied Materials & Interfaces, 2016. **8**(36): p. 23533-23541.

264. Liu, W., et al., *Carbon dots: surface engineering and applications.* Journal of Materials Chemistry B, 2016. **4**(35): p. 5772-5788.

265. Wang, S., et al., *Structure of the D2 dopamine receptor bound to the atypical antipsychotic drug risperidone.* Nature, 2018. **555**(7695): p. 269-+.

266. Hyman, S.E. and R.C. Malenka, *Addiction and the brain: The neurobiology of compulsion and its persistence.* Nature Reviews Neuroscience, 2001. **2**(10): p. 695-703.

267. Robinson, D.L., et al., *Monitoring rapid chemical communication in the brain.* Chemical Reviews, 2008. **108**(7): p. 2554-2584.

268. Daubner, S.C., T. Le, and S. Wang, *Tyrosine hydroxylase and regulation of dopamine synthesis.* Arch Biochem Biophys, 2011. **508**(1): p. 1-12.

269. Jancso, G., *A rapid fluorescence microscopic method for the study of the capillary DOPA-dopamine barrier.* J Neurochem, 1975. **24**(3): p. 579-80.

270. Wang, H.Y. and B.T. Yue Sun, *Study on fluorescence property of dopamine and determination of dopamine by fluorimetry.* Talanta 2002. **57**: p. 899-907.

271. d'Ischia, M., et al., *Polydopamine and eumelanin: from structure-property relationships to a unified tailoring strategy*. Acc Chem Res, 2014. **47**(12): p. 3541-50.

272. Liu, M., et al., *Recent developments in polydopamine: an emerging soft matter for surface modification and biomedical applications.* Nanoscale, 2016. **8**(38): p. 16819-16840.

273. Liu, Y., K. Ai, and L. Lu, *Polydopamine and its derivative materials: synthesis and promising applications in energy, environmental, and biomedical fields.* Chem Rev, 2014. **114**(9): p. 5057-115.

274. Sun, Y.P., et al., *Host-guest carbon dots for enhanced optical properties and beyond.* Scientific Reports, 2015. **5**.

275. Ding, H., et al., *Full-color light-emitting carbon dots with a surface-state-controlled luminescence mechanism.* Acs Nano, 2016. **10**(1): p. 484-491.

276. Hola, K., et al., *Graphitic nitrogen triggers red fluorescence in carbon dots.* Acs Nano, 2017. **11**(12): p. 12402-12410.

277. Medintz, I.L., et al., *Quantum-dot/dopamine bioconjugates function as redox coupled assemblies for in vitro and intracellular pH sensing.* Nature Materials, 2010. **9**(8): p. 676-684.

278. Zhang, T.X., et al., *A novel mechanism for red emission carbon dots: hydrogen bond dominated molecular states emission.* Nanoscale, 2017. **9**(35): p. 13042-13051.

279. Wu, M.H., et al., *Scalable synthesis of organic-soluble carbon quantum dots: superior optical properties in solvents, solids, and LEDs.* Nanoscale, 2017. **9**(35): p. 13195-13202.

280. Urbanc, B., et al., *Dynamics of plaque formation in Alzheimer's disease.* Biophysical journal, 1999. **76**(3): p. 1330-1334.

281. Wright, A.L., et al., *Neuroinflammation and neuronal loss precede Aβ plaque deposition in the hAPP-J20 mouse model of Alzheimer's disease.* PLOS ONE, 2013. **8**(4): p. e59586.

282. Rudnitskaya, E.A., et al., *Melatonin attenuates memory impairment, amyloid-beta accumulation, and neurodegeneration in a rat model of sporadic Alzheimer's disease.* J Alzheimers Dis, 2015. **47**(1): p. 103-16.

283. Arya, M.A., et al., *Nanotechnology approaches for enhanced CNS delivery in treating Alzheimer's disease.* Journal of Drug Delivery Science and Technology, 2019. **51**: p. 297-309.

284. Yang, X., et al., *Melatonin ameliorates Alzheimer-like pathological changes and spatial memory retention impairment induced by calyculin A.* J Psychopharmacol, 2011. **25**(8): p. 1118-25.

285. Poeggeler, B., et al., *Melatonin reverses the profibrillogenic activity of apolipoprotein E4 on the Alzheimer amyloid Abeta peptide.* Biochemistry, 2001. **40**(49): p. 14995-5001.

286. Pappolla, M., et al., *Inhibition of Alzheimer beta-fibrillogenesis by melatonin.* J Biol Chem, 1998. **273**(13): p. 7185-8.

287. Rosales-Corral, S.A., et al., *Alzheimer's disease: pathological mechanisms and the beneficial role of melatonin.* Journal of Pineal Research, 2012. **52**(2): p. 167-202.

288. Feng, Z. and J.-t. Zhang, *Melatonin reduces amyloid β-induced apoptosis in pheochromocytoma (PC12) cells.* Journal of Pineal Research, 2004. **37**(4): p. 257-266.

289. Hoppe, J.B., et al., *Amyloid-β neurotoxicity in organotypic culture is attenuated by melatonin: involvement of GSK-3β, tau and neuroinflammation.* Journal of Pineal Research, 2010. **48**(3): p. 230-238.

290. Johnstone, D.M., et al., *Turning on lights to stop neurodegeneration: The potential of near infrared light therapy in Alzheimer's and parkinson's disease.* Frontiers in neuroscience, 2016. **9**: p. 500-500.

291. Kim, S.H., et al., *Photothermal conversion upon near-infrared irradiation of fluorescent carbon nanoparticles formed from carbonized polydopamine.* RSC Advances, 2016. **6**(66): p. 61482-61491.

292. Xing, Y., et al., *Temporally controlled photothermal/photodynamic and combined therapy for overcoming multidrug resistance of cancer by polydopamine nanoclustered micelles.* ACS Appl Mater Interfaces, 2019. **11**(15): p. 13945-13953.

293. You, Y.H., et al., *Polydopamine-coated gold nanostar for combined antitumor and antiangiogenic therapy in multidrug-resistant breast cancer.* Nanotheranostics, 2019. **3**(3): p. 266-283.

294. Cheng, W., et al., *Versatile polydopamine platforms: synthesis and promising applications for surface modification and advanced nanomedicine.* ACS Nano, 2019.

295. Cai, Y., et al., *Optical nano-agents in the second near-infrared window for biomedical applications.* Chemical Society Reviews, 2019. **48**(1): p. 22-37.

296. Liu, S., et al., *Dynamically PEGylated and borate-coordination-polymer-coated polydopamine nanoparticles for synergetic tumor-targeted, chemo-photothermal combination therapy.* Small, 2018. **14**(13): p. e1703968.

297. Xiong, N., et al., *Design of LVFFARK and LVFFARK-functionalized nanoparticles for inhibiting Amyloid β-protein fibrillation and cytotoxicity.* ACS Applied Materials & Interfaces, 2015. **7**(10): p. 5650-5662.

298. Salvadores, N., et al., *Detection of misfolded Aβ oligomers for sensitive biochemical diagnosis of Alzheimer's disease.* Cell Reports, 2014. **7**(1): p. 261-268.

299. Saa, P. and L. Cervenakova, *Protein misfolding cyclic amplification (PMCA): Current status and future directions.* Virus Res, 2015. **207**: p. 47-61.

300. Verbon, E.H., J.A. Post, and J. Boonstra, *The influence of reactive oxygen species on cell cycle progression in mammalian cells.* Gene, 2012. **511**(1): p. 1-6.

301. Chen, X., C. Guo, and J. Kong, *Oxidative stress in neurodegenerative diseases.* Neural regeneration research, 2012. **7**(5): p. 376-385.

302. Reiter, R.J., et al., *Mitochondria: Central organelles for melatonin's antioxidant and anti-aging actions.* Molecules (Basel, Switzerland), 2018. **23**(2): p. 509.

303. Yaron, A. and B. Zheng, *Navigating their way to the clinic: Emerging roles for axon guidance molecules in neurological disorders and injury.* Developmental Neurobiology, 2007. **67**(9): p. 1216-1231.

304. Krishtal, J., et al., *In situ fibrillizing amyloid-beta 1-42 induces neurite degeneration and apoptosis of differentiated SH-SY5Y cells.* PLOS ONE, 2017. **12**(10): p. e0186636.

305. Muche, A., T. Arendt, and R. Schliebs, *Oxidative stress affects processing of amyloid precursor protein in vascular endothelial cells.* PLOS ONE, 2017. **12**(6): p. e0178127.

306. Humpel, C., *Organotypic brain slice cultures: A review.* Neuroscience, 2015. **305**: p. 86-98.

307. Baker, S. and J. Götz, *A local insult of okadaic acid in wild-type mice induces tau phosphorylation and protein aggregation in anatomically distinct brain regions.* Acta Neuropathologica Communications, 2016. **4**(1): p. 32.

308. Foidl, B.M. and C. Humpel, *Differential hyperphosphorylation of Tau-S199, -T231 and -S396 in organotypic brain slices of Alzheimer mice. A model to study early Tau hyperphosphorylation using okadaic acid.* Frontiers in aging neuroscience, 2018. **10**: p. 113-113.

309. Mewes, A., H. Franke, and D. Singer, *Organotypic brain slice cultures of adult transgenic P301S mice—A Model for Tauopathy studies.* PLOS ONE, 2012. **7**(9): p. e45017.

310. Verbeek, M.M., et al., *Accumulation of intercellular adhesion molecule-1 in senile plaques in brain tissue of patients with Alzheimer's disease.* The American journal of pathology, 1994. **144**(1): p. 104-116.

311. Wachholz, S., et al., *Microglia activation is associated with IFN-α induced depressive-like behavior.* Brain, Behavior, and Immunity, 2016. **55**: p. 105-113.

312. Rotello, V.M. and U.H.F. Bunz, *ORGN 43-Protein sensing using fluorescent polymers and nanoparticle-polymer complexes.* Abstracts of Papers of the American Chemical Society, 2008. **235**.

313. Bunz, U. and V.M. Rotello, *POLY 563-Protein and bacteria sensing using nanoparticle-fluorescent polymer complexes.* Abstracts of Papers of the American Chemical Society, 2008. **236**.

314. Bogdanovic, J., et al., *A label-free nanoparticle aggregation assay for protein complex/aggregate detection and study.* Analytical Biochemistry, 2010. **405**(1): p. 96-102.

315. Huo, Q., *Protein complexes/aggregates as potential cancer biomarkers revealed by a nanoparticle aggregation immunoassay.* Colloids and Surfaces B-Biointerfaces, 2010. **78**(2): p. 259-265.

316. Mayavan, S., et al., *Self-organization, interfacial interaction and photophysical properties of gold nanoparticle complexes derived from resilin-mimetic fluorescent protein rec1-resilin.* Biomaterials, 2011. **32**(11): p. 2786-2796.

317. Gunawan, C., et al., *Nanoparticle-protein corona complexes govern the biological fates and functions of nanoparticles.* Journal of Materials Chemistry B, 2014. **2**(15): p. 2060-2083.

318. Ren, D.M., F. Kratz, and S.W. Wang, *Engineered drug-protein nanoparticle complexes for folate receptor targeting.* Biochemical Engineering Journal, 2014. **89**: p. 33-41.

319. Cedervall, T., et al., *Understanding the nanoparticle-protein corona using methods to quantify exchange rates and affinities of proteins for nanoparticles.* Proceedings of the National Academy of Sciences of the United States of America, 2007. **104**(7): p. 2050-2055.

320. Du, L.B., et al., *Mechanism and Cellular Kinetic Studies of the Enhancement of Antioxidant Activity by Using Surface-Functionalized Gold Nanoparticles.* Chemistry-a European Journal, 2013. **19**(4): p. 1281-1287.

321. Walkey, C.D. and W.C.W. Chan, *Understanding and controlling the interaction of nanomaterials with proteins in a physiological environment.* Chemical Society Reviews, 2012. **41**(7): p. 2780-2799.

322. Lynch, I. and K.A. Dawson, *Protein-nanoparticle interactions.* Nano Today, 2008. **3**(1-2): p. 40-47.

323. Selkoe, D.J., *Cell biology of protein misfolding: the examples of Alzheimer's and Parkinson's diseases.* Nat Cell Biol, 2004. **6**(11): p. 1054-61.

324. Reinke, A.A., G.A. Abulwerdi, and J.E. Gestwicki, *Quantifying prefibrillar amyloids in vitro by using a "thioflavin-like" spectroscopic method.* Chembiochem, 2010. **11**(13): p. 1889-1895.

325. Patra, D. and C. Barakat, *Synchronous fluorescence spectroscopic study of solvatochromic curcumin dye.* Spectrochim Acta A Mol Biomol Spectrosc, 2011. **79**(5): p. 1034-41.

326. Komaba, H., et al., *Survival advantage of lanthanum carbonate for hemodialysis patients with uncontrolled hyperphosphatemia.* Nephrology Dialysis Transplantation, 2015. **30**(1): p. 107-114.

327. Gros, B., et al., *Lanthanum carbonate for hyperphosphatemia in chronic kidney disease before and during dialysis: Acost-Effectiveness Analysis in Spain.* Nephrology Dialysis Transplantation, 2014. **29**: p. 270-271.

328. Inaba, M., et al., *Restoration of parathyroid function after change of phosphate binder from calcium carbonate to lanthanum carbonate in hemodialysis patients with suppressed serum parathyroid hormone.* Journal of Renal Nutrition, 2015. **25**(2): p. 242-246.

329. Beaubien-Souligny, W., et al., *The effect of lanthanum carbonate on metabolic acidosis in patients with chronic kidney disease stage IV, V and V-D.* International Urology and Nephrology, 2015. **47**(7): p. 1165-1171.

330. Takahara, Y., et al., *Efficacy and safety of lanthanum carbonate in pre-dialysis CKD patients with hyperphosphatemia: a randomized trial.* Clinical Nephrology, 2014. **82**(3): p. 181-190.

331. Wang, F., et al., *Determination of protein by fluorescence enhancement of curcumin in lanthanum-curcumin-sodium dodecyl benzene sulfonate-protein system.* J Fluoresc, 2011. **21**(1): p. 25-34.

332. Turci, F., et al., *An integrated approach to the study of the interaction between proteins and nanoparticles.* Langmuir, 2010. **26**(11): p. 8336-8346.

333. Pink, M., et al., *Precipitation by lanthanum ions: A straightforward approach to isolating phosphoproteins.* Journal of Proteomics, 2011. **75**(2): p. 375-383.

334. Guzel, Y., et al., *Highly efficient precipitation of phosphoproteins using trivalent europium, terbium, and erbium ions.* Analytical and Bioanalytical Chemistry, 2012. **403**(5): p. 1323-1331.

335. Jiang, X., et al., *Quantitative analysis of the protein corona on FePt nanoparticles formed by transferrin binding.* Journal of the Royal Society Interface, 2010. **7**: p. S5-S13.

336. Cerasoli, E., M. Ryadnov, and B. Austen, *The elusive nature and diagnostics of misfolded Aβ oligomers.* Frontiers in Chemistry, 2015. **3**(17).

337. Ono, M. and H. Saji, *Molecular approaches to the treatment, prophylaxis, and diagnosis of Alzheimer's disease:A novel pet/spect imaging probes for diagnosis of alzheimer disease.* Journal of Pharmacological Sciences, 2012. **118**(3): p. 338-344.

338. Sabaté, R. and J. Estelrich, *Pinacyanol as effective probe of fibrillar β-amyloid peptide: Comparative study with Congo Red.* Biopolymers, 2003. **72**(6): p. 455-463.

339. Satzer, P., et al., *Protein adsorption onto nanoparticles induces conformational changes: Particle size dependency, kinetics, and mechanisms.* Eng Life Sci, 2016. **16**(3): p. 238-246.

340. Wang, F., et al., *Quantitative determination of proteins based on strong fluorescence enhancement in curcumin-chitosan-proteins system.* J Fluoresc, 2012. **22**(2): p. 615-22.

Vitae

Anup K. Srivastava

Ph.D. Research Scholar
Institute of Nano Science and Technology (INST)
&
Indian Institute of Science Education and Research (IISER),
Mohali, Punjab
India

Anup Kumar Srivastava is a Ph.D. research fellow at the Institute of Nano Science and Technology & Indian Institute of Science Education and Research, Mohali, India. As a CSIR junior research fellow, He started his Ph.D. research in biological sciences, where he focused on the novel bioinspired nanostructures development for epigenetic regulation in highly devastating neurodegenerative disease and biosensing of the neurological disease biomarkers. After schooling, He did his B.Sc. in Industrial Microbiology from Gorakhpur University, Uttar Pradesh, India and then completed his M.Sc. in biotechnology from the School of Biotechnology, Banaras Hindu University (BHU), India. He authored several research articles, reviews and book chapters and presented his research outcomes in the meetings both at the national and international platforms. His present research interested is translational nanoscience and biomaterials development for novel disease-modifying therapy against debilitating neurological disorders and CNS cancers.